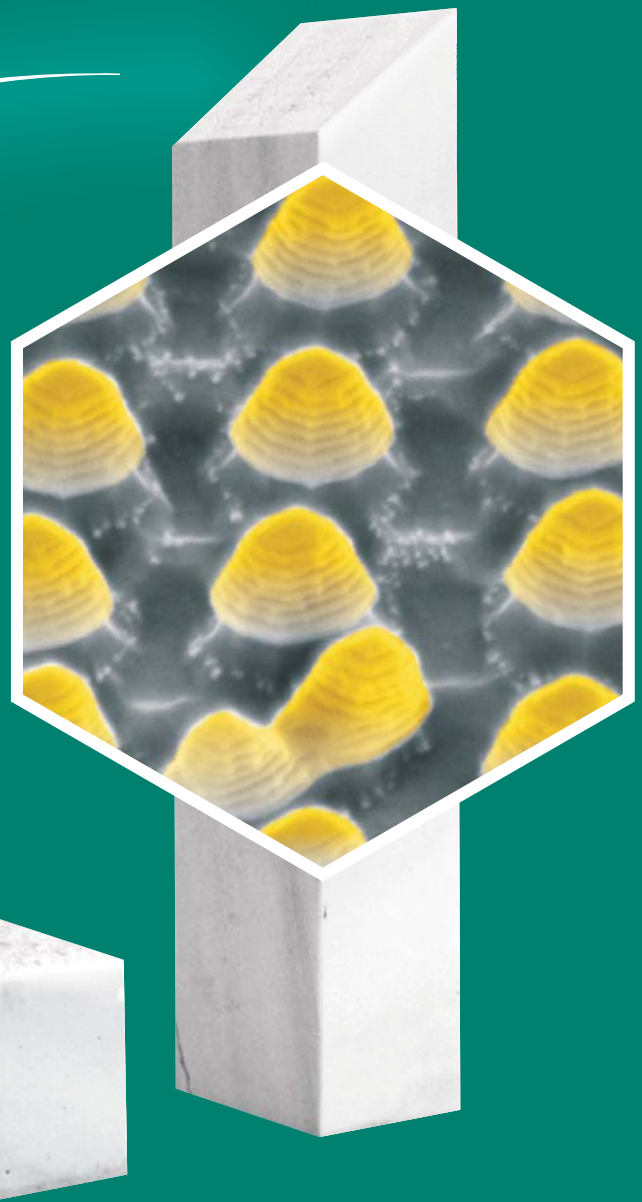


Max-Planck-Institut für Festkörperforschung Stuttgart



für Festkörperforschung

2005



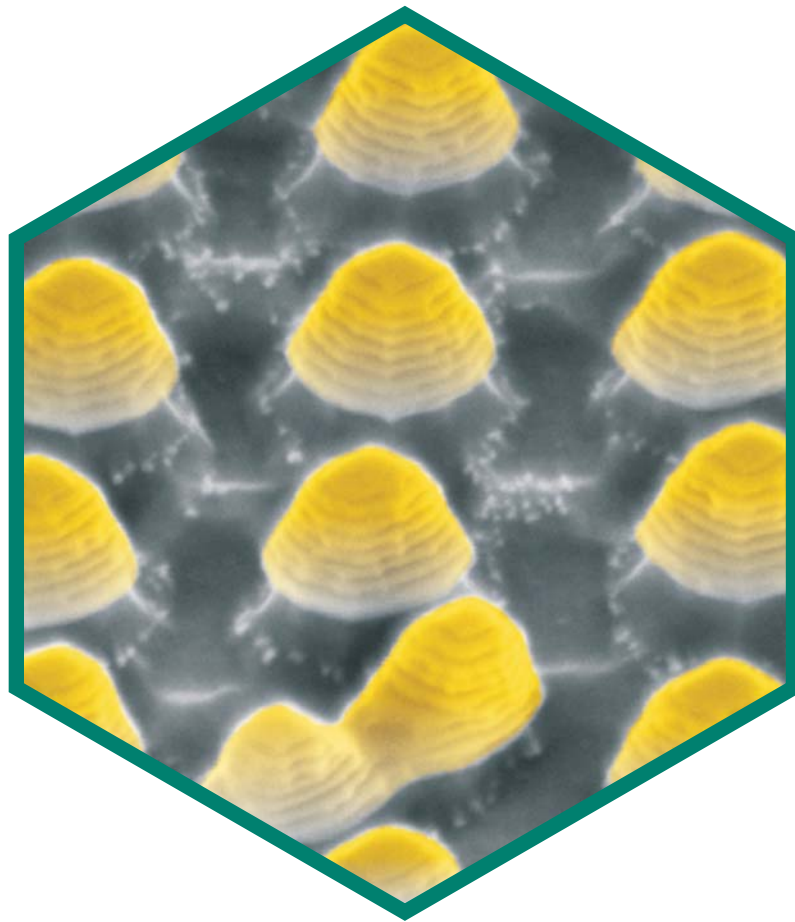


MAX-PLANCK-INSTITUT FÜR FESTKÖRPERFORSCHUNG
STUTT GART

ANNUAL REPORT

JANUARY 1st – DECEMBER 31st, 2005

Max-Planck-Institut für Festkörperforschung
Heisenbergstraße 1, D–70569 Stuttgart
Postfach: 80 06 65, D–70506 Stuttgart
Telefon: (0711) 6 89 – 0
Telefax: (0711) 6 89 – 10 10



ABOUT THE HEXAGON ON THE TITLE PAGE

Three dimensional view of free-standing stacks of GeSi/Si islands. The structure was realized by a two-step process: 1. Epitaxial growth of multiple GeSi/Si island layers on a patterned Si(001) substrate. 2. Selective wet chemical etching of the sample with KOH. The second step removes the Si material surrounding the stacked GeSi/Si islands, which leads to the modulated periodic GeSi/Si pillar structures displayed in the hexagon.

The image was published as cover page of Applied Physics Letters **87**, Issue 26, 2005.

Corresponding article:

Zhong, Z., G. Katsaros, M. Stoffel, G. Costantini, K. Kern, O.G. Schmidt, N.Y. Jin-Phillipp and G. Bauer. Periodic pillar structures by Si etching of multilayer GeSi/Si islands. Applied Physics Letters **87**, 263102 (2005).

In this report we intend to give an impression of the manifold scientific activities at the Max-Planck-Institut für Festkörperforschung during the year 2005. In the first part, we present some highlights of the scientific accomplishments in our Departments and Scientific Service Groups. In the second part, we give a complete list of publications as well as other useful information on our Institute. Details can be found on our web page <http://www.fkf.mpg.de>.

This year we had the pleasure to welcome Dr. Hagen Klauk, who won a Max Planck Society-wide competition for Independent Junior Research Groups, to our Institute. Dr. Klauk's group works on organic electronics and complements the expertise available at the Institute in this important area.

We thank all the members of the Institute in Stuttgart for their hard work and dedication. It is thanks to their efforts and performance that the Institute has been able to maintain its high standard of research.

Stuttgart

DAS KOLLEGIUM

March 2006

Contents

Selected research reports	13
Publications	115
Habilitations & PhD theses & Diploma theses	151
Invention reports & patent applications	153
Organization and budget	154
Colloquia	160
Guest scientists	163
PhD students and Master/Diploma students	168
Staff scientists	173



SELECTED RESEARCH REPORTS

General information on Abteilungen and Scientific Service Groups	1
---	---

Carbon and organic based materials

Low-voltage, low-power organic complementary circuits with self-assembled monolayer gate dielectric H. Klauk and U. Zschieschang	13
Theoretical studies of 'magic' C_{60} -alkali metal compound clusters E. Zurek and J. Autschbach; A. Enders and N. Malinowski	16
Bond alternation as a means to determine the ground state of C_{60}^{-2} -ions in compounds G. Stollhoff, H. Brumm, M. Schulz-Dobrick and M. Jansen	19
Superconductivity in hole-doped diamond L. Boeri and O.K. Andersen; J. Kortus	22
Atomistic structure of the surface planes in SiC pores U. Starke and W.Y. Lee; C. Coletti and S.E. Saddow; R.P. Devaty and W.J. Choyke	26

Nanostructures

One-dimensional metal-organic coordination networks at surfaces T. Classen, G. Costantini and K. Kern; G. Fratesi, S. Fabris, S. de Gironcoli and S. Baroni	30
Tracing the footprints of self-assembled strained islands A. Rastelli, M. Stoffel, U. Denker, G.S. Kar and O.G. Schmidt	33
Periodic defects in metallo-dielectric photonic crystal superlattices T. Zentgraf, A. Christ and J. Kuhl; S.G. Tikhodeev and N.A. Gippius; H. Giessen	37
Functional renormalization group: new applications to quantum wires and quantum dots S. Andergassen, T. Enss and W. Metzner; V. Meden and K. Schönhammer; U. Schollwöck	40

Strong electronic correlation phenomena

Wigner crystallization in copper oxide chain compounds P. Horsch, M. Sofin, M. Mayr, L. Capogna, M. Jansen and B. Keimer	43
Bose-Einstein condensation or just strongly coupled electronic bilayers ? R.D. Wiersma, J.G.S. Lok, W. Dietsche and K. von Klitzing	47
Soft Fermi surfaces and a new route to non-Fermi liquid behavior S. Andergassen, L. Dell'Anna, W. Metzner and D. Rohe	50

Raman scattering in the Mott insulators LaTiO_3 and YTiO_3 : evidence for orbital excitations C. Ulrich, M. Guennou, G. Khaliullin and B. Keimer; A. Gössling, M. Grüninger, H. Roth, M. Cwik and T. Lorenz; G. Ghiringhelli and L. Braicovich	52
First results from the new TRISP spectrometer: magnon linewidths in MnF_2 and phonon linewidths in lead S.P. Bayrakci, T. Keller, P. Aynajian, K. Buchner, M. Ohl, H. Klann and B. Keimer; K. Habicht	56

Spin interactions

Kondo effect of molecular complexes at surfaces: ligand control of the local spin coupling P. Wahl, L. Diekhöner, G. Wittich, L. Vitali, M.A. Schneider and K. Kern	59
Giant spin-splitting in the $\text{Bi}/\text{Ag}(111)$ surface alloy C.R. Ast, P. Wahl, G. Wittich, R. Vogelgesang and K. Kern; D. Pacilé, M. Falub, L. Moreschini, M. Papagno and M. Gironi	63
Spin and charge dynamics in Na_xCoO_2 S.P. Bayrakci, C. Bernhard, A. Boris, N.N. Kovaleva, G. Khaliullin, A. Pimenov, L. Yu, D.P. Chen, C.T. Lin and B. Keimer; P. Bourges, I. Mirebeau and Y. Sidis (CEA Saclay, France); J. Mesot; M. Enderle	66
Hard ferromagnetism in 2D FePt surface alloys J. Honolka, T.Y. Lee, K. Kuhnke, A. Enders and K. Kern; K. Fauth, M. Heßler and G. Schütz	69
Quasiparticle injection into YBCO thin films – does spin matter ? H.-U. Habermeier, S. Soltan, J. Albrecht and G. Cristiani	72

Transport of charge, mass and heat

Polarization dependent study of the microwave induced zero-resistance in a two-dimensional electron system J.H. Smet, B. Gorshunov and C. Jiang; L. Pfeiffer; V. Umansky; M. Dressel; F. Kuchar; K. von Klitzing	76
Overlap of depletion layers in nanocrystalline SrTiO_3 P. Balaya; J. Jamnik; J. Fleig; L. Kienle and G. Cristiani; W. Sigle; J. Maier	80
AgI nanoplates with extremely high mesoscopic ion conductivity at room temperature Y.-G. Guo, J.-S. Lee and J. Maier	83
Oxygen incorporation into ‘electron-poor’ and ‘electron-rich’ oxides: mechanistic studies of the surface reaction on $\text{Sr}(\text{Fe}_x\text{Ti}_{1-x})\text{O}_{3-\delta}$ R. Merkle and J. Maier	85
Isotope effect on the heat capacity of the monatomic and diatomic semiconductors diamond and zinc oxide R.K. Kremer, M. Cardona, G. Siegle and R. Lauck; S.K. Estreicher; A.H. Romero; M. Sanati; J. Serrano; T.R. Anthony	88

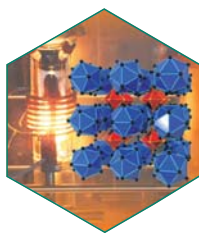
Structure of complex solids

Layered cobalt oxides under pressure X. Wang, I. Loa, K. Kunc, K. Syassen and C. Lin; M. Amboage and M. Hanfland	92
Chlorartinite, a volcanic exhalation product also found in industrial magnesia screed K. Sugimoto, R.E. Dinnebier and T. Schlecht	95
Floating zone growth of lithium iron (II) phosphate single crystals D.P. Chen, G. Götz and C.T. Lin	98
Determining the structure(s) of the amorphous ceramic α - $\text{Si}_3\text{B}_3\text{N}_7$ – a case study J.C. Schön and A. Hannemann; L. van Wüllen; M. Jansen	101
Cluster disorder and ordering principles in Al-stabilized ‘LaI’ O. Oeckler; T. Weber; L. Kienle, Hj. Mattausch and A. Simon	104
Geometric variations and electron localizations in intermetallics: PbFCl type compounds J. Nuss, U. Wedig and M. Jansen	107
Unusual lone pairs in tellurium S. Deng, J. Köhler and A. Simon	110

Scientometrics

An individual’s research impact in a number: the Hirsch index W. Marx	113
--	-----

Chemistry



JANSEN's department puts its main emphasis on basic research in the field of preparative solid state chemistry with the goal of developing modern materials.

Classes of materials currently under investigation include oxides and nitrides of metals and nonmetals as well as fullerenes, e.g., new binary and ternary oxides synthesized under high oxygen pressure, ionic conductors, structural oxide-ceramics and pigments, amorphous inorganic nitridic covalent networks, or endohedral fullerenes and fullerides.

Besides employing traditional solid state synthesis methods, a large number of alternative techniques is used, e.g., the sol-gel process, synthesis under high pressure, via an rf-furnace, at low temperatures in liquid ammonia, by electrochemical methods, or by low-temperature atomic beam deposition. Optimizing the syntheses of these materials is only a first, though

crucial step, however. In addition, their chemical and physical properties, in particular optical, electrical and magnetic behavior, are analyzed both at high and low temperatures, with particular emphasis on X-ray diffraction and spectroscopic methods. This provides the basis for placing the results in the proper context regarding structure-property relationships and modern concepts of bond-theory. A long-term goal of the department is to increase the predictability of solid state chemistry, i.e., to predict the existence of not-yet synthesized compounds, calculate their properties, and finally provide prescriptions for their synthesis. This work involves both theoretical and synthetic aspects. On the theoretical side, structure candidates are determined by studying the energy landscapes of chemical systems using global exploration techniques, while on the preparative side kinetically controlled types of reactions that allow low-temperature synthesis of (possibly metastable) compounds are being developed. [19,43,101,107]

⬡ LHS: When simultaneously evaporating graphite and a metal in an rf-furnace (shown), endohedral fullerenes can be synthesized in relatively high yields. RHS: Synthesis at high oxygen pressures produces novel materials with interesting electronic, chemical and physical properties. Compounds such as $\text{Ag}_{13}\text{OSO}_6$ (shown) are characterized using various spectroscopic, physical and diffractive methods.



MAIER's department is concerned with physical chemistry of the solid state, more specifically with chemical thermodynamics and transport properties. Emphasis is laid on ion conductors (such as inorganic or organic proton, metal ion and oxygen ion conductors) and mixed conductors (typically perovskites). As local chemical excitations (point defects) are responsible for ion transport and simultaneously represent the decisive acid-base active centers, a major theme of the department is the understanding of mass and charge transport, chemical reactivities and catalytic activities in relation to defect chemistry.

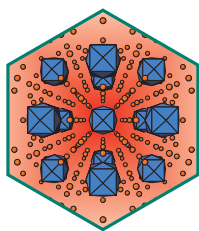
This includes experiments (in particular electrochemical studies) as well as theory (in particular phenomenological modelling), and comprises investigations of elementary processes but also of overall system properties. In this context, interfaces and nanosystems are to the fore. Since electrochemical investigation immediately affects the coupling of chemical and electrical phenomena, the research is directed towards both basic solid state problems and the technology of energy and information conversion or storage (fuel cells, lithium-batteries, chemical sensors).

Conceptually speaking, we want to address the following questions: Can we – given the materials, the control parameters and the driving

force – understand or even predict concentrations, mobilities and reactivities of ionic charge carriers? How do these properties change at interfaces and in confined systems? What are

the basic mechanisms of ion transport and ion transfer? How can we use this fundamental knowledge to develop at will materials for given (or novel) applications? [80,83,85]

⬡ Ionic and electronic charge carriers (point defects) are the relevant particles as far as chemical kinetics and mass transport is concerned. They are establishing the interaction with the neighboring phases and act on electrical and chemical driving forces.



SIMON's department emphasizes the investigation of metal-metal bonding with main group, *d*- and *f*-metals. The purpose of the work is on one side the development of structural concepts (e.g.

condensed cluster concept) and on the other side the search for new materials, their phase relationships and relations between structure, chemical bonding and properties.

Targets are metal-rich compounds of transition metals, particularly oxides and halides, reduced rare earth metal halides, hydride, carbide, boride, boride carbide, aluminide and silicide halides of the rare earth metals, alkali and alkaline earth metal suboxides and subnitrides.

Electron microscopy is used to characterize microcrystalline phases up to full structure refinement as well as analysis of real structure. Superconductivity is of special interest following a chemical view of the phenomenon in terms of a tendency towards pairwise localization of conduction electrons in a flat band–steep band scenario. New colossal magnetoresistance materials result from an interplay of *d*- and *f*-electrons.

Other fields of interest are structures of molecular crystals, in particular, *in situ* grown crystals of gases and liquids. Experimental techniques like diffractometry with X-rays and neutrons, XPS, UPS, HRTEM and measurements of magnetic susceptibility as well as electrical transport properties are used. [104,110]

⬡ $\text{Ba}_{14}\text{CaN}_6\text{Na}_{14}$ – subnanodispersed salt in a metal.

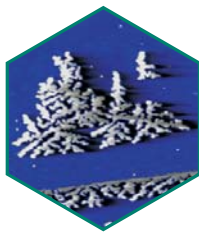
Physics



KEIMER's department studies the structure and dynamics of highly correlated electronic materials by spectroscopic and scattering techniques. Topics of particular current interest include the interplay between charge, orbital and spin degrees of freedom in transition metal oxides and the mechanism of high-temperature superconductivity. Experimental techniques being used include elastic and inelastic neutron scattering, normal and anomalous X-ray scattering, Raman scattering off and in resonance, spectral ellipsometry (including synchrotron radiation as a source), and infrared, Raman, and X-ray measurements under high magnetic fields. Experiments at external neutron sources are carried out on a regular basis, and a spectrometer at the new research reactor FRM-II in Munich

has recently been completed. The latter instrument uses a novel combination of triple axis and neutron spin echo techniques to optimize the energy resolution and allow the determination of lifetimes of magnetic and lattice vibrational excitations throughout the Brillouin zone. The group operates a high-magnetic field facility for X-ray scattering at the National Synchrotron Light Source (NSLS) at Brookhaven National Lab (USA). At the ANKA synchrotron in Karlsruhe, the group also operates Fourier ellipsometers for the far infrared spectral range. Close collaborations also exist with the theory and chemistry departments at the MPI-FKF; with the crystal growth service group where large, high-quality single crystals of oxide compounds are prepared with optical furnaces; and with the technology service group that prepares state-of-the-art oxide heterostructures and superlattices. [43,52,56,66]

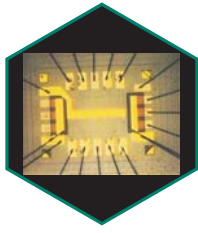
⬡ Investigation of a mosaic of crystals of a high-temperature superconductor with neutron beams (yellow). Neutrons are elementary particles that generate a magnetic field through their internal rotation ('spin'), similar to a tiny bar magnet. When a neutron beam falls onto a magnetic material, the neutron spin is flipped and the beam is deflected. In experiments with neutron beams, Max Planck scientists are studying an unusual, fluctuating magnetic order in high-temperature superconductors that could be of central importance for an explanation of this phenomenon.



Research efforts in KERN's department are centered on nanometer-scale science and technology, primarily focusing on solid state phenomena that are determined by small dimensions and interfaces. Materials with controlled size, shape and dimension ranging from clusters of a few atoms to nanostructures with several hundred or thousand atoms, to ultrathin films with nanometer thickness are studied. A central scientific goal is the detailed understanding of interactions and processes on the atomic and molecular scale. Novel methods

for the characterization and control of processes on the atomic scale as well as tools to manipulate and assemble nanoobjects are developed. Of particular interest are: fundamentals of epitaxial growth and self-organization phenomena, atomic scale fabrication and characterization of metal, semiconductor and molecular nanostructures, quantum electronic transport in nanostructures, atomic scale electron spectroscopy and optics on the nanometer-scale. As surface phenomena play a key role in the understanding of nanosystems, the structure, dynamics and reactivity of surfaces in contact with gaseous or liquid phases are also in the focus of interest. [30,59,63,69]

⬡ The scanning tunneling microscope image in the logo of the Abteilung Kern shows a silver dendrite grown at 130 K on a platinum (111) surface.



Electronic properties of heterostructures, quantum wells, superlattices and carbon based quantum structures, in particular the influence of quantum phenomena on the transport and optical response are the main topics in the VON KLITZING's department. Optical and transport measurements in magnetic fields up to $B = 20$ Tesla and temperatures down to 20 mK and scanning probe techniques are used to characterize the systems. Picosecond sampling techniques are developed for ultrafast time-resolved measurements on nanodevices.

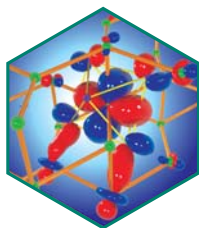
The quantum Hall effect is studied by analyzing time-resolved transport, edge channels, the behaviour of composite fermions and the response on microwave radiation and surface acoustic waves. Electron-phonon interactions in low-dimensional systems and the phonon transmission through interfaces are investigated with ballistic phonon techniques.

Time-resolved photoconductivity, luminescence, and Raman measurements in magnetic fields are methods of characterizing the low-dimensional electronic systems. A strong current interest is the preparation of nanostructures either by self-organized growth or by lithographic and synthetic routes. Coupled two- and zero-dimensional electronic systems are produced by highly specialized molecular beam epitaxy growth and by electron beam lithography.

Phenomena like electron drag, Kondo resonance, Coulomb blockade, ballistic transport, commensurability phenomena in periodically modulated two-dimensional systems and the interaction between electron and nuclear spins are investigated. The detection and generation of terahertz radiation using low-dimensional electron systems is one of the new research activities. The experiments are supported within the group by theoretical investigations of the transport and dynamic response of these low-dimensional electronic systems. [47,76]

⬡ Demanding technologies are needed for the preparation of devices used in quantum transport experiments. The figure shows a typical example where the combination of interrupted epitaxial growth, special etching processes, focused ion beam writing, contact diffusion, and gate evaporation leads to two electron layers with a distance of only 10 nm and separate contacts.

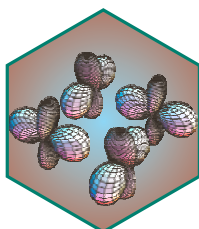
Theory



Condensed matter consists of atoms. The bonding between the atoms is effected by the electrons, with a fine balance existing between the quantum mechanical kinetic energy of the electrons and their electrostatic interaction both with the nuclei and between themselves. The electrons play the key role not only for the cohesive, but also for the electrical, magnetic and optical properties. The members of Abteilung ANDERSEN attempt to improve the understanding of these properties by calculating electronic structures and developing methods for such calculations. We perform calculations on novel materials with interesting properties, using the density-functional formalism (DF), we improve the Muffin-Tin-Orbital (MTO) method, and we derive and treat system-specific model Hamil-

tonians. In 2005 we studied electron-phonon mediated superconductivity in heavily hole-doped diamond and in heavily electron-doped (pseudo)graphite. In the cuprates which become high-temperature superconductors upon hole-doping, the electronic correlations are strong. We have shown how this modifies the electron-phonon interaction, how the latter influences the photoemission spectra for undoped cuprates, and that these are well within the polaronic limit. Finally, for a number of cuprates and transition metal oxides studied experimentally in Keimer's department and in the high-pressure group, we have derived DF-NMTO Wannier functions and Hubbard Hamiltonians. By solving the latter in the dynamical and/or static mean-field approximations (in collaboration with members of Metzner's department) we could throw light on physical properties such as metal-insulator transitions. [16,22]

⬡ One of the three congruent t_{2g} NMTO Wannier-like orbitals for V_2O_3 . Lobes of opposite signs are respectively red and blue.



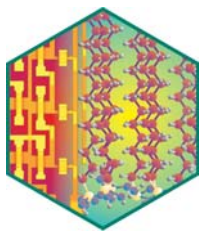
Electronic properties of solids are analyzed and computed in METZNER's department with a main emphasis on systems where electronic correlations play a crucial role, such as cuprates, manganites and other transition metal oxides. Besides symmetry-breaking phase transitions leading to magnetism, orbital and charge order, or superconductivity, correlations can also cause electron localization and many other striking many-body effects not described by the generally very successful independent electron approximation.

Our present research focuses in particular on high-temperature superconductors with their complex interplay of magnetic, superconducting and charge correlations, and also on man-

ganites and vanadates, whose electronic properties are determined by the interplay of orbital, spin and charge degrees of freedom. Another topic is the influence of lattice degrees of freedom on electronic properties, via Jahn-Teller distortion and electron-phonon interaction. Besides bulk properties of one-, two- and three-dimensional systems also problems with a mesoscopic length scale such as quantum dots and inhomogeneous quantum wires are being studied. The correlation problem is attacked with various numerical and field-theoretical techniques: exact diagonalization, density matrix renormalization group (DMRG), dynamical mean-field theory (DMFT), functional renormalization group and $(1/N)$ -expansion. Modern many-body methods are not only being applied, but also further developed within our group. [40,43,50]

⬡ Orbital order in a single layer of undoped $LaMnO_3$. The study of electronic properties of doped manganites, which show such remarkable phenomena like the colossal magnetoresistance, is an active research field because of the subtle interplay of charge, orbital, spin and lattice degrees of freedom.

Independent Junior Research Group



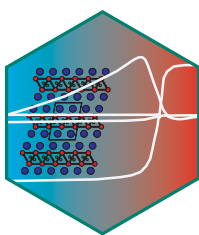
Research in the ORGANIC ELECTRONICS Group (Klauk) focuses on the development of materials and manufacturing processes for the fabrication of high-performance organic electronic devices.

Particular emphasis is on the advancement of organic thin-film transistors. Unlike transistors based on inorganic semiconductors, such as silicon, organic transistors can be created at or near room temperature and thus on a variety of unconventional substrates, including glass, plastics and even paper. This allows, for example, the implementation of mechanically flexible large-area sensors for the spatially resolved detection of chemical, biological, thermal or mechanical inputs. Other applications include flexible information displays in which organic

transistors are needed for the pixel drive, row select and column decoder circuits. In a broader sense we pursue the design and application of a wide range of advanced functional organic materials for electronic, micro-electro-mechanical or nanoscale devices and circuits, and to study condensed matter physics in organic materials. One example are self-assembled monolayers. Although the spontaneous self-assembly of aliphatic molecules on solid surfaces was first described more than 60 years ago, the tailoring of the electrical properties of molecular monolayers and their use in functional electronic devices remain virtually unexplored. Scientific work in organic electronics is highly interdisciplinary and involves the design, synthesis and processing of materials, the development of fabrication processes, device and circuit design, manufacturing, and characterization. [13]

⬡ n-Octadecylphosphonic acid $C_{18}H_{37}PO(OH)_2$ forms dense, insulating monolayers on natively oxidized metal substrates, such as aluminum. As a high-capacitance gate dielectric, these monolayers allow organic transistors and large-scale digital circuits (background) to operate with low voltage (1.5 V) and low power (1 nW per gate).

Scientific Service Groups



The CHEMICAL SERVICE GROUP (Kremer) develops techniques, provides experimental facilities and carries out routine measurements to support all experimental groups of the Institute with

the characterization of electrical, thermal and magnetic properties of new compounds and samples. This objective requires a great versatility of the supported experimental methods including the development and cultivation, e.g. of experimental techniques to perform measurements on chemically highly sensitive and reac-

tive small samples under inert gas conditions. Presently available are two commercial SQUID magnetometers, home-built ac-susceptometers, dc- and ac-electrical resistivity setups and calorimeters in a broad range of temperature and magnetic fields. Materials currently under investigation are novel superconductors (rare-earth carbides and carbide halides, intercalated graphite, magnesium diboride), new or unusual magnetoresistive materials (rare-earth halides and hydride halides), low-dimensional and frustrated magnetic systems and systems with unusual magnetic ground states (spin-Peierls systems, frustrated quantum chain systems). [88]

⬡ $Y_2C_2X_2$ – A halide superconductor. The white solid lines symbolize the electrical resistivity, the heat capacity and the magnetic susceptibility proving $Y_2C_2I_2$ to be a superconductor with a T_c of 10 K.

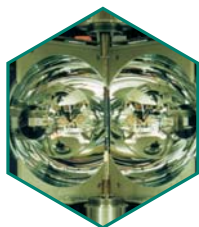


The COMPUTER SERVICE GROUP (Burkhardt) runs the Institute's central mail, print, software, backup and web servers, as well as the nine servers providing department specific services. All these servers use the Linux operating system. The individual server storage subsystems are currently replaced by a Fibre Channel based Storage Area Network (SAN) which allows us to add additional storage when needed without service interrupt. Backup remains based on Tivoli Storage Manager (TSM); currently the total backup data volume is about 20 Tbyte. The servers remained online even under difficult power and AC conditions caused by the ongoing renovation and modernization of the 2E server room. In the last five years the group integrated more than 600 new PCs into the network, bringing the

estimated total number to about 1000 PCs used as desktops and for data acquisition purposes. Of these about seventy percent run Windows and thirty percent run the Linux operating system.

In 2005 the IBM BladeCenter System has been extended to 122 JS20 PowerBlades (244 CPUs) and remains the main computational resource for the theory oriented groups. The machine runs under SuSE Linux Enterprise server, but it is source code compatible to the AIX machines IBM p655 (32 POWER4 CPUs) and IBM SP (60 POWER3 CPUs). To the users of the theory groups they all look alike as they use the same set of compilers, libraries and batch systems. Four Linux clusters with a total of 148 Intel Xeon (IBM xSeries 335) and 60 AMD Athlon CPUs (FSC hpcline) are a cost effective computational resource for the Jansen, Maier and Metzner departments.

⬡ View inside the Tape library of the DV-FKF. Every night the data of 150 computers in the Institute is backed up. At the moment the total TSM backup and archive volume amounts to 20 Terabytes.



The CRYSTAL GROWTH SERVICE GROUP (Lin) applies, modifies and develops techniques, such as traveling solvent floating zone with infrared image furnace, Bridgman, top seeded solution growth, flux and Czochralski methods to grow single crystals from the melt or solution. A wide variety of crystals have been supplied to the physics and chemistry departments at the MPI-FKF and to outside collaborators. These range from isotopically pure semiconductors to fullerenes and transition metal oxides. Two floating zone furnaces are used predominantly to grow large single crystals of

transition metal oxides for neutron and optical spectroscopy. Typical examples are superconducting oxides $\text{Bi}_2\text{Sr}_2\text{Ca}_{n-1}\text{Cu}_n\text{O}_{2+4n+\delta}$, $\text{REBa}_2\text{Cu}_3\text{O}_{7-\delta}$, $\text{RE}_{2-x}\text{M}_x\text{CuO}_4$, and cobaltates Na_xCoO_2 .

Gas phase methods are modified to grow crystals of II-VI and III-V compounds with defined isotopic components from low amounts of source materials. The grown crystals are accurately characterized through the measurements of superconductivity, magnetization, and structure. The in situ observation using high-temperature optical microscopy reveals oxides melting/dissolution, nucleation and phase transformation under various growth conditions. [98]

⬡ A view of the inside chamber of the four ellipsoidal infrared image (TSFZ) furnace.



Research within the HIGH PRESSURE SERVICE GROUP (Syassen) is concerned with the effects of hydrostatic pressure on structural, lattice dynamical, and electronic properties of crystalline solids and their high-pressure phases. Advantage is taken of recent developments in diamond anvil cell techniques, including progress in analytical methods that utilize synchrotron X-ray radiation (diffraction as well as inelastic scattering), synchrotron infrared radiation, and laboratory-based low-temperature optical spectroscopy. The subjects of interest range from improving the understanding of chemical bonding and

phase formation at high densities to illuminating the interplay between subtle changes in crystal structure, electron delocalization, magnetism, and superconductivity in correlated electron systems of different dimensionality. In terms of materials, the interest in covalently bonded semiconductors and nanostructures continues, while the 'simple' alkali metals have attracted attention due to their surprisingly complex structural and electronic behavior at high density.

The main focus, though, is on the physics of transition metal compounds with metal ions in high oxidation states, i.e. systems being located close to the insulator-metal borderline and undergoing pressure-driven Mott-like delocalization transitions. [92]

 Schematic view of a diamond window high-pressure cell.



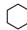
The CENTRAL INFORMATION SERVICE (Marx/Schier) for the institutes of the CPT division of the Max Planck Society, located at the Max Planck Institute for Solid State Research in Stuttgart, has access to many external commercial databases (in particular from the host STN International, FIZ Karlsruhe).

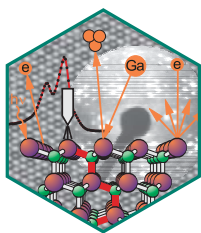
The information service offers searches for scientists at Max Planck Institutes, which cannot be done by themselves due to complexity or lack of access.

Furthermore, the scientists are welcome to ask for help and support concerning end user databases and in all questions related to scientific information. Today, databases are a major tool in processing the actual information flood in science. Bibliographic databases provide

links to the original scientific literature. They are mostly online versions of printed abstract services like Chemical Abstracts or Physics Abstracts. Compound or material related searches are done in the files of the Chemical Abstracts Service (CAS), which also cover material science and physics.

Beside these databases, covering general topics of science, there are many highly specialized databases on specific topics like computer science, material science, engineering, environmental sciences and many others. In addition various national and international patent files are available. Factual databases enable to search numerical data like chemical and physical properties of substances. The Science Citation Index provides the possibility to retrieve the citing papers of publications as well as total citation statistics of scientists or research institutes for research evaluation. [113]

 The archives of science are growing from the flood of information: one of the about 30 million substances in the compound file of the American Chemical Abstracts Service. Effective databases and search systems in conjunction with document delivery systems produce relief.



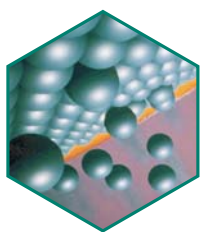
The INTERFACE ANALYSIS SERVICE GROUP (Starke) investigates the atomic and electronic structure of solid-solid and gas-solid interfaces. Using electron spectroscopy techniques, quantitative low-energy electron diffraction, scanning probe microscopy and secondary ion mass spectrometry (SIMS), the atomic geometry and morphology as well as the chemical composition and bond coordination are determined for the sample surface and its immediate vicinity. Thin films and buried interfaces are accessible by sputtering techniques or sample cleavage methods.

Experimental facilities available include a time-of-flight SIMS machine to quantify the chemical composition at the surface, within the film and at interfaces. Chemical and electronic prop-

erties are investigated in a multicomponent chamber containing high-resolution electron spectroscopy for chemical analysis. A scanning Auger microscope yields spectroscopic images with high lateral resolution. Sample morphology can be studied using an atomic force microscope and a white-light interferometer. The research activities of the group are directed towards growth and analysis of surfaces and ultrathin films of novel materials for semiconductor technology, e.g., wide band gap semiconductors (SiC, GaN), metal silicides, as well as epitaxial metal films.

Material growth, heterojunctions, metallization and ferromagnetic layers are investigated on an atomic level for a detailed understanding of the fundamental interactions involved in the growth process. In addition, molecular adsorbates are studied on these surfaces as model systems for a variety of applications. [26]

⬡ Chemical composition, electronic structure and atomic geometry are investigated for complex compound systems such as 4H-SiC (bottom). Scanning probe techniques provide real-space images (background), electron diffraction yields accurate geometry data (right), photoelectron spectra are analyzed for chemical information (left).



Main subject in the MBE SERVICE GROUP (Dietsche/Schmidt) is the preparation and characterization of III/V and group IV semiconductor heterostructures. We apply molecular beam epitaxy (MBE) for the material systems AlGaAs/GaAs and InGaAs on GaAs substrate, and SiGe/Si on Si substrate.

Our main interest is the preparation of low-dimensional nanostructures. Lateral confinement is achieved by island formation in epitaxial growth of strained heterostructures. We

are particularly interested in controlling the spatial position of self-assembled nanostructures. For this purpose we grow quantum dots on lithographically patterned substrates, and investigate an atomic-layer precise in situ etching technique based on AsBr₃. The group IV element MBE activities concentrate on the self-assembly of Ge/Si nanostructures and on devices such as inter- and intraband tunneling devices. Another subject is the formation of free-standing semiconductor nanotubes. The preparation is controlled by selective under-etching of strained epitaxial semiconductor bilayers. [33]

⬡ Atoms impinge, diffuse and nucleate on the surface of a heated crystalline substrate under ultrahigh vacuum conditions. This process is called molecular beam epitaxy.



The OPTICS AND SPECTROSCOPY SERVICE GROUP (Kuhl) comprises the spectroscopy service lab and the ultrafast optics lab. The spectroscopy service lab provides experimental facilities

for studying the optical properties of condensed matter by standard spectroscopic techniques. The laboratory is equipped with commercial grating and Fourier-spectrometers which allow absorption and reflection measurements over the total range from the ultraviolet to the far infrared. Data can be routinely taken at temperatures between 4 K and 300 K. Recently, the sample characterization techniques have been extended by standard Raman spectroscopy.

The primary research subject of the ultrafast optics lab are time-resolved studies of ultrafast optical and electrical phenomena in solids. Several pico- and femtosecond laser systems including devices for the generation of sub-10 fs pulses as well as for the amplification of 150 fs pulses to 5 μ J at 200 kHz are available. Broad tunability of the photon energy is attainable by

optical parametric amplifiers. Time-resolved photoluminescence, pump-probe experiments, degenerate four-wave-mixing and coherent Raman techniques are employed to investigate the coherent and incoherent relaxation dynamics of excitons, free carriers (electrons and holes) and phonons as well as carrier transport phenomena.

Materials preferentially under investigation are III-V and II-VI semiconductors, in particular low-dimensional systems (quantum wells, quantum wires, and quantum dots). The variation of the relaxation processes and times as a function of the dimensionality of the carrier system are a central topic of the research. Besides studies on semiconductors, investigations of the linear and nonlinear optical properties of metallic photonic crystal structures have become a major research field of the group.

Important current research projects are dealing with coherent light/matter coupling, control of light/matter interaction by nanostructuring, generation and dynamics of coherent phonons, generation and characterization of ultrashort optical, electrical and terahertz pulses. [37]

⬡ Optical parametric amplifier generating tunable femtosecond pulses for coherent semiconductor spectroscopy.

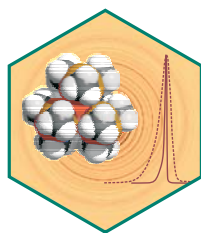


The TECHNOLOGY SERVICE GROUP (Habermeier) offers service work in the fields of thin film preparation, microlithography and fabrication of contacts to semiconductors and ceramic

materials. The experimental facilities include high-vacuum evaporation and sputtering (dc, rf and reactive) techniques. Additionally, pulsed laser deposition systems are installed to prepare thin films with complex chemical composition such as high-temperature superconductors [HTS] and perovskites with colossal magnetoresistance [CMR]. Dry etching tech-

niques complement the spectrum of experimental techniques available. The research activities are closely related to the service tasks. Thin film deposition of doped Mott insulators such as HTS and CMR materials play a central role. The main focus of interest is the study of epitaxial strain in CMR and HTS thin films. Additionally, the preparation and investigation of magnetic and superconducting oxide superlattices (manganites, ruthenates and cuprates) and their mutual electronic interaction as well as the study of special oxide heterostructures are designed for polarized spin injection, exchange bias effects and magnetic flux-line pinning phenomena are of central interest. [72]

⬡ Pulsed laser deposition has become a widespread technique for the fabrication of epitaxial thin films of multicomponent materials like doped lanthanum manganites and superconducting materials.



The X-RAY DIFFRACTION SERVICE GROUP (Dinnebier) provides X-ray diffraction measurements of single crystals and powders in the laboratory at room and low temperature. Research within the X-ray diffraction service group is mainly concerned with the determination of crystal structures and microstructural properties (strain, domain size) of condensed matter from powder diffraction data. In addition, methodological development within this area is pur-

sued. Special expertise in the field of solution and refinement of crystal structures from powder diffraction data can be provided. Scientific cooperation in the field of nonroutine structure determination (phase transitions, disorder, anisotropic peak broadening, etc.) from powders is offered. This includes the performance of experiments at synchrotron and neutron sources at ambient and non-ambient conditions. Materials currently under investigation include organometallic precursors, binary and ternary oxides, ionic conductors, electronic and magnetic materials, and rotator phases. [95]

⬡ Quasispherical molecule of tetrakis(trimethylstannyl)silane with underlying two dimensional image plate powder diffraction pattern. The superimposed Bragg reflections demonstrate the difference in resolution between laboratory and synchrotron data.

Carbon and organic based materials

Carbon and carbon containing materials offer a vast playground for fundamental studies and applications alike. Carbon materials derive much of their interest from their strength, rich transport and widely tunable band structure properties and most of all from the fact that they appear in every dimensionality: 3D versions like graphite and diamond, 2D graphene sheets, 1D nanotubes and finally 0D fullerenes. By adding additional atoms for building more complex organic molecules, the degree of freedom to tailor various properties becomes sheer endless. Much of this spectrum is covered in the research activities at the Institute. Here we highlight theoretical work on the origin of superconductivity in hole doped diamond, the stability of fullerene-alkali metal compound clusters and the ground state of negative fullerene ions. Experimental work addresses the suitability of organic based thin film transistors with self-assembled monolayer dielectrics for complementary logic circuits and the atomistic structure of the surface planes in SiC pores of relevance for instance for applications in gas sensing and biotechnology.

Low-voltage, low-power organic complementary circuits with self-assembled monolayer gate dielectric

H. Klauk and U. Zschieschang

The electronic properties of conjugated organic materials (organic semiconductors) have been under scientific investigation since the early 1900s. Applications for organic semiconductors include light emitters, photovoltaic cells, and thin film transistors (TFTs). Organic TFTs were first reported in 1986, with carrier mobilities in the range of $10^{-5} \text{ cm}^2/\text{Vs}$. Advances in synthetic chemistry, material selection, purification, device design, and manufacturing have led to significant improvements in the performance of organic TFTs. Today, mobilities greater than $0.1 \text{ cm}^2/\text{Vs}$ are routinely obtained with a variety of polymeric and small-molecule organic semiconductors. Field effect transistors based on high-quality organic single-crystals have shown field effect mobilities as large as $15 \text{ cm}^2/\text{Vs}$.

Unlike transistors based on inorganic materials, such as silicon, organic TFTs can be created at or near room temperature and thus on a variety

of unconventional substrates, including glass, plastics and even paper. Over the past five years, many groups worldwide have shown that organic TFTs can be used as pixel drivers in active-matrix displays, as mechanical force or bending sensors, and as chemical or biological sensors. Perhaps the most challenging application for organic TFTs is in integrated circuits.

Early organic circuits made exclusive use of *p*-channel TFTs [1], since *n*-channel organic semiconductors often suffer from low mobility or poor stability in air. The problem with circuits designed with only one type of transistor (either *p*-type or *n*-type) is the power dissipation due to static currents. In addition, the gate dielectric layers of these early TFTs had very small capacitances, usually less than 10^{-8} F/cm^2 . As a result, voltages in excess of 30 V were often required to induce sufficient charge in the transistor channel to operate the transistors ($Q = C \cdot V$, where Q is the charge, C

is the capacitance, and V is the gate voltage). For circuit applications much smaller voltages (around 2 V) are highly desirable. One obvious approach to increase the dielectric capacitance is to use materials with larger permittivity, but such materials tend to also lead to lower mobilities in the organic carrier channel and to increased gate leakage.

To reduce the operating voltage of high-mobility organic TFTs without introducing prohibitive gate leakage we have recently developed a gate dielectric process based on molecular self-assembled monolayers [2]. These ultra-thin (< 3 nm) monolayers form spontaneously by the covalent bonding of long-chain hydrocarbons with reactive head groups to solid substrates bearing a sufficient density of suitable grafting sites. Self-assembly is initiated either in the gas phase or in solution and has the ability to provide densely packed, highly ordered organic monolayer films with extreme chemical inertness and mechanical robustness.

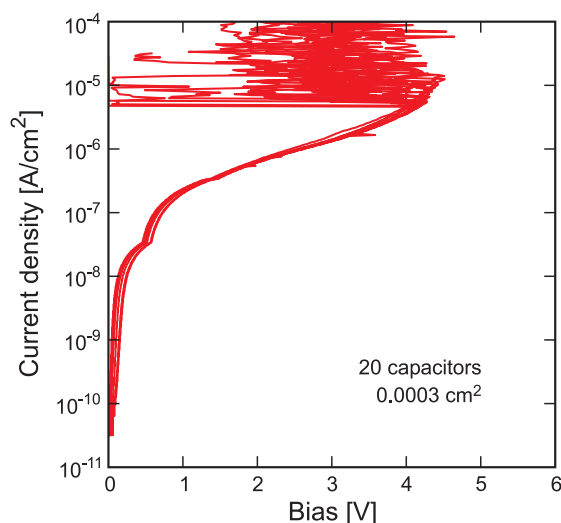


Figure 1: Leakage current and breakdown characteristics of 20 monolayer capacitors with Al bottom electrode and Au top electrode. (Note: The kink at a current density of $3.3 \cdot 10^{-8}$ A/cm² is an artefact of the measurement instrumentation. This current density corresponds to 10 pA total current at which the instrument changes the measurement range.)

With a capacitance near 10^{-6} F/cm², monolayer gate dielectrics allow organic TFTs and

simple digital circuits to operate with voltages as low as 1.5 V. Perhaps more importantly, the leakage currents through these monolayer dielectrics are comparable to or smaller than the leakage currents through high-quality SiO₂ dielectrics of similar thickness, which are commonly used in silicon microelectronic circuits. Figure 1 shows the leakage current density measured for 20 monolayer dielectric capacitors (in which the monolayer is sandwiched between an aluminum bottom electrode and a gold top electrode). At a voltage of 2.5 V, which corresponds to an electric field of about 5 MV/cm, the current density is about 1 μ A/cm², and breakdown occurs at (4.2 ± 0.1) V (≈ 8 MV/cm).

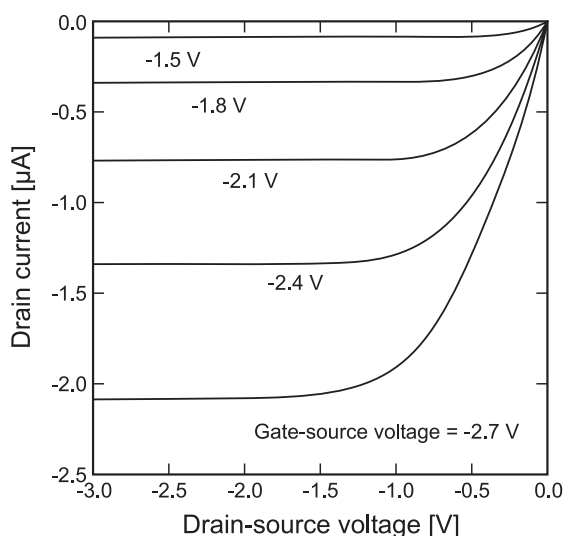


Figure 2: Current-voltage characteristics of a pentacene TFT with monolayer gate dielectric.

Figure 2 shows the current-voltage characteristics of a *p*-channel organic TFT with monolayer gate dielectric. Pentacene was used as the organic semiconductor and deposited by evaporation in vacuum. From the electrical characteristics, a mobility of 0.5 cm²/Vs is extracted. This is sufficient for most of the applications for which organic transistors are envisioned. For example, amorphous silicon TFTs, which are widely used in active-matrix liquid-crystal displays, typically have mobilities between 0.1 and 0.5 cm²/Vs.

Pentacene *p*-channel TFTs with monolayer gate dielectrics have been used to implement simple digital circuits [3]. These circuits operate with supply voltages as low as 1.5 V, the smallest supply voltage reported for organic circuits. However, since these circuits rely exclusively on *p*-channel transistors, they still suffer from large power dissipation due to permanent static currents.

Implementing low-power circuits requires the use of *p*-channel and *n*-channel transistors in a complementary logic. In a complementary gate, only half of the transistors are conducting in either of the two steady states, while the other transistors are nonconducting. Therefore static currents in complementary circuits are close to zero and power is dissipated only during signal switching. In silicon IC technology, realizing *n*-channel and *p*-channel transistors is straightforward, since silicon has excellent ambipolar characteristics and since the contacts of silicon transistors are readily doped. Unfortunately, reliable contact doping for organic TFTs is complicated by the fact that dopants in organics are not covalently bound and hence, they tend to diffuse under the influence of electric fields. In addition, organic materials, including pentacene, generally do not exhibit ambipolar characteristics.

To demonstrate low-voltage, low-power organic complementary circuits we have developed a process to implement *p*-channel pentacene and *n*-channel F₁₆CuPc TFTs with a monolayer gate dielectric on the same substrate. Like pentacene, F₁₆CuPc is commercially available and – unlike most *n*-channel organic semiconductors – is reasonably stable against oxidation in ambient air. Unfortunately, *n*-type conduction is much less favorable in organic materials, and the best mobility we (and others) have obtained with F₁₆CuPc is only about 0.02 cm²/Vs. Nonetheless we were able to integrate F₁₆CuPc

and pentacene TFTs with monolayer gate dielectrics on glass substrates and demonstrated – for the first time – low-voltage, low-power organic circuits (Fig. 3).

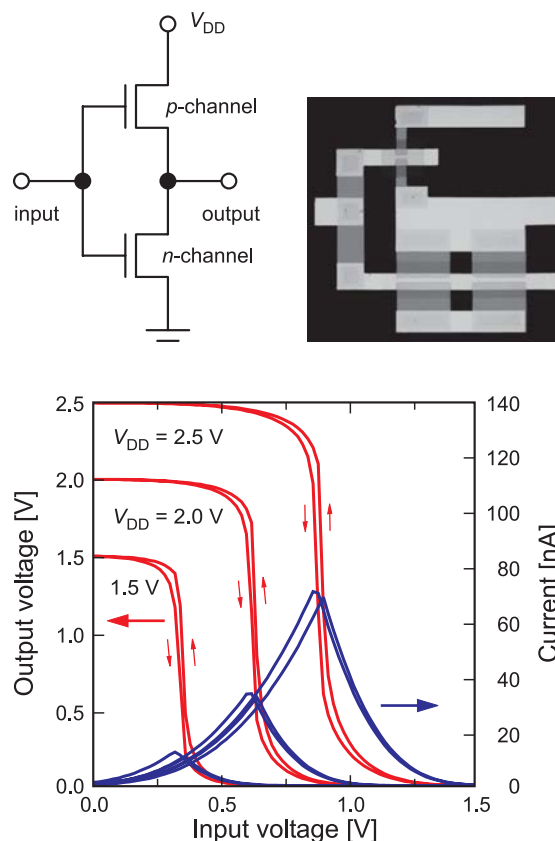


Figure 3: Low-voltage, low-power organic complementary inverter.

Our complementary inverters show sharp switching with rail-to-rail output level swings, large gain, and negligible hysteresis for supply voltages as low as 1.5 V (Fig. 3). 2-input NAND gates were also implemented and show the correct logic function. Static currents are very small, always well below 1 nA (and less than 100 pA in most cases) for supply voltages between 1.5 and 2.5 V. Thus, static power dissipation is less than 1 nW per logic gate – a record for organic circuits.

Complementary 5-stage ring oscillators were also fabricated and showed reasonably stable oscillations for supply voltages between 2 and 3 V, with rail-to-rail output voltage signals and delays of about 10 ms per inverter stage. The dynamic performance of our circuits is currently limited by the poor mobility of the *n*-channel F₁₆CuPc TFTs (0.02 cm²/Vs), the large channel length (50 μm), and the large source/drain-to-gate overlap (50 μm). Future work will therefore focus on the synthesis of air-stable organic *n*-channel materials with mobilities similar to that of pentacene, and on patterning methods with higher resolution and bet-

ter layer-to-layer registration. With improved materials and manufacturing methods, signal delays of a few microseconds per stage appear feasible.

-
- [1] Klauk, H., D.J. Gundlach and T.N. Jackson. IEEE Electron Device Letters **20**, 289-291 (1999).
 - [2] Halik, M., H. Klauk, U. Zschieschang, G. Schmid, C. Dehm, M. Schütz, S. Maisch, F. Effenberger, M. Brunnbauer and F. Stellacci. Nature **431**, 963-966 (2004).
 - [3] Klauk, H., M. Halik, F. Eder, G. Schmid, C. Dehm, U. Zschieschang, D. Rohde, R. Brederlow, S. Briole, S. Maisch and F. Effenberger. 2004 International Electron Device Meeting Technical Digest, 369-372 (2004).

Theoretical studies of ‘magic’ C₆₀-alkali metal compound clusters

E. Zurek and J. Autschbach (University at Buffalo, USA);
A. Enders and N. Malinowski

Experimental work on fullerenes coated with alkali-metal atoms, alkaline-earth metal atoms and transition metal atoms has revealed that each metal-fullerene cluster displays very different behaviour and properties. The thermal stability of such clusters can be measured by Time of Flight (TOF) mass spectrometry. Particularly stable structures may be identified by a set of pronounced, commonly dubbed as *magic*, peaks in the mass spectrum. The enhanced stability of Ba₃₂C₆₀ was attributed to so-called geometrical shell filling [1]. It was postulated that each Ba atom lies on top of one of the 12 pentagonal or 20 hexagonal faces of the fullerene and completion of this first metallic layer leads to increased stability. On the other hand, similar experiments showed that (K₆C₆₀)_n⁺ is magic due to electronic shell filling [2]. The C₆₀ LUMO (Lowest Unoccupied Molecular Orbital) is triply degenerate and can therefore accommodate six electrons. Thus, a transfer of the valence 4s¹ electrons from 6 K atoms would yield a particularly stable structure.

Recent work using a novel experimental set-up has revealed a different set of magic peaks for Potassium and Barium fullerene clusters [3], which cannot be explained by either geometric or electronic shell filling. It was found that for *m* C₆₀ molecules the magic clusters contain *n* = 2*m* – 1 Ba atoms if *m* ≤ 4 and *n* = 2*m* or more Ba atoms if *m* > 4. Similar experiments indicated that the most stable clusters contain *n* = 2*m* and *n* = 2*m* + 1 K atoms for *m* ≤ 4 and *m* > 4, respectively. That is, the smallest observed magic clusters were found to be Ba₃(C₆₀)₂ and K₄(C₆₀)₂. Our theoretical work was inspired by the recent experimental findings and here we present the results of density functional calculations whose aim is to gain insight into the bonding mechanisms and the origin of the thermal stability within these newly observed magic clusters.

Due to the formidable computational cost the *ab initio* calculations were limited to clusters of composition M_{*n*}(C₆₀)₂ with (1 ≤ *n* ≤ 6,

M = K, Ba). The geometries of two main sets of structures were fully optimized. In Set A, all of the metal atoms were sandwiched between the two fullerenes yielding a C_{60} - M_n - C_{60} configuration. The clusters in Set B had an M - C_{60} - M_{n-2} - C_{60} - M arrangement and $n \geq 3$. For the most energetically stable cluster of a given n , frequency calculations were performed in order to determine the enthalpic and entropic contributions to the Gibbs free energy and therefore the cluster distribution at the experimental temperature and pressure.

We define the bonding energy per metal atom, BEM, as the total bonding energy of $M_n(C_{60})_2$ with respect to two C_{60} molecules and n metal atoms divided by n . The most stable structural alternatives for the Ba clusters (*lowest* BEM) all belong to Set A. A detailed bonding analysis reveals an interplay between ionic and covalent interactions. The former, BEM_{ionic} , is a result of electron transfer from the Ba $6s^2$ orbitals to the unoccupied molecular orbitals of the two fullerenes (LUMO and other higher lying orbitals). The latter, $BEM_{covalent}$, arises from back donation into the empty Ba $5d$ orbitals leading to covalent Ba $5d$ - C_{60} - π^* bonding.

Figure 4(b) shows the dependence of the main bonding mechanisms on n for the Ba clusters belonging to Set A. For $1 \leq n \leq 3$, the dominant interaction arises from ionic bonding. The magnitude of BEM_{ionic} decreases steadily with increasing n , as does the average Mulliken charge per metal atom (Fig. 4(a)). However, the magnitude of $BEM_{covalent}$ increases with increasing n , being the dominant interaction for $n = 5, 6$. For $n = 4$, $BEM_{ionic} \sim BEM_{covalent}$. For large n , only partial electron donation to the fullerene orbitals can occur, since the electrostatic repulsion between Ba^{x+} ($x \approx 2$) ions would be too large for the cluster to be stable. Instead, as n increases so does the back donation to the Ba $5d$ orbitals, stabilizing clusters where all of the Ba atoms are located between the two fullerenes. Thus, the d -element character of Ba is essential when attempting to rationalize the structural features of, and bonding within, these clusters.

The BEM indicates that $Ba_3(C_{60})_2$ is energetically the most stable cluster. Its stability results from a balance mainly between two reverse trends: on the one hand a decreasing cluster stabilization from the $Ba \rightarrow C_{60}$ electron transfer and on the other hand an increasing stability from $C_{60} \rightarrow Ba$ back donation, as n increases. However, in order to verify that this cluster is magic, it is necessary to take into account finite temperature effects. The Gibbs free energy per metal atom, GFM, can be defined as: $GFM = BEM + H_{EC}M - T \cdot SM$. Here, T is the temperature and $H_{EC}M$ and SM are the change in the finite temperature enthalpy correction and in the entropy per metal atom for the formation of $M_n(C_{60})_2$ from free metal atoms and two C_{60} molecules, respectively.

Figure 4(c) shows that $-T \cdot SM$ decreases with increasing n , implying that the entropic contribution to the GFM has a greater destabilizing effect on smaller clusters than on larger ones. To understand why this should be the case consider a reaction between $2n$ C_{60} molecules and n Ba atoms. The two limiting cases would be the production of the largest and the smallest possible clusters. The former yields $Ba_n(C_{60})_2$ and $(2n-2)$ C_{60} (a total of $2n-1$ molecules), and the latter produces $n(Ba(C_{60})_2)$ (a total of n molecules). Clearly, the formation of the largest possible cluster, along with $(2n-2)$ free fullerenes is entropically the more favorable reaction since it yields the greatest number of molecules. In general the $H_{EC}M$ (not shown) stabilizes smaller clusters, however it is about an order of magnitude smaller than the entropic term and therefore has little effect on the total GFM. The GFM, given in Fig. 4(d), confirms that $Ba_3(C_{60})_2$ is magic at the experimental temperature and pressure.

Geometry optimizations of the $K_n(C_{60})_2$ clusters indicate that for $n < 5$ the structures from Set A yield the lowest BEM. However, a structural transition to Set B is predicted for $n \geq 5$. In all cases, the bonding is purely of an ionic nature, with an almost full transfer of the valence K $4s^1$ electrons to the unoccupied orbitals of the $(C_{60})_2$.

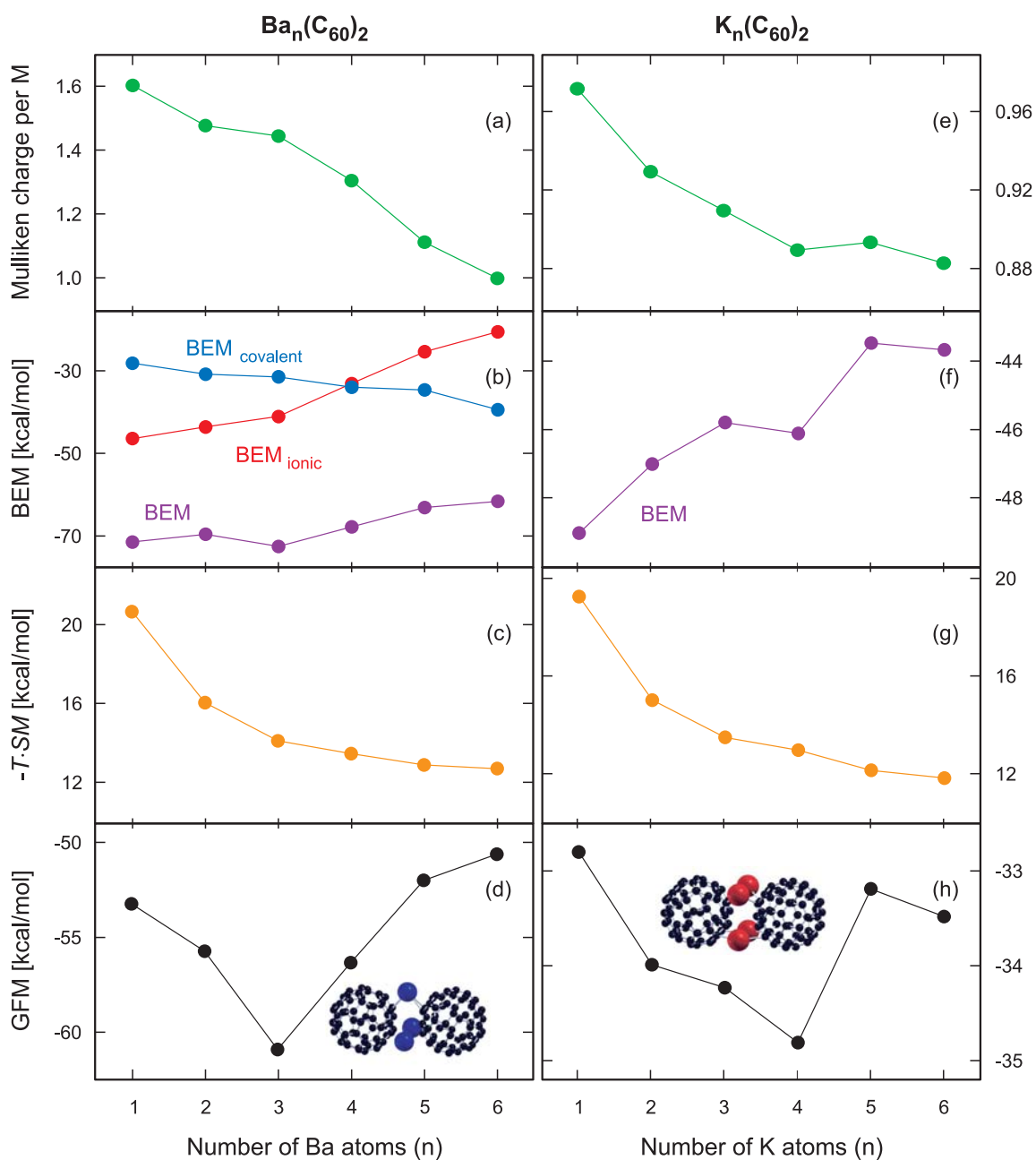


Figure 4: (a/e) The average Mulliken charge per metal atom; (b/f) BEM, and for $M = \text{Ba}$ the covalent and ionic contributions to BEM; (c/g) $-T \cdot SM$ and (d/h) GFM for the most stable $M_n(\text{C}_{60})_2$ clusters at the experimental temperature (150 K) and pressure (10^{-6} Torr).

Figure 4(e) illustrates that the charge per K atom decreases with increasing n . This is due to the fact that for large n full electron donation cannot occur due to increased Coulomb repulsion between the positively charged potassium ions. Simple models reveal that the most stable structures for a given n tend to minimize the to-

tal electrostatic energy. The BEM indicate that the most stable species is $\text{K}(\text{C}_{60})_2$ (Fig. 4(f)). However, inclusion of finite temperature effects is crucial in predicting which cluster is magic. The $-T \cdot SM$, shown in Fig. 4(g), display the same trend as for the Ba clusters and once again the H_{ECM} are an order of magnitude smaller.

Inspection of the GFM in Fig. 4(h) illustrates that inclusion of entropic and enthalpic terms changes the order of stability of the clusters, with $K_4(C_{60})_2$ yielding the lowest GFM.

In full agreement with experimental results, the GFM confirms that $Ba_3(C_{60})_2$ and $K_4(C_{60})_2$ are the most stable structures (and therefore appear as magic clusters) at the experimental temperature and pressure. The stability and geometry of the Ba clusters is determined by the interplay between covalent and ionic bonding mechanisms. On the other hand, for the K clusters the bonding is completely ionic and the energetically most favorable structures minimize the total electrostatic energy. Thus, while K acts in the expected manner for an alkaline metal atom, Ba exhibits a considerable *d*-element character which is in-line with known experimental

data. The inclusion of finite temperature effects is crucial, especially for the K clusters, in deducing absolute stability. The entropic contribution destabilizes clusters with a large amount of metal atoms to a lesser extent than those with small *n*. Thus, the density functional calculations were not only able to simulate, but also to explain the stability and bonding within the newly observed magic clusters.

-
- [1] Zimmermann, U., N. Malinowski, U. Näher, S. Frank and T.P. Martin. *Physical Review Letters* **72**, 3542-3545 (1994).
 - [2] Martin, T.P., N. Malinowski, U. Zimmermann, U. Näher and H. Schaber. *The Journal of Chemical Physics* **99**, 4210-4212 (1993).
 - [3] Enders, A., N. Malinowski, D. Ievlev, W. Branz and K. Kern. *MPI-FKF Wissenschaftlicher Tätigkeitsbericht* **2003**, 43-47 (2004).

Bond alternation as a means to determine the ground state of C_{60}^{-2} -ions in compounds

G. Stollhoff, H. Brumm, M. Schulz-Dobrick and M. Jansen

The proper electronic ground state of C_{60}^{-2} ions in compounds has not yet been experimentally determined. Here, one faces a so-called open-shell problem. The two added electrons partially occupy the lowest unoccupied molecular orbital (LUMO) of the neutral C_{60} -molecule which has t_{1u} -symmetry and is 3-fold degenerate. In the symmetry equivalent case of the C-atom, Hund's rule applies and the ground state is a triplet. However, no evidence for a magnetic state has been found for C_{60}^{-2} -compounds. A singlet ground state can only be achieved by a Jahn-Teller distortion. It would be a superposition of singlet states of different symmetries. In the case of C_{60} , such a broken symmetry can be realized by an external field that lowers the symmetry, but also by a symmetry lowering of the C_{60} -cage itself. In both cases evidence for such a Jahn-Teller effect should

be seen in the experimentally determined structure. However, it has so far escaped detection. The open-shell problem extends to all ions short of C_{60}^{-6} when the LUMO is completely filled. For C_{60}^{-4} which is equivalent to C_{60}^{-2} , very recently, in tunnel experiments, evidence for a Jahn-Teller distorted singlet ground state was found.

Here, we introduce an internal degree of freedom of C_{60} that is very sensitive to any kind of symmetry breaking, namely bond alternation. Bond alternation means the difference between the two kinds of bonds in the molecule, namely the ones linking two hexagons (called l_{66}) and the larger ones linking a hexagon and a pentagon (called l_{65}). Both sets form bond alternation patterns on the hexagons. It is known from a symmetry analysis and from earlier theoretical calculations that bond alternation is max-

imal for the neutral molecule and strongly reduces with charging. The anisotropic charge distribution in a Jahn-Teller distorted ion is therefore expected to cause an anisotropic bond alternation pattern.

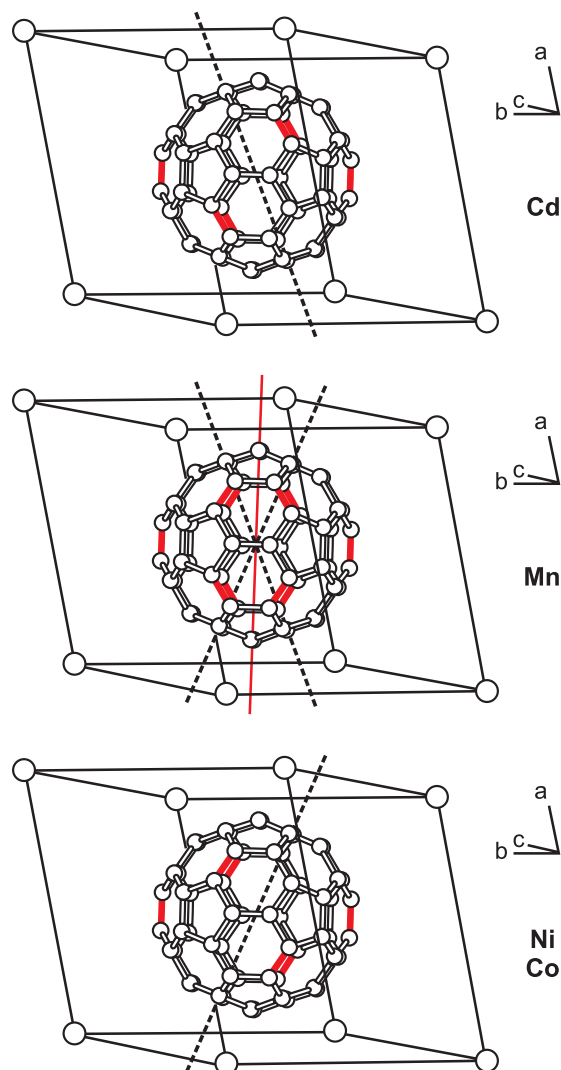


Figure 5: Positions of the most extended l_{66} -bonds (in red) and corresponding symmetry axes for C_{60} in $[M(NH_3)_6]C_{60} \cdot 6NH_3$ -compounds with $M = Cd, Mn, Ni$. The axes for D_{3d} are broken black lines, the one for D_{2h} is a red line.

The quality of single crystal structure determinations on a series of compounds of C_{60}^{-2} -ions was so good that reproducible bond alternation patterns beyond background noise could be extracted. Figure 5 represents the positions of the most strongly enhanced l_{66} -bonds

in C_{60} for a series of $[M(NH_3)_6]C_{60} \cdot 6NH_3$ -compounds with $M = Cd, Mn, Ni$. Here, the uppermost (Cd) and lowest (Ni,Co) figures show the same patterns but are represented by different symmetry axes with a local D_{3d} symmetry each. Each symmetry axis is going through the center of two hexagons. For each case, six out of thirty l_{66} -bonds are significantly elongated, three each above and below the inversion plane. The same pattern was also found for $[Ba(NH_3)_7]C_{60} \cdot 4NH_3$. In the latter case, the local symmetry axis coincides with a crystal C_3 -symmetry axis. The isostructural transition metal compounds however, have a low symmetry, and the orientation of the threefold axis varies with decreasing ionic radii of the transition metal ions. The experimental findings for the Mn-compound (middle part of Fig. 5) can be interpreted in two ways, either as an incoherent superposition of the two extremal D_{3d} cases (caused, e.g. by crystallographic twinning) or as a D_{2h} -representation where the symmetry axis goes through two l_{66} -bonds. Here, the two bonds crossing the D_{2h} mirror plane change most, and another eight bonds change somewhat less. In further C_{60}^{-2} compounds, mostly patterns were found that correspond to the D_{3d} -representation.

These experimental findings have been used to unequivocally determine a singlet state as the ionic ground state from theoretical calculations. The theoretical treatment was not simple, even for the isolated ion. We applied the Local Ansatz (LA), and restricted the calculation to the isolated ion, but comparison to experiment was made for solids.

All relevant electronic states of the ion have anisotropic bond alternation patterns. These differ partially only by magnitude, being largest for the singlet state with maximal symmetry lowering, and smallest for individual triplet states. With the magnitude determined experimentally with high precision, one may distinguish between singlet and triplet states, and may even determine the size of the Jahn-Teller hybridization of the singlet ground state.

Before dealing with the symmetry reduction itself, the mean bond alternations for the different ions were determined. Figure 6 contains the averaged experimental results from different C_{60} and C_{60}^{-2} -compounds in comparison to theoretical Density Functional (DF), Hartree-Fock (HF), and LA-results. The same basis sets were used in all schemes. The DF- and HF-results were converged with respect to this basis to which bond alternation is very sensitive. The difference between the different theoretical schemes has the following origin.

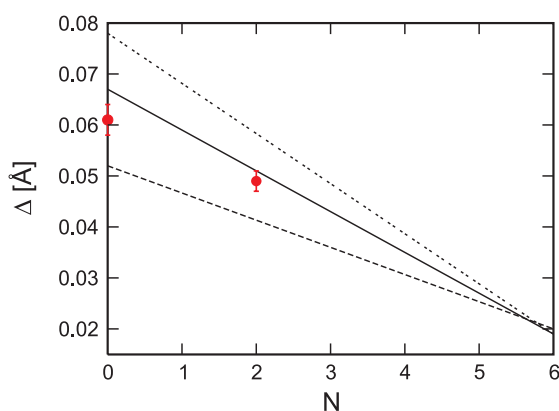


Figure 6: Experimental bond alternation in comparison to DF (lower broken line), HF (double dotted line), and LA (solid line) results for different C_{60} -ions. Given is the difference Δ between the mean l_{65} and l_{66} bond lengths [Å] as a function of negative ionic charge N .

Bond alternation is maximal for C_{60} because it allows the π -electrons to localize. It is known from polyacetylene and Li that partially screened nonlocal exchange contributions sizably influence the magnitude of localization, and thus of bond alternation, and similar effects were predicted for C_{60} . Such contributions are not covered by DF-calculations. The difference between DF and HF represents the full non-screened exchange contributions, while the one between HF and LA is mostly due to screening corrections. The limiting case of C_{60}^{-6} is insensitive to these details because there, electrons can no more be localized by small structural changes. The experiments are closest to the LA result, in particular for the most accurately determined C_{60}^{-2} -compounds. The LA-

results are expected to overestimate the true theoretical limit for bond alternation of the neutral molecule by 0.003 Å due to a non-perfect treatment of long range screening.

Next, the symmetry broken singlet states were computed. In the calculations only these degrees of freedom 99 were reoptimized which could be compared to experiment, namely the changes in the l_{66} . The atomic positions were kept on a sphere. The bond alternation patterns fit very well to experiment (Fig. 5). Here, we only compare the experimental variance δ of the l_{66} -bonds in the C_{60}^{-2} -ions to theory. For the most accurately determined compound, $[Ba(NH_3)_7]C_{60} \cdot 4NH_3$, the experimental variance amounts to 0.026 ± 0.002 Å. For the ion in D_{3d} -symmetry itself, the result of the LA for the extremal symmetry broken singlet state is 0.027 Å, and for the true singlet ground state 0.026 Å. This is in perfect agreement with experiment. The proximity to the limiting singlet state indicates a small magnetic energy which can be represented by an effective screened atomic interaction of the π -electrons of $U = 4$ eV. Larger local interactions are ruled out since they would lead to a too small δ . The DF-result for the variance δ of the extremal singlet state is only 0.019 Å, demonstrating again the relevance of the screened exchange.

The structures were determined at 100 K. The proximity to the theoretical limit demonstrates that thermal excitations can not play any significant role. Therefore, all other singlet and triplet states with a different pattern or a smaller variance must be at least 500 K above the ground state, indicating an external crystal field of this size.

The theoretical calculations were also performed for a C_{60}^{-2} -ion in D_{2h} -symmetry. There, the theoretical variance turned out to be 10% larger than for the D_{3d} -symmetry. In the experiments, no enhancement was found for the in-between state, but the error bar is of the size of the theoretical difference. Other experimental details, though, indicate rather a coherent

D_{2h} -state. The computed energies of the singlet states in D_{3d} and D_{2h} symmetry turned out to be identical for the free ion. The energy landscape between neighboring D_{3d} -axes is therefore expected to be very flat. Consequently, the direction of the Jahn-Teller distortion may well be determined by the external crystal field, and may move (almost) continuously through the molecule as is apparently the case for the compounds displayed in Fig. 5.

For the singlet ground state, the energy gained from the reoptimization of bond alternation in comparison to the one of neutral C_{60} amounts to 170 meV when computed by the LA but only to 80 meV in DF approximation. When compared to a triplet state (also with anisotropic bond alternations), the structural energy gain is still 76 meV. This is somewhat smaller than the magnetic interaction that favors the triplet states (98 meV). Degrees of freedom left out in

the computation like deviations from the spherical form of the ion might well lower the singlet energy below the triplet energy for the free ion. The external crystal field deduced from experiment also stabilizes the singlet ground state in the solid. Its energy (50 meV) is comparable in size to the other contributions.

To conclude, we have shown that a specific anisotropy in the bond alternation pattern of C_{60}^{-2} as observed experimentally is the first manifestation of a static Jahn-Teller distortion in bulk, crystalline compounds. Theoretical analyses allow to unequivocally assign a diamagnetic singlet ground state and produce excellent quantitative agreement with respect to the bond alternation pattern. They also demonstrate that electron-lattice coupling may be strongly enhanced by nonlocal screened exchange contributions.

Superconductivity in hole-doped diamond

L. Boeri and O.K. Andersen; J. Kortus (Technische Universität Bergakademie Freiberg)

Diamond is usually considered the prototype of band insulators: it came as a big surprise, therefore, when it was shown that, under extremely high boron doping (i.e. 3%), diamond undergoes a superconducting transition with a critical temperature of 4 K [1]. After the initial report in polycrystalline samples, the result has also been confirmed in thin films, with T_c 's as high as 11 K. Besides creating an obvious technological interest, as diamond is a promising material for application in electronics, these findings posed fundamental questions concerning the superconducting mechanism and the possibility of observing superconductivity in other doped semiconductors. Our investigations based on first-principles electronic structure calculations suggest that the observed superconductivity in hole-doped diamond is due to an electron-phonon mechanism. We assume that at these doping concentrations, which are

one order of magnitude larger than those at which an insulator-metal transition takes place, B-doped diamond can be described as a degenerate metal. A similar point of view has been adopted in several other subsequent works [2], while in Ref. [3] a purely electronic mechanism valid for impurity bands was proposed. Our results not only show that electron-phonon interaction is a very likely explanation for the observed superconductivity, but also allow us to discover an unexpected similarity between hole-doped diamond and the record electron-phonon superconductor MgB_2 .

We have performed first-principles calculations of the electronic and phononic properties of hole-doped diamond and other tetrahedral group-IV semiconductors, silicon and germanium, using Savrasov's Linear Response LMTO program. In the following we shall fo-

cus mainly on diamond, but, unless differently stated, the arguments and results apply to all the tetrahedral semiconductors studied. To model the effect of doping we used the Virtual Crystal Approximation (VCA): we approximated the real lattice, in which a fraction x of Carbon atoms is randomly replaced by Boron atoms, with a regular lattice of *virtual atoms* with a non-integer number of protons (Z_{virt}), which is a weighted average of those of Carbon and Boron: $Z_{\text{virt}} = (1 - x)Z_C + xZ_B$. This allowed us to evaluate the physical properties of hole-doped diamond, silicon and germanium for different doping, up to $x = 0.1$.

Even at $x = 0.1$, the band structure of hole-doped diamond, shown as solid blue lines in Fig. 7, is still almost identical to that of the pure material: the $4sp^3$ hybrids on each C atom form 4 bonding (valence) and 4 anti-bonding (conduction) bands, separated by a large gap. The exceptional hardness of diamond derives from the fact that the only states which are full are all of σ bonding character, and these form bonds which are among the strongest in nature.

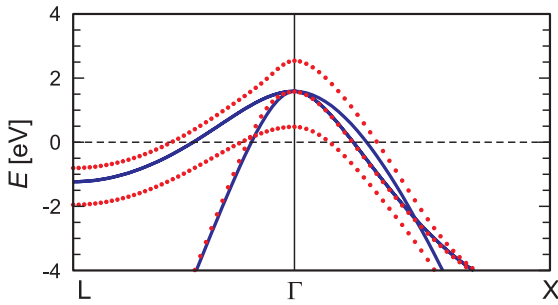


Figure 7: The band structure of hole-doped diamond in the VCA approximation (blue solid line) is almost identical to that of the pure material, even at $x = 0.1$; however, boron doping drives holes into the valence band, which couple strongly to the bond-stretching phonon at $q \simeq 0$. The red dotted line shows the effect of a frozen optical zone-center phonon on the band structure.

With boron doping, electrons are removed from the crystal and holes form at the top of the triply-degenerate valence band: diamond becomes metallic, with the holes forming three distorted spherical Fermi surfaces around the

center of the Brillouin zone. The average radius of the spheroids grows with doping as $k_F \simeq (x/3)^{1/3}k_{\text{BZ}}$; the Density of States (DOS) has a typical $3d$ behavior, and its value at the Fermi level, $N(\epsilon_F)$, grows as $x^{2/3}$. This picture has recently been confirmed by the ARPES measurements of B-doped diamond films by Yokoya *et al.* [1], who have shown that around E_F the band structure of B-doped diamond is very similar to that of the pure material, with E_F moving to lower energies with doping.

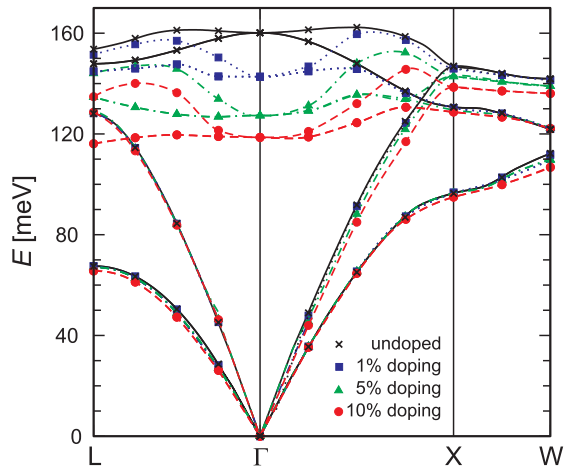


Figure 8: Phonon dispersion of pure and hole-doped diamond for different values of boron concentration x : we observe a pronounced softening of the frequency of the zone-center optical phonon with respect to the pure case, which increases as a function of x .

The effect of doping on the phonon spectrum is shown in Fig. 8: there is a sizeable reduction (softening) of the frequency of the zone-center optical phonon; as x is increased, the softening increases and extends to a larger region in \mathbf{q} -space. This effect can easily be understood in terms of the standard electron-phonon theory: in metals, the interaction of conduction electrons with a phonon causes a reduction of its frequency, which grows with the strength of the interaction; also, the theory shows that only phonons with $q < 2k_F$ are allowed to couple. Figure 8 thus shows that in this system only the optical mode is coupled, with a strength increasing with doping.

A simple physical argument explains why in this material electrons couple strongly to some lattice vibrations: the optical phonon, which at the zone-center has the same symmetry as the electronic states at the top of the valence band, is a bond-stretching mode which distorts the stiff σ -bonds. In fact, when the ions are moved along the eigenvector of the Γ optical mode, the triple degeneracy of the top of the σ -band at the Γ -point is removed, with one band moving to lower and one to higher energies, the third band being fixed (dotted red lines in Fig. 7 correspond to a frozen distortion of reduced amplitude $u=0.05\text{\AA}$). As discussed by Cardona [2], this mechanism is also responsible for the zero-point renormalization of the optical gap in pure semiconductors. The same, strong coupling between bond-stretching phonons and holes at the top of doubly-degenerate σ -bonding bands is at the basis of the exceptional superconducting properties of Magnesium Diboride. Hole-doped diamond is, after five years of intense theoretical and experimental research in the field of MgB_2 , the first example of an existing material which is so similar to MgB_2 that the theoretical knowledge derived there can be applied to and tested on.

In MgB_2 a surprisingly close estimate of the total electron phonon coupling λ , is given by the Hopfield formula, which is exact for parabolic bands with $k_F \ll k_{BZ}$:

$$\lambda = \frac{N(\epsilon_F)D^2}{M\omega^2}, \quad (1)$$

where $N(\epsilon_F)$ is the density of σ states at the Fermi level, M is the reduced mass of the optical bond-stretching phonon, and D is the energy splitting of the doubly-degenerate top of the σ -band produced by the displacement \mathbf{e} of the same bond-stretching phonon, with normalized eigenvector \mathbf{e} . There is a feedback effect between λ and the phonon frequency, since ω is renormalized with respect to its bare value ω_0 by the interaction with electrons: $\omega^2 = \omega_0^2 / (1 + 2\lambda)$.

Once ω and λ are known, the critical temperature can be evaluated using the formula:

$$T_c = \omega \exp\left(\frac{-1}{\frac{\lambda}{1+\lambda} - \mu^*}\right) \quad (2)$$

These results can be generalized to diamond, with a few differences due to dimensionality. MgB_2 is in fact a layered material very similar to graphite, the 2D form of carbon, which unlike diamond is based on sp^2 -bonding. Instead of four σ -bands, there are three σ and one π -band; the top of the σ -band, which contains the superconducting holes, is doubly degenerate, with the same symmetry as the bond-stretching phonon mode. In MgB_2 all the σ electrons couple to each of the degenerate phonon vibrations, whereas in diamond only 2 bands out of 3 are coupled to each degenerate phonon vibration. Therefore, the formula for the renormalization of the phonon frequencies in diamond reads: $\omega^2 = \omega_0^2 / (1 + 2(\frac{2}{3})\lambda)$.

Equation(1) shows that the total electron-phonon coupling is determined by material-dependent parameters, such as the density of states at the Fermi level and the deformation potential, and to a large extent by the phonon softening, which in turn is dominated by dimensionality. To discriminate between these two effects, it is useful to introduce a bare electron-phonon coupling $\lambda_0 = N(\epsilon_F)D^2 / M\omega_0^2$, which only contains material-dependent parameters: while D is a measure of the geometrical distortion of the electronic bands due to phonons, ω_0 measures the hardness of the material. The total electron-phonon coupling is then $\lambda = \frac{\lambda_0}{1 - 2\alpha\lambda_0}$, with $\alpha = 1$ in 2D and $2/3$ in 3D. Table 1 contains the values entering the definition of λ according to Eq.(1) for MgB_2 , diamond, Si and Ge and the relative λ_0 . It can be noticed that, even if at $x=0.1$, due to the compensating effect of a larger deformation potential and phonon frequency, diamond has the same λ_0 as MgB_2 , its effective electron-phonon coupling is much lower (0.6 instead of 1.0); this reduction is completely due to dimensionality effects, represented by the factor α . The value of λ in diamond grows sensibly with doping, following the increase of $N(\epsilon_F)$.

Table 1: Values of the parameters which determine the total electron-phonon coupling λ according to the Hopfield Eq.(1). $N(\epsilon_F)$ is in states/eV/spin/f.u., D is in eV/Å and ω in cm^{-1} . The total electron-phonon coupling obtained by the numerical integration of the full Eliashberg function (λ_{num}) is also reported.

	$N(\epsilon_F)$	D	ω	λ_0	λ	λ_{num}
MgB ₂	0.15	12.4	536	0.33	1.01	1.02
C	0.00	21.6	1292	0	0	0
3%C	0.07	21.1	1077	0.21	0.30	0.30
5%C	0.08	20.8	1027	0.25	0.37	0.36
10%C	0.11	20.4	957	0.32	0.57	0.56
Si	0.00	6.8	510	0	0	0
5%Si	0.17	6.3	453	0.13	0.16	0.30
10%Si	0.24	6.1	438	0.17	0.22	0.40
Ge	0.00	5.8	317	0	0	0
10%Ge	0.20	4.4	282	0.08	0.09	0.32

In the same table, the value of λ obtained by the numerical integration of the total Eliashberg function $\alpha^2F(\omega)$, evaluated on a very fine $(1/12)^3$ grid in \mathbf{q} -space is also reported (λ_{num}). In diamond, the agreement between the approximate Hopfield formula and the numerical result, which takes into account the full complexity of the electronic and vibrational spectrum, is striking. In fact, the shape of the Eliashberg function indicates that the electron-phonon coupling is actually concentrated in the bond-stretching phonon branch.

As far as the other tetrahedral semiconductors are concerned, their bare and total electron-phonon coupling parameters are always lower than the corresponding ones of diamond, mainly because the deformation potentials are lower. Furthermore, in this case the agreement between the Hopfield formula and the numerical estimate of λ is less good, as the Eliashberg function shows that other phonon branches are involved in the coupling.

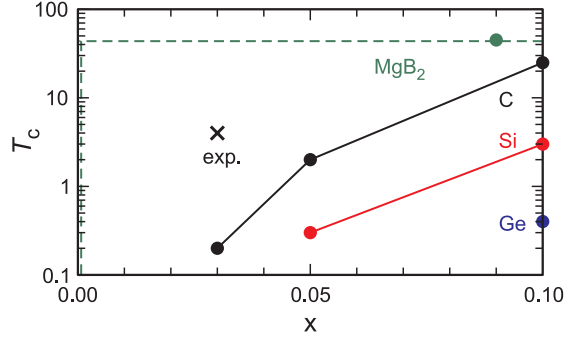


Figure 9: Critical temperature T_c (Eq.(2)) as a function of x for hole-doped diamond, Si and Ge, in comparison to MgB₂, using $\mu^* = 0.1$.

Finally, Fig. 9 shows the critical temperatures for hole-doped diamond, silicon and germanium given by Eq.(2); given the approximations in the formula for T_c and in the determination of doping, the results for diamond are in reasonable agreement with the experiment, indicating that electron-phonon coupling is a likely mechanism for the superconductivity in this system. Our results show that, unless very high doping levels can be obtained, it is very unlikely to observe superconductivity in Si or Ge.

- [1] Ekimov, E.A., V.A. Sidorov, E.D. Bauer, N.N. Mel'nik, N.J. Curro, J.D. Thompson and S.M. Stishov. *Nature* **428**, 542-545 (2004); Umezawa, H., T. Takenouchi, Y. Takano, K. Kobayashi, M. Nagao, I. Sakaguchi, M. Tachiki, T. Hatano, G. Zhong, M. Tachiki and H. Kawarada. *cond-mat* 0503303; Yokoya, T., T. Nakamura, T. Matsushita, T. Muro, Y. Takano, M. Nagao, T. Takenouchi, H. Kawarada and T. Oguchi. *Nature* **438**, 647-650 (2005).
- [2] Lee, K.-W. and W.E. Pickett. *Physical Review Letters* **93**, 237003 (2004); Blase, X., C. Adessi and D. Connétable. *Physical Review Letters* **93**, 237004 (2004); Xiang, H.J., Z. Li, J. Yang, J.G. Hou and Q. Zhu. *Physical Review B* **70**, 212504 (2004); M. Cardona. *Solid State Communications* **133**, 3-18 (2005); Ma, Y., J.S. Tse, T. Cui, D.D. Klug, L. Zhang, Y. Xie, Y. Niu and G. Zou. *Physical Review B* **72**, 014306 (2005).
- [3] Baskaran, G. *cond-mat*/0404286 and *cond-mat*/0410296.

Atomistic structure of the surface planes in SiC pores

U. Starke and W.Y. Lee; C. Coletti and S.E. Sadow (University of South Florida);
R.P. Devaty and W.J. Choyke (University of Pittsburgh)

Porous SiC has shown intriguing perspectives for a variety of possible applications in electronic devices, gas sensors, fuel cells and bio-technology. Among several pore morphologies discovered so far, one important pore type found is a triangular shaped pore channel with surfaces inclined by about 62° with respect to the basal plane. In 4H-SiC these tilted pore edges correspond to a $(\bar{1}10\bar{2})$ -surface orientation. This 4H-SiC $(\bar{1}10\bar{2})$ surface and its isomorphic opposite, i.e. the 4H-SiC $(1\bar{1}02)$ surface have been studied using atomic force microscopy (AFM), low-energy electron diffraction (LEED) and Auger electron spectroscopy (AES).

Figure 10 shows the orientation of these surfaces within the 4H-SiC bulk. As demonstrated by the schematics in panel (b), the $(\bar{1}10\bar{2})$ plane (red) is tilted with respect to the c -axis. Panel (a) displays an atomic model of the 4H-SiC crystal with 4 bilayers per unit cell and a layer stacking ABCBA. The blue bond train shows that slabs of two bilayers in identical orientation (linear stacking) are alternatingly stacked together by a 60° rotation (hexagonal stacking). The $(\bar{1}10\bar{2})$ plane, as symbolized by the red line, runs parallel to this bond train for two bilayers. In the second half of the unit cell it runs approximately perpendicular to the bond train.

The bulk truncated surface can have different surface terminations. The possibilities range from fully Si terminated to fully C terminated, depending on which of the six different layers is terminating the surface. Such different terminations are possible for both the $(\bar{1}10\bar{2})$ and the $(1\bar{1}02)$ surfaces. The full Si terminated $(\bar{1}10\bar{2})$ surface is shown in Fig. 10(c) in a side view along the $[\bar{1}\bar{1}20]$ direction (the (1×1) -surface unit cell and the 4H-SiC bulk unit cell are depicted). Figure 10(d) shows the respective top view and indicates the surface unit cell (red,

solid line rectangle). Stripes of different surface bond configuration, which will be discussed below, are marked.

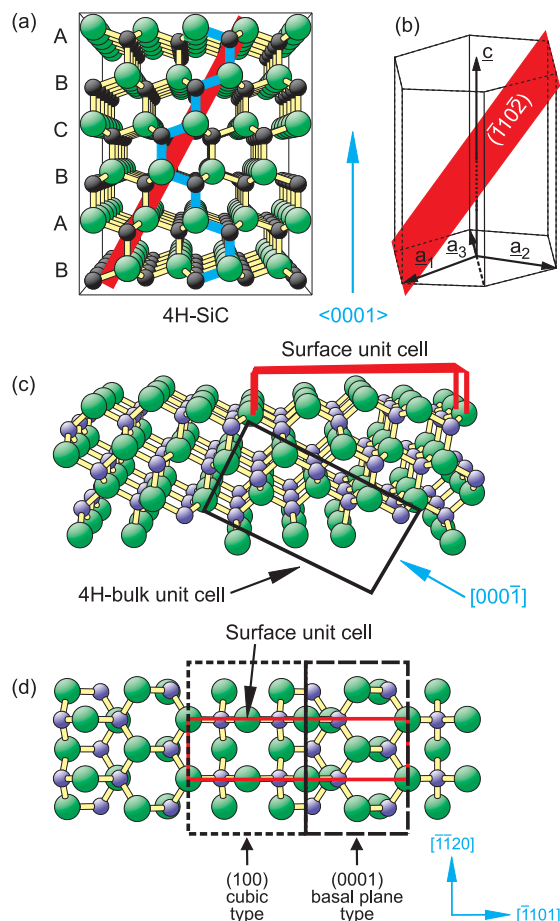


Figure 10: (a) Atomic model of 4H-SiC in side-view perspective along the $[\bar{1}\bar{1}20]$ direction. Bonds within the $(\bar{1}10\bar{2})$ plane are marked by blue lines and the orientation of the $(\bar{1}10\bar{2})$ plane by a red line. (b) Schematic plane orientation and lattice vector construction. (c) Bulk truncated, Si terminated 4H-SiC $(\bar{1}10\bar{2})$ surface in side view. The surface unit cell and the 4H-bulk unit cell are highlighted. (d) SiC $(\bar{1}10\bar{2})$ surface shown in top view. The (1×1) unit cell (red) as well as the separation in cubic (100) type (bounded by dotted lines) and (0001) basal plane type (bounded by dashed lines) patches and crystal directions (blue) are indicated. Large green atoms represent Si, small dark or blue atoms C.

In order to analyze the atomic structure of these surfaces, mechanically polished samples of both orientations were etched in hydrogen flux at 1500°C to eliminate the polishing damage and to obtain ordered surfaces as commonly obtained for the basal plane surfaces from such procedures [1]. AFM images acquired under ambient conditions (Fig. 11) indeed show that the residual polishing scratches are to a large extent removed. The residual misorientation (of less than 0.5 degrees) of the samples results in step arrays parallel and perpendicular to the $[\bar{1}101]$ -direction. However, the step heights and terrace widths are drastically different for the two surface orientations as demonstrated by the line profiles plotted in Fig. 11.

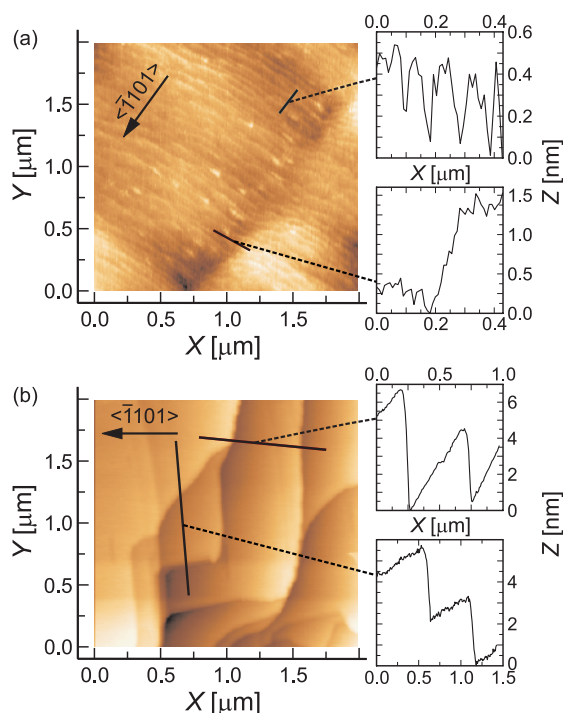


Figure 11: AFM images obtained after hydrogen etching of (a) 4H-SiC($\bar{1}10\bar{2}$) and (b) 4H-SiC($1\bar{1}02$). Line profiles parallel and perpendicular to the $[\bar{1}101]$ direction are shown on the right.

On SiC($\bar{1}10\bar{2}$), the steps perpendicular to the $[\bar{1}101]$ -direction are very small (typically 0.2–0.8 nm height), whereas the parallel steps are larger with a typical height of 1.5–2.0 nm. This results in a stripe pattern morphology (50 nm \times 1 μ m terraces) as visible in the AFM-image (Fig. 11(a)). On SiC($1\bar{1}02$), on the other

hand, large terraces (0.5 μ m \times 2–3 μ m) are found with step heights of 2–5 nm (see Fig. 11(b)).

The hydrogen-etched samples were subsequently introduced into an ultrahigh vacuum (UHV) surface analysis chamber. Both surface orientations display a sharp (1×1)-LEED pattern as shown in Fig. 12(a) and (c) with some residual background from atmospheric contamination. The (1×1) spot arrangement indicates a bulk-like periodicity with the surface unit cell shaped as drawn in Fig. 10. The surfaces are obviously terminated by a thin oxide layer. This is inferred from the significant oxygen-peak in AES (differentiated AES-signal $dN(E)/dE$, cf. Fig. 12(e) and (f), top curves). In addition to the identical bulk-like surface periodicity in this ‘as-etched’ condition, the chemical composition appears to be quite similar for the two orientations as determined from the Si to C AES peak ratio (insets in Figs. 12(e) and (f)). Yet, this is not too surprising, since in both orientations the bulk terminated surface corresponds to an alternating stripe pattern of basal-plane like (0001) and cubic type (100) surface patches. This can be seen in the top view atomic model in Fig. 10(d). In this figure the red solid line rectangle defines the surface unit cell. The area surrounded by a dashed line on the right side of the unit cell highlights a stripe with triangular bond coordination of the topmost Si to the next C layer, which is typical for a hexagonal basal plane (0001) bilayer. The short dashed lines on the left side of the unit cell enclose a patch where one finds the characteristic 90° rotation of the in-plane component of the Si-C bond direction in alternating layers, which is common for the cubic (100) surface. Due to the strict alternation of Si and C layers on 3C-SiC(100) the same surface termination is possible on such patches for both our surfaces. The basal plane like patches are different for our two surfaces, corresponding to (0001) and (000 $\bar{1}$) termination. Yet, on the Si-face and C-face basal plane surfaces two very similar oxide structures exist [2], so that the two surfaces in the present work, i.e. SiC($\bar{1}10\bar{2}$) and SiC($1\bar{1}02$) may well be covered by similar oxide structures.

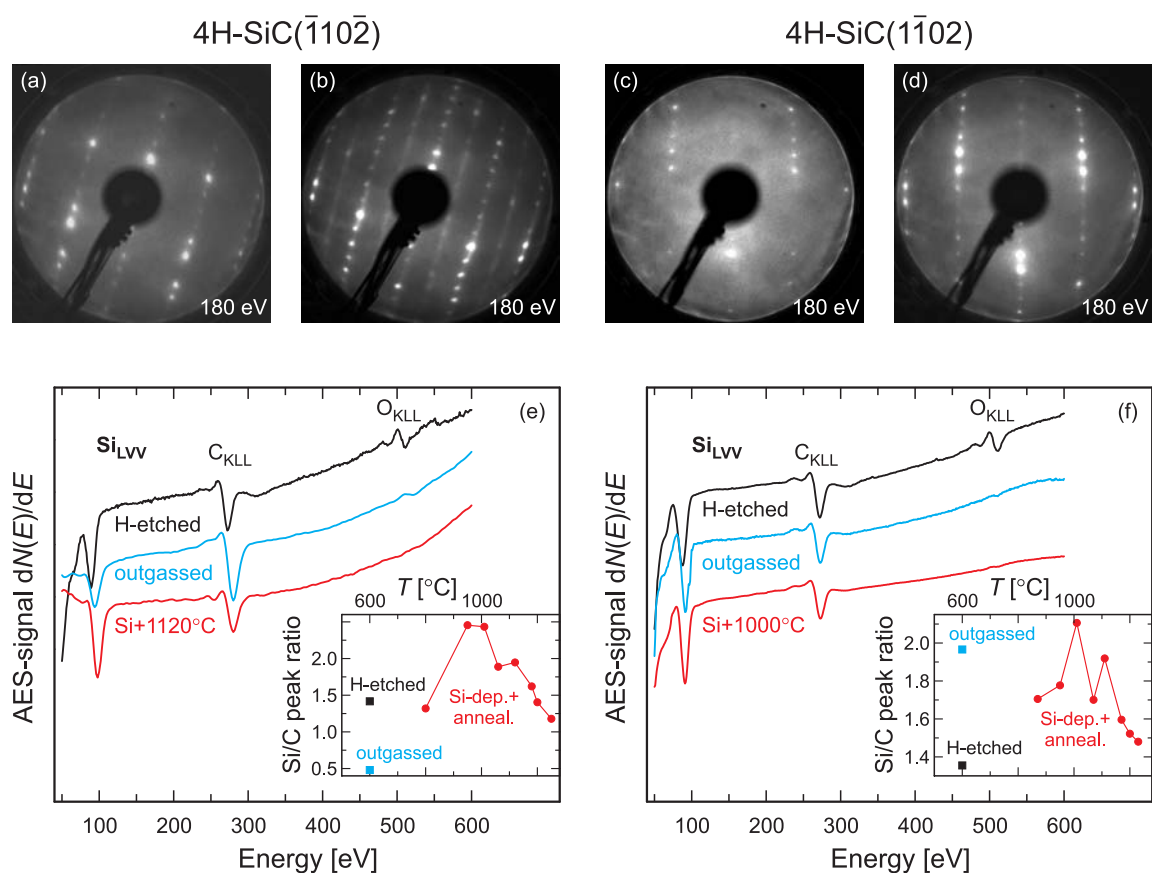


Figure 12: LEED patterns of (a,b) 4H-SiC($\bar{1}10\bar{2}$) and (c,d) 4H-SiC($1\bar{1}02$) as observed immediately after hydrogen etching (a,c) and upon Si-deposition and annealing (b,d). Corresponding AES spectra for (e) 4H-SiC($\bar{1}10\bar{2}$) and (f) 4H-SiC($1\bar{1}02$). The Si, C and O AES transitions have been marked. AES spectra are also shown after outgassing. The insets show Si/C AES-peak ratios.

The oxygen can practically be removed by flashing in UHV to about 1200°C. The corresponding AES spectra are shown in the middle curves of Fig. 12(e) and (f). The Si/C ratio is depicted in the insets, which for reasons not understood at present behaves quite differently on the two surfaces upon this flash. Si deposition and subsequent annealing lead to a well-ordered surface with the best LEED pattern obtained after about 1120°C and 1000°C heating, respectively, for the two surfaces (cf. Fig. 12(b) and (d)). The corresponding AES spectra are shown in Fig. 12(e) and (f) (bottom curves). Interestingly, the Si/C composition ratio increases up to 1000°C (cf. Si/C ratios in the insets), before at

higher temperatures, once again the Si content drops. LEED spot intensity curves clearly indicate a different structure for the UHV treated surface as compared to the ‘as-etched’ surface condition. Here, the chemical difference between the two orientations becomes more obvious with quite different LEED spot intensities for the two surfaces. Apparently, the different polarities of the (0001) type patches of the unit cell are manifested in the overall surface structure. To resolve the detailed atomic structure of the surfaces, LEED spot intensity spectra were acquired for a quantitative LEED structure analysis. This analysis is currently under way.

In summary, 4H-SiC($\bar{1}10\bar{2}$) and 4H-SiC($1\bar{1}02$) surfaces have been investigated using AFM, LEED and AES. The surfaces develop a well-defined step arrangement after hydrogen etching with steps parallel and perpendicular to the $[\bar{1}101]$ -direction. Yet drastically different morphologies for the two isomorphic orientations are observed. Both surfaces display a sharp (1×1) , i.e. bulk-periodic LEED pattern and are terminated by a thin ordered oxide layer

as seen from AES. In UHV, Si deposition and subsequent annealing leads to an oxygen free, well-ordered surface with a maximum Si content after heating to approximately 1000°C.

-
- [1] Starke, U. 'Atomic structure of SiC surfaces'.
In: Silicon Carbide, Recent Major Advances,
W.J. Choyke, H. Matsunami, G. Pensl (Eds.).
Springer, Berlin, 2004, p. 281.
 - [2] Bernhardt, J., J. Schardt, U. Starke and K. Heinz.
Applied Physics Letters **74**, 1084-1086 (1999).

Nanostructures

The fabrication and investigation of nanostructured materials is one important area of research at the Institute. The first report deals with the deposition of metal-organic coordination networks on a Cu(110) surface which form periodic one-dimensional chains. Scanning tunneling microscopy investigations agree quite well with theoretical calculations which might help to engineer similar systems with specific magnetic, electronic, or catalytic properties. The following report studies the evolution of self-assembled SiGe islands on Si surfaces after the deposition of Ge, using atomic force microscopy. The optical properties of a one-dimensional photonic crystal structure of nanowires have been studied as a function of disorder inside the supercell without perturbing the overall periodicity. Finally, a new theoretical method, the functional renormalization group method, has been applied to a one-dimensional fermionic lattice model for quantum wires. This method allows to include a hard-core repulsion between the fermions and also various types of impurities. Results for the conductance and the density of states are given.

One-dimensional metal-organic coordination networks at surfaces

T. Classen, G. Costantini and K. Kern; G. Fratesi, S. Fabris, S. de Gironcoli
and S. Baroni (SISSA and INFN-CNR DEMOCRITOS, Trieste, Italy)

Metal-organic coordination networks (MOCNs) formed by coordination bonding between metallic centers and organic ligands can be efficiently engineered to exhibit specific magnetic, electronic, or catalytic properties. Instead of depositing prefabricated MOCNs onto surfaces, it has been recently shown that two dimensional (2D) MOCNs can be directly grown at metal surfaces in ultrahigh vacuum (UHV), thus creating highly regular 2D networks of metal atoms [1,2]. These grids have been pointed out to be potentially relevant for devices involving sensing, switching, and information storage. Here, we show that by using the substrate as a template it is possible to predefine the MOCN geometry and to direct the formation of novel metal-organic coordination chains (MOCCs) [3].

Cu(110) was chosen as a prototypical highly anisotropic substrate. In order to evidence its strong 1D templating effect, a molecule with a triangular symmetry, 1,3,5-benzenetricarboxylic acid (trimesic acid, TMA), was se-

lected as organic ligand. The UHV deposition of TMA on Cu(110) at room temperature and the subsequent annealing to 380–410 K results in the formation of straight and highly periodic 1D chains running along the $\langle 1\bar{1}0 \rangle$ substrate direction (Fig. 13). At low coverage, chains predominantly attach to step edges, while by increasing the coverage chain nucleation takes place also on terraces.

The deposition temperature is high enough to provide mobile Cu adatoms via evaporation from kinks and steps onto the terraces. These adatoms have been found by XPS analysis of similar systems to catalyze the deprotonation of the molecular carboxylic groups and are furthermore necessary for the formation of Cu carboxylate complexes [4].

The chains, hereafter referred to as MOCC-I, consist of triangles alternating with round protrusions (Fig. 13(b) and (c)). The apparent height of the two units is significantly different: 140 ± 30 pm and 75 ± 20 pm, respectively,

when scanning at -1 V and 1 nA. The triangles are identified as flat-lying TMA molecules, while the round protrusions can be attributed to Cu adatoms coordinated by two of the carboxylate groups of the TMA molecule. The third TMA functional group is pointing out of the chain with no preferential up or down orientation (Fig. 13(b)).

The periodicity of the MOCC-I along $\langle 1\bar{1}0 \rangle$ is 5 Cu lattice spacings (12.70 ± 0.15 Å). High-resolution STM images indicate that the distance between the Cu-protrusion and the O atom of the molecular carboxylate groups is ≈ 2.8 Å, a rather large value when compared to the typical Cu-O bond length of 1.9 – 2.2 Å. The simplest $[-\text{TMA-Cu-}]_n$ chain model for the MOCC-I adsorption geometry seems therefore to be outruled by these observations.

Indeed, the lowest energy MOCC-I structure predicted by density functional theory (DFT) calculations is a $[-\text{Cu-TMA-Cu-}]_n$ chain in which a dimer of Cu metal adatoms forms unidentate Cu carboxylate bonds with adjacent TMA molecules (Fig. 13(d)). The dimer binds to the surface by 6.3 eV with respect to isolated Cu atoms and each adatom is 5 -fold coordinated to the substrate. This structure has the right $5\times$ periodicity. Its simulated STM image (Fig. 13(e)) closely agrees with the experimental one, the Cu-Cu dimer being imaged as a single spot centered between the adatoms. The resulting Cu-O distance is 2.02 Å, therefore in the range of the typical Cu-O bond lengths. Finally, also the calculated apparent heights, 170 pm for the TMA and 90 pm for the Cu-protrusion, are in good agreement with the experimental ones.

The theoretical analysis provides an unprecedented level of insight into the adsorption geometry of surface MOCNs. The molecule stands 1.14 Å above the outermost Cu layer, the carboxylate groups bending towards the surface by as much as 0.69 Å. With respect to a neutral Cu atom, surface Cu-complexation weakly reduces the metal center occupations of both the s and d electronic states by ≈ 0.2 electrons.

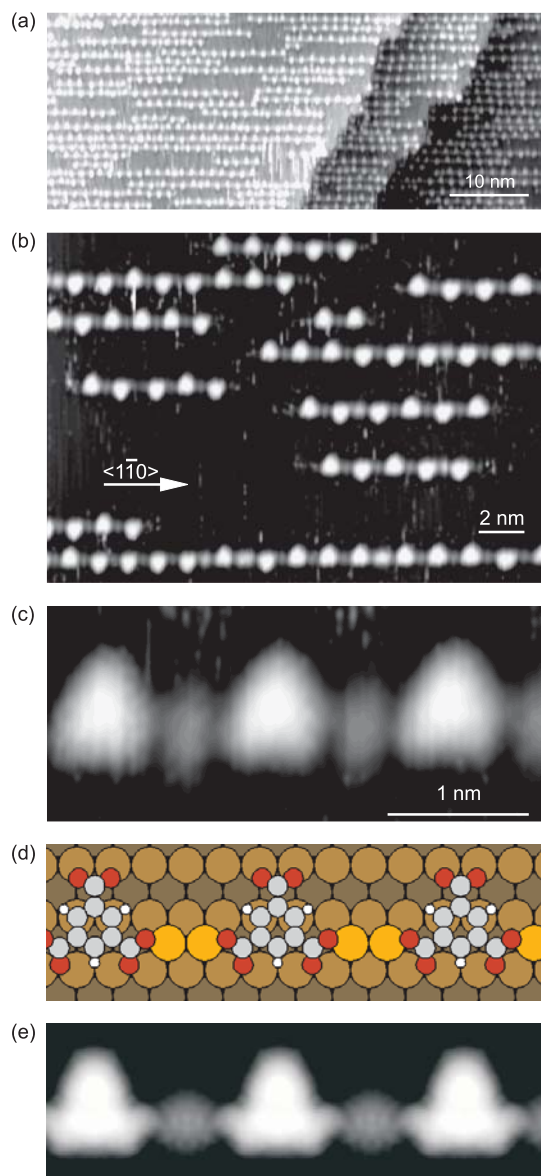


Figure 13: STM representative images of $[-\text{Cu-TMA-Cu-}]_n$ chains (MOCC-I) on Cu(110) for TMA coverages of (a) 0.36 and (b) 0.13 monolayer (ML), respectively. Comparison of (c) the high-resolution STM image of MOCC-I, (d) the atomistic MOCC-I model, and (e) the corresponding DFT simulated STM image.

$[-\text{Cu-TMA-Cu-}]_n$ chains are the intrinsic nanostructures on Cu(110), but functional MOCCs require also different elements than Cu as metallic centers. Extrinsic $[-\text{TMA-Fe-}]_n$ chains (MOCC-II) were created by holding the Cu(110) crystal at 230 K and by depositing first TMA and then Fe at coverages higher

than 0.04 ML. The sample was then annealed to 390 K for one minute. The number of chains increased with the amount of deposited Fe and saturation was reached for a coverage of ≈ 0.08 ML of Fe. Further Fe deposition results in the nucleation of Fe islands.

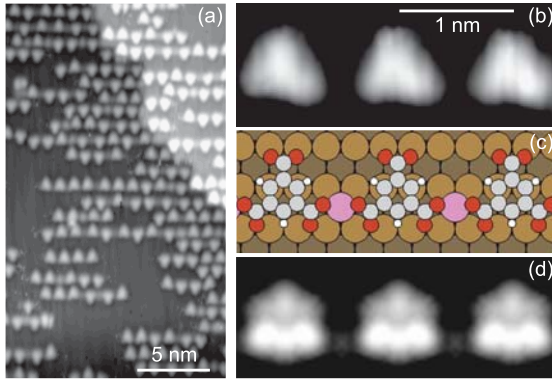


Figure 14: $[-\text{TMA-Fe}]_n$ chains (MOCC-II): (a) Overview image of the coordination chains formed upon deposition of 0.04 ML Fe and 0.40 ML TMA. Comparison of (b) the high-resolution STM image, (c) the atomistic MOCC-II model, and (d) the corresponding DFT simulated STM image.

The $4\times$ in-chain periodicity of these chains (Fig. 14) leaves space for just one Fe metal center between TMAs. The TMA-TMA distances are therefore shorter when linked by Fe than when linked by Cu, similarly to what was reported for 2D MOCN on the Cu(001) surface. According to DFT calculations, the geometry of the adsorbed TMA molecule is weakly dependent on the metal center. The metal-carboxylate bond is still unidentate and the Fe-O distance is 1.95 \AA , thus 0.07 \AA shorter than the Cu-O one in MOCC-I. Single metal centers lead to very weak features in the simulated STM image (Fig. 14(d)), in agreement with experiment (Fig. 14(b)). With respect to a neutral Fe atom, surface Fe-complexation strongly reduces the occupations of the Fe s states by 1.3 electrons while increases that of the d states by 0.5 electrons.

Insight into the potentially interesting magnetic properties of these Fe-complexated MOCC-II can be gained by projecting the electron density on the atomic Fe d orbitals (Fig. 15(b)). The projected density of electronic states (DOS) displays a large splitting between the majority *spin-up* and minority *spin-down* electron d states. The former are completely filled and well-hybridized with the substrate Cu d states, extending from -5 to -1 eV in the total DOS of the $[-\text{TMA-Fe}]_n$ chain (Fig. 15(a)). The latter are only partially filled and extend in the energy region dominated by the substrate s states.

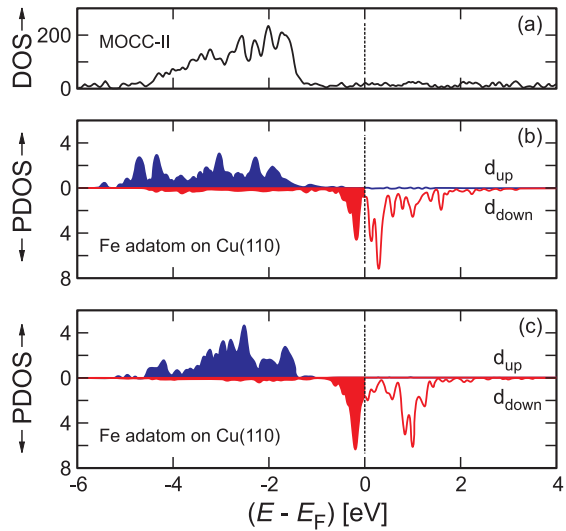


Figure 15: (a) Total DOS (in states/eV with respect to the Fermi energy E_F) of the $[-\text{TMA-Fe}]_n$ chain (MOCC-II), and projected DOS on the atomic d -states of (b) the Fe center in the MOCC-II and (c) a Fe atom isolated on the Cu(110) surface.

As a consequence, the Fe atoms are strongly magnetized, with a spin polarization of $3.3 \mu_B$ per Fe atom. The polarization of a Fe adatom isolated on the Cu(110) surface is very similar, $3.2 \mu_B$, and the corresponding projected DOS is shown in Fig. 15(c). The comparison shows that the coordination with the carboxylate group does not affect the electron localization at the Fe adatoms, thus not producing any relevant quenching of the spin magnetic moment.

This is a necessary (although not sufficient) condition for the emergence of intriguing magnetic properties induced by the low dimensionality, such as giant magnetic anisotropy. Because of their high thermal stability, MOCNs similar to those presented here could thus be convenient model systems to explore the occurrence of low-dimensional magnetism.

[1] Dmitriev, A., H. Spillmann, N. Lin, J.V. Barth and K. Kern. *Angewandte Chemie International Edition* **42**, 2670-2673 (2003).

[2] Stepanow, S., M. Lingenfelder, A. Dmitriev, H. Spillmann, E. Delvigne, N. Lin, X. Deng, C. Cai, J.V. Barth and K. Kern. *Nature Materials* **3**, 229-233 (2004).

[3] Classen, T., G. Fratesi, G. Costantini, S. Fabris, F.L. Stadler, C. Kim, S. de Gironcoli, S. Baroni and K. Kern. *Angewandte Chemie International Edition* **44**, 6142-6145 (2005).

[4] Lin, N., D. Payer, A. Dmitriev, T. Strunskus, C. Wöll, J.V. Barth and K. Kern. *Angewandte Chemie International Edition* **44**, 1488-1491 (2005).

Tracing the footprints of self-assembled strained islands

A. Rastelli, M. Stoffel, U. Denker, G.S. Kar and O.G. Schmidt

The most elegant and convenient method to fabricate nanometer-scale objects is to exploit the capability of certain material systems to self-assemble nano-structures. For instance, defect-free semiconductor ‘quantum dots’ can be created by means of lattice-mismatched heteroepitaxial growth. In the Stranski-Krastanow growth mode, the elastic strain stored in the growing film is relaxed by the formation of three dimensional islands on top of a thin, pseudomorphic wetting layer. Among the different material combinations, the Ge/Si(001) system can be considered as a model playground for understanding the physics of self-assembled island growth.

At typical growth temperatures (550–850°C), islands first appear as shallow unfaceted ‘prepyramids’. With increasing size they undergo a shape transition to {105} faceted pyramids and then to multifaceted islands bounded by steeper facets, referred to as ‘domes’ and ‘barns’. Further growth leads to the introduction of dislocations (‘superdomes’). Several other phenomena, such as Si-Ge intermixing, modification of the wetting layer surface reconstruction, formation of *trenches* at the island

perimeter provide additional strain-relaxation mechanisms. Many different microscopy techniques have been used to characterize self-assembled islands, both during growth and at room temperature (RT) after growth. The former approach allows the direct imaging of the growth dynamics, but is limited in resolution or accessible growth conditions. The latter can only give access to snapshots of the surface ‘frozen’ at RT.

Here we report on the observation and interpretation of unique *footprints* left by SiGe islands on the substrate surface. Such footprints consist of trenches forming at the island perimeter when the growth is performed at sufficiently high temperatures. We show that new insights into the temporal evolution of the islands can be deduced from these footprints, which we study by RT atomic force microscopy (AFM). The most unexpected result of this analysis is that islands move laterally on the surface during post-growth annealing. We interpret this phenomenon as a mechanism for alloying exclusively via surface diffusion, and hence strain relaxation.

The samples studied here were grown by solid-source molecular beam epitaxy (MBE). After deoxidation and Si-buffer growth, Ge was deposited at a rate of 0.04 monolayers/s (ML/s) at a substrate temperature T_s between 740°C and 840°C. The samples were cooled to RT before characterization. Some specimens were also etched with a mixture of HF:1 H₂O₂:2 CH₃COOH:3 (BPA solution), which is known to etch selectively SiGe alloys over pure Si.

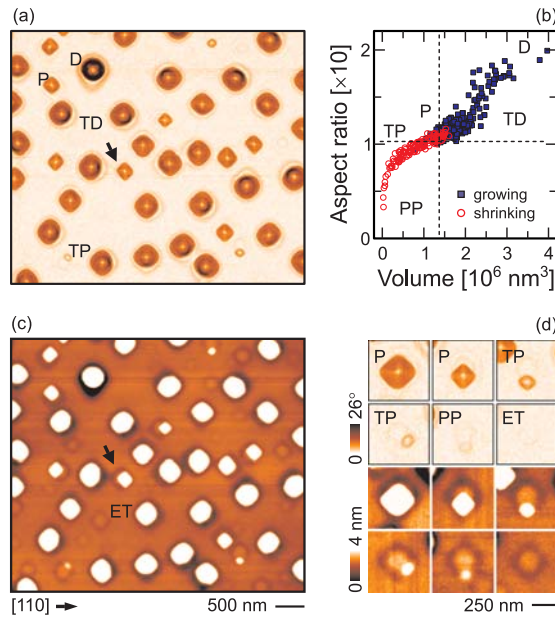


Figure 16: AFM image of SiGe islands obtained by deposition of 6 ML Ge on Si(001) at 840°C with color scale according to surface slope (a) and height (c). (b) Statistical analysis of island shape versus volume. Islands at different stages of evolution are observed: prepyramids (PP), truncated pyramids (TP), pyramids (P), islands with shape intermediate between pyramids and domes (TD), and domes (D). In (c), empty trenches (ET) are also seen. (d) Sequence of AFM magnifications illustrating shrinking pyramids and the pyramid-to-prepyramid transformation.

Figure 16(a) shows an AFM image of a sample obtained after deposition of 6 monolayers (ML) of Ge on Si(001) at $T_s = 840^\circ\text{C}$. The color scale according to the local surface slope with respect to the (001) plane allows steep and shallow facets to be distinguished. We observe

different island morphologies, such as domes (D), islands with an intermediate shape between pyramids and domes (TD), pyramids (P), truncated pyramids (TP) and unfaceted prepyramids (PP, not shown in Fig. 16(a)). The plot of the aspect ratio r vs. volume (Fig. 16(b)) indicates that different island sizes correspond to different shapes (here r is defined as the ratio between height and square root of the base area).

The information contained in Fig. 16(a) is however not sufficient to establish how each island evolved before the sample was cooled to RT. In particular we do not know whether the small TPs were in the process of growing and transforming to pyramids or shrinking and disappearing. An answer to this question is provided by Fig. 16(c), in which the color scale enhances the corrugations of the wetting layer. We observe trenches (dark in the figure) surrounding each island, but also ‘empty’ trenches (ET), which do not surround any island. The latter were obviously created by islands which formed, grew, then shrunk and disappeared before the measurement was performed. In Fig. 16(c) we can also identify shrinking islands, such as that pointed at by an arrow in Fig. 16(a) and (c), whose base area is smaller than the trench area. Their relative position with respect to the trench center suggests that part of the material initially composing the shrinking islands has migrated towards the larger nearby TDs or domes. A detailed analysis shows indeed that shallow islands (Ps, TPs, PPs) are shrinking to the advantage of islands with large aspect ratio (TDs, Ds). The latter are growing, as indicated in Fig. 16(b). This observation is consistent with an anomalous ripening process [1].

A closer inspection of islands at different stages of the shrinking process (Fig. 16(d)) leads us to draw another important conclusion: While shrinking, islands undergo a reverse morphological transition from P to TP and eventually to PP as a result of their volume decrease, in agreement with thermodynamic models.

The above discussion demonstrates that, due to the trenches, the RT scanning probe microscopy data provide much more information than simple snapshots of the surface morphology. Since the Si-Ge island material is more mobile than the trenches carved into the Si substrate, we can aim to reveal trenches buried below the islands by selectively etching the SiGe alloy. This simple method enables us to gather new insight into the intermixing-induced dome-to-pyramid transition occurring during post-growth annealing and in the evolution of dislocated superdomes.

Figure 17(a) shows an AFM image of a sample obtained upon deposition of 10 ML of Ge on Si(001) at $T_s = 740^\circ\text{C}$. The islands have an average height of $(41 \pm 4)\text{ nm}$ and have a dome or barn shape. Figure 17(b) shows an AFM image of a sample with 10 ML of Ge annealed at $T_s = 740^\circ\text{C}$ for 20 min. During annealing, most of the barns and domes transform back to TDs and pyramids as a consequence of Si-Ge intermixing. AFM scans of the same areas taken after selective etching in BPA solution are shown in Figs. 17(c) and (d). Prior to annealing (Fig. 17(c)), circular Si plateaux remain, which are surrounded by an approximately square trench with sides parallel to the [100] and [010] directions. The etching of the annealed sample reveals that portions of the original Si-plateaux buried under the islands are still present (Fig. 17(d)). While prior to annealing the Si-plateaux are close to the island centers, after annealing they are at the island edge. We can thus conclude that during annealing islands do not only intermix and change their shape, but also *move* laterally on the surface. This is better seen in Figs. 17(e)–(f), where line scans of the representative islands marked in Figs. 17(a)–(b) are plotted before and after etching in BPA solution.

With reference to Figs. 17(e)–(f), we can qualitatively describe the island motion as due to material removal from the left side of the island and deposition on the right side. As a consequence of the motion, a part of the initially circular Si-plateau becomes uncapped

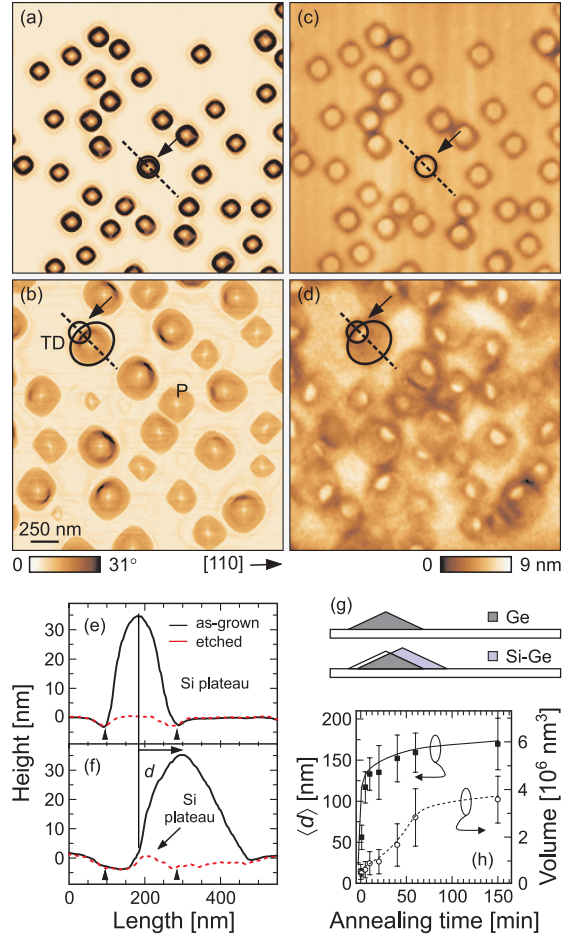


Figure 17: Representative AFM images of SiGe islands before (a,b) and after selective etching in BPA solution (c,d) of samples with 10 ML Ge grown at 740°C . In (a,c) the sample was cooled to RT immediately after growth while in (b) and (d) the sample was annealed for 20 min at 740°C . Circles pointed at by arrows in (c) and (d) indicate representative Si-plateaux. Line scans of two representative SiGe islands before (e) and after annealing (f). Triangles mark the position of the Si-plateau edges before annealing. The arrow in (f) represents the displacement d undergone by the island center during annealing. (g) Schematic illustration of island motion. (h) Average displacement and volume of islands as a function of annealing time.

and the Si atoms composing it migrate away from the compressed region at the foot of the new islands left edge. In contrast, the remaining part of the Si-plateau buried under the island is preserved, because its modification would require the contribution of bulk interdiffusion.

At the same time, the right islands edge advances gradually generating a new, shallower trench at its foot (visible as a dark area in Fig. 17(d)). The Si removed from the island perimeter is probably added onto the growing front of the island together with material of the original island, leading to an *efficient Si-Ge intermixing* exclusively due to surface diffusion. Therefore, the island volume increases and the average Ge fraction of the material composing the island decreases. As a result of strain release, domes and barns become unstable and their shape changes to TD or pyramid. From Fig. 17(f), we also notice that the left side of the TD island, which we interpret as a remainder of the island before annealing, is still dome-like consistent with a Ge-rich composition, while the right side is pyramid-like because of the Si added during the motion.

The origin of the island motion can be understood with a simple thermodynamic model for a strictly faceted pyramidal island of pure Ge, as shown schematically in cross-section in the top panel of Fig. 17(g). By assuming an initial small motion (bottom panel of Fig. 17(g)) it is possible to show that the motion is self-sustaining and proceeds until most of the original island has intermixed with Si from the substrate [2]. From the AFM images taken after selective etching we determine the displacement d of an island as the distance between the position of the island center prior to and after annealing (see small and large circles in Fig. 17(d)). The average displacement is shown in Fig. 17(h) as a function of annealing time and indicates that the motion is initially fast and then slows down as expected. Meanwhile, the average island volume (Fig. 17(h)) also increases as a result of Si incorporation and, possibly, island ripening.

A final question concerns the conditions required to initiate self-sustaining lateral motion and mixing. For islands very close to each other prior to annealing, we measure a strong

correlation between the direction of motion and the direction away from the nearest neighbor, suggesting that an environmental asymmetry, such as a strain gradient, triggers the motion. We also find that the *magnitude* of the motion is always comparable to the island radius and shows no obvious correlation with environment, suggesting that the motion is self-sustaining and the role of the environment acts only as an initial trigger. We note that the island motion during annealing can be suppressed if the island position is fixed by surface strain energy modulations caused by a buried island layer [3]. We observe this effect on a sample consisting of a stack of two layers of islands separated by a 90 nm thick Si spacer layer (islands were obtained with the same growth parameters used for the samples shown in Fig. 17).

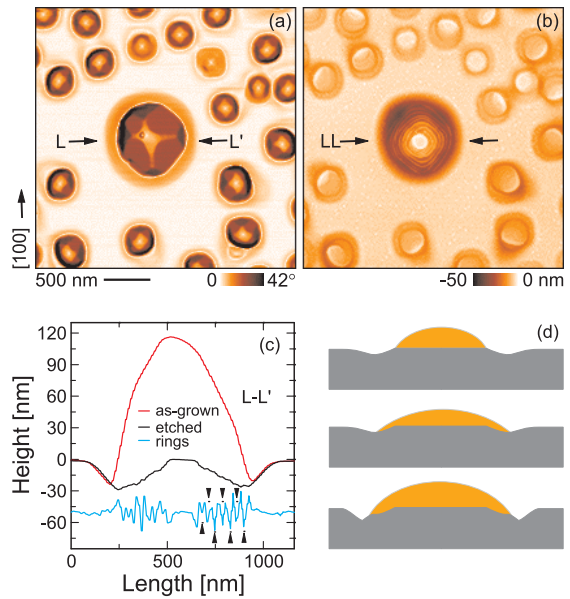


Figure 18: AFM images of a SiGe superdome prior to (a) and after etching in BPA solution (b). The colorscale of (b) is enhanced by a second derivative filtering. (c) Line scans (L-L') of the AFM images along the [010] direction. The bottommost line scan represents the numerical second derivative of the topograph shown in (b), with triangles indicating the ring positions. (d) A schematic representation of the mechanism leading to the formation of the ring structure seen in (b).

Trench formation and intermixing are effective ways to release strain and to delay the introduction of dislocations. However, dislocated islands (also referred to as ‘superdomes’) are often observed for large amounts of deposited Ge. In Fig. 18(a) we show an AFM image of a sample obtained after deposition of 15 ML of Ge at $T_s = 800^\circ\text{C}$. The island at the center of the image is a superdome. The selective etching of this sample in BPA solution reveals that superdomes leave behind a complex ‘tree ring’ or staircase structure (see Fig. 18(b)). Line scans of the superdome prior and after etching are shown in Fig. 18(c). The bottommost curve represents the second derivative (in arbitrary units) of the AFM topograph of the etched sample and allows a clear identification of the ring positions. At least seven rings, pointed at by arrows, can be identified. Following the arguments above we can easily understand the observation as due to a discontinuous expansion of the superdome perimeter and the formation of new, deeper trenches for every cycle (see Fig. 18(d)). This phenomenon was previously observed in real-time. We can thus interpret the number of rings as the number of dislocations

introduced in the island during its growth and hence gain insight into the morphological ‘age’ of the island.

In conclusion, we have reported on the observation and interpretation of footprints left behind by strained self-assembled islands. Different processes and phenomena occurring during the island evolution were unambiguously traced back by studying such footprints:

- (i) We followed the disappearance of small islands during ripening; (ii) Upon post-growth annealing, islands were observed to move laterally to achieve alloying exclusively through surface diffusion; (iii) A tree ring structure was discovered buried under dislocated islands, with each ring corresponding to a dislocation.

-
- [1] Rastelli, A., M. Stoffel, J. Tersoff, G.S. Kar and O.G. Schmidt. *Physical Review Letters* **95**, 026103 (2005).
 - [2] Denker, U., A. Rastelli, M. Stoffel, J. Tersoff, G. Katsaros, G. Costantini, K. Kern, N.Y. Jin-Phillipp, D.E. Jesson and O.G. Schmidt. *Physical Review Letters* **94**, 216103 (2005).
 - [3] Stoffel, M., A. Rastelli, S. Kiravittaya and O.G. Schmidt. *Physical Review B* **72**, 205411 (2005).

Periodic defects in metallo-dielectric photonic crystal superlattices

T. Zentgraf, A. Christ and J. Kuhl;
S.G. Tikhodeev and N.A. Gippius (General Physics Institute Moscow);
H. Giessen (Universität Stuttgart)

During recent years, research on photonic crystal structures has been very active. Structures with a periodically modulated dielectric permittivity, which yield Bragg diffraction of light, have attracted not only fundamental but also technological interest. In particular, the analysis of periodic structures with a structured elementary supercell came to the fore. Such superlattice geometries have been used in a wide variety of different physical fields and many interesting fundamental effects have been demon-

strated. In the optical regime for instance, dielectric superlattice structures have been shown to support photonic Bloch oscillations.

In our work, we study experimentally and theoretically the optical properties of metallic photonic crystal superlattice slabs. Such slabs consist of metal nanowire supercells that are periodically deposited on top of a dielectric waveguide slab. The combination of the metallic nanowires in a photonic crystal structure with a dielectric waveguide causes a strong

coupling between the light of the waveguide mode and plasmon resonances [1]. New collective states are formed (waveguide-plasmon polaritons), which lead to an impressive modification of the optical properties due to a changed photonic density of states of the vacuum light modes.

In this polaritonic photonic crystal, the superperiod of the lattice determines the spectral positions of the existing quasiguided modes, whereas the specific supercell geometry affects the excitation efficiencies of these modes. Our analysis is based on optical transmission measurements in a conventional white-light setup as well as numerical simulations using a scattering-matrix formalism and Fourier decomposition.

Figure 19 shows a schematic view of the sample geometry. Electron beam lithography was used to prepare on a quartz substrate gold nanowire arrays with a size of $100 \times 100 \mu\text{m}^2$ on top of a 140-nm-thick indium-tin-oxide (ITO) waveguide layer. This 1D active photonic crystal supports electronic resonances in the form of localized surface plasmons in the gold nanowires as well as photonic resonances in the form of quasiguided waveguide modes in the dielectric ITO layer.

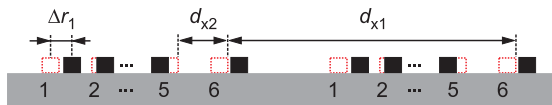


Figure 19: Schematic view of the superlattice sample geometry. For the experiments, defects Δr_i in the positions of the nanowires were introduced. The dotted squares mark the cross-section of the original positions of the nanowires without displacement. Notice that the same set of Δr_i is used in each supercell.

In contrast to grating structures with a simple unit cell, the design here is characterized by as many as three essential parameters. Generally, the nanowire gratings were split into individual supercells, which were arranged with a superperiod d_{x1} . Each supercell contains six single

gold nanowires which are arranged according to a second periodicity (subcell period) d_{x2} .

The arrangement of the nanowires within a supercell acts as structure factor of the excitation efficiencies of the higher order modes. From solid state physics, it is well-known that the diffraction intensities in X-ray scattering experiments strongly depend on the temperature of the crystal due to the structural disorder associated with the excitation of lattice vibrations. As a consequence, the peak intensities of the scattered light of the diffraction orders are reduced while the linewidths are preserved.

This concept was applied to our superlattice design by introducing periodic defects (small random displacements) in the wire positions (see Fig. 19). The superperiod d_{x1} was chosen as an exact multiple of the subcell period d_{x2} . The deviations Δr_i of the individual positions were calculated by $\Delta r_i = f R_i$ ($i = 1, 2, \dots, 6$), where f is a weighting factor and R_i a set of six random distances of a uniform distribution. To obtain theoretical results with the scattering matrix calculation, we used the identical displacement (same set of R_i) in each supercell of the lattice. We notice that this kind of disorder is very special and only a rough approximation of thermal disorder. For example, the spectral distance between the Bragg resonances is fixed because the super-periodicity d_{x1} is not destroyed at all.

For the first sample without any periodic defects ($f=0$), one strong peak is visible in TE polarization. This peak can be attributed to the seventh Bragg resonance at the zone center of the reciprocal lattice with period $2\pi/d_{x1}$. Since the superperiod is an exact multiple of the subcell period, only higher order Bragg resonances of the superperiod which are multiples of seven (7^{th} , 14^{th} , etc.) can be efficiently excited. By diminishing the influence of the subcell periodicity d_{x2} through the introduction of defects, the excitation of distinct waveguide modes can no longer take place. Therefore, all higher order resonances of the lattice period d_{x1} will become more pronounced.

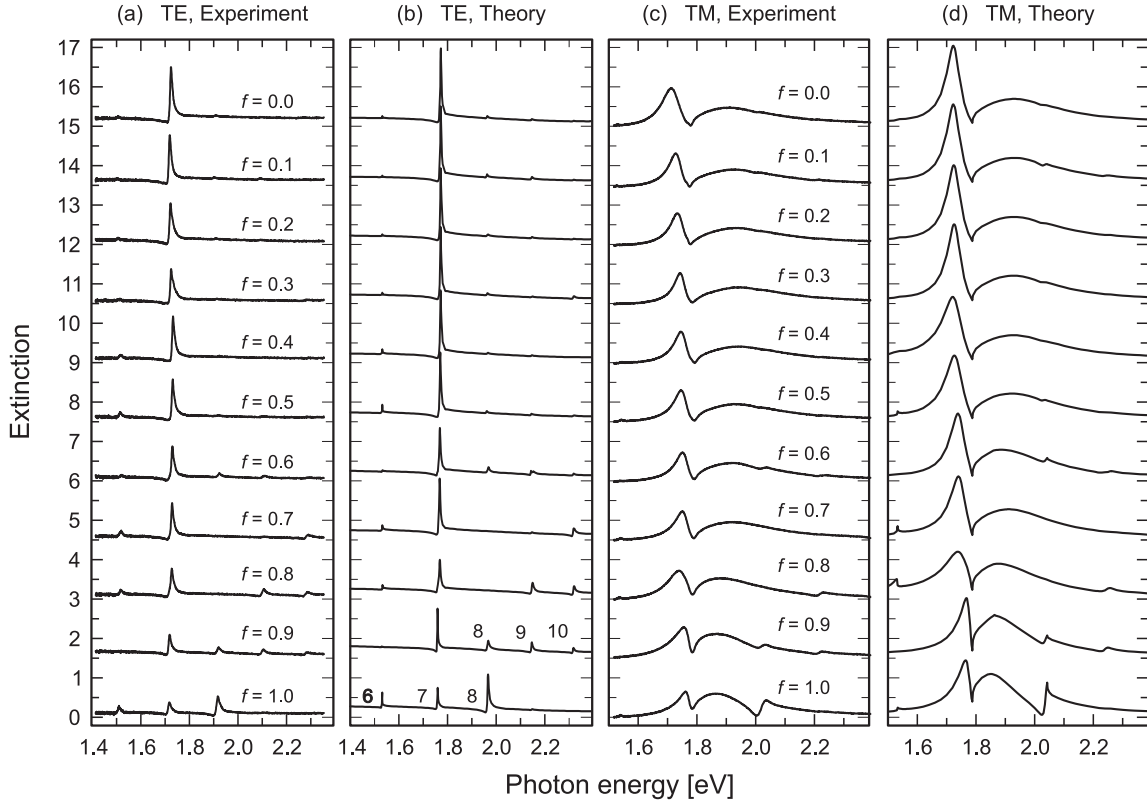


Figure 20: Measured (a),(c) and calculated (b),(d) extinction spectra of the metallo-dielectric superlattice structures for normal light incidence and both polarization directions. The spectra are shifted upwards in each panel for clarity. While the subcell period d_{x2} , the number of nanowires, and the superperiod d_{x1} have been kept constant for all samples, a random displacement in the position of the nanowires was introduced with a varying strength f from $f=0$ (no displacement) to $f=1.0$ (maximum displacement) in steps of 0.1. All spectra in (a) are multiplied by a factor of two for better visibility of the peaks.

Indeed, in Fig. 20(a) additional peaks arise both below and above the single resonance at the spatial frequency of $7 \cdot 2\pi/d_{x1}$ for the curve with $f=0$ when the random displacement of the wires within the supercell is turned on and increased. The subcell periodicity is destroyed by the random displacement and no longer acts as a structure factor for the superperiod anymore.

For TM polarization and normal light incidence, the spectra show the same behavior as for TE polarization. The additional quasiguided modes couple to the localized particle plasmon resonance and lead to further dips in the extinction spectra. This behavior is most clearly observed for the strongest displacement ($f=1.0$), where the plasmon resonance shows two pronounced dips.

In the case of strong displacements of the wire positions ($f > 0.6$), some modes are missing in the measured and calculated optical extinction spectra. To clarify the origin of the low excitation efficiency of these modes, the structure factor for each sample was calculated by Fourier decomposition of the lattice geometry (Fig. 21). For a certain weighting factor f , several harmonics vanish and then reappear when changing f . This behavior is a result of the very specific design of our samples. The periodic defects lead to special structure factors of the lattice for each strength (f) of the displacements. Theoretical calculations show that a change in the disarrangement of the wires (other set of R_i) for the same weighting factor can lead to completely different excitation efficiencies of the modes.

Therefore, depending on the specific wire positions some modes can vanish and reappear in the different samples.

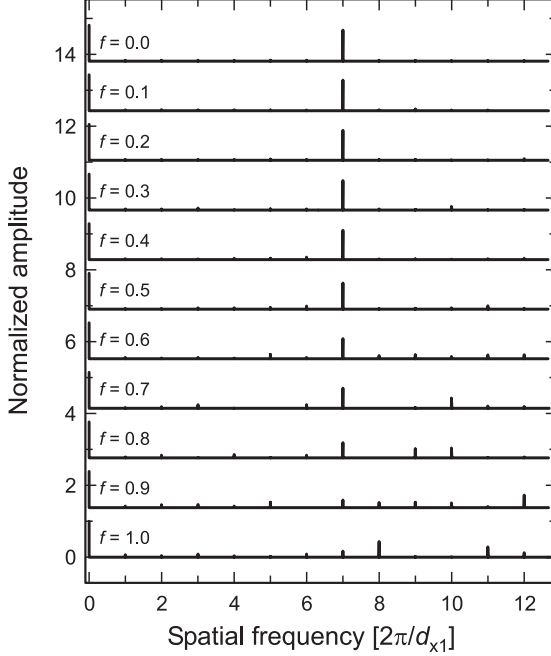


Figure 21: Fourier decomposition of the grating structures plotted as a function of the spatial frequency. The strength f of the displacements $\Delta r_i = f R_i$ serves as a parameter. The Fourier spectra are shifted upwards for clarity.

In conclusion, our experiments demonstrate that superlattice structures in metallo-dielectric planar photonic crystals strongly modify the

optical extinction properties. The superperiod d_{x1} determines the energy positions of the observed resonances whereas the subcell period acts as a structure factor for these modes. Hence, the excitation efficiency and the energy position of the quasiguided modes can be influenced independently.

All higher order Bragg resonances which energetically overlap with the nanowire plasmons, couple to these plasmon modes and form waveguide-plasmon polaritons. The coupling strength depends on the excitation efficiencies of the quasiguided modes. When introducing periodic defects in the position of the nanowires, the influence of the structure factor of the supercell can be reduced and other higher order Bragg resonances can be excited more efficiently.

By an appropriate choice of the superlattice geometry, it should be possible to engineer the photonic bands and therefore the band gaps in metallic photonic crystals. This approach gives more freedom in the design of photonic band gap structures than using only refractive index changes.

-
- [1] Christ, A., S.G. Tikhodeev, N.A. Gippius, J. Kuhl and H. Giessen. Physical Review Letters **91**, 183901 (2003).

Functional renormalization group: new applications to quantum wires and quantum dots

S. Andergassen, T. Enss and W. Metzner;

V. Meden and K. Schönhammer (Universität Göttingen); U. Schollwöck (RWTH Aachen)

In the last couple of years *functional renormalization group* (RG) methods have been established as a new computational tool in the theory of interacting Fermi systems. These methods are particularly powerful in low dimensions. The low-energy behavior usually described by

an effective field theory can be computed ab initio for a concrete microscopic model, by solving a differential flow equation with the energy scale as the flow parameter. Thereby also the nonuniversal behavior at intermediate energy scales is obtained.

We have applied such a functional RG scheme to one-dimensional fermionic lattice models for *quantum wires* with short-range interactions and various types of impurities. The RG flow equations are non-perturbative in the impurity strength while perturbative in the two-particle interaction. However, a comparison with exact numerical results for systems with up to 1000 sites showed that the truncated flow equations are generally rather accurate also for sizable interaction strengths. The most relevant observables such as the local density of states, the density profile, and the conductance were calculated. The expected Luttinger liquid universality of one-dimensional systems characterized by power-laws and universal scaling functions has been confirmed by the functional RG, but it turned out that very large systems (more than 10^4 sites) are required to reach the universal regime for moderate impurity and interaction parameters. Due to the flexibility of the functional RG we are able to treat several distinct impurity potentials such as local site impurities, hopping impurities (weak links) and also double barriers enclosing a small ‘*quantum dot*’ region.

Recently, we have extended our previous work on one-dimensional systems with impurities from spinless to spin- $\frac{1}{2}$ fermions [1]. For fermions with spin, vertex renormalization is crucial to take into account that two-particle backscattering of fermions with opposite spins at opposite Fermi points scales to zero in the low-energy limit.

Two-particle backscattering of interacting electrons in quantum wires leads to two important effects, not present for spinless fermions. First, the expected decrease of the local density of states near a boundary or impurity at low energy scales is preceded by a pronounced *increase*, if the interaction is short-ranged (that is, screened). An example for this behavior is shown in Fig. 22, where functional RG results for the density of states at the boundary of a

Hubbard chain are presented. Similarly, in the presence of sizable two-particle backscattering the asymptotic decrease of the conductance across an impurity sets in only at very low temperature. Second, the asymptotic power laws are usually modified by *logarithmic corrections*.

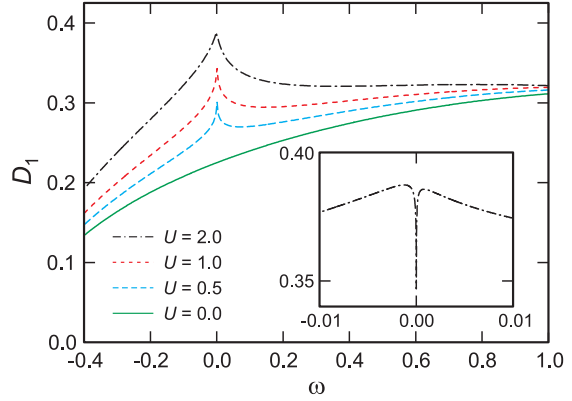


Figure 22: Local density of states at the boundary of a Hubbard chain of length $L=4096$ at quarter-filling and various interaction strengths U ; the inset shows results for $U=2$ and $L=10^6$ at very low ω .

For one-dimensional systems with long-range interactions, two-particle backscattering is strongly reduced compared to forward scattering. This seems to be the case in carbon nanotubes. Hence, the conductance can be expected to follow the asymptotic power law at accessible temperature scales for sufficiently strong impurities in the system, as is indicated also by experiments. However, the effects due to two-particle backscattering should be observable in systems with a screened Coulomb interaction.

Even more interesting is the transport through a double barrier enclosing a small quantum dot region containing only one or a few sites. Already for spinless fermions the conductance through such a barrier exhibits resonances which can be tuned by a gate voltage shifting the single-particle energy levels on the dot, as shown in Fig. 23.

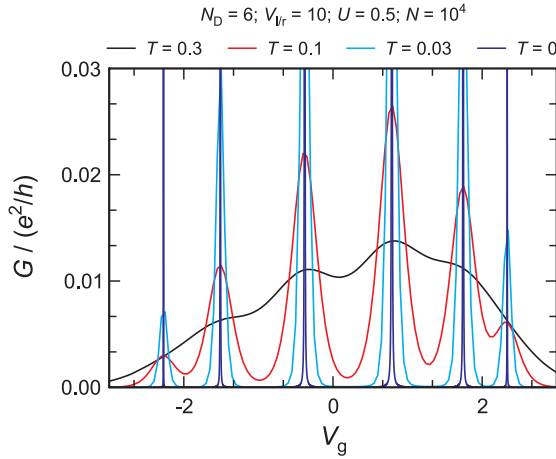


Figure 23: Conductance as a function of gate voltage for a wire containing spinless fermions with nearest-neighbor hopping and nearest-neighbor interaction $U=0.5$, and two large site impurities of strength $V_{lr}=10$ which enclose a dot region with $N_D=6$ sites; interaction parameters and temperature are given in units of the hopping amplitude. The resonances become extremely sharp at low temperatures due to Luttinger liquid effects.

The resonances become extremely sharp at low temperatures due to the Luttinger liquid behavior of the interacting fermions in the wire connected to the dot. For spin- $\frac{1}{2}$ fermions and sufficiently strong barriers, as realized for example by a small tunneling amplitude between the dot region and the rest of the wire, new effects related to *Kondo physics* come into play. In particular, the average electron number in the dot region gets pinned to integer values, and the conductance as a function of the gate voltage exhibits pronounced plateaus at the unitarity limit $2e^2/h$ at $T=0$.

The plateaus are associated with an odd integer filling of the dot. Functional RG results showing this behavior for a dot region with six sites

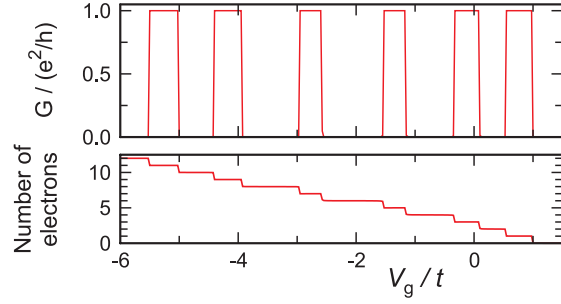


Figure 24: Conductance as a function of gate voltage V_g for a wire modeled by an extended Hubbard chain with nearest-neighbor hopping t , Hubbard interaction $U/t=1$, and nearest-neighbor interaction $U'/t=0.5$; two weak links with a small hopping amplitude $t'=0.1 t$ enclose a quantum dot with six sites; the wire (10^4 sites) is connected to infinite noninteracting leads. Lower panel: Average number of electrons in the dot region.

embedded in a wire with 10^4 sites are presented in Fig. 24. Luttinger liquid properties of the electrons in the wire have only little influence on the conductance in this case, which is almost exclusively determined by interaction effects in the dot region for the parameters chosen for the plot. Combined effects of Luttinger liquid and Kondo correlations occurring for longer wires or weaker barriers (than those in Fig. 24) are also well-captured by the functional RG within our relatively simple approximation scheme. Thanks to the flexibility of the method, also more complex quantum dot arrays, as realized in recent experiments, can be treated.

-
- [1] Andergassen, S., T. Enss, V. Meden, W. Metzner, U. Schollwöck and K. Schönhammer. Physical Review B **73**, 045125 (2006).
 - [2] Andergassen, S., T. Enss and V. Meden. cond-mat/0509576.

Strong electronic correlation phenomena

Strongly correlated electronic systems such as quasi-one-dimensional chains, two-dimensional electron gases, or transition metal oxides with or without orbital degeneracy are important research topics at the Institute where chemistry as well as experimental and theoretical physics are involved. One example for such an interdisciplinary cooperation is described in the first contribution dealing with the synthesis of novel copper oxide chains, their physical properties as well as their theoretical interpretation in terms of Wigner crystallization of electrons. The following two reports deal with two-dimensional systems and illustrate the close interrelation of theory and experiment: a theoretical proposal for exciton condensation in interacting layers is examined experimentally, whereas the described route to non-Fermi liquid behavior may be related to experimental observations in the cuprates. Raman scattering has been carried out in two Mott insulators. A new peak above the phonon spectrum has been detected and interpreted in terms of orbital excitations. Finally, a new experimental neutron scattering technique has been set up and also successfully tested. It allows the determination of intrinsic lifetimes of excitations with unprecedented resolution.

Wigner crystallization in copper oxide chain compounds

P. Horsch, M. Sofin, M. Mayr, L. Capogna, M. Jansen and B. Keimer

The role of strong electron correlations and the concomitant appearance of *spatially modulated charge structures* constitutes a central issue in current solid state physics. The most prominent example are charge stripes in high- T_c superconductors. We report here the synthesis of novel, *doped* edge-sharing chain systems $\text{Na}_3\text{Cu}_2\text{O}_4$ and $\text{Na}_8\text{Cu}_5\text{O}_{10}$, which form insulating states with commensurate charge order [1]. We identify these systems as one-dimensional Wigner lattices (WL), where the charge order is determined by the long-range Coulomb interaction and the number of holes in the d -shell of Cu. The possibility of investigating systems with different electron concentrations and commensurabilities, yet with basically the same chemical environment, provides a basis for a deeper exploration of the more subtle interplay of spin and charge degrees of freedom in cuprates.

Following a new route in the synthesis of alkaliometallates, recently discovered by Trinschek and Jansen, several members of a

new class of quasi-1D cuprates $\text{Na}_{1+x}\text{CuO}_2$ could be synthesized. These *intrinsically doped* edge-sharing chain systems provide a unique opportunity to study the condensation of charge order (CO) at high temperature and the formation of spatially modulated Heisenberg spin systems at low temperature. Edge-sharing chains are also building blocks of the intensively studied $\text{Sr}_{14-x}\text{Ca}_x\text{Cu}_{24}\text{O}_{41}$ system; due to exchange of electrons with ladders, however, the degree of doping is difficult to determine in those compounds. Here, we argue that these doped chains can be understood as realizations of one-dimensional Wigner lattices, as proposed by Hubbard in the late 70's in connection with TCNQ charge transfer salts. He suggested that the distribution of electrons is controlled by the Coulomb interaction rather than by the kinetic energy (\sim bandwidth), such that they form a *generalized Wigner lattice* on the underlying TCNQ chain structure. This view suggests a strikingly different nature of charge excitations, namely as domain walls with fractional charge

rather than particle-hole excitations as in common metals and semiconductors. Hubbard's proposal, however, can be challenged on the grounds that the resulting periodicity of charge modulation can alternatively be explained by a $4k_F$ charge density wave (CDW) arising from an instability of the Fermi surface even in models with short-range interactions.

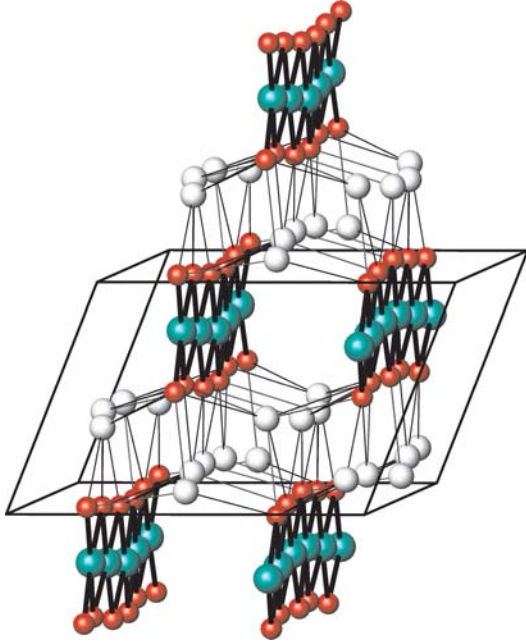


Figure 25: Structure of the edge-sharing copper-oxygen chain compound $\text{Na}_8\text{Cu}_5\text{O}_{10}$. Cu (O,Na) atoms are drawn as green (red, grey) spheres, respectively. The Cu^{2+} and Cu^{3+} charge order along the b (chain) direction leads to a unit cell with 5 Cu atoms. The charge order of $\text{Na}_8\text{Cu}_5\text{O}_{10}$ is displayed in Fig. 26(b).

The edge-sharing arrangement of CuO_4 squares meets the WL criterion of small bandwidth in an optimal way due to the almost 90° Cu–O–Cu bonds (Fig. 25). Unexpected complexity is added because, apart from a small nearest-neighbor hopping matrix element t_1 , the second neighbor hopping t_2 has to be considered which turns out larger as a consequence of the structure. While this unusual feature does not affect the classical WL order imposed by the Coulomb interaction, it changes the Fermi surface topology, and thereby allows to distinguish the WL from the CDW on the basis of the modulation period.

Neutron diffraction and Raman experiments on NaCu_2O_2 , a compound containing *undoped* Cu–O chains that are otherwise identical to those of $\text{Na}_3\text{Cu}_2\text{O}_4$ and $\text{Na}_8\text{Cu}_5\text{O}_{10}$, directly demonstrate the unusual dominance of longer range magnetic interactions [2]. Neutron diffraction data reveal that this material exhibits a helically ordered ground state at low temperatures. The pitch angle of the helix is determined by the ratio of nearest-neighbor and next-nearest-neighbor exchange constants, which turned out to be $\approx 20\%$. This ratio is proportional to $(t_1/t_2)^2$. The magnetic excitation spectra determined by Raman spectroscopy on NaCu_2O_2 single crystals confirm these conclusions.

The $\text{Na}_{1+x}\text{CuO}_2$ compounds thus provide a first example where an unambiguous distinction between the generalized WL and a Fermi surface related $4k_F$ CDW is possible. We also show that for these edge-sharing compounds even the magnetic and thermodynamic properties can only be explained by invoking a WL ground state emerging from the truly long-range Coulomb interaction.

Samples were prepared by the azide/nitrate route. As a source for the alkali metal component, mixtures of the respective alkali azides and nitrates (or nitrites) are used instead of the alkali oxides. Conveniently, besides the metals' ratio, also the oxygen content and thus the degree and kind of doping of the desired product can be effectively controlled using the weighed portions of the starting materials. Following this procedure the compounds $\text{Na}_3\text{Cu}_2\text{O}_4$ ($x = 1/2$) and $\text{Na}_8\text{Cu}_5\text{O}_{10}$ ($x = 3/5$) have been prepared as microcrystalline, pure phases in gram-amounts. The new oxocuprates (II/III) belong to the compositional series $\text{Na}_{1+x}\text{CuO}_2$, with the end members NaCuO_2 and the still elusive Na_2CuO_2 . The most prominent structural feature, common to all representatives known thus far, is a one-dimensional polyanion CuO_2^{n-} constituted

of CuO_4 -square units sharing edges in transposition. These anionic entities are embedded by sodium ions which achieve coordination numbers of 4–6 with Na–O bond lengths ranging from 2.27 to 2.79 Å. The geometric data as determined by single crystal structural analyses give clear evidence for a CO at the Cu sites. The Cu^{3+} and Cu^{2+} oxidation states can be clearly identified by the Cu–O distances, which for $\text{Na}_3\text{Cu}_2\text{O}_4$ are in the range 1.826–1.857 Å and 1.923–1.942 Å, respectively. The way of linking the primary structural units together with the variations of the copper to oxygen distances inevitably leads to deviations of the O–Cu–O angles from the ideal 90° . As monitored by differential scanning calorimetry measurements CO disappears above the WL melting temperature $T_m = 455$ K and 540 K for $\text{Na}_3\text{Cu}_2\text{O}_4$ and $\text{Na}_8\text{Cu}_5\text{O}_{10}$, respectively. DC and AC conductivity measurements show also a clear transition from an Arrhenius behavior below T_m to an almost temperature independent conductivity regime above T_m .

For the theoretical analysis one has to recognize that Cu^{2+} is in a d^9 configuration with spin 1/2, while Cu^{3+} is in a d^9 -ligand hole (d^9L_h) state, also known as Zhang-Rice singlet state. In contrast to high- T_c cuprates the edge-sharing geometry (Fig. 25) leads to strongly reduced hopping matrix elements. This sets the stage for the long-range Coulomb force as dominant interaction

$$H_{\text{Coul}} = U \sum_i n_{i,\uparrow} n_{i,\downarrow} + \sum_{i,l \geq 1} V_l n_i n_{i+l}, \quad (3)$$

where the on-site interaction U suppresses charge fluctuations involving Cu^{1+} (d^{10}) configurations. In the model we associate the d^9L_h (d^9, d^{10}) ionization state with 0 (1,2) electrons, respectively, and $n_{i,\sigma}$ ($\sigma = \uparrow, \downarrow$) counts the number of electrons with spin σ , while $n_i = n_{i,\uparrow} + n_{i,\downarrow}$. The Coulomb interaction V_l in general is screened by the polarization of neighboring chains as well as by core electrons. Here we assume a generic Coulomb law $V_l = \frac{V}{l}$, $l = 1, 2, \dots$ with V (≈ 1 eV) as parameter.

For commensurate doping concentration $x = m/n$ the interaction V_l selects a unique CO pattern, i.e., provided that the second derivative of the interaction $V_l'' = V_{l-1} - 2V_l + V_{l+1}$ is always positive. This pattern is immediately obvious for filling fractions $x = 1/2$ and $3/4$ (Fig. 26(a),(d)) which involve an equidistant arrangement of the Cu^{3+} sites (red circles in Fig. 26). For a general ratio $x = m/n$ this leads to complex structures with unit cell size n . In case of $x = 3/5$ we encounter in Fig. 26(b) the charge order observed for $\text{Na}_8\text{Cu}_5\text{O}_{10}$.

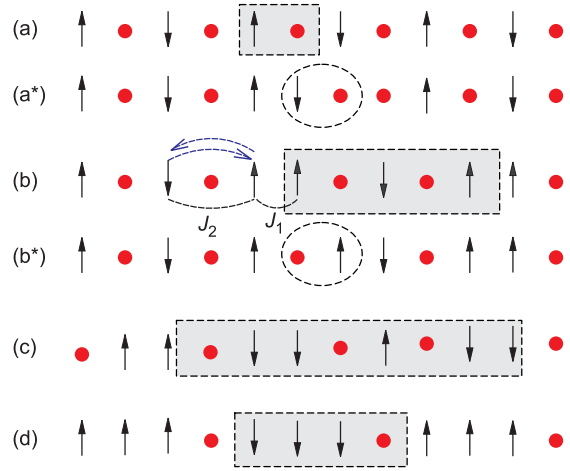


Figure 26: Wigner charge order resulting from Coulomb repulsion and associated modulated Heisenberg spin structure for $x = 1/2, 3/5, 5/8$ and $3/4$ doping (a)–(d). The spin-1/2 of Cu^{2+} (arrows) is responsible for magnetism; Cu^{3+} (circles) is non-magnetic. The spin arrangement is drawn for ferromagnetic exchange J_1 and antiferromagnetic J_2 , where the two excitations $d^9 \cdot d^9 \leftrightarrow d^9L_h \cdot d^{10}$ contributing to J_2 are indicated by dashed arrows in (b). The charge unit cells (shaded) contain 2, 5, 8, 4 sites, respectively. The structures (a) and (b) are realized in $\text{Na}_3\text{Cu}_2\text{O}_4$ and $\text{Na}_8\text{Cu}_5\text{O}_{10}$, respectively, and the dashed circles in (a*) and (b*) indicate charge excitations $\propto V$ in these structures. (d) Typical modulation for charge stripes in cuprates at doping $1/8$.

Charge localization, however, is not perfect in Wigner insulators as electrons still undergo virtual transitions to neighboring sites (Fig. 26(a*, b*)) in order to retain partially their kinetic energy. The energy of the lowest excitations and the impact of kinetic energy depend strongly on x , e.g., the energy of the

excitation in Fig. 26(a*) relative to the ground state Fig. 26(a) is $\sim V_2''$ while the excitation for $x=3/5$ in Fig. 26(b*) is $\sim V_5''$, about an order of magnitude smaller.

To investigate the role of kinetic energy we explore the dynamics of electrons starting from the 1D *Hubbard-Wigner model* $H_{\text{HW}} = H_{\text{Coul}} + H_{\text{Kin}}$, where

$$H_{\text{Kin}} = - \sum_{i,l,\sigma} t_l (c_{i+1,\sigma}^\dagger c_{i,\sigma} + c_{i,\sigma}^\dagger c_{i+1,\sigma}) \quad (4)$$

describes the hopping of an electron with spin σ . Due to the almost 90° Cu–O–Cu angle the hopping t_1 between nearest neighbor Cu sites results mainly from direct *d-d* exchange, while t_2 originates from hopping via a Cu–O–O–Cu path (Fig. 25), leading to the remarkable fact $|t_2| > |t_1|$. Our numerical simulations of the quantum model show, that for the parameters estimated for edge-sharing chain compounds the WL charge modulation is realized, while a CDW state would only appear for significantly larger hopping matrix elements or smaller interaction strength.

The *magnetic susceptibility* $\chi(T)$ provides an important test of the WL scenario. The susceptibility was measured in the temperature range from 5 K to 350 K using a SQUID magnetometer. The data (Fig. 27) reveal strikingly different temperature dependencies for the two compounds: $\chi(T)$ for $\text{Na}_3\text{Cu}_2\text{O}_4$ displays some similarity with a nearest neighbor Heisenberg antiferromagnetic chain, whereas the $\text{Na}_8\text{Cu}_5\text{O}_{10}$ data show continuous increase down to low temperature until its maximum near 25 K is reached. Both systems reveal antiferromagnetic correlations, yet magnetic order is observed only for $\text{Na}_8\text{Cu}_5\text{O}_{10}$ at $T_N = 23.5$ K. For a calculation of $\chi(T)$ we assume that the spins remain fixed at their positions \mathbf{R}_i as given by the structural analysis and by H_{HW} (Fig. 26). This leads to a generalized Heisenberg model

$$H_{\text{Heis}} = \frac{1}{2} \sum_{i,j} J(\mathbf{R}_i - \mathbf{R}_j) \mathbf{S}_i \cdot \mathbf{S}_j, \quad (5)$$

where the exchange constants depend on the distance $|\mathbf{R}_i - \mathbf{R}_j|$ between the spins and on the direction (parallel to the chains or perpendicular). For $x=0.5$ only the exchange constants J_2, J_4, \dots along the chains contribute, while for $x=0.6$ J_1, J_2, J_3, \dots are relevant (see Fig. 26). Apart from the modulated spin pattern, superexchange in WL's shows further novel features, namely fluctuations of (a) spin positions and of (b) exchange integrals $J_1 \sim 4t_1^2/(U + \Delta(V))$ due to the low energy charge fluctuations.

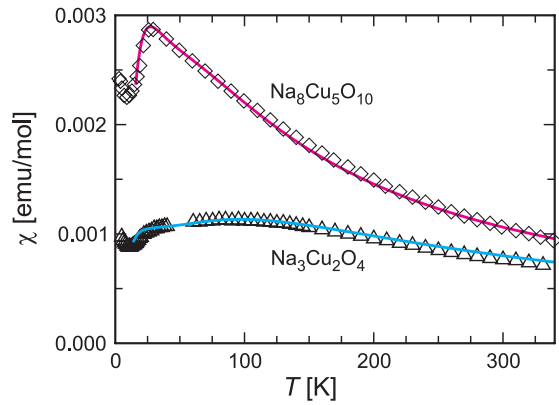


Figure 27: Temperature dependence of susceptibility $\chi(T)$ for $\text{Na}_3\text{Cu}_2\text{O}_4$ and $\chi(T)/3$ for $\text{Na}_8\text{Cu}_5\text{O}_{10}$. Multiplication by 1/3 in the latter case provides a comparison per spin. Theoretical results calculated by finite temperature diagonalization are indicated by lines.

Figure 27 gives a comparison of experimental and theoretical $\chi(T)$. The strong increase of $\chi(T)$ in $\text{Na}_8\text{Cu}_5\text{O}_{10}$ at low T results from a small ferromagnetic J_1 coupling. Remarkably the strongest (antiferromagnetic) interaction J_2 is larger in $\text{Na}_3\text{Cu}_2\text{O}_4$ (≈ 172 K) than in $\text{Na}_8\text{Cu}_5\text{O}_{10}$ (≈ 113 K). This surprising feature can be explained as a consequence of the different strength of charge fluctuations due to the different commensurability. At low T $\text{Na}_8\text{Cu}_5\text{O}_{10}$ orders due to interchain interactions, and the expected structure consists of ferrimagnetic planes that are coupled antiferromagnetically.

The new compounds provide a unique opportunity to investigate the competition between two entirely different states, the classical WL dictated by the long-range Coulomb interaction and the CDW of quantum mechanical origin, i.e., resulting from a Fermi surface instability. These materials highlight the importance of long-range Coulomb interaction in strongly correlated systems, – and provide a unique possibility to study charge condensation as function

of temperature as well as the subsequent emergence of quantum spin chains with spatially modulated distances between spins.

-
- [1] Horsch, P., M. Sofin, M. Mayr and M. Jansen. *Physical Review Letters* **94**, 076403 (2005).
 [2] Capogna, L., M. Mayr, P. Horsch, M. Raichle, R.K. Kremer, M. Sofin, A. Maljuk, M. Jansen and B. Keimer. *Physical Review B* **71**, 140402(R) (2005).

Bose-Einstein condensation or just strongly coupled electronic bilayers ?

R.D. Wiersma, J.G.S. Lok, W. Dietsche and K. von Klitzing

The Bose-Einstein Condensation is one of the most fascinating phenomena in physics. It has been observed in superconductors, superfluid helium and more recently in atom gases. Similar condensation processes had been predicted to occur in dilute exciton gases in semiconductors. Unfortunately, experiments with optically excited excitons failed or were ambiguous at best. More recently, there seemed to open up another road to this elusive goal by using two electronic quantum wells in close proximity [1]. These quantum wells are prepared by sandwiching GaAs layers (15 nm thick) between suitably doped $\text{Al}_{0.3}\text{Ga}_{0.7}\text{As}$ material. The barrier between the layers (an AlAs/GaAs superlattice) is typically 15 to 20 nm thick. Two-dimensional electron gases form in each layer which can be separately contacted and density-tuned individually [2].

In a large magnetic field the continuous electron energy spectrum splits into discrete Landau-levels separated by the cyclotron energy. This Landau quantization is also the origin of the Quantum-Hall Effect. In bilayers it is possible to form exciton-like particles if the lowest Landau level in both layers is just half full. In this case, one can consider the non-occupied electron states as the holes which can pair

with the electrons in the respective other layer. Figure 28 demonstrates this. It had been speculated since the mid seventies that these excitonic particles could undergo a BEC-transition, i.e. form a superfluid.

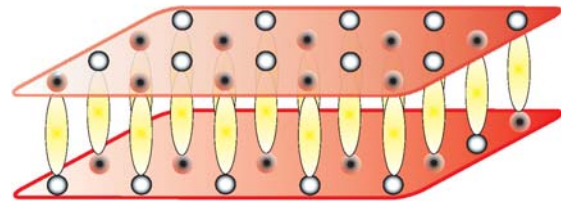


Figure 28: Cartoon showing the interaction between occupied electron states (dark) in one layer with unoccupied ones (white) in the other layer. At low electron densities, the occupied and unoccupied electron states can form a correlated new state.

Recent data demonstrate that the long-anticipated BEC may indeed occur in this system [2,3]. There are, however, very severe requirements to observe this novel state. One is that the ratio of the Coulombic interactions between the electrons within the individual layers and between them must be small enough. This is expressed by the parameter d/ℓ_B where d is the distance between the layers and ℓ_B is the magnetic length which is proportional to the

mean distance between electrons within the layers. The other requirement is an extremely low impurity level, otherwise the electrons become localized in potential fluctuations before the novel state is formed. Only samples grown by L. Pfeiffer (Bell Labs) [3] and by the authors in collaboration with W. Wegscheider (Universität Regensburg) show the possible BEC [2].

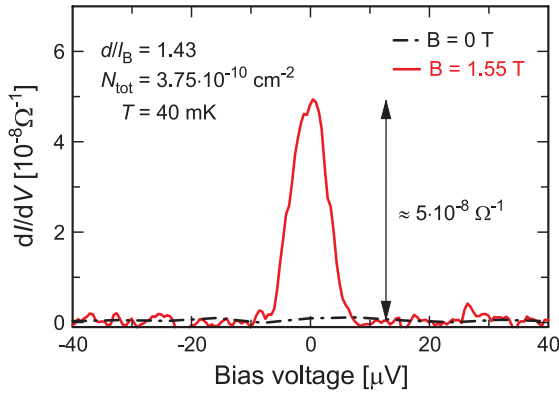


Figure 29: Tunnel conductivity as function of bias voltage at zero magnetic field and at total filling factor 1. Tunneling occurs only at zero bias and if the lowest Landau level in each layer is half full. This indicates the existence of a large density of states at the Fermi energy which could be caused by Bose-Einstein condensation.

An important evidence for the excitonic BEC is the tunnel conductivity at the filling factor $1/2$ in each layer. Our results are shown in Fig. 29. At zero magnetic field one finds no tunneling conductance because the barrier between the two quantum wells is rather thick in our samples. If, however, both Landau levels are half full, then a distinct conductivity maximum is observed. The width of this maximum is less than $10 \mu\text{V}$. It is thought that this maximum is caused by the macroscopic quantum states which form in the layers by the Bose-Einstein condensation. This would then be similar to the Josephson tunneling between two superconductors where the large tunnel current at zero bias originates from the coherent quantum states of the two superconductors.

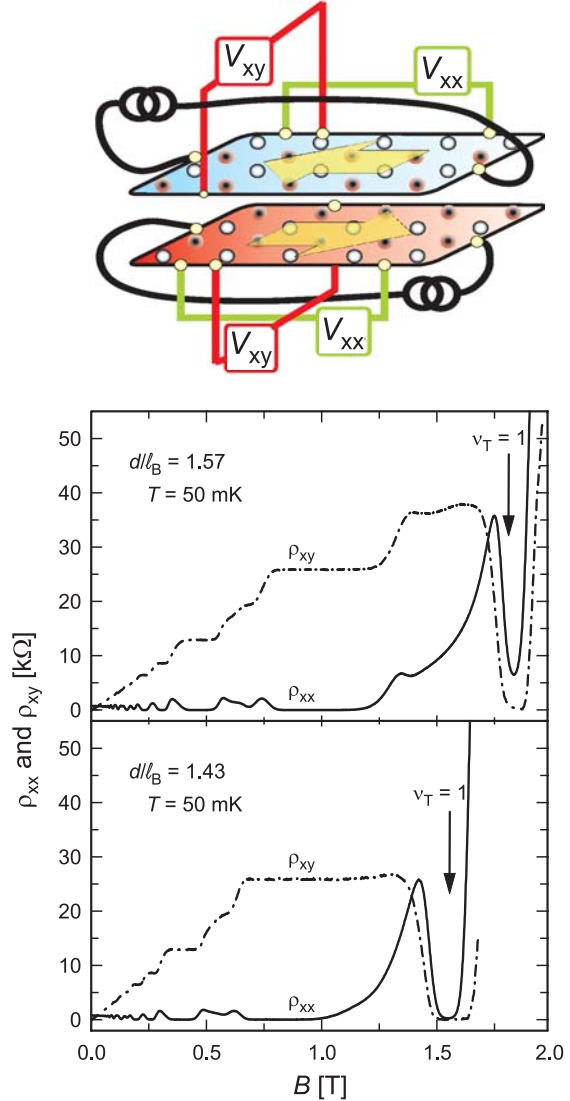


Figure 30: Top: Schematic of the setup to observe the vanishing of both the longitudinal and transverse resistance. Equal but oppositely directed current is drawn through the two layers. At half filled Landau levels in both layers one observes a vanishing of both resistivity components. At all other filling factors (set by the magnetic field) the two layers act like independent layers.

Electric behavior resembling superconductivity can be demonstrated with the set-up of Fig. 30 (top). In this case, equal currents are passed through both layers in opposite directions. Voltages along (V_{xx} which are proportional to ρ_{xx}) and across the individual layers (V_{xy} proportional to ρ_{xy}) are measured as function of magnetic field. The densities in the two layers are

equal and of the order of $2 \cdot 10^{-10} \text{ cm}^{-2}$. Two data sets for two different d/ℓ_B values are shown in Fig. 30 (bottom). These were obtained by slightly varying the densities in both layers. At small magnetic field values the ρ_{xx} and ρ_{xy} show the behavior expected for individual layers. At the magnetic fields corresponding to half-filled Landau levels, however, we find a pronounced minimum of both the longitudinal and the transverse resistance. The measured resistances at the minima are not completely zero, but continue to decrease with decreasing temperature. This behavior (the minima of both resistivity components) has been taken as evidence for superfluidity in the system [1].

The resistance minima disappear at temperatures above about 100 mK. We studied the temperature dependence and found an exponential behavior from which an activation energy could be obtained [1]. This activation energy, which is typically less than 0.5 K, increases with decreasing d/ℓ_B . One might ask if these activation energies are related to the condensation energy of a BEC. The results of the following experiment indicate that this is most likely not the case.

In our samples we can vary the electron densities in the layers such that the total density remains constant but the individual densities are out of balance. Surprisingly, we find that the novel state extends over a rather large range of imbalance. Up to $\delta n/n_{\text{tot}}$ of more than one 10% one can still find the near vanishing of both longitudinal and Hall resistance in the counter flow geometry. This allows to determine the activation energies separately for the two layers. The results are plotted in Fig. 31 as the open symbols as function of imbalance. In the balanced case ($\delta n/n_{\text{tot}} = 0$), the gaps of the two layers are, of course, equal. The activation energies diverge with increasing imbalance, however. The layer which happens to contain the larger density shows a near linear increase with imbalance while the one of the other layer decreases linearly.

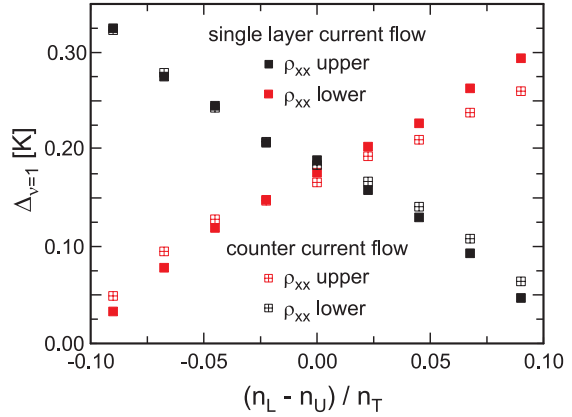


Figure 31: Activation energies derived from the exponential decrease of the longitudinal resistance at 1/2 filling of a Landau level in both layers. Only at matched densities one finds an activation energy which is equal in both layers. Otherwise, the activation energy increases in the layer with the larger density with density imbalance while it decreases in the other one.

A similar behavior of the activation energy is observed if current is passed through only one layer. In this case the longitudinal resistance vanishes in a similar fashion as in the counter flow geometry and the extracted gap energies are nearly the same (full symbols). This is a surprising result. One would have expected that the excitonic state is more stable if electrons and holes move in phase to each other as they do in the counter flow geometry. On the other hand, it is questionable if the activation energy measured here is directly related to the condensation energy of a possible BEC state, because we would have expected the same activation energy everywhere in a macroscopic quantum system. Thus, although a strong correlation between the layers exists, it is not yet clear if our results are evidence of a BEC state in the bilayer system.

-
- [1] Eisenstein, J.P. and A.H. MacDonald. *Nature* **432**, 691-694 (2004).
 - [2] Wiersma, R.D., J.G.S. Lok, S. Kraus, W. Dietsche, K. von Klitzing, D. Schuh, M. Bichler, H.-P. Tranitz and W. Wegscheider. *Physical Review Letters* **93**, 266905 (2004).
 - [3] Kellogg, M., J.P. Eisenstein, L.N. Pfeiffer and K.W. West. *Physical Review Letters* **93**, 036801 (2004).

Soft Fermi surfaces and a new route to non-Fermi liquid behavior

S. Andergassen, L. Dell'Anna, W. Metzner and D. Rohe

Under suitable circumstances electron-electron interactions can generate a spontaneous breaking of the rotation symmetry of an itinerant electron system without breaking translation invariance. From a Fermi liquid perspective such an instability is driven by forward scattering interactions and leads to a symmetry breaking deformation of the Fermi surface. Alluding to a stability limit for forward scattering derived long ago by Pomeranchuk, it is therefore frequently referred to as ‘*Pomeranchuk instability*’. For electrons on a two-dimensional square lattice, a Pomeranchuk instability with $d_{x^2-y^2}$ symmetry, where the Fermi surface expands along the k_x axis and shrinks along the k_y axis as in Fig. 32 (or vice versa), is the most natural possibility [1,2]. A Pomeranchuk instability usually has to compete with other instabilities, but can also coexist with other symmetry breaking order.

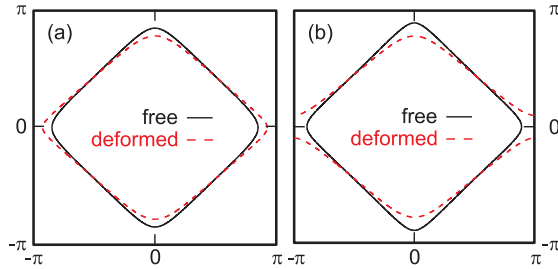


Figure 32: Schematic plot of Fermi surface deformations breaking the square lattice symmetry; the deformed surface may be closed (a) or open (b).

Electron systems in the vicinity of a Pomeranchuk instability have peculiar properties due to a ‘*soft*’ Fermi surface, which can be easily deformed by anisotropic perturbations. In particular, dynamical fluctuations of such a soft Fermi surface lead to a strongly enhanced decay rate for single-particle excitations and thus to non-Fermi liquid behavior [3]. To explore this qualitatively plausible effect, we have analyzed a phenomenological model with an interaction which drives Fermi surface symmetry breaking, but no other instability. In

standard second quantized notation, the model Hamiltonian reads

$$H = \sum_{\mathbf{k},\sigma} \epsilon_{\mathbf{k}} n_{\mathbf{k}\sigma} + \frac{1}{2V} \sum_{\mathbf{k},\mathbf{k}',\mathbf{q}} f_{\mathbf{k}\mathbf{k}'}(\mathbf{q}) n_{\mathbf{k}}(\mathbf{q}) n_{\mathbf{k}'}(-\mathbf{q}), \quad (6)$$

where $\epsilon_{\mathbf{k}}$ is a single-particle dispersion, $n_{\mathbf{k}}(\mathbf{q}) = \sum_{\sigma} c_{\mathbf{k}-\mathbf{q}/2,\sigma}^{\dagger} c_{\mathbf{k}+\mathbf{q}/2,\sigma}$, and V is the volume of the system. Since the Pomeranchuk instability is driven by interactions with vanishing momentum transfers, that is forward scattering, we choose a function $f_{\mathbf{k}\mathbf{k}'}(\mathbf{q})$ which contributes only for relatively small momenta \mathbf{q} . For a simplified treatment, which however fully captures the crucial physics, we consider an interaction of the form

$$f_{\mathbf{k}\mathbf{k}'}(\mathbf{q}) = u(\mathbf{q}) + g(\mathbf{q}) d_{\mathbf{k}} d_{\mathbf{k}'} \quad (7)$$

with $u(\mathbf{q}) \geq 0$ and $g(\mathbf{q}) < 0$, and a form factor $d_{\mathbf{k}}$ with $d_{x^2-y^2}$ symmetry, such as $d_{\mathbf{k}} = \cos k_x - \cos k_y$. The coupling functions $u(\mathbf{q})$ and $g(\mathbf{q})$ vanish if $|\mathbf{q}|$ exceeds a certain small momentum cutoff Λ . This ansatz mimics the effective interaction in the forward scattering channel as obtained from renormalization group calculations [1] for the two-dimensional Hubbard model. The uniform term originates directly from the repulsion between electrons and suppresses the electronic compressibility of the system. The d -wave term drives the Pomeranchuk instability. For a suitable choice of $\epsilon_{\mathbf{k}}$ and interaction parameters the model has a *quantum critical point* in the phase diagram spanned by electron density and temperature [4].

Near the instability, critical Fermi surface fluctuations lead to a *singular* dynamical (frequency-dependent) effective interaction of the form

$$\Gamma_{\mathbf{k}\mathbf{k}'}(\mathbf{q}, \omega) \propto \frac{d_{\mathbf{k}} d_{\mathbf{k}'}}{\xi^{-2} + |\mathbf{q}|^2 - i \frac{\omega}{c|\mathbf{q}|}} \quad (8)$$

for small \mathbf{q} and ω , where ξ is the correlation length of the fluctuations and c a positive constant.

To clarify the properties of single-particle excitations, we have computed the electronic self-energy $\Sigma(\mathbf{k}, \omega)$. The dominant contributions due to singular forward scattering are proportional to $d_{\mathbf{k}}^2$. For \mathbf{k} near the Fermi surface this leads to a strong tangential momentum dependence of $\Sigma(\mathbf{k}, \omega)$. The singular contributions vanish on the diagonal of the Brillouin zone, and have the largest amplitude near the van Hove points. At the quantum critical point ($T=0$, $\xi=\infty$), the real and imaginary parts of the self-energy scale as $|\omega|^{2/3}$ with energy. This leads to a complete destruction of quasiparticles near the Fermi surface except on the Brillouin zone diagonal, due to the prefactor $d_{\mathbf{k}}^2$. The dispersion of the maxima of the spectral function for single-particle excitations $A(\mathbf{k}, \omega)$ flattens strongly for momenta \mathbf{k} near the Fermi surface away from the zone diagonal. In the vicinity of the quantum critical point, that is for a large finite correlation length ξ , the ground state self-energy still exhibits non-Fermi liquid behavior over a wide energy range, as seen in Fig. 33.

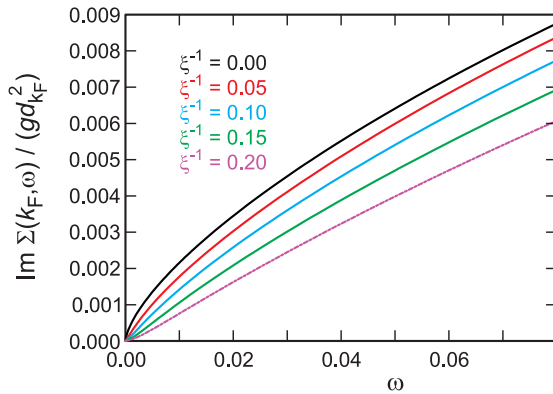


Figure 33: Imaginary part of the electronic self-energy $\text{Im}\Sigma(\mathbf{k}_F, \omega)$, divided by $g d_{\mathbf{k}_F}^2$, as a function of ω in the ground state ($T=0$) for various choices of the correlation length ξ .

Fermi liquid behavior is recovered only at very low energies below a scale $\omega_\xi \propto \xi^{-3}$. In the quantum critical regime at $T > 0$ the self-energy consists of a ‘classical’ and a ‘quantum’ part with very different dependencies on T and ω . The classical part, which is due to classical fluctuations, dominates at $\omega=0$,

where it yields a contribution proportional to $T\xi(T) \propto \sqrt{T/\log T}$ to $\text{Im}\Sigma(\mathbf{k}_F, \omega)$. The quantum part is generated by quantum fluctuations and obeys (ω/T) -scaling in the quantum critical regime.

Could soft Fermi surfaces and critical Fermi surface fluctuations play a role in cuprate superconductors? Due to the coupling of electron and lattice degrees of freedom a symmetry-breaking Fermi surface deformation is generally accompanied by a lattice distortion, and vice versa. Structural transitions which reduce the lattice symmetry of the cuprate planes are quite frequent in cuprates. Close to a Pomeranchuk instability of the electronic system, electronic properties can be expected to react unusually strongly to slight lattice distortions which break the symmetry of the electronic system explicitly. Such ‘overreactions’ of electronic properties have indeed been observed in several cuprate compounds. Strong Fermi surface fluctuations could be at least partially responsible for the non-Fermi liquid behavior observed in the ‘strange metal’ regime of cuprate superconductors near optimal doping. In our model calculation we have obtained a strongly anisotropic anomalously large decay rate for single-particle excitations and a flattening of the dispersion relation near the Fermi surface away from the nodal direction. Extended flat bands in the van Hove region have been observed experimentally by various groups already in the early 1990s. Large anisotropic decay rates have been extracted from the linewidth of low-energy peaks in the photoemission spectra observed in optimally doped cuprates.

-
- [1] Halboth, C.J. and W. Metzner. Physical Review Letters **85**, 5162-5465 (2000).
 - [2] Yamase, H. and H. Kohno. Journal of the Physical Society of Japan **69**, 332-335 (2000).
 - [3] Metzner, W., D. Rohe and S. Andergassen. Physical Review Letters **91**, 066402 (2003); Dell’Anna, L. and W. Metzner. Physical Review B **73**, 045127 (2006).
 - [4] Yamase, H., V. Oganesyan and W. Metzner. Physical Review B **72**, 035114 (2005).

Raman scattering in the Mott insulators LaTiO_3 and YTiO_3 : evidence for orbital excitations

C. Ulrich, M. Guennou, G. Khaliullin and B. Keimer;

A. Gössling, M. Grüninger, H. Roth, M. Cwik and T. Lorenz, (Universität zu Köln);

G. Ghiringhelli and L. Braicovich (Politecnico di Milano, Italy)

Transition metal oxides with orbital degeneracy exhibit a host of intriguing physical properties, such as ‘colossal magnetoresistance’ in manganites or unconventional superconductivity in ruthenium oxides. Collective oscillations of the valence electrons between different atomic orbitals (termed ‘orbitons’) contain a wealth of information about the microscopic interactions underlying this behavior. Experiments introducing Raman scattering as a direct probe of orbitons in LaMnO_3 have thus opened up new perspectives for a quantitative understanding of colossal magnetoresistance [1]. The results, however, have proven to be quite controversial, because the modes observed in LaMnO_3 are difficult to discriminate from ordinary two-phonon excitations [2].

Insulating titanates such as LaTiO_3 and YTiO_3 have only one valence electron residing on the Ti^{3+} ions. Despite their similar, nearly cubic lattice structures, the magnetic ground states of LaTiO_3 and YTiO_3 are quite different: Whereas LaTiO_3 orders antiferromagnetically at $T_N \approx 150$ K, YTiO_3 is a ferromagnet with Curie temperature $T_C \approx 30$ K. The origin of this difference lies in the large degeneracy of the quantum states available to the valence electron. In addition to its spin degeneracy, this electron can occupy any combination of the three t_{2g} -orbitals xy , xz and yz . The six single-ion states on neighboring sites are coupled by the superexchange interaction and collective lattice distortions, which generate a plethora of nearly degenerate many-body states with different spin and orbital ordering patterns.

The mechanisms selecting the ground state out of this large manifold of states have recently been a focus of intense research. Two theoretical approaches have emerged, which emphasize either the lifting of orbital degeneracy by subtle

lattice distortions or collective quantum dynamics of the orbitals. Orbital excitations have the potential to discriminate between these conflicting scenarios. When the orbital dynamics is quenched by lattice distortions, one expects a number of transitions between well-defined crystal field levels, with selection rules dictated by the symmetry of these distortions. In an orbitally fluctuating state, on the other hand, the orbital excitations are collective modes with selection rules controlled by many-body effects and hence are very different from local crystal field excitations. Therefore, the observation of orbital excitations and comparison of their properties in YTiO_3 and LaTiO_3 , two materials with different lattice distortions and magnetic ground states, is of crucial importance for the understanding of this hotly debated issue.

We have used Raman scattering and resonant inelastic X-ray (RIXS) scattering to search for orbital excitations in pure and lightly oxygen doped $\text{LaTiO}_{3+\delta}$, and in pure YTiO_3 . Figure 34 shows the Raman spectra of LaTiO_3 and YTiO_3 single crystals measured over a wide energy range. Up to 80 meV, the spectra are dominated by one-phonon excitations. A series of weak features extends up to 170 meV. At still higher frequencies, around 235 meV, a pronounced broad peak is observed in both compounds. The latter feature has hitherto not been reported and constitutes the central observation of this work. In order to establish whether the broad peak can be attributed to two-phonon excitations, we have evaluated the two-phonon density of states (2-DOS) of YTiO_3 . The 2-DOS, responsible for the weak features between 80 and 170 meV, terminates at about 170 meV. The broad peak thus occurs well above the two-phonon spectral range, in

contrast to the features around 160 meV discussed for LaMnO_3 . Since higher phonon orders are expected to appear even weaker, lattice vibrations can be ruled out as the origin of the high-energy Raman peak.

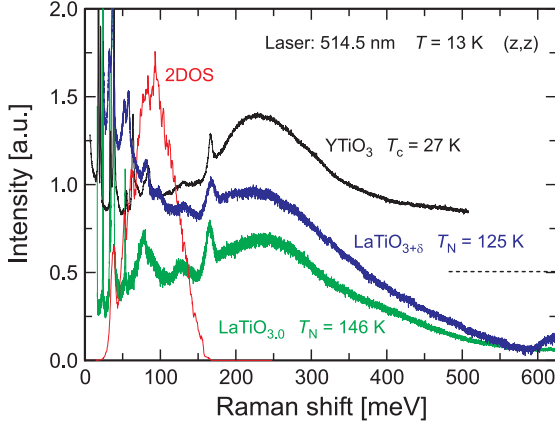


Figure 34: Raman spectra of LaTiO_3 , $\text{LaTiO}_{3+\delta}$, and YTiO_3 measured at $T = 13$ K using the 514.5 nm line of an Ar^+/Kr^+ mixed gas laser. The intensities were calibrated by using a white light source (Ulbricht-sphere) as reference. The red line shows the calculated two-phonon density of states.

In order to rule out photoluminescence as a cause of the broad peak, we have repeated the Raman measurements with different laser lines between 457.9 nm and 568.2 nm (Fig. 35).

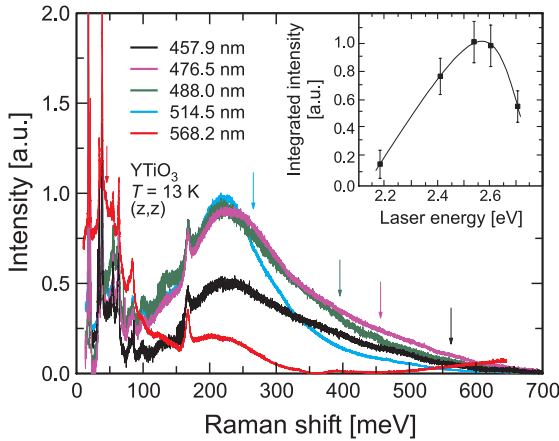


Figure 35: Raman spectrum of YTiO_3 measured at $T = 13$ K for different laser lines. A frequency independent background has been subtracted from every profile. The arrows depict the position of the photoluminescence peak at 2.14 eV for the different laser lines. The inset shows the integrated intensity of the broad high-energy peak.

The peak at 235 meV does not shift as the laser frequency is changed, ruling out photoluminescence as origin and demonstrating that the peak position corresponds to a genuine excitation frequency. The inset of Fig. 35 shows that the integrated spectral weight of the 235 meV mode in YTiO_3 exhibits a pronounced resonant enhancement at a laser frequency of ≈ 2.54 eV. For the investigation of the influence of oxygen defects on the Raman intensity, we have repeated the experiment on $\text{LaTiO}_{3+\delta}$ samples whose Néel temperatures are reduced by a significant oxygen non-stoichiometry. Representative data are shown in Fig. 34. The 235 meV mode remains almost unchanged. This demonstrates that this feature does not arise from oxygen defects. Furthermore, since the increase in the number of charge carriers does not lead to an increase of the spectral weight of the 235 meV peak, polarons can be ruled out as an explanation.

The intensity of the mode depends strongly on the light polarization (Fig. 36). In a cubic crystal, the Raman intensity for parallel and crossed polarizations can be expressed via E_g , T_{2g} and A_{1g} symmetry components: $I_{\parallel} = (2/3 - a_{\theta} - b_{\theta})E_g + (a_{\theta} + b_{\theta})T_{2g} + 1/3 A_{1g}$, $I_{\perp} = b_{\theta}E_g + (1/2 - b_{\theta})T_{2g}$, where θ is the angle between the incident electric field vector and the c -axis, $a_{\theta} = 1/2 \sin^2 \theta$, $b_{\theta} = 3/8 \sin^2 2\theta$. $\theta = 90^\circ$ corresponds to the a - (or b -) axis. These relations provide a good description of the observed polarization dependencies in both compounds (insets in Fig. 36).

We now turn to the interpretation of the 235 meV mode. Having ruled out phonons, luminescence, and oxygen defects, we attribute the mode to electronic scattering. Its lineshape, temperature (not shown in this paper), and polarization dependence shows striking similarities (elaborated later on) with the Raman scattering from spin-pair excitations in the insulating parent compounds of the superconducting cuprates. However, a simple two-magnon origin of the broad band is ruled out here because

YTiO₃ is ferromagnetic, and because the peak energy is much higher than twice the magnon energies found by neutron scattering: ≈ 20 meV in YTiO₃ and ≈ 44 meV in LaTiO₃. We thus attribute the broad Raman mode to the orbital degrees of freedom of the valence electron.

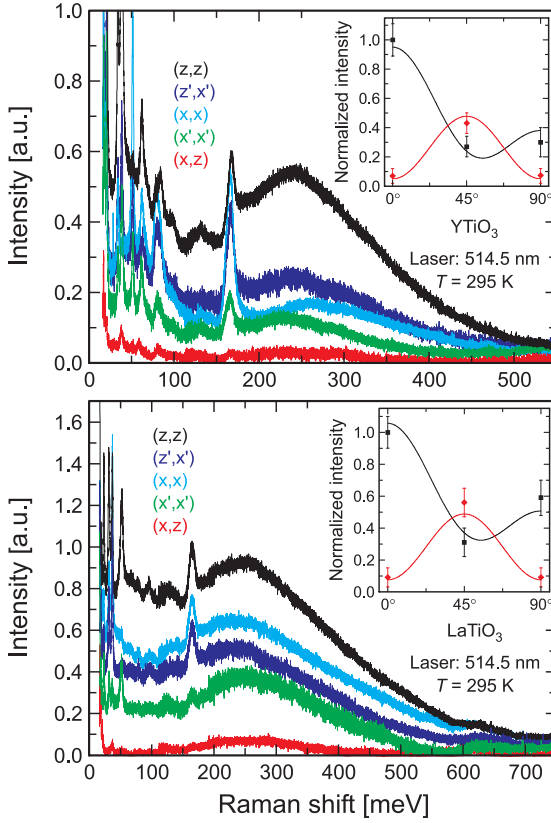


Figure 36: Polarization dependencies of the Raman spectra of YTiO₃ and LaTiO₃ at room temperature. Note that the polarization $z \parallel c$ is along the nearest-neighbor Ti–Ti bond whereas x is along the next-nearest-neighbor Ti–Ti direction in the ab -plane. The z' and x' directions are rotated by 45° from z and x . Insets: scattering intensities for the parallel (black) and crossed (red) polarizations as function of angle θ . Solid lines are obtained with relative intensities $E_g : A_{1g} : T_{2g} \approx 1 : 0.3 : 0.1$ ($1 : 0.5 : 0.1$) in YTiO₃ (LaTiO₃).

In order to confirm the assignment of the observed Raman feature at 235 meV to excitations from the t_{2g} orbitals, we performed resonant inelastic X-ray experiments at the $L_{2,3}$ edge ($2p \rightarrow 3d$) of Ti³⁺ (i.e. 456 eV). The experiment was carried out at the soft-X-ray beamline ID08 at the ESRF in Grenoble. Figure 37 shows the

resulting RIXS spectra taken at the t_{2g} -peak excitation. XAPS spectra were taken in addition to ensure a good surface quality and the stability of the X-ray beam.

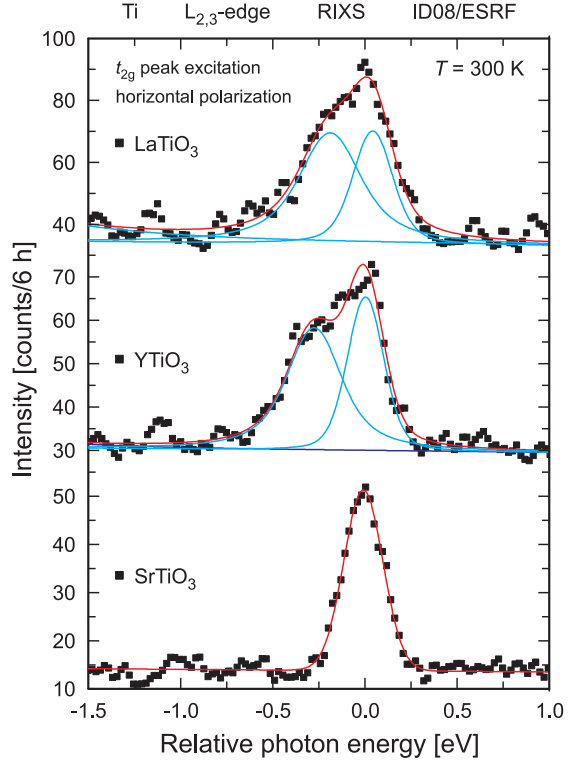


Figure 37: Resonant inelastic X-ray scattering (RIXS) spectra of LaTiO₃ and YTiO₃ taken at t_{2g} -edge of the $L_{2,3}$ resonance of Ti³⁺. For comparison, the spectrum of SrTiO₃ is also shown. Horizontal polarization of the incident X-ray beam was chosen.

All spectra exhibit a peak at zero energy, which arises from elastic diffuse scattering. The linewidth of this peak indicates the resolution of the spectrometer, i.e. 0.24 eV. The RIXS spectra of LaTiO₃ and YTiO₃ show an additional peak at an energy of 0.23 ± 0.03 eV and 0.26 ± 0.04 eV, respectively. Within the experimental error, this peak corresponds exactly, in position and linewidth, to the observed structure in the optical Raman scattering experiments. As reference we have also measured SrTiO₃ where the Ti-ion is in the 4+ state, i.e. no electrons occupy the t_{2g} -level. In this case the additional feature at 0.23 eV has clearly disappeared. Furthermore, the inelastic signal

at 0.23 eV in LaTiO_3 and YTiO_3 disappeared when the experiment was performed at an incident energy different from the $L_{2,3}$ resonance of Ti^{3+} . This confirms that the observed Raman feature is of electronic origin and arises from the $3d$ electrons.

The resonance energy yields an important clue to the microscopic origin of the broad Raman peak. As it falls in the range of intersite $d_i \rightarrow d_j$ excitations in optical spectra, *two* Ti sites must be involved in the Raman process. This means that the t_{2g} -electron is first transferred to a neighboring site by the incident photon that matches the $d_i \rightarrow d_j$ transition energy. The intermediate state then relaxes back, leaving behind flipped orbitals either on one or on both sites, depending on the actual orbital pattern. In the framework of the lattice-driven orbital picture, the orbital excitations probed by light polarized along different crystal axes are fundamentally different. In particular, the selection rules for the four-sublattice pattern $(xz \pm xy)/\sqrt{2}$, $(yz \pm xy)/\sqrt{2}$ suggested for YTiO_3 allow a single orbital-flip for *ab*-plane polarization, but only two-orbital excitations may occur in case of light polarization along the *c*-axis. This selection rule (which results from a mirror symmetry of the Ti-O-Ti bonds along the *c*-axis) is in contrast to the observed polarization independence of the peak position.

In an alternative picture the orbitals are regarded as quantum objects much like the spins of the correlated electrons, and interact with each other via the superexchange mechanism. In the superexchange-driven orbital state of YTiO_3 , the light scattering from fluctuations of the *orbital-exchange* bonds, described by P_{orb} , leads to a two-orbital Raman band of cubic E_g symmetry, as observed. The A_{1g} and T_{2g} components are explained due to next-nearest-neighbor orbital exchange terms that are enhanced by resonant scattering, in complete anal-

ogy to the theory of magnetic Raman scattering in the cuprates. From an analysis of the spin-wave data, the highest orbiton energy was determined as $\sim 2r_1 J_{\text{SE}}$ with $r_1 J_{\text{SE}} \approx 60$ meV and $r_1 \approx 1.5$, in reasonable agreement with a two-orbital peak at the experimental value of 235 meV. Since the orbital excitations are strongly damped because of frustrating interactions, their response is broad in both momentum and energy, as observed.

In summary, we found orbital excitations in LaTiO_3 and YTiO_3 at approximately 235 meV. The superexchange-driven quantum orbital picture provides a consistent description of this observation as well as the polarization and temperature dependence of these excitations. In this picture, the high-energy Raman peak is due to light scattering from exchange-bond fluctuations, a process which is basically identical to magnetic Raman scattering in copper oxides. A pseudospin-like behavior of quantum orbitals explains why the Raman response of two apparently different degrees of freedom exhibit very similar features. In fact, the energies of the two-orbital Raman mode in the titanates (≈ 235 meV) and the two-magnon mode in the cuprates (≈ 350 meV) are related by the simple scaling relation for the exchange-pair energy $\Omega_{\text{pair}} \sim (z-1)J_{\text{SE}}$, where J_{SE} and z are the strength and number of exchange bonds, respectively. These considerations, which can be readily extended to other transition metal compounds with more than one valence electron (or hole), provide a glimpse of an underlying universality in the electronic spectra of these complex materials.

-
- [1] Saitoh, E., S. Okamoto, K.T. Takahashi, K. Tobe, K. Yamamoto, T. Kimura, S. Ishihara, S. Maekawa and Y. Tokura. *Nature* **410**, 180-183 (2001).
 - [2] Grüninger, M., R. Rückamp, M. Windt, P. Reutler, C. Zobel, T. Lorenz, A. Freimuth and A. Revcolevschi. *Nature* **418**, 39-40 (2002).

First results from the new TRISP spectrometer: magnon linewidths in MnF_2 and phonon linewidths in lead

S.P. Bayrakci, T. Keller, P. Aynajian, K. Buchner, M. Ohl, H. Klann and B. Keimer;
K. Habicht (HMI Berlin)

The NRSE-TAS spectrometer TRISP constructed by the Keimer department at the FRM-II research reactor in Garching is now operational. A schematic and photograph of the instrument are shown in Fig. 38. The fusion of the neutron resonance spin-echo (NRSE) and triple-axis spectrometry (TAS) techniques allows the determination of the intrinsic lifetimes of elementary excitations such as magnons and phonons with unprecedented resolution. The energies of such excitations lie in the 1–100 meV range, and the energy resolution of conventional neutron TAS at these energy transfers is typically 0.1–10 meV. With the NRSE-TAS method, however, linewidths in the μeV -range can be resolved. This opens up entirely new fields of investigation, as no other technique permits high-resolution measurements over a range of momentum transfers which extends over the entire Brillouin zone.

Extensive theoretical literature developed over several decades [1] addresses the energy renormalization and lifetime of spin waves in Heisenberg antiferromagnets. Until now, such predictions were only testable at $q=0$ and over narrow regions of temperature. In MnF_2 , one of the most intensively studied antiferromagnets, the magnon lifetime $1/\Gamma$ has only been investigated at temperatures close to T_N , in the critical region. Only there is the linewidth sufficiently broad that TAS measurements are not resolution-limited. A study [2] of the low-temperature damping in the nearly isotropic antiferromagnet RbMnF_3 found partial agreement with theory [1]. However, the extracted linewidths were in many cases significantly smaller than the instrumental resolution, in some cases constituting a fraction as low as 2%. This illustrates the limitations of conventional TAS experiments.

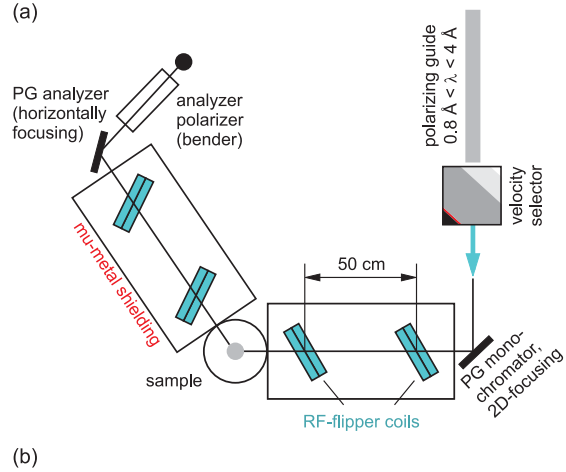


Figure 38: (a) Schematic of the TRISP NRSE-TAS spectrometer. (b) The TRISP spectrometer, with the sample table at the center and the monochromator shielding (green) at right.

The NRSE-TAS technique will also allow accurate measurements of the intrinsic linewidths and energies of recently-discovered novel magnetic excitations in low-dimensional quantum magnets such as Haldane spin chains, and also of spin-Peierls and spin-ladder systems. These systems are not described by conventional spin wave theory. For some of them, detailed and quantitative predictions of the linewidth are presently becoming available.

In a first study of magnon linewidths in the antiferromagnet MnF_2 using the TRISP spectrometer, an energy resolution down to $1 \mu\text{eV}$ was obtained, representing an improvement of two orders of magnitude over conventional TAS. The polarized neutron flux of $4 \cdot 10^7 \text{ cm}^{-2} \text{ s}^{-1}$ at the sample (for $k_i = 3 \text{ \AA}^{-1}$) is competitive with the best polarized TAS instruments. The background at the detector of 1 count per 10 minutes is very low. The accessible range for the incident wavevector lies between 1.6 and 8 \AA^{-1} .

We investigated magnons in MnF_2 with q ranging from 0 – 0.5 r.l.u. at temperatures between 3 K and 40 K (0.04 – $0.6 T_N$). We focused first on magnons propagating along q_c in the antiferromagnetic Brillouin zone centered at (100) , as in this configuration no losses of beam polarization due to spin-flip processes during scattering occur.

In the NRSE-TAS technique, the polarization of the scattered neutrons is measured as a function of the spin-echo time τ . This polarization is the Fourier transform of the spectral lineshape. The observed polarizations decay as $P(\tau) = \exp(-\Gamma \cdot \tau)$, which corresponds to a Lorentzian lineshape. From a fit to such a polarization, we obtain the linewidth Γ . Sample polarization data are shown in Fig. 39(a) for the $q_c = 0.1$ r.l.u. magnon measured at two different temperatures. A difference in linewidth as small as $9 \mu\text{eV}$ can be clearly resolved in the raw data.

Raw linewidth data (HWHM) is shown in Fig. 39(b) over the full Brillouin zone and a range of temperatures. At small q and low temperature, we observe an instrumental broadening of the linewidths which is primarily due to the curvature of the dispersion and the finite momentum resolution. These instrumental effects can be corrected for by applying an analytical resolution function [3]. Remaining contributions at small q probably result from scattering by bulk and surface inhomogeneities.

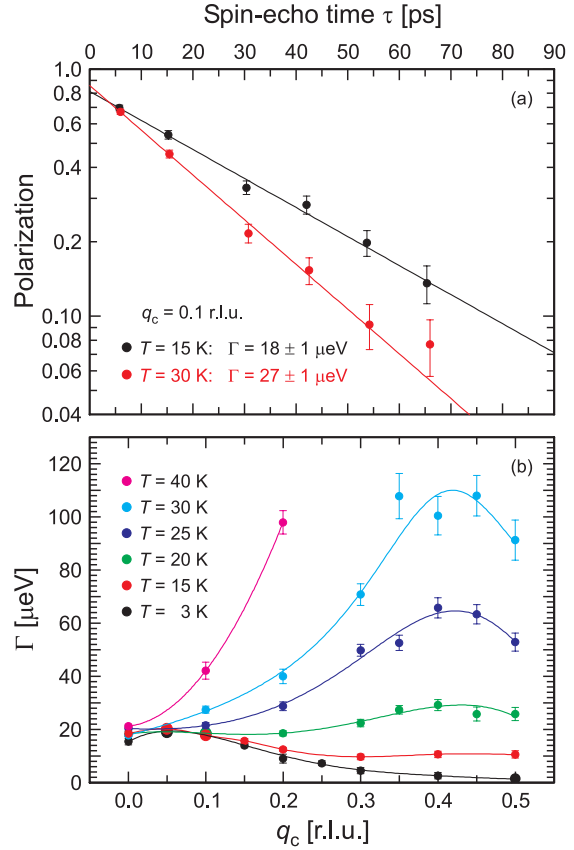


Figure 39: (a) Measured polarization following the spin ‘echo’ as a function of spin-echo time for the $q_c = 0.1$ r.l.u. magnon in MnF_2 at 15 K and 30 K . (b) Raw linewidth data for the q_c magnon in MnF_2 at different temperatures over the full antiferromagnetic Brillouin zone.

The linewidth at a given q increases monotonically with increasing temperature within experimental error. A broad peak at intermediate q is present for temperatures of 20 K and above. Several theoretical results in the literature have suggested the existence of such a peak. However, so far these theories have been evaluated fully only for the special cases of high applied magnetic field and/or small q . Given the new impetus provided by the present experimental data, these calculations can now be revisited and their results evaluated numerically.

Another class of experiments which becomes accessible with the new spectrometer concerns the electron-phonon interaction, which is responsible for superconductivity in elemental metals. Modern ab initio band structure

calculations for such metals (carried out by O.K. Andersen's group at the MPI-FKF, among others) predict the electron-phonon coupling of each phonon over the entire Brillouin zone, as well as its contribution to the superconducting condensation energy. Measurements of the corresponding phonon linewidth broadening using the NRSE-TAS technique should help to provide a quantitative understanding of the electron-phonon interaction and superconductivity in simple metals. This is a prerequisite for development of microscopic models of more complex compounds.

We have measured the linewidths of phonons in the elemental superconductor Pb. If the superconducting energy gap is $\Delta(T)$, then at a given temperature $T < T_C$, phonons with energy less than $2\Delta(T)$ cannot decay through Cooper pair-breaking processes. Consequently, their linewidths should decrease to zero as the temperature is lowered and the system passes into the superconducting state. Figure 40 shows the linewidth of the transverse acoustic phonon $[\xi\xi 0]T_1$ for $\xi = 0.32$, at different temperatures in the vicinity of T_C . For $T < 5.04$ K, the energy of this phonon is less than $2\Delta(T)$. The linewidth just above the gap is $7 \pm 1 \mu\text{eV}$ larger than that measured 1.3 K below the gap. This step-like behavior suggests that the linewidth at and slightly above the gap reflects the electron-phonon coupling rather than phonon-phonon interactions. This is the first measurement in Pb which confirms a change in the lifetime of low-energy phonons upon entering the superconducting state.

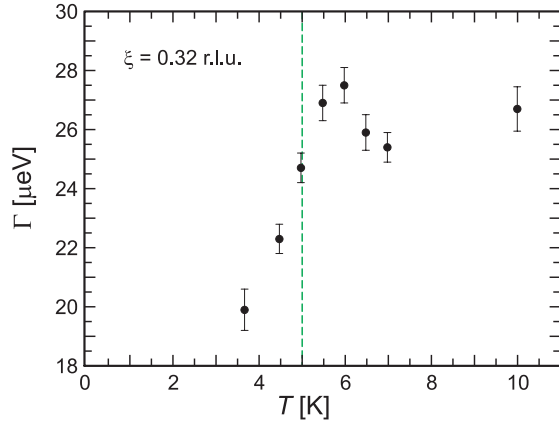


Figure 40: Linewidth of the $[\xi\xi 0]T_1$ phonon in lead for $\xi = 0.32$ at various temperatures. The dashed line represents the temperature at which the energy of this phonon equals $2\Delta(T)$. As in the case of MnF_2 , a residual linewidth is present at low temperatures. The instrumental broadening can be corrected for by applying an analytical resolution function.

In conclusion, we have inaugurated the new spectrometer TRISP by performing NRSE-TAS linewidth measurements on two relatively simple systems: the Heisenberg antiferromagnet MnF_2 and the superconducting metal Pb. Our results provide grist for comparison with elementary theoretical predictions which were hitherto untestable. Moreover, the excellent linewidth resolution and flux offer promise for measurements on more complex systems.

-
- [1] See, e.g., Harris, A., D. Kumar, B.I. Halperin and P.C. Hohenberg. *Physical Review B* **3**, 961-1024 (1971).
 - [2] Windsor, C., D.H. Saunderson and E. Schedler. *Physical Review Letters* **37**, 855-858 (1976).
 - [3] Habicht, K., T. Keller and R. Golub. *Journal of Applied Crystallography* **36**, 1307-1318 (2003).

Spin interactions

The detailed investigation of the spin degrees of freedom in condensed matter renders new and deeper insights into their complex, rich and often counterintuitive interactions with other spins, orbital degrees of freedom and charge excitations. These interactions may have profound consequences for transport, the density of states, the band structure as well as dynamical properties. Examples highlighted here include giant spin-splitting as a result of spin-orbit interaction in bismuth-silver surface alloys, the Kondo effect when a molecular spin interacts with a metallic surface, unusual optical properties in layered cobaltates due to strong spin-charge couplings, hard ferromagnetic behaviour in FePt nanostructures and spin-polarized quasi-particle injection in cuprate superconductors.

Kondo effect of molecular complexes at surfaces: ligand control of the local spin coupling

P. Wahl, L. Diekhöner, G. Wittich, L. Vitali, M.A. Schneider and K. Kern

The ability to control and manipulate individual spins (represented by the magnetic moment of atoms or molecules) and their coupling to a substrate is at the basis of prospective quantum technologies, where miniaturization reaches the atomic or molecular level. The detailed understanding of the interactions of a spin with its surroundings and the possibility to tune this coupling are therefore essentials in nanotechnology. Here we present the study of the interaction of a molecular spin with a metal surface [1]. The spin center of a magnetic molecule is imaged, manipulated and its interaction analyzed quantitatively by employing a single tool, the Scanning Tunneling Microscope (STM) operating at a temperature of 6 K in ultrahigh vacuum.

We investigated the properties of cobaltcarbonyl molecules on the Cu(100) surface. Cobaltcarbonyl molecules are created by a surface reaction between single cobalt adatoms and carbon monoxide molecules in ultrahigh vacuum. The primary product of that reaction was the cobalt-tetracarbonyl (CoCO_4). The STM was not only used to image the molecules but also to locally dissociate single

CO molecules in order to produce other species of CoCO_n with $n=2, 3$. To investigate the changes in magnetic properties resulting from the controlled ligand detachment, we exploit the Kondo effect. The Kondo effect is a many-body effect, which arises from the interaction of a localized spin (here the molecule) with the delocalized spins of the substrate electrons. At sufficiently low temperatures, this interaction leads to a pronounced resonance ('Kondo resonance') in the local density of states (LDOS) which is detected by scanning tunneling spectroscopy (STS) [2]. From the width of the measured resonance the characteristic Kondo temperature T_K is obtained and used to characterize the magnetic properties of single spin impurities on the atomic scale. We have shown previously how hybridization of an adatom spin with the substrate is reflected in the value of T_K [2]. Here we demonstrate how the coupling of the spin of a single magnetic adatom to the substrate can be controlled by changing its local environment through ligand attachment. Furthermore, we demonstrate, how the Kondo resonance can be used to spatially localize a spin center within a single molecule.

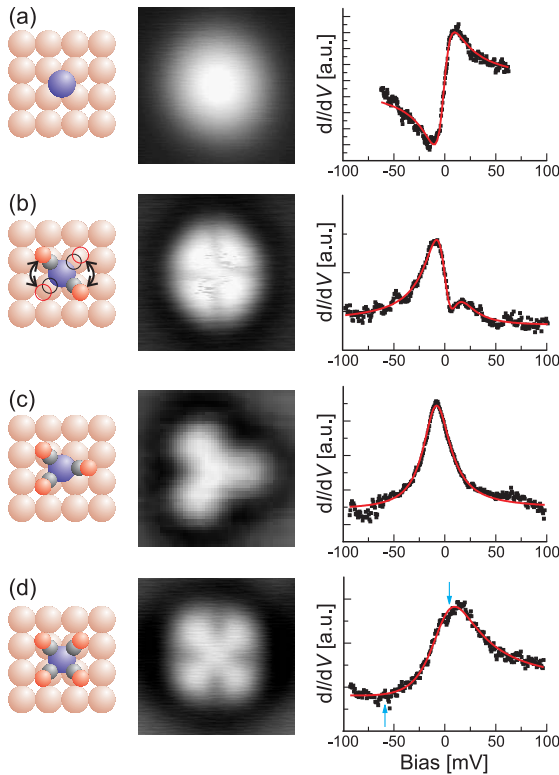


Figure 41: Models, STM topographies and STS spectra in the center of the Co adatoms and complexes under investigation: (a) Cobalt adatom, (b) $\text{Co}(\text{CO})_2$ (constantly flipping; from the spectrum a linear background has been removed), (c) $\text{Co}(\text{CO})_3$, (d) $\text{Co}(\text{CO})_4$. The solid lines in the spectra are fits to a Fano function.

As the central result, STM images of a cobalt adatom and of the carbonyl species are summarized in Fig. 41(a)–(d) together with the dI/dV spectra acquired on these molecules. A single cobalt adatom (Fig. 41(a)) is imaged as a spherical bump. The STM image of the dicarbonyl molecule (Fig. 41(b)) exhibits a fourfold symmetry – as does the image of the tetracarbonyl molecule (Fig. 41(d)). In the case of the dicarbonyl molecule, the four-fold symmetry is due to a continuous flipping of the two CO molecules between the two equivalent configurations (as indicated in the model in Fig. 41(b)). The tricarbonyl molecule shows three lobes. Two CO-molecules point towards the nearest neighbor Cu atom in the substrate while the third is directed towards a bridge site (Fig. 41(c)). For the $\text{Co}(\text{CO})_4$ -molecule, all four CO molecules point in the directions of the next on-top sites (Fig. 41(d)).

Tunneling spectra acquired at the center of the molecules show a pronounced resonance near the Fermi energy in all cases which we identify as Kondo resonance. The line shape found in dI/dV spectra is the Fano function. From fits to this function we extract the Kondo temperature T_K (approximately the half width of the peak structure in Figs. 41(b)–(d)). It is plotted as a function of the number of ligands attached to the central cobalt atom. The Kondo temperature is found to increase with the number of ligands from 88 K for the single cobalt adatom to about 280 K for the cobalt tetracarbonyl complex.

The Kondo resonance is the result of the interaction of the spin of the adatom with the conduction electrons of the host. By adding carbon monoxide molecules, not only the electronic properties of the cobalt atom are modified – this leads to a drastic change in the apparent height of the complex compared to a single cobalt adatom and probably also induces the change in the line shape – but also its magnetic properties are affected. Carbon monoxide is a strong-field ligand and thus increases the splitting between the molecular orbitals – especially those derived from the cobalt d -orbitals. It is known that free cobalt carbonyl molecules have an odd number of valence electrons with one unpaired electron. Thus the narrow feature at the Fermi energy can be rationalized as the Kondo resonance of the spin of the unpaired electron in the cobalt $3d$ -orbital which is coupled to a bath of conduction electrons.

The behavior of the Kondo temperature of the complexes as a function of the number of ligands can be understood in the Kondo model [3]. The Hamiltonian of this model describes the interaction between a localized spin in an impurity orbital with a surrounding sea of conduction electrons by the exchange coupling J . An increased hybridization between the orbital which carries the spin and the conduction band of the host leads to an increased exchange coupling J , and so does a reduced on-site Coulomb repulsion between electrons of opposite spin in

the same orbital [4]. The bond between the CO molecules and the cobalt adatom consists of a donation of electrons from the σ -orbital to the transition metal adatom and a backdonation from the d -orbitals to the $2\pi^*$ orbital of the CO molecules [5]. This backdonation causes to a delocalization of the d -electrons and therefore reduces the Coulomb repulsion and eventually increases the coupling to the substrates conduction band electrons. Both effects increase the exchange coupling J . Within a simple model, we assume that the product of exchange coupling and density of states at the Fermi energy $J\rho_0$ scales linearly (apart from an additive constant J_0) with the number n of CO molecules attached to the cobalt atom

$$J\rho_0 = J_0 + c_J \cdot n, \quad (9)$$

where c_J is the proportionality constant. The characteristic Kondo temperature T_K and hence the width of the Kondo resonance can now be calculated within the Kondo model from

$$k_B T_K \sim D e^{-\frac{1}{J\rho_0}}. \quad (10)$$

Here, D is the width of the conduction band. In addition to the increased hybridization, geometric effects, especially for the carbonyls with two and three ligands, might come into play. They are neglected within our simple model. Describing the coupling as discussed above, we treat D , J_0 and c_J as fitting parameters. Figure 42 shows a fit of Eq.(10) to the experimental data of the Kondo temperature. Within the errors, the agreement between the model and our data is very good. From the fit we obtain $D = 1.83$ eV, $J_0 = 0.182$ and $c_J = 0.01$. The value for D is of the order of magnitude which is typically assumed for the bandwidth of metals, and the value of J_0 compares reasonably with a similar fit for cobalt impurities.

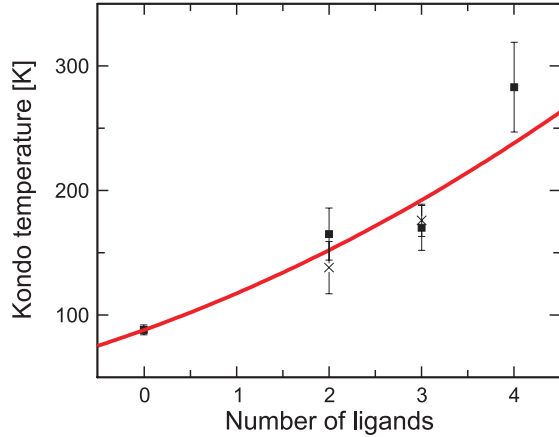


Figure 42: From the molecule spectra in Fig. 41 the Kondo temperature T_K is extracted and plotted as function of the number of ligands. A monotonous increase of T_K with the number of ligands is observed due to the increased coupling of the localized spin on the Co atom to the electrons of the substrate.

The STM is able to go a step beyond spectroscopically characterizing the Kondo resonance by exploiting its spatial resolution. In Fig. 43 we show the spatial mapping of the amplitude of the resonance for a cobalt tetracarbonyl molecule. The height of the resonance defined by the difference in the dI/dV signal at the voltages marked by arrows (Fig. 41(d)) is shown as intensity in Fig. 43(b), while Fig. 43(a) shows the simultaneously acquired topography. The spectroscopic image does not reflect the four-fold symmetry of the molecule. It rather shows a spherically symmetric maximum in the center of the molecule, localized within a radius of ≈ 2.5 Å. It is this position where the cobalt adatom is located in the complex and accordingly where the spin of the complex originates from. Thus we can detect the spin by STS via the Kondo resonance and localize it within the molecule.

The spatial mapping of the Kondo resonance can be easily applied to more complicated species with more than one cobalt atom. In Fig. 43(c)–(f), similar measurements as for the $\text{Co}(\text{CO})_4$ -molecule are shown for binuclear cobalt carbonyl complexes, namely $(\text{Co}(\text{CO})_2)_2$ and $(\text{Co}(\text{CO})_3)_2$. Figure 43(c) and (e) display the topographies of the two species.

The spatial mapping (Fig. 43(d) and (f)) of the resonance found on these species allows for a localization of the cobalt atoms and the corresponding spin centers on the complex with atomic precision.

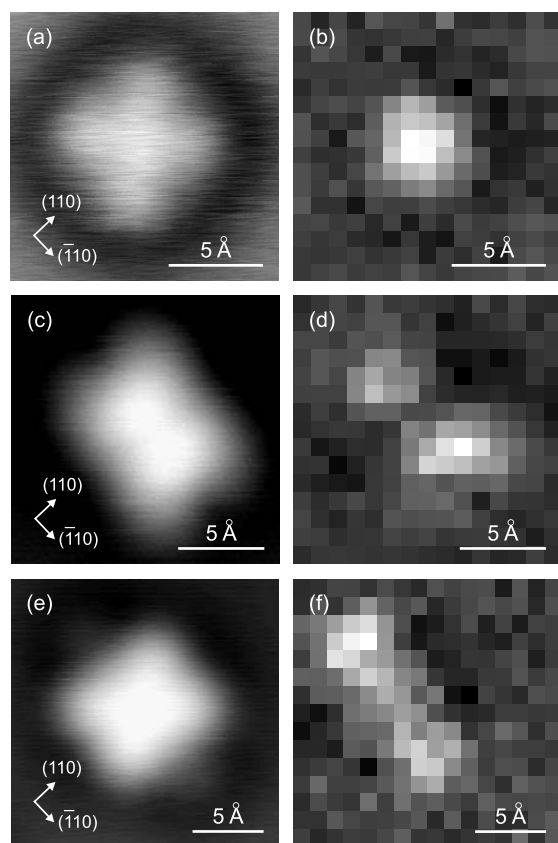


Figure 43: (a) Topography and (b) simultaneously acquired Kondo map of a cobalt tetracarbonyl molecule. (c) and (d) show topography and Kondo map for $(\text{Co}(\text{CO})_2)_2$, (e) and (f) for $(\text{Co}(\text{CO})_3)_2$.

In conclusion, we have characterized the coupling of magnetic complexes at surfaces by exploiting the Kondo effect. We have shown how the coupling of an individual spin to the substrate can be tuned by attaching ligands to a cobalt adatom thereby increasing the coupling of the spin to the substrate's conduction electrons. Thus it becomes possible to control the balance between magnetic coupling among neighboring spins and screening of the spin by the substrate's conduction electrons. Moreover, the combination of spectral and spatial resolution of STM enables to localize the spin center with an unprecedented resolution. This method can serve as a powerful technique to study the coupling of spin centers in magnetic molecules in contact to metallic substrates and even interactions between magnetic molecules.

-
- [1] Wahl, P., L. Diekhöner, G. Wittich, L. Vitali, M.A. Schneider and K. Kern. *Physical Review Letters* **95**, 166601 (2005).
 - [2] Wahl, P., L. Diekhöner, M.A. Schneider, L. Vitali, G. Wittich and K. Kern. *Physical Review Letters* **93**, 176603 (2004).
 - [3] Kondo, J. *Physical Review* **169**, 437-440 (1968).
 - [4] Schrieffer, J.R. and P.A. Wolff. *Physical Review* **149**, 491-492 (1966).
 - [5] Blyholder, G. *Journal of Physical Chemistry* **68**, 2772-2778 (1964).

Giant spin-splitting in the Bi/Ag(111) surface alloy

C.R. Ast, P. Wahl, G. Wittich, R. Vogelgesang and K. Kern;
D. Pacilé, M. Falub, L. Moreschini, M. Papagno and M. Grioni (EPFL, Lausanne)

The spin-orbit interaction is a relativistic effect which couples an electron's spin and orbital degrees of freedom. It becomes an important contribution to the electronic band structure of heavy elements, because it can drastically change the energy dispersion. In particular, it lifts the spin-degeneracies in environments where space inversion symmetry is broken, as is the case at surfaces. Spin split surface states of gold and bismuth can exhibit energy separations as large as 100 meV, exceeding typical values of semiconductors by an order of magnitude. To further enhance the effect at surfaces so far only the asymmetry has been exploited by depositing adatoms and changing the potential gradient. We show by angle-resolved photoemission spectroscopy (ARPES) that surface alloying is an attractive alternative that can result in a dramatically increased spin-splitting [1]. The two-dimensional Bi-Ag surface alloy, where each bismuth atom is surrounded by six silver atoms, shows an unprecedented energy band separation up to 935 meV. We also demon-

strate that the spin-splitting can be studied on a local scale by scanning tunneling spectroscopy (STS) through the associated strong divergence in the local density of states.

Clean surfaces of elemental metals show a trend of strong atomic spin-orbit coupling. It causes a large spin-splitting of their surface states (see Tab. 2), which can be further enhanced by the adsorption of adatoms. This is a promising path to create a new class of nanoscale structures where morphology and chemistry are used to tune the spin-splitting of interface states. Surface alloying, in particular, provides interesting opportunities as the adatoms *replace* substrate atoms of the topmost monolayer in their lattice sites. This changes the orbital hybridization within the layer and thereby creates a new two-dimensional electronic structure.

Figure 44(a) shows a topographic scan of the long-range ordered hexagonal Bi/Ag(111) surface alloy (5 Å lattice constant) taken with STM. Bright spots correspond to Bi atoms, each

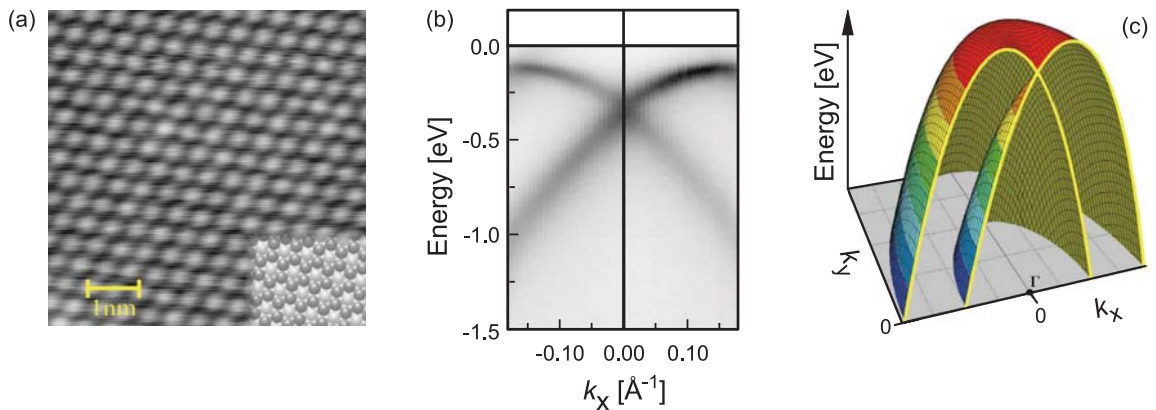


Figure 44: (a) Topography measured with STM of the long-range ordered $\sqrt{3} \times \sqrt{3}R30^\circ$ Bi/Ag(111) surface alloy (bias voltage: -3 mV; tunneling current: 1 nA). (b) ARPES band structure image near the $\bar{\Gamma}$ -point, i.e. the center of the surface Brillouin zone and for $k_y = 0 \text{ \AA}^{-1}$. It shows the spin-split bands of the Bi/Ag(111) surface alloy. The intensity scale is linear with dark areas corresponding to the highest intensity. (c) Calculated dispersion near the $\bar{\Gamma}$ -point.

of which is surrounded by six Ag atoms, as indicated by the model in the inset. The corresponding band structure measured by ARPES near the $\bar{\Gamma}$ -point at the center of the surface Brillouin zone (SBZ) (Fig. 44(b)) shows two identical and nearly parabolic bands with negative effective mass. They replace the nearly free electron-like surface states of the bare Ag(111) surface and accommodate the p -electrons donated by the Bi atoms. Their maxima are shifted to the left and right of $\bar{\Gamma}$ by an amount $k_0 = 0.13 \text{ \AA}^{-1}$ at 77 K. The observation of two symmetrically offset bands is, as for the surface state of the clean Au(111) surface, a clear indication of spin-orbit induced spin-splitting.

These observations can be qualitatively understood on the basis of a simple nearly free electron model. The Hamiltonian describing the spin-orbit coupling at the surface is linear in momentum with a proportionality constant called the Rashba parameter α_R . The resulting energy dispersion is:

$$E(\vec{k}_{\parallel}) = \frac{\hbar^2}{2m^*} (k_{\parallel} - k_0)^2 + E_0. \quad (11)$$

Here m^* is the effective mass and k_0 is the offset by which the parabola is shifted away from $\bar{\Gamma}$. This offset is a function of α_R . E_0 is an offset in energy. The energy dispersion is rotationally symmetric as can be seen in Fig. 44(c).

Figure 45(a)–(d) shows theory and experiment in comparison. Two regions can be identified in the data, which differ in the behavior of the density of states (DOS). The DOS is constant in region II like in the two-dimensional free electron model without spin-orbit splitting (Fig. 45(b)). In region I, it follows a $1/\sqrt{E}$ -behavior reminiscent of the van Hove singularity in one-dimensional models. This singularity can be measured in the dI/dV spectrum using STS (Fig. 45(d), green dots). It is proportional to the local density of states (LDOS) of the sample and enables the study of spin-splitting on the local scale. The model compares well with the data (see fitted red line in Fig. 45(d)) when taking the experimental broadening into account.

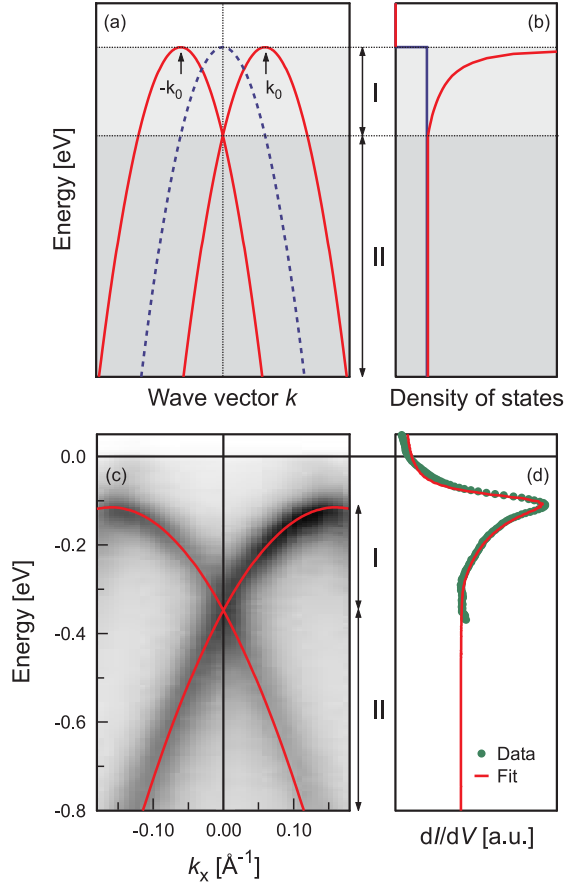


Figure 45: Direct comparison of theory and experiment: (a) Calculated energy dispersion in the nearly free electron model with (red lines) and without (blue dashed line) spin-orbit coupling. (b) The corresponding density of states. (c) ARPES map of the band dispersion (red line as a guide to the eye). (d) Local density of states measured with STS (green dots) with a fit from the nearly free electron model (red line).

It is interesting to note that in the present system the high-Z element is the dopant at the surface. Moreover, neither clean Ag(111) ($k_0 = 0.004 \text{ \AA}^{-1}$) [3] nor the pristine Bi(111) surfaces ($k_0 \approx 0.05 \text{ \AA}^{-1}$) [6] exhibit such a strong spin splitting effect. The Rashba parameter for the Bi/Ag(111) alloy is with 3.2 eV\AA about one order of magnitude larger than what would be expected from the virtual crystal approximation for a Bi-Ag alloy (see Tab. 2) [4]. We conclude that the silver substrate plays only a subordinate role in determining the Rashba parameter for the alloy. We propose that

the strong enhancement of the spin splitting is a result of the dilution of the high-Z element Bi, which gives rise to a reduced orbital hybridization.

Table 2: Selected materials and parameters characterizing the spin splitting: Typical energy separation between split states ΔE , momentum offset k_0 , and Rashba parameter α_R .

Material	ΔE [meV]	k_0 [Å ⁻¹]	α_R [eVÅ]	Ref.
InGaAs/InAlAs	5	0.028	0.07	[2]
Ag(111) Surface State	2	0.004	0.03	[3],[4]
Au(111) Surface State	110	0.01	0.66	[4],[5]
Bi(111) Surface State	≈ 100	≈ 0.05	1.07	[6]
Bi/Ag(111) Surface Alloy	935	0.13	3.2	this work

The giant spin-splitting observed in the Bi/Ag(111) surface alloy is not a unique phenomenon particular to this combination of materials, but rather a property of a new class of materials. In particular, experiments on the Pb/Ag(111) surface alloy have shown an almost equally large spin-splitting with the band maximum in the unoccupied states. This suggests that a tuning of the Fermi level across the spin-split bands may be achieved by doping the

bismuth/silver alloy with lead atoms. This may offer an ideal playground to test fundamental ideas.

On a broader perspective, this work suggests that surface alloys can be tailored for specific applications. Spin-split bands in a surface alloy on a semiconductor substrate may offer exciting perspectives in spintronics. Applying the spin-splitting parameters of the bismuth/silver alloy to the problem of the spin transistor, we find for the spin precession that a phase difference of $\Delta\theta = \pi$ is reached after a distance of $L = \Delta\theta/k_0 = 2.6$ nm, which is about two orders of magnitude smaller than for a semiconductor.

-
- [1] Ast, C.R., D. Pacilé, M. Falub, L. Moreschini, M. Papagno, G. Wittich, P. Wahl, R. Vogelgesang, M. Grioni and K. Kern. cond-mat/0509509 for more details.
 - [2] Nitta, J., T. Akazaki, H. Takayanagi and T. Enoki. Physical Review Letters **78**, 1335-1338 (1997).
 - [3] Popović, D., F. Reinert, S. Hüfner, V.G. Grigoryan, M. Springborg, H. Cercellier, Y. Fagot-Revurat, B. Kierren and D. Malterre. Physical Review B **72**, 045419 (2005).
 - [4] Cercellier, H., Y. Fagot-Revurat, B. Kierren, F. Reinert, D. Popovi and D. Malterre. Physical Review B **70**, 193412 (2004).
 - [5] LaShell, S., B.A. McDougall and E. Jensen. Physical Review Letters **77**, 3419-3422 (1996).
 - [6] Koroteev, Y.M., G. Bihlmayer, J.E. Gayone, E.V. Chulkov, S. Blügel, P.M. Echenique and Ph. Hofmann. Physical Review Letters **93**, 046403 (2004).

Spin and charge dynamics in Na_xCoO_2

S.P. Bayrakci, C. Bernhard, A. Boris, N.N. Kovaleva, G. Khaliullin, A. Pimenov, L. Yu, D.P. Chen, C.T. Lin and B. Keimer; P. Bourges, I. Mirebeau and Y. Sidis (CEA Saclay, France); J. Mesot (PSI Villigen, Switzerland); M. Enderle (ILL Grenoble, France)

The cobaltate $\text{Na}_x\text{CoO}_2 \cdot y\text{H}_2\text{O}$ has recently enjoyed intense attention. The composition with $x \approx 0.30$, $y \approx 1.4$ has been shown to be superconducting over a narrow range of x , with a maximum transition temperature $T_c \approx 5$ K. This compound is particularly interesting because its structure is similar to that of the high- T_c copper oxide superconductors. In both materials, superconducting sheets containing oxygen and a spin-1/2 transition metal are separated by layers of lower conductivity in an anisotropic crystal structure. However, a number of characteristics suggest that the superconductivity in this compound may be unusual in different ways from what is found in the cuprates. For example, some experiments indicate that the symmetry of the Cooper pair wavefunction may be p -wave.

The unhydrated parent compound Na_xCoO_2 is interesting in its own right because of its exceptionally high thermopower over the range $0.5 \leq x \leq 0.9$, which, uncommonly, accompanies low resistivity and low thermal conductivity. The thermopower was found to exhibit an unusually large magnetic field dependence. Moreover, early susceptibility and μSR experiments indicated the presence of a magnetically ordered phase in the phase diagram of $\text{Na}_x\text{CoO}_2 \cdot y\text{H}_2\text{O}$. These findings suggest that coupling between spin and charge excitations may play an important role in determining the macroscopic properties of these materials, again in analogy to the copper oxides. In order to provide microscopic insight into these interactions, we have carried out neutron scattering and infrared spectroscopy experiments.

Neutron scattering was used to determine the spin structure and dynamics in the magnetically ordered phase of unhydrated $\text{Na}_{0.8}\text{CoO}_2$

below $T_N = 20$ K [1]. The magnetic structure is that of an A-type antiferromagnet, namely, antiferromagnetically coupled ferromagnetic layers (inset in Fig. 46). Surprisingly, inelastic magnetic neutron scattering data revealed that the antiferromagnetic interlayer exchange constant is almost as large as the intralayer ferromagnetic exchange, despite the layered lattice structure (Fig. 46). This observation implies that the unhydrated material is magnetically three-dimensional, and that water intercalation is required to generate a two-dimensional spin Hamiltonian. This specifies one important role for the hydration procedure, which has thus far remained elusive.

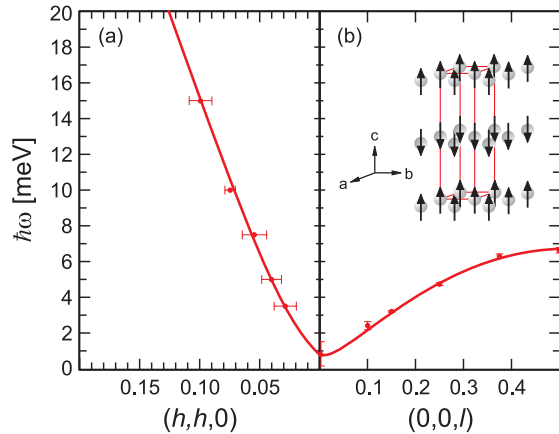


Figure 46: Spin wave dispersions of $\text{Na}_{0.8}\text{CoO}_2$ (a) parallel and (b) perpendicular to the CoO_2 layers. The in-plane dispersion is steeper, but because of the larger number of nearest neighbors in the plane, the magnitudes of in-plane and out-of-plane exchange parameters are comparable. The inset displays the antiferromagnetic ordering pattern.

The microscopic origin of the surprisingly large ratio of inter- and intralayer exchange constants is still under debate. A possible origin of our observation is an in-plane charge-ordered superstructure.

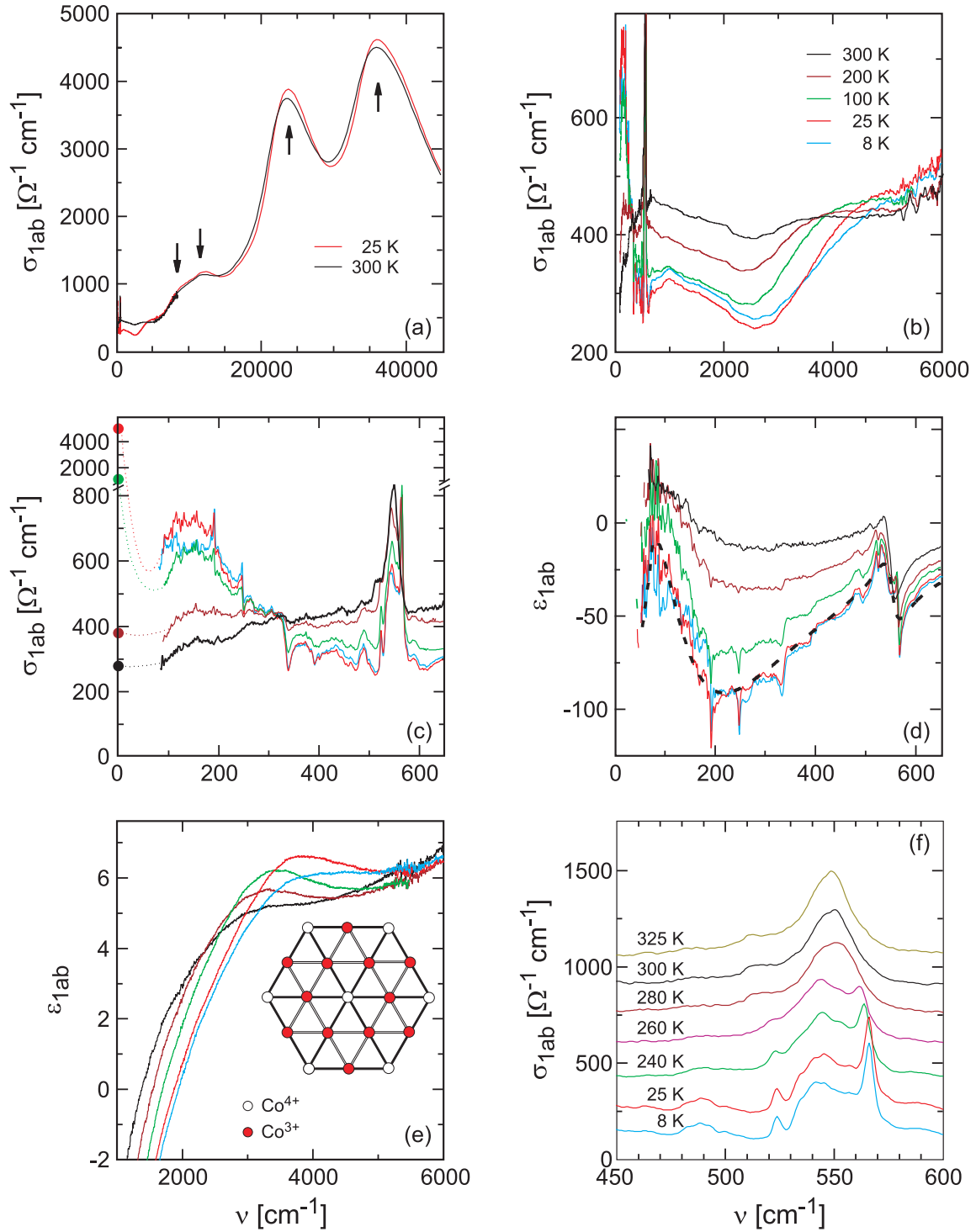


Figure 47: In-plane dielectric properties of $\text{Na}_{0.8}\text{CoO}_2$ in terms of the real parts of the optical conductivity, σ_{1ab} , and the dielectric function, ϵ_{1ab} . dc values of σ_{1ab} are shown by solid circles, low-frequency extrapolations by dotted lines. Corresponding spectra of ϵ_{1ab} are shown in (d) and (e). The arrows in panel (a) mark interband transitions. The black dotted line in panel (d) shows a Drude-Lorentz fit at 25 K. The inset of panel (e) gives a sketch of the suggested charge ordering pattern.

If all of the Co ions are in low-spin local-moment states (that is, $S=1/2$ for Co^{4+} and $S=0$ for Co^{3+}), then for $x=0.82$ the spin lattice is dilute, with only 18% of the Co sites occupied by $S=1/2$ spins. One possible arrangement of these spins, achievable exactly for $x=0.75$, is that of a triangular lattice with lattice constant $2a$ (where a is the Co–Co distance in the CoO_2 planes; inset in Fig. 47(e)). Since this is comparable to the out-of-plane Co–Co distance, isotropic spin wave dispersions would be a natural consequence.

A parallel series of infrared ellipsometry experiments provides complementary evidence of charge ordering [2]. Figure 47 displays the in-plane dielectric properties of $\text{Na}_{0.8}\text{CoO}_2$ between 8 K and 300 K in terms of the real part of the optical conductivity, $\sigma_{\text{lab}} = 1/4\pi \cdot \nu \cdot \epsilon_{2\text{ab}}$, and the dielectric function, ϵ_{lab} . Figure 47(a) shows σ_{lab} for the full range from 80 to $44,000 \text{ cm}^{-1}$ at 25 and 300 K. The solid arrows mark four bands corresponding to interband transitions. Based on band structure calculations, we assign the two lower bands to transitions between Co $3d$ derived bands and the stronger high frequency ones to charge transfer transitions between O- $2p$ and Co- $3d$ bands.

Figures 47(b)–(e) detail the range below these interband transitions. First we concentrate on the spectra at $T > T_N = 20 \text{ K}$. At 300 K the spectral shape of σ_{lab} is characteristic of an incoherent transport mechanism. Whereas it is almost constant between 600 and 6000 cm^{-1} (Fig. 47(b)), σ_{lab} decreases below 600 cm^{-1} and extrapolates well towards the dc -value (black solid circle in Fig. 47(c)). Below 300 K the optical spectra undergo marked changes. With decreasing T a partial gap, a so-called pseudogap (PG), develops which gives rise to a progressive decrease of σ_{lab} between 300 and 4500 cm^{-1} (Fig. 47(b)). Its onset is marked by an absorption band at higher energies, which most likely corresponds to charge excitations across the PG rather than to a conventional interband transition. At 300 K this band is still fairly weak and broad, whereas at lower

T it sharpens, gains additional spectral weight, and exhibits a sizeable blue-shift from about 3500 cm^{-1} at 300 K to 4500 cm^{-1} at 25 K. We argue below that they originate from a partially charge ordered state and the excitations thereof. A precursor of the PG and the absorption band is still evident at 300 K indicating that short range charge ordered clusters persist at higher T .

As detailed in Figs. 47(c) and (d), the PG formation is accompanied by the growth of two distinct low-frequency electronic bands. The band near 150 cm^{-1} develops concomitantly with the PG. The simultaneous appearance of several anomalous phonon modes (Fig. 47(f)) suggests that this low-frequency electronic excitation is strongly coupled to IR-active lattice vibrations. It is hence indicative of a polaronic mode. The substantial spectral weight shift at T_N further suggests a strong coupling to spin excitations. In addition, we identify a very narrow Drude-like band at the origin which accounts for the metallic T -dependence of the dc -conductivity.

In an attempt to interpret the unusual optical response of $\text{Na}_{0.82}\text{CoO}_2$, we note that strong polaronic features are well-known in the related compound $\text{La}_{1-y}\text{Sr}_y\text{CoO}_3$. There it was suggested that a charge-induced spin-state transition of the Co^{3+} ions takes place, which gives rise to a sizeable spin-charge coupling. The underlying idea is that a localized positive charge of a Co^{4+} ion and a subsequent displacement of the neighboring oxygens towards Co^{4+} lowers the local symmetry of the adjacent Co^{3+} ions, thus inducing a transition from a low-spin (LS, $S=0$) to an intermediate-spin state (IS, $S=1$).

As noted above, a perfect triangular Wigner lattice of Co^{4+} ions could be realized at quarter filling, i.e. for $x=0.75$, as sketched in the inset of Fig. 47(e). In this state, the Co^{3+} sites are arranged on a Kagomé lattice, and their IS state can be stabilized due to the axial crystal field originating from the two neighboring Co^{4+} ions. This scenario accounts for the PG in terms of an incomplete charge excitation gap. The large frequency scale of the PG of about

4500 cm⁻¹ is explained by the gain in Hund coupling, J_H , associated with the LS to IS transition. It also provides a strong spin-charge coupling and therefore naturally explains the large magneto-polaronic effects that occur in the anti-ferromagnetic state.

In conclusion, both neutron scattering and infrared spectroscopy experiments provide evidence of strong spin-charge coupling in the layered cobaltates. The influence of this interaction on the macroscopic properties and phase

behavior of these materials, including in particular the unconventional superconducting state, is an interesting subject of further investigation.

-
- [1] Bayrakci, S.P., I. Mirebeau, P. Bourges, Y. Sidis, M. Enderle, J. Mesot, D.P. Chen, C.T. Lin and B. Keimer. *Physical Review Letters* **94**, 157205 (2005).
 - [2] Bernhard, C., A.V. Boris, N.N. Kovaleva, G. Khaliullin, A.V. Pimenov, L. Yu, D.P. Chen, C.T. Lin and B. Keimer. *Physical Review Letters* **93**, 167003 (2004).

Hard ferromagnetism in 2D FePt surface alloys

J. Honolka, T.Y. Lee, K. Kuhnke, A. Enders and K. Kern;
K. Fauth, M. Heßler and G. Schütz (Max-Planck-Institut für Metallforschung)

The rapidly increasing information density in magnetic storage media during the last decades is an achievement of the successful down-scaling of bit structures into the sub-micrometer regime. Since a few years, physics has set off to study the regime of miniaturization where the limits of magnetic storage are reached. The goal is to push forward to magnetic properties of nanostructures with a countable number of atoms [1]. Smallness is, however, not the only goal. Equally important is the stability of the magnetization with respect to heat and other external factors that may lead to erasure of magnetically stored information. One group of materials studied by industry and applied physics research groups are alloys containing two elements, one ferromagnetic, like Co and Fe and the other nonmagnetic, like Pt. In fact, such alloys have favorable properties: In contrast to what one might expect, the nonmagnetic Pt stabilizes the magnetism of Fe or Co instead of reducing it. This effect is especially pronounced in FePt systems with $L1_0$ structure where high magnetic fields of several Tesla are needed to flip the magnetization. The significant magnitude of these so-called coercive fields reflects the considerable magnetic anisotropy present in these systems.

So far FePt alloys have only been studied in the bulk phase or as larger clusters on surfaces. Their magnetic properties are highly sensitive to changes in the crystal structure as well as the degree of disorder. Although there has been a lot of theoretical effort to understand the reasons behind their special magnetic properties the mechanisms are still under debate. By preparing defined nanostructured alloys on surfaces we were able to show the importance of a well-concerted Fe-Pt coordination for stabilizing their magnetization.

A vicinal Pt(997) substrate was used to prepare two-dimensional FePt systems. The high regularity of its periodically stepped surface (step-step distance 2 nm) is well-established and makes them natural nanotemplates for the growth of 1D magnetic nanostructures [2]. The growth mode of Fe evaporated on Pt(997) has been characterized by thermal energy He scattering experiments. Below 450 K a pure Fe adlayer grows initially by step decoration, followed by step flow growth resulting in Fe stripes at sub-monolayer (ML) coverage. Between 500 K and 550 K a FePt surface alloy is formed by intermixing of Fe with the topmost

Pt layer only. Above 600 K Fe atoms efficiently diffuse into the Pt bulk. Various well-defined Fe nanostructures can thus be formed by controlling coverage and substrate temperature. Of particular interest in this paper is the $\text{Fe}_{50}\text{Pt}_{50}$ surface alloy obtained by deposition of 0.5 ML Fe at 525 K. The idealized alloy structure of monoatomic Fe chains embedded in the Pt substrate, as sketched in Fig. 48, is concluded from the scattering experiments and from the comparison to the alloy formation of Fe on Pt(111) [3].

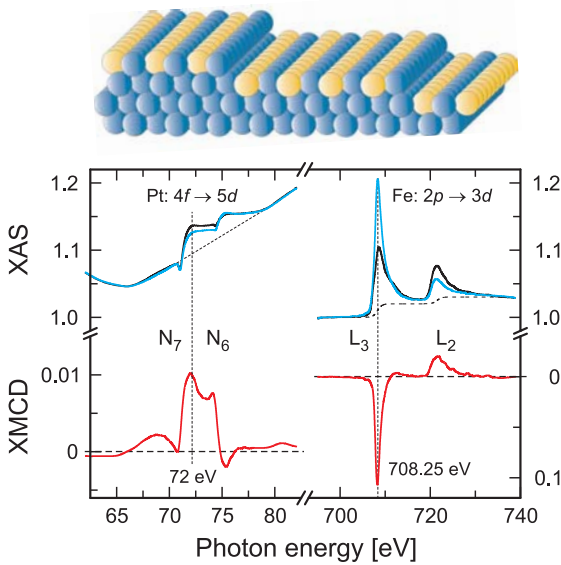


Figure 48: top: Idealized structure of the $\text{Fe}_{50}\text{Pt}_{50}$ surface alloy obtained by deposition of 0.5 ML Fe (yellow balls) at 525 K. bottom: X-ray absorption spectra of the 0.5 ML FePt alloy at the Pt $N_{7,6}$ edges (left) and at the Fe $L_{3,2}$ edges (right). The difference between the total XAS for opposite magnetization (blue and black traces) yields the XMCD spectra (red traces).

We remark that for the real structure entropy leads to a reduced chain length with deviations from perfectly parallel alignment. Alternatively to the alloy, 1 nm wide Fe stripes covering one half of the substrate terraces can be prepared by deposition of 0.5 ML at 350 K. The in situ magnetic characterization of the FePt surface alloys was done using the X-ray magnetic circular dichroism (XMCD) (the experiments were performed at BESSY II) technique at a fixed

sample temperature of $T = (12 \pm 1)$ K. From the difference between absorption spectra (XAS) of circularly polarized light parallel and antiparallel to the sample magnetization \mathbf{M} the magnetic moments per atom can be determined. The magnetization \mathbf{M} is switched by applying a magnetic field parallel and antiparallel to the photon beam.

Figure 48 shows examples of XAS spectra obtained for \mathbf{M} parallel and antiparallel to the photon beam. The XAS measurements were done at the Fe $2p-3d$ and Pt $4f-5d$ absorption lines to gain magnetic information for Fe and Pt separately. A strong XMCD signal is not only observed in the magnetic Fe but also in the Pt absorption lines which reveals a large induced magnetic moment in the Pt. The Pt-moment is due to the strong hybridization between Fe $3d$ and Pt $5d$ states, as will be discussed later. The dichroism of the Fe L_3 and the Pt N_7 absorption edges has been exploited to obtain element-specific magnetization loops. The photon energy was kept constant at the corresponding peak energies, identified in Fig. 48, while the field was ramped between ± 2.5 T.

For magnetic fields along the surface normal a nearly square shaped hard ferromagnet hysteresis loop is found. Angular-dependent measurements show that the preferred magnetic orientation – also called the magnetic easy axis – is in the perpendicular direction. The large coercive field $H_c = 0.71$ T of the 2D alloy is of the same order of magnitude as the ones found in the bulk FePt L_{10} phase and demonstrates the presence of a considerable anisotropy energy barrier which must be overcome in order to reverse the magnetization. In the saturated state the total magnetic moment per Fe-atom adds up to $(2.9 \pm 0.2)\mu_B$. The total moment consists of the orbital and spin contributions. If one tries to magnetize the sample 70° away from the easy axis the loops lose their square shape (blue and red curves in Fig. 49 measured along and perpendicular to the substrate steps). The coercivities for the two 70° measurements slightly differ and reflect the reduced symmetry on the vicinal substrate. Magnetization loops of Pt shown in

the bottom panel of Fig. 49 were recorded in the same geometry as for Fe in the top panel. The Pt hysteresis loops are congruent with those of Fe and it can be shown that the Fe and Pt magnetic moments are aligned parallel. Moreover, the relative size of the XMCD signal at the Pt N_7 edge suggests that the induced moment of Pt within the alloy layer is significantly larger than for example in bulk CoPt_3 . For the latter, a Pt moment of $0.26 \mu_B/\text{atom}$ was determined from neutron scattering [4].

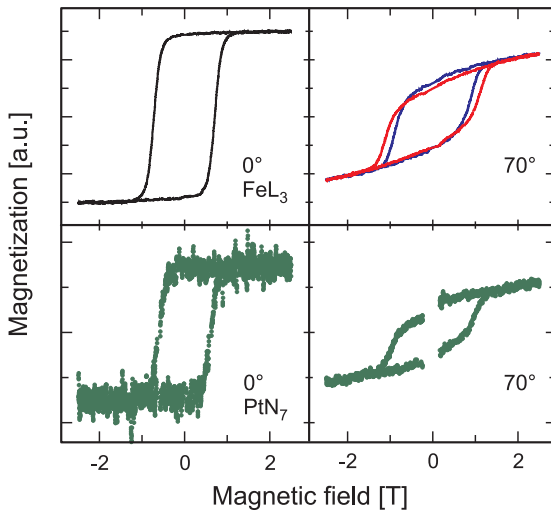


Figure 49: top: Hysteresis curves of the $\text{Fe}_{50}\text{Pt}_{50}$ alloy taken at the Fe L_3 -edge at an angle of 0° and 70° with respect to the surface normal. The two Fe-spectra for 70° correspond to measurements parallel (blue) and perpendicular (red) to the substrate steps. bottom: Corresponding measurements for the same samples and geometry as in (a) but at the Pt N_7 -edge. The photon energies on which the magnetization loops are measured for Fe and Pt are marked by vertical dotted lines in Fig. 48.

It can be concluded from the magnetic behavior of the $\text{Fe}_{50}\text{Pt}_{50}$ surface alloy that a 3D L_{10} structure is not required for the existence of high-magnetic anisotropies in FePt systems. To gain a better understanding of magnetism in FePt nanostructures we have studied two additional systems with different Fe-Pt coordination. In Fig. 50 the perpendicular magnetization curve of the $\text{Fe}_{50}\text{Pt}_{50}$ surface alloy (a) is compared with loops of a surface alloy layer formed of only 0.35 ML Fe at 525 K (b), and

nonalloyed Fe stripes of 4 atoms width formed of 0.5 ML Fe at 350 K (c). The data in Fig. 50(b) show clearly that a dilution of the Fe concentration in the surface alloy by 30% significantly alters the shape of the magnetization curve: Instead of the square loop of the $\text{Fe}_{50}\text{Pt}_{50}$ alloy, S-shaped hysteresis loops with the remanence reduced by 78% and the coercivity reduced by 68% are found. A field of 2.5 T is still insufficient to saturate the magnetization. The overall shape of the loop (b) is very similar to the magnetization curve of the nonalloyed Fe stripes of 0.5 ML Fe (c). Full alignment of the magnetic moments of the stripes is achieved only for external fields of $H > 6$ T.

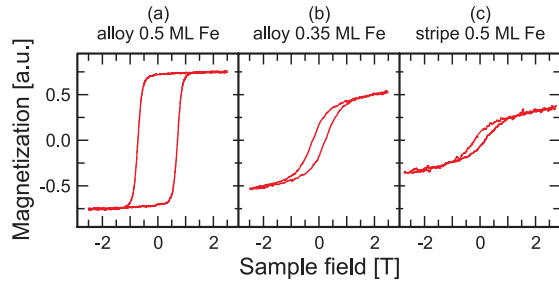


Figure 50: Hysteresis loops perpendicular to the surface at the Fe L_3 edge (a) of the FePt alloy prepared with 0.5 ML Fe, (b) an alloy prepared with 30% less Fe, and (c) a non-alloyed Fe-stripe with 0.5 ML Fe. All three samples exhibit a magnetic easy direction perpendicular to the surface. Remanence and coercive field are significantly increased when compared with the optimum 0.5 ML FePt surface alloy.

What makes the coercivity of the $\text{Fe}_{50}\text{Pt}_{50}$ surface alloy large? One main difference between the Fe stripe and the 2D FePt alloy is that the latter shows a much stronger tendency towards magnetic ordering. Only for the $\text{Fe}_{50}\text{Pt}_{50}$ surface alloy the saturation magnetization is fully maintained in remanence. We ascribe this fact to a strong indirect exchange interaction between adjacent Fe chains by polarization of surrounding Pt atoms, which stabilizes the magnetization. However, to gain hard magnetic properties a strong exchange mechanism is necessary but not sufficient. In addition a high-magnetic anisotropy is needed to increase the coercivity and prevent domain wall nucleation.

We assign the high anisotropy to the splitting of strongly hybridized $3d$ and $5d$ band states in the presence of the large spin-orbit coupling energy of Pt, $\xi_{\text{Pt}} = 0.6$ eV (compare to Fe, $\xi_{\text{Fe}} \approx 0.08$ eV). This hybridization effect is expected to be also present in the case of $\text{Fe}_{35}\text{Pt}_{65}$ alloy. However, it seems that here, due to the increased average distance between Fe atoms, the indirect exchange coupling between Fe atoms is weakened, which destroys the hard magnetic properties of the system.

The key result of this work is the identification of the role of Pt for the hard magnetic properties of FePt alloys, such as high-magnetic anisotropy and large coercive field: Pt mediates the indirect exchange interaction between Fe

atoms which is crucial for stabilizing the magnetization of the 2D alloy. At the same time Pt provides the high spin-orbit coupling constant needed to push the coercive fields to high values.

-
- [1] Gambardella, P., S. Rusponi, M. Veronese, S.S. Dhesi, C. Grazioli, A. Dallmeyer, I. Cabria, R. Zeller, P.H. Dederichs, K. Kern, C. Carbone and H. Brune. *Science* **300**, 1130-1133 (2003).
 - [2] Gambardella, P., A. Dallmeyer, K. Maiti, M.C. Malagoli, W. Eberhardt, K. Kern and C. Carbone. *Nature* **416**, 301-304 (2002).
 - [3] Schmid, M. and P. Varga. In: *The Chemical Physics of Solid Surfaces* **10**, 118-151 (2002). D.P. Woodruff (Ed.), Elsevier.
 - [4] Menzinger, F. and A. Paoletti. *Physical Review* **143**, 365-372 (1966).

Quasiparticle injection into YBCO thin films – does spin matter ?

H.-U. Habermeier, S. Soltan, J. Albrecht and G. Cristiani

Non-equilibrium effects in cuprate superconductors e.g. arising from spin-polarized quasiparticle injection by ferromagnetic electrodes into the superconductor or other metals with strong electron correlation have generated much interest during the past few years. These activities are nurtured from attempts to understand spin-dependent transport properties in such systems as well as the correlated spin dynamics. Eventually, novel concepts for three-terminal devices can emerge from these activities. Furthermore, it has been suggested that injection of spin-polarized quasiparticles (SPQs) can shed some light on fundamental properties of cuprate superconductors such as spin-charge separation [1] and the superconducting mechanism itself [2]. In a review, however, published by Gim *et al.* [3] the studies available till 2001 have been carefully analyzed and it has been argued that ‘all spin injection experiments to date can be explained by ordinary (unpolarized) quasiparticle injection or simple current summation’. The conclusion was, that spin-related ef-

fects are either nonexistent or negligibly small. Subsequently, only a few papers dealing with spin injection into YBCO thin films appeared and claimed spin related effects of marginal size only.

In this contribution we re-examine this view using an improved sample design to probe the spin effect on the change of the resistive superconducting transition temperature upon SPQ injection into $\text{YBa}_2\text{Cu}_3\text{O}_{7-x}$ (YBCO) thin films. This work serves as a case study for other experiments. Appropriate $\text{La}_{2/3}\text{Ca}_{1/3}\text{MnO}_3$ (LCMO) electrodes are applied with a theoretically 100% spin-polarization below their Curie temperature of ≈ 270 K.

First, a brief description of the theoretical background is given, based on current concepts to describe nonequilibrium phenomena in superconductors in general, then the sample design is described and the experimental results are analyzed in view of the theory.

Since the 1970's nonequilibrium superconductivity has been studied with the focus on spin-degenerate QP injection and photon-induced Cooper-pair breaking associated with QP redistribution/recombination in both, conventional and cuprate superconductors. Quasiparticle injection (spin degenerate as well as spin-polarized) causes an excess QP density, weakens the pairing interaction and thus reduces the gap energy, Δ_k . For the quantification two models have been developed describing the nonequilibrium situation as a modification of the gap energy. They start from the usual BCS gap equation

$$\Delta_k = \sum_{k'} V_{kk'} \Delta_{k'} / 2E_{k'} [1 - f_{\uparrow}(E_{k'}) - f_{\downarrow}(E_{k'})] \quad (12)$$

with $E_k = (\epsilon_k^2 + \Delta_k^2)^{1/2}$ and $f_{\sigma}(E_k)$ being the spin-dependent QP distribution functions (σ being either \uparrow or \downarrow) and ϵ_k the dispersion of the electrons in the normal state. The distribution functions are parameterized in a perturbative ansatz by the introduction of an extra chemical potential, μ_G^* , and a modified temperature T^* to account for the increased number of excess quasiparticles beyond the thermal equilibrium population: $f_{\sigma}(E) = [1 + \exp(E - \mu_G^*) / k_B T^*]^{-1}$.

In the approximation of Owen and Scalapino the nonequilibrium situation is treated by the modified chemical potential μ_G^* only to fulfill the additional constraint that the number of excess QPs is much smaller than the total number of electrons. This approach is realized when the QPs thermalize with low energy phonons more frequently compared to recombination into pairs. In this limit, the QPs are in steady state at T but have an excess number giving rise to μ_G^* . Assuming complete spin polarization of the charges in the ferromagnet, Bhattacharjee and Sardar [2] expanded the Owen-Scalapino model by introducing a different μ_G^* for the spin-up QPs only, and solved the corresponding gap equation for s - and d -wave symmetry of the order parameter. The results reveal a stronger gap reduction for the SPQ versus ordinary QP injection in both cases as well as much stronger effects in the case of anisotropic

s -wave and d -wave compared to s -wave symmetry for the same amount of QP injection.

Alternatively, if recombination is more likely than thermalization, the recombining pairs emit phonons with the energy $\omega > 2\Delta$ causing an effective temperature $T^* > T$. The steady state distribution of the QP's is regarded as equilibrium, however, with $T = T^*$. Based on this concept, the reduced gap $\Delta(n_{QP})$ is determined by $\Delta(n_{QP}) = \Delta(0) - n_{QP} / 2N(0)$ with n_{QP} being the density of excess QPs and $N(0)$ the density of states at $T = 0$ K. The excess QP density n_{QP} is related to the injected QP flux, I_{ini} / e , the thickness of the perturbed region, t , and the effective relaxation time τ_{eff} by $n_{QP} = I_{ini} \tau_{eff} / e t$. Gim *et al.* [3] treated this concept quantitatively drawing the following conclusions:

(i) QP injection in general causes a reduction of the superconducting gap with increasing injection current. This reduction is proportional to the effective relaxation time, τ_{eff} , according to $\delta\Delta / \Delta_{inj} = -\tau_{eff} / 2 e N(0) t$. The effective relaxation time is mainly governed by the QP relaxation time $\tau_R = \tau_0 [\Delta(T) / k T]^{1/2} \exp[\Delta(T) / k T]$ with τ_0 being a characteristic intrinsic relaxation time. With decreasing temperature the nonequilibrium effects are expected to be increasingly stronger due to the reduction of the density of thermal QPs.

(ii) SPQ injection changes the situation drastically due to the requirement of spin randomization before they can recombine into singlet Cooper-pairs. In a background with a low thermal QP density spin-flip scattering is required for the recombination and the effective recombination time is the sum of the spin-flip scattering time τ_{sf} and the charge relaxation time τ_R . According to these arguments, SPQ injection effects are expected to be large for $T \ll T_c$ and not to deviate from ordinary QP injection effects in the normal state in view of the large density of thermal QPs in the system for $T > T_c$. In conclusion, in both limiting cases a stronger reduction of the energy gap upon injection of SPQs compared to ordinary QPs is predicted.

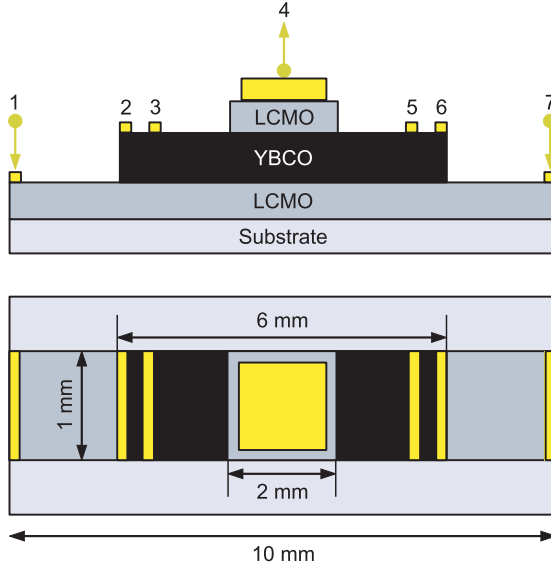


Figure 51: Sketch for the sample geometry chosen for the injection of spin-polarized quasiparticles (side view and top view).

It is obvious that SPQ- injection related changes of the transport properties are only experimentally accessible if the SPQs can cross the interface without appreciable spin-flip into a volume determined by the injection area and the spin diffusion length ($\approx 10\text{--}20\text{ nm}$). Consequently, we used for our experiments a sample design as depicted in Fig. 51. It is characterized by relatively large area injection electrodes (2 mm^2 on top) and a superconductor film embedded in between the sources for spin injection. These epitaxial heterostructures of $\text{YBa}_2\text{Cu}_3\text{O}_{7-x}$ and $\text{La}_{2/3}\text{Ca}_{1/3}\text{MnO}_3$ films are grown by pulsed laser deposition onto (100) oriented single crystal SrTiO_3 substrates. The thickness of the $\text{La}_{2/3}\text{Ca}_{1/3}\text{MnO}_3$ films is 50 nm and that of the $\text{YBa}_2\text{Cu}_3\text{O}_{7-x}$ in between is 100 nm. During deposition the substrate is kept at a constant temperature of 780°C , adjusted and controlled by a far infrared pyrometer. The oxygen pressure during film growth was 0.6 mbar for the YBCO and 0.4 mbar for the LCMO layers.

After deposition the films were in situ annealed at 530°C for 60 minutes in an oxygen pressure of 1 bar to ensure high crystalline quality, sharp interfaces and complete oxygenation. Room temperature X-ray analysis

revealed single-phase textured growth of the films and a slight tensile strain of 0.4% for the $\text{YBa}_2\text{Cu}_3\text{O}_{7-x}$. The Curie temperature of the bottom LCMO layer and the T_c of YBCO have been determined as 240 K and 64 K, respectively. Both are substantially reduced as compared to their bulk values (275 K for LCMO and 92 K for YBCO) due to electronic interface interactions based on the competing ordering mechanisms.

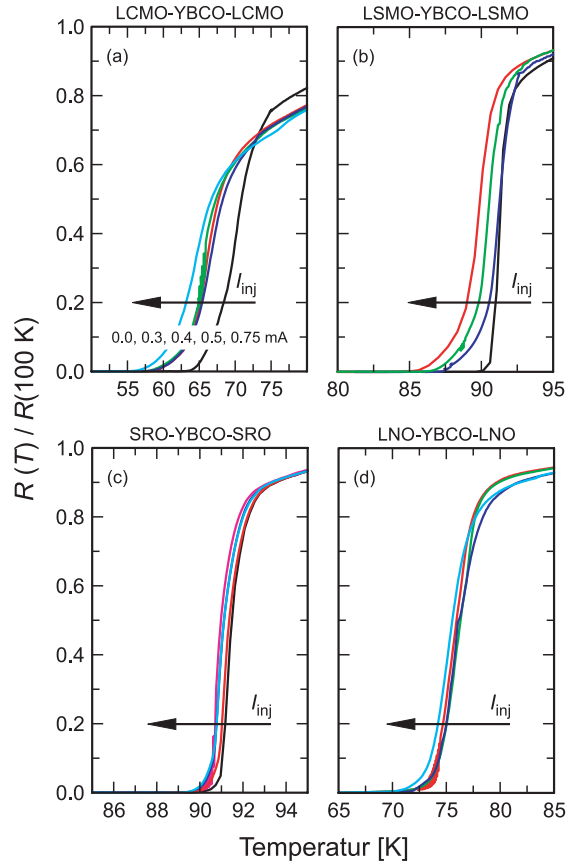


Figure 52: In-plane resistance as a function of temperature and injection current of YBCO normalized to the room temperature value for samples with electrodes of different degree of spin-polarization (a)–(d). The reduction of T_c is more pronounced for manganite electrodes as compared to paramagnetic metals (LaNiO_3) or weakly spin polarized metals (SrRuO_3).

For the spin-injection experiments we pass a current of 0.1 mA through the YBCO layer (contacts 2 and 6) and pick up the voltage via contacts 3 and 5. The injection current of $0 < I_{\text{inj}} < 1\text{ mA}$ is applied through the contacts

1,7 and 4. The ratio of the current densities is $< 10^{-3}$. The sample geometry chosen ensures a symmetric current path and the comparison of the current densities for the probing and injected current indicates the small perturbation of the system by current injection. Figure 52 shows the resistive transitions to superconductivity for 4 different specimens, 2 with highly spin-polarized electrodes (LCMO and LSMO) one with a weakly spin polarized (SrRuO_3) and one with a paramagnetic electrode (LaNiO_3) for current injection. It can clearly be seen that the spin-polarized current injection causes a much stronger reduction of T_c as compared to the two others.

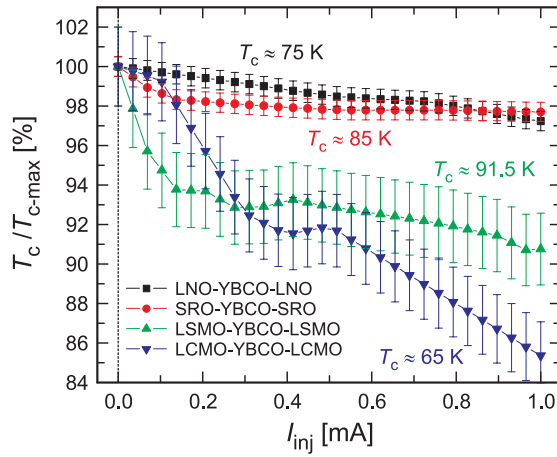


Figure 53: Normalized transition temperature $T_c/T_{c-\max}$ versus injection current taken from Fig. 52. The error bars correspond to the onset and offset of the transition, the symbols represent the midpoint.

More quantitatively, the relative T_c reduction is plotted in Fig. 53 for the 4 different specimens. The specimens with LaNiO_3 electrode show the smallest effect followed by the one with SrRuO_3 electrodes. Electrodes with a high spin polarization, however, show a reduction of T_c up to 14% for injection current densities of $5 \cdot 10^{-2} \text{ A/cm}^2$.

This result is the first direct experimental evidence for spin-polarized quasiparticle injection into cuprate superconductors. It is tempting to compare these results with the theoretical predictions of Bhattacharjee and Sardar for the momentum averaged gap values for both unpolarized and spin polarized quasiparticle injection as a function of QP overpopulation. Keeping the limitations of the model in mind, we find a surprising agreement. For an ordinary QP overpopulation causing a 2% gap reduction, theory claims a 13% reduction for the same overpopulation of SPQs. The experiment shows a T_c reduction of 15% for LCMO and 10% for LSMO. Further work on both theory and experiment will pave the way for a deeper understanding of nonequilibrium effects in cuprate superconductors.

- [1] Si, Q. *Physical Review Letters* **78**, 1767-1770 (1997).
- [2] Bhattacharjee, S. and M. Sardar. *Physical Review B* **62**, R6139-R6142 (2000).
- [3] Gim, Y., A.W. Kleinsasser and J.B. Barner. *Journal of Applied Physics* **90**, 4063-4077 (2001).

Transport of charge, mass and heat

The understanding of transport phenomena in solids is important from a fundamental point of view as well as for practical applications. The first contribution addresses charge transport reporting a careful study of the polarization dependence of microwave-induced zero resistance in two-dimensional electron systems. The absence of such a dependence contradicts available theoretical models. The next two reports demonstrate the drastic effects of space charge layers on electronic as well as ionic conductivity especially for nanostructured materials. Overlapping depletion layers in SrTiO₃ with grain sizes below 100 nm let the bulk response disappear in ac-conductivity measurements. In AgI nanoplates, which can be regarded as a nanometer-scaled heterostructure composed of the cubic and hexagonal AgI phase, space charge layers comprising the entire domains enhance the ionic conductivity hugely. The following contribution illustrates the close connection of mass transport from the gas phase into an oxide with the respective surface reaction rate, the mechanistic interpretation being far from trivial. The last report is a detailed study of the isotope effect on the heat capacities of diamond and ZnO. The results are in good agreement with *ab initio* calculations.

Polarization dependent study of the microwave induced zero-resistance in a two-dimensional electron system

J.H. Smet, B. Gorshunov and C. Jiang; L. Pfeiffer (Bell Laboratories);
V. Umansky (Weizmann Institute of Science); M. Dressel (Universität Stuttgart);
F. Kuchar (Montanuniversität Leoben); K. von Klitzing

Zero resistance is a common Hall mark of such fundamental phenomena as superconductivity and the quantum Hall effects. Recently, zero resistance was also discovered in a different and certainly surprising context. When a two-dimensional electron system is exposed to quasi-monochromatic microwave radiation and a minute perpendicular magnetic field, transport along the direction of current flow may proceed in a dissipationless fashion. An important prerequisite is that the sample is of exceptional purity. A dramatic example is illustrated in Fig. 54(a). The longitudinal dc-resistivity oscillates as a function of the ratio ω/ω_c , where ω is the microwave frequency and ω_c the cyclotron frequency. As the radiation intensity is enhanced, the amplitude of the oscillations in-

creases and the minimum resistance values saturate as they approach zero. Original photoconductivity experiments on lower quality samples only revealed the intuitively expected resistance increase due to resonant heating at the cyclotron resonance. A temperature-dependent study of the deepest resistance minima suggests activated transport, which is normally associated with the existence of a gap at the chemical potential. One might imagine that this exponential temperature dependence and the vanishing of the resistance indicate the formation of a new strongly correlated many-body quantum Hall state, but in fact the Hall resistivity behaves classically as expected at low magnetic fields and remains largely unaffected by the microwave radiation.

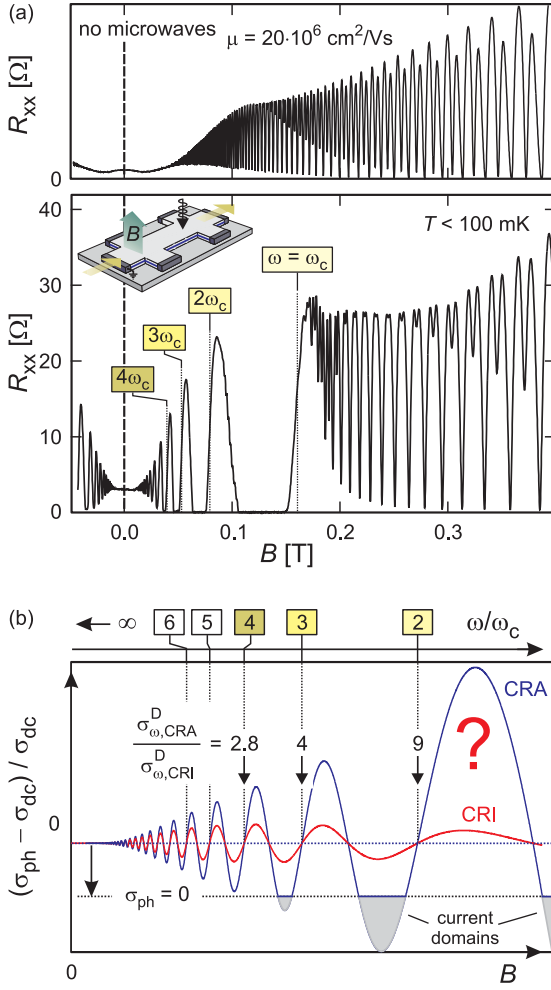


Figure 54: (a) DC-Magneto-resistance of a state-of-the-art two-dimensional electron system in the absence (top panel) and presence of 73 GHz microwave radiation (bottom panel). (b) Predicted oscillations in the magnetoconductivity (or resistivity) for both circular polarization directions based on a model which takes into account a nonequilibrium distribution of the charge carriers. The photo-conductivity σ_{ph} is normalized to the dark conductivity σ_{dc} . According to theory, an instability develops when σ_{ph} drops below zero. The formation of current domains prevents the resistance from crossing the $\sigma_{ph} = 0$ -line.

These experimental observations stirred up the community and triggered a large body of theoretical works. The majority of theoretical accounts subdivides the argumentation to explain the zero resistance into two main points. First, some mechanism produces an oscillatory photoconductivity contribution that may

turn the overall dissipative conductivity negative near the minima. Proposed mechanisms include a spatial displacement of electrons against the dc-electric field with the assistance of impurity or phonon scattering, the establishment of a nonequilibrium distribution function, photon assisted quantum tunneling and non-parabolicity effects. This list is not exhaustive. An example of predicted oscillations obtained when adopting the nonequilibrium distribution scenario is shown in Fig. 54(b). Second, it is argued that negative values of the dissipative conductivity render the initially homogeneous system unstable and an inhomogeneous current domain pattern develops, which results in zero resistance in experiment. Some more speculative theoretical work does not invoke an instability driven formation of current domains to explain zero resistance.

The sheer multitude of models and their divergence underline that no consensus has been reached on the origin of this nonequilibrium phenomenon. In order to assist in isolating the proper microscopic picture, a detailed polarization-dependent study was carried out. In previous work, microwaves were guided to the sample with oversized waveguides or coaxial dipole antennas. These approaches do not permit control over the polarization. Here, we have chosen an unconventional, all quasi-optical approach to guide the microwaves onto the sample and to produce any circular or linear polarization. Circular polarization offers the advantage that the cyclotron resonance absorption can be activated or deactivated by reversing the rotation for a given B -field orientation. Knowledge of the polarization dependence of the microwave induced oscillations may turn out an important litmus test for theoretical models. For some models these oscillations do not survive when switching from linear to circular polarization. The mainstream theories based on a nonequilibrium distribution function and on the phonon- or impurity-assisted displacement of electrons both predict oscillations for the two senses of circular polarization, however with substantially different

amplitudes. Other models have assumed linear polarization and have not been analyzed for the case of circular polarization.

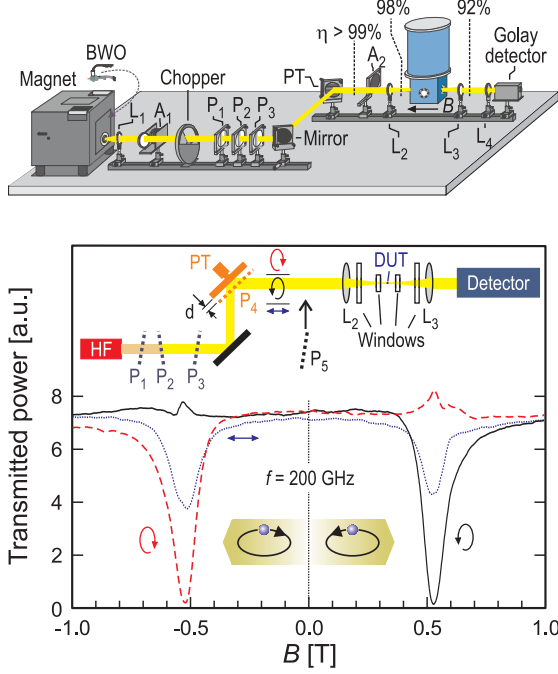


Figure 55: Top panel: Quasi-optical setup. The various components are discussed in the text except for A_1 , which is a fixed attenuator, and A_2 , which is an absorber to block the radiation beam. Bottom panel: Transmission data for 200 GHz linear, left and right hand circular polarized radiation. The data are taken at 1.8 K. The inset highlights optical components controlling or affecting the polarization state.

A schematic drawing of the quasi-optical setup is depicted in Fig. 55. A state-of-the-art two-dimensional electron system (electron mobility of $20 \cdot 10^6 \text{ cm}^2/\text{Vs}$) is mounted in the Faraday geometry in the variable temperature insert of an optical cryostat with a split coil. Backward wave oscillators generate quasi-monochromatic radiation (bandwidth $\Delta f/f \approx 10^{-5}$). Our studies focused on frequencies from 100 GHz up to 350 GHz. The radiation passes through three dense wire grid polarizers (P_1 , P_2 , P_3) as well as a so-called polarization transformer (PT). The latter consists of another fixed wire grid P_4 and a mobile metallic mirror placed in parallel at a tunable distance d (see inset to the bottom panel of Fig. 55). Grid P_4 reflects the compo-

nent of the incident radiation with the electric field vector aligned along the wires. The remainder of the beam polarized perpendicular to the wires passes undisturbed through the grid. It is reflected by the mirror and hence acquires an additional phase shift $\Delta\phi = 2\pi d \sqrt{2}/\lambda$. Grids P_1 , P_2 and P_3 serve to continuously adjust the overall intensity as well as to ensure equal intensities of the radiation components with electric field vectors aligned with and perpendicular to wire grid P_4 , so that proper adjustment of d (or $\Delta\phi$) yields linear or any circular polarization state. The quartz lens L_2 focuses the radiation onto the sample, while quartz lens L_3 recollimates the beam after transmission through the cryostat. The degree of circular polarization η is verified at various locations along the beam by recording the power with a pneumatic (Golay) detector (used in conjunction with the chopper) and an additional dense wire grid P_5 for two orthogonal directions (\parallel and \perp) of the electric field vector: $\eta = 1 - |P_{\perp} - P_{\parallel}| / (P_{\perp} + P_{\parallel})$. Typical values for the circular polarization purity η before and after the transmission through the cryostat of the radiation beam have been included as percentages at the top of Fig. 55. After the first quartz lens, but before entering the cryostat, η exceeds 98%. The warped Mylar windows of the cryostat and the quartz lenses deteriorate somewhat the polarization state, but the circular polarization character remains better than $\eta > 92\%$ after transmission through the cryostat and sample holder in the absence of a sample.

The bottom panel of Fig. 55 displays the outcome of a transmission experiment with the quasi-optical setup for both circular polarization directions and linear polarization of the incident radiation. Data are shown for both positive and negative values of B . Active cyclotron resonance absorption should only occur for the proper sense of circular polarization with respect to the B -field orientation, so that the radiation field accelerates the electron along its cyclotron motion. Indeed, the transmitted power drops nearly to zero for cyclotron resonance

absorption in the active sense of the polarization (CRA), whereas reversing the B -field orientation while maintaining the circular polarization direction turns the cyclotron resonance mode inactive (CRI). For linear polarization, the transmitted power does not drop below 50% as it should. These transmission data confirm the quality of the various polarization states. Noteworthy is also the absence of absorption features at the harmonics of ω_c . This contrasts with the magnetoresistance, which exhibits microwave induced oscillations up to the 10th harmonic of the cyclotron resonance (Fig. 54(a) and Fig. 56).

Figure 56(a) illustrates the influence of the circular polarization sense on the microwave induced resistance oscillations for different frequencies: 200, 183 and 100 GHz. The absorption signals for 200 GHz have been included at the top to easily compare the position of features with the cyclotron resonance. At fields below the cyclotron resonance absorption (the regions on the left of the dotted lines which mark the $\omega = \omega_c$), where the microwave induced oscillations occur, the magnetoresistivity traces for both senses of circular polarization are nearly indistinguishable. This is true for the entire frequency range (100–350 GHz) covered in our experiments. The same conclusion holds for linearly polarized radiation irrespective of the orientation of the electric field vector (an example is shown below in Fig. 56(b)). Hence, the experiments here only support theoretical mechanisms in which the polarization state of the microwaves is not relevant. Only at fields near the cyclotron resonance, where significant absorption takes place, deviations between the CRA and CRI curves do arise, likely because resonant heating at the cyclotron resonance produces a second contribution to the photoresistivity. In microwave photoconductivity experiments prior to the discovery of the zero resistance phenomenon, the cyclotron resonance absorption was already detected as a small resistance increase.

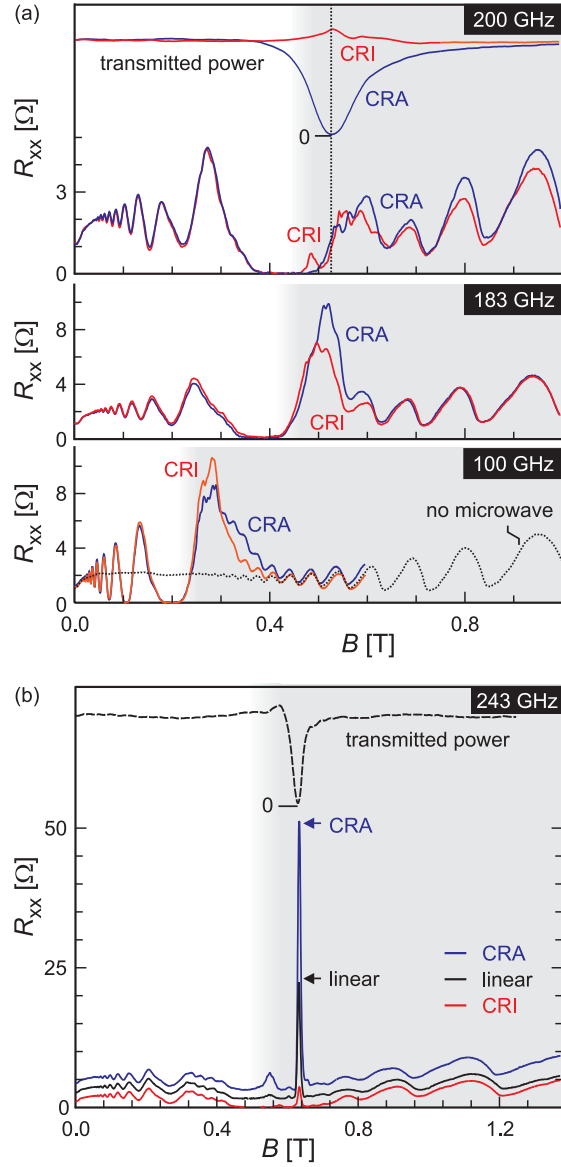


Figure 56: (a) Comparison of the magnetoresistivity R_{xx} under microwave radiation for both senses of circular polarization at three frequencies and a temperature of 1.8 K. The transmitted power P_{trans} (arb. units) at 200 GHz is plotted at the top for comparison with the 200 GHz transport data. The black dotted curve in the bottom panel displays R_{xx} in the absence of microwaves. (b) R_{xx} for 243 GHz radiation for various polarizations at the highest available power. Curves are offset for clarity. The dashed line represents the transmitted microwave power (no ordinate shown). Resonant heating at the cyclotron resonance is held responsible for the sharp resistance peak. This peak as opposed to the oscillatory photo-resistance is very sensitive to the polarization state.

In the context of the recently discovered microwave induced resistance oscillations, signatures of the cyclotron resonance absorption in the magnetoresistivity remained unidentified, presumably because they were masked by the much larger microwave induced resistance oscillations. The insensitivity of the latter on the polarization state (as proven above) and the ability to alter the circular polarization direction *in situ* make it straightforward to reveal the bolometric cyclotron resonance contribution. A striking examples at the highest microwave power we have available is illustrated in Fig. 56(b) for 243 GHz. The resistance enhancement at the cyclotron resonance can be surprisingly large and develops fine structure. Its close connection to the cyclotron resonance is established by comparing with transmission data and by comparing its amplitude for the different polarization states. We conclude that we can distinguish two microwave induced contributions to the resistance: the bolometric and polarization-dependent resistance enhancement at the cyclotron resonance due to resonant heating of the electron system and the polarization insensitive contribution related to the oscillatory photoresistivity near and below ω_c .

The complete immunity of the microwave induced resistance oscillations to the polarization state may be regarded as a crucial test for theories. For instance, this can not be reconciled with the two most frequently cited the-

ories: the nonequilibrium distribution function scenario and the picture based on impurity- and phonon-assisted electron displacement against the dc electric field. For both mechanisms, a dependence on the sense of circular polarization enters through the ac Drude conductivity σ_ω^D . Excluding the narrow vicinity of the cyclotron resonance, σ_ω^D is proportional to $(\omega - \omega_c)^{-2}$ if the microwave field accelerates electrons (CRA) and $(\omega + \omega_c)^{-2}$ if the microwaves decelerate electrons (CRI). For small dc-fields and not too strong a microwave field, the correction to the dark dc dissipative conductivity is linearly proportional to σ_ω^D and hence is a factor $(\omega + \omega_c)^2/(\omega - \omega_c)^2$ larger for the CRA polarization sense. For the maxima (or minima) near $\omega = 2\omega_c$ and $\omega = 3\omega_c$, this amounts to a factor of about 9 and 4 respectively! We refer to Fig. 54(b) where theoretical predictions for both senses of circular polarization are compared. For large microwave powers, the microwave induced correction to the dark dc conductivity no longer obeys a linear law but rather a sub-linear dependence on the microwave power and these factors are reduced. However, the dramatic difference with experiment here remains. This puzzling discrepancy reinvigorates the controversy on the origin of the microwave induced oscillations and zero resistance and there is clearly a strong need to analyze the polarization dependence of other proposed theoretical mechanisms.

Overlap of depletion layers in nanocrystalline SrTiO₃

P. Balaya; J. Jamnik (National Institute of Chemistry, Ljubljana); J. Fleig (University of Vienna); L. Kienle and G. Cristiani; W. Sigle (Max Planck Institute for Metals Research); J. Maier

In a systematic approach we are tackling size effects on ion and electron transport in electroceramics. In principle each of the contributions to the electrochemical potential of the charge carriers may lead to mesoscopic situation, where the length scales such as grain size and the space charge length become compara-

ble. Examples of interest are the impact of narrowly spaced boundaries on the local free energy of point defects, or the effect of interface curvature on transport and storage [1]. More significant are effects which are due to anomalously enhanced transport or mass storage as studied in nanocomposite or multilayer

systems. Here we report on the overlap of charge carrier depletion layers that we predicted and studied in SrTiO_3 nanocrystalline materials. Unlike accumulation layers, depletion layers can be unambiguously detected from the impedance spectra as they appear in series to the bulk response and give rise to an independent signal. In this context, an inherent difficulty had to be overcome, namely to prepare nano-size grained and simultaneously sufficiently dense ceramics.

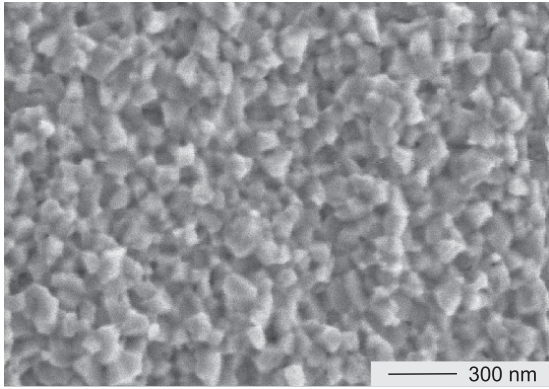


Figure 57: FESEM image of a freshly fractured surface of nanocrystalline SrTiO_3 pellet.

SrTiO_3 nanopowder was synthesized by a solution co-precipitation method with $\text{Sr}(\text{NO}_3)_2$ and Ti as starting precursors and EDTA being used as complexing agent in an aqueous medium. This procedure avoids a major problem of the formation of amorphous TiO_2 frequently experienced in aqueous environment. The dried gel precipitate upon calcination at 1000°C for one hour, yields well-crystallized SrTiO_3 with an average grain size of 30 nm. The impurity level as inferred from ICP analysis is found to be below 250 ppm with Fe being the major impurity around 100 ppm. Sintering to a dense pellet (93% of theoretical density) with grain sizes below 80 nm (Fig. 57) has been achieved by a pressure-assisted two-stage sintering process using a hot press. The grain boundaries of the SrTiO_3 nano-ceramic are found to be free of any amorphous or intergranular phases. Larger grain sizes could be achieved by different sintering conditions.

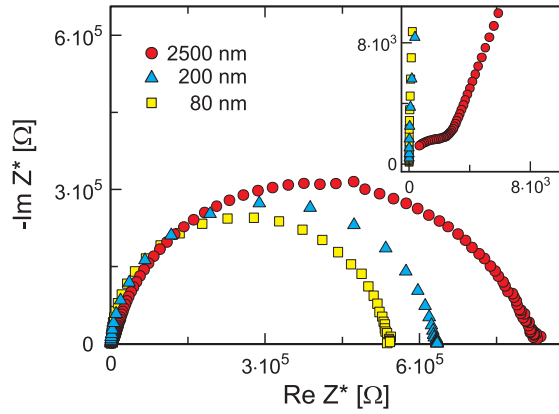


Figure 58: Impedance (Z^*) plot for micro- (2500 nm), submicro- (200 nm), and nanocrystalline (80 nm) SrTiO_3 samples measured at 420°C under oxygen pressure of 1 bar. The inset clearly reveals the bulk response at higher resolution for the 2500 nm sample.

The impedance measurements were made on SrTiO_3 with different grain sizes (80 nm, 200 nm and 2500 nm) using $\text{YBa}_2\text{Cu}_3\text{O}_{7-\delta}$ as reversible electrodes. Figure 58 shows the Cole-Cole plots at 420°C . In the case of the microcrystalline sample (2500 nm grain size), clearly two semicircles are observed, the large one at low frequencies being due to space charge depletion layers at grain boundaries and the small one at high frequencies being due to the bulk. For the purpose of a more quantitative treatment, we consider the Bode plots (Figs. 59(a), 59(b)) which better resolve the contributions from the more conductive grain interior.

As seen from Figs. 59(a) and 59(b), two relaxation times are clearly identified for the microcrystalline sample. In nanocrystalline SrTiO_3 with a grain size of 80 nm on the other hand only a single relaxation time referring to the low frequency signal remains. Thus we face the striking observation that unlike microcrystalline SrTiO_3 which shows both bulk as well as interfacial contributions to conduction, in nanocrystalline SrTiO_3 the bulk contribution disappears and space charge effects are observed throughout. These experimental results are supported in great details by continuum level simulations

performed using linear irreversible thermodynamics for a single crystal with a given Schottky barrier height at both edges.

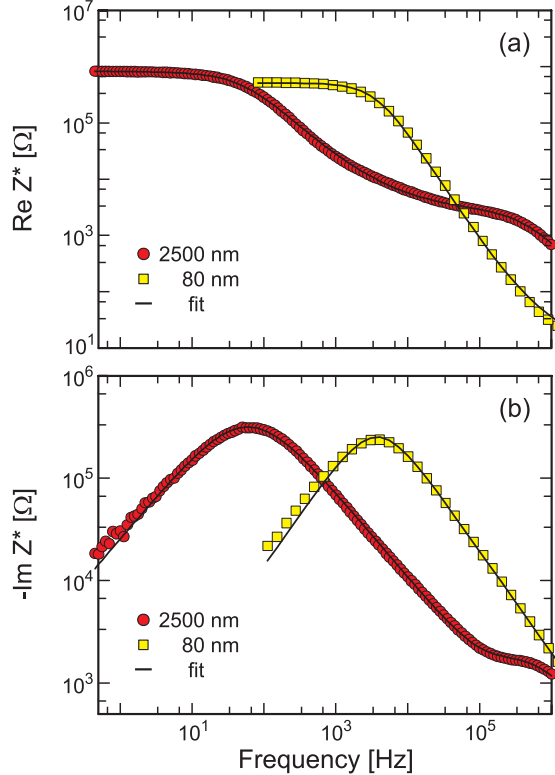


Figure 59: (a),(b) Frequency dependencies of the real and the imaginary part of the complex impedance of the microcrystalline (2500 nm) and nanocrystalline (80 nm) samples.

The capacitance of the nanocrystalline SrTiO_3 (80 nm) is found to be the same as the bulk capacitance of SrTiO_3 . Thus it is interesting to note that even though the nanocrystalline sample exhibits space charge resistance, it is characterized by a bulk-like capacitance that no longer originates from space charge polarization because of fixed charge concentrations and the grain boundary core and its neighboring space charge zones.

While the parameter n in the frequency dispersion of the capacitance term (modelled by a constant phase element: $(i\omega C)^{-n}$) which measures the depression of the impedance arc, deviates from unity if we go over from a bicrystal to a polycrystal (as a consequence of the contribution in grain boundary properties), it becomes rather close to unity (ideal behavior) again when the grain becomes nanosized. This is in agreement with our interpretation that the boundary layers now seize the whole grain and the situation becomes more homogeneous and thus less affected by the grain-size distribution.

The reason why the bulk semicircle disappears already below a grain size of 100 nm can be attributed, on the one hand, to the high dielectric constant and, on the other hand, to the low mobile carrier concentration in the depletion layers, both enhancing the screening length.

As we know from earlier measurements, and also from our theoretical work, the oxygen vacancies, being double charged ionic carriers, are even more significantly depleted in the space charge regions [2]. Future studies, e.g. with electron blocking electrodes, will reveal the combined effect on ionic and electronic motion serving then as an example of size effects on mixed conductors which forms the general case and from which purely ionic and electronic conductors follow as special cases.

-
- [1] Maier, J. *Nature Materials* **4**, 805-815 (2005).
 - [2] Guo, X., J. Fleig and J. Maier. *Journal of the Electrochemical Society* **148**, J50-J53 (2001); Leonhardt, M., J. Jamnik and J. Maier. *Electrochemical and Solid-State Letters* **2**, 333-335 (1999).

AgI nanoplates with extremely high mesoscopic ion conductivity at room temperature

Y.-G. Guo, J.-S. Lee and J. Maier

Ion conduction is the major prerequisite for the operation of electrochemical devices such as batteries or electrochemical sensors. In contrast to liquid phases, the availability of solid electrolytes renders possible easy integration and miniaturization. In the context of room-temperature electrochemical devices, and in particular in view of future nanoscale devices, the palette of suitable electrolytes is extremely restricted. It is not only the conductivity which is typically poor at room temperature, also the electrode reaction (exchange rate) is typically very sluggish. Here the silver ions play an exceptional role not only due to a high mobility but also in view of a very high exchange rate which relies on their high polarizability. Therefore silver ion conductors have been discussed as battery electrolytes in spite of high materials cost and low energy density. α -AgI shows an extremely high ionic conductivity due to a partially molten Ag sublattice, yet only above 150°C; stabilization of the high-temperature properties down to room temperature is viable in a ternary compound RbAg_4I_5 , however, at the expense of chemical stability. Here we report on very high ion conductivities in single or assembled (thin films, nanocrystalline pellets) AgI nanoplates [1]. The room temperature conductivity is enhanced by as much as four orders of magnitude compared to that of macroscopically β -AgI phase in the wurtzite structure. To the best of the authors' knowledge, it is the highest room temperature ion conductivity ever measured for a binary solid electrolyte.

By applying capping agents for directing nucleation and growth of AgI nanoparticles precipitated from silver nitrate and potassium iodide solution, we have been able to synthesize AgI nanoplates in large quantity. The nanoplates have a typical size of ≈ 300 nm in diameter and

≈ 50 nm in thickness (Fig. 60). Rietveld refinement of X-ray diffraction of the nanoplates evidenced the presence of very unusual modifications of AgI, namely, a nine-layer structure 9R-AgI and a seven-layer structure 7H-AgI in addition to the well-known low temperature phases of β -AgI and γ -AgI.

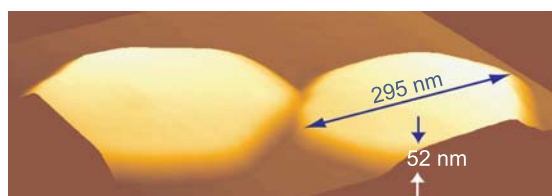


Figure 60: AFM image of the AgI nanoplates with a typical size of ≈ 300 nm in diameter and ≈ 50 nm in thickness.

The 7H and 9R structures are composed of close-packed layers of AgI_4 tetrahedra with the stacking sequences *cchhchh* and *chhchhchh*, with *c* denoting γ -AgI-like cubic stacking and *h* for β -AgI-like hexagonal stacking (Fig. 61). These long-period polytypes can thus be considered as zinc-blende/wurtzite polytype heterostructures (as indicated by differently colored layers) or γ/β superlattices. Given the necessity of an ion redistribution at γ/β interfaces, an exceeding disorder is expected on account of the tiny size of each domain [2]. In this respect the mechanism is, on one hand, related to the high fluoride conductivities found in $\text{CaF}_2/\text{BaF}_2$ heterolayers of nanometer periods, which have been recently prepared by molecular beam epitaxy (MBE) [3]. If, on the other hand, we compare the latter ion conductor heterolayers with the well-established MBE grown semiconductor heterolayers, the self-assembled stacking-fault heterolayers presented here find their semiconductor counterpart in the polytype heterostructures of SiC.

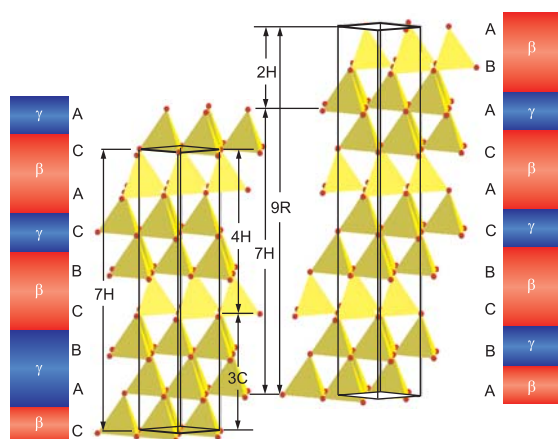


Figure 61: 7H (left) and 9R (right) structures of AgI represented by close-packed layers of AgI₄ tetrahedra. The stacking sequence can be considered as γ/β heterostructures as indicated in differently colored layers.

The bulk conductivity of AgI nanoplates (measured on pressed pellets) at room temperature is enhanced by as much as four orders of magnitude compared to that of the pristine AgI (Fig. 62). An anomalous phase transition to the high-temperature phase (α -AgI) with a large hysteresis of $\approx 50^\circ\text{C}$ can be clearly seen in the differential scanning calorimetry (DSC) and conductivity curves. A similar hysteresis has been observed in AgI: Al₂O₃ composites [4], but both heating and cooling transition temperatures being shifted to higher temperatures by 10°C in these composites. While the characteristics of AgI: Al₂O₃ composites are affected by size, volume fraction and distribution of the alumina dispersoids, the present results clearly show that the features of high conductivity and large hysteresis in phase transition are inherent characteristics of 7H- and 9R-AgI polytypes.

In addition to performing conductivity measurements on pressed pellets of nanoplates, we have been able to measure the AC impedance of individual AgI nanoplates by using a conductive AFM tip at room temperature (Fig. 63). Note that the conductivity of a single nanoplate was measured along the c -axis. The results clearly show that the average $\sigma_{\parallel c}$ (using the fractions of

respective nanoplate types) is close to the parallel conductivity of a nanoplate film which represents the conductivity perpendicular to c -axis ($\sigma_{\perp c}$) (see Fig. 62). The conductivity of pellets with randomly oriented nanoplates is also of similar magnitude. This is in striking contrast to the large conductivity anisotropy in β -AgI at room temperature. The remarkable conductivity isotropy of AgI nanoplates is, in view of the extreme conductivity enhancement and the layered structure, a further support of a fully mesoscopic ionic conductivity in the polytype heterostructures (7H and 9R polytypes) with very pronounced silver ion disorder.

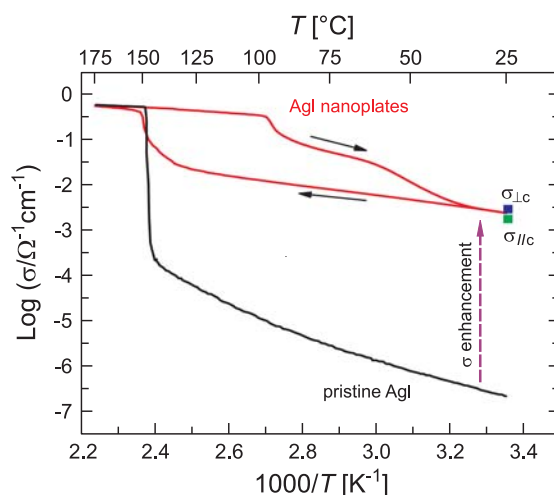


Figure 62: Conductivity of pressed pellets of AgI nanoplates as a function of temperature (red line) in comparison with that of the pristine β -AgI (black line). The average conductivity of single nanoplates ($\sigma_{||c}$) measured at room temperature using AFM conducting tips (see Fig. 63) and the conductivity measured on nanoplate films ($\sigma_{\perp c}$) are indicated.

The drastic conductivity enhancement and the conductivity isotropy of AgI nanoplates is hence the outcome of a double size-effect: (i) owing to the small thicknesses of the plates stacking faults which otherwise only occur at AgI interfaces penetrate the whole material. (ii) Owing to the tiny size of the stacking period disorder seizes the whole arrangement. Not only is this mesoscopic ionic conductivity effect a further striking evidence of the power of nano-scale interfacial design on ionic conductivity properties, the AgI nanoplates, owing to

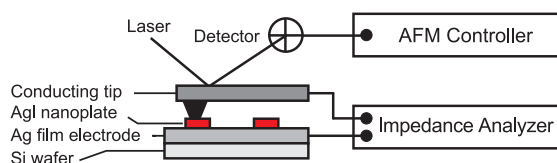


Figure 63: Experimental configurations for conductivity measurements of individual AgI nanoplates using AFM tips.

to conductivity, stability and shape, are also ideal candidates for electrolytes in nanoscale electrochemical devices such as miniaturized sensors or nano-integrated batteries. In such devices the favorable kinetics of silver ions is most important while materials cost issues become negligible. It can be anticipated that owing to mobility and exchange rate, protonic devices and devices based on lithium and silver conduc-

tors are most promising whereby the first are ideal for fuel cells while the latter ones are the candidates of choice for all solid state systems. While Li-ion batteries are to be preferred if energy density matters, the Ag-ion based ones are unbeatable in terms of reversibility and switching speed and hence will be most promising in the light of a future nanotechnology.

-
- [1] Guo, Y.-G., J.-S. Lee and J. Maier. *Advanced Materials* **17**, 2815-2819 (2005).
 - [2] Maier, J. *Progress in Solid State Chemistry* **23**, 171-263 (1995).
 - [3] Sata, N., K. Eberman, K. Eberl and J. Maier. *Nature* **408**, 946-949 (2000).
 - [4] Lee, J.-S., S. Adams and J. Maier. *Journal of the Electrochemical Society* **147**, 2407-2418 (2000).

Oxygen incorporation into ‘electron-poor’ and ‘electron-rich’ oxides: mechanistic studies of the surface reaction on $\text{Sr}(\text{Fe}_x\text{Ti}_{1-x})\text{O}_{3-\delta}$

R. Merkle and J. Maier

Many perovskites are mixed electronic and ionic (O^{2-}) conductors at elevated temperatures, and serve as key component of a number of electrochemical devices such as fuel cells, permeation membranes or gas sensors. Often the transformation of O_2 from the gas phase into oxide ions in the solid (‘oxygen incorporation’) is the crucial step for the equilibration of the bulk oxygen stoichiometry with the gas phase. $\text{Sr}(\text{Fe}_x\text{Ti}_{1-x})\text{O}_{3-\delta}$ materials exhibit a significant range of oxygen non-stoichiometry δ up to $x/2$ and can thus serve as model materials for the investigation of the oxygen incorporation surface reaction. Unlike the transport step, it is indeed the surface reaction which remained mainly ‘terra incognita’ in the treatment of gas-solid reactions. One reason is the problem of interpreting kinetic data involving solids, the other is the manifold of kinetic path-

ways. By applying a whole arsenal of theoretical and experimental methods we were able to draw reliable conclusions on the mechanistic situation.

Since almost all $\text{Sr}(\text{Fe}_x\text{Ti}_{1-x})\text{O}_{3-\delta}$ compositions exhibit the cubic perovskite structure, this solid solution series allows one to study the effect of compositional variation on reaction rate and mechanism, while the crystallographic structure remains essentially unmodified. The most drastic difference shows up in the electronic properties which change from the large band gap semiconductor $\text{SrTiO}_{3-\delta}$ to high electronic or even metallic conduction in $\text{SrFeO}_{3-\delta}$. The change in the electronic structure can already be recognized in the color (samples with more than 3% Fe are black) and in more detail in the UV-vis spectra (Fig. 64). In addition to

the bands at 2.1–2.9 eV (originating from localized O^{2-} to Fe^{4+} charge transfer), for 3% of iron a new absorption at 1 eV appears which becomes very prominent at $\geq 10\%$ Fe and can be related to the presence of an iron impurity band.

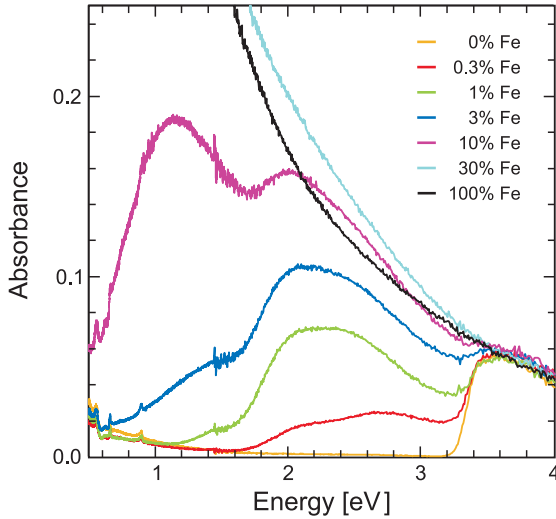


Figure 64: Absorbance of $Sr(Fe_xTi_{1-x})O_3$ in the UV-vis region, calculated from diffuse reflection measurements at room temperature.

Figure 65 shows the variation of the electronic conductivity σ_{eon} (known to be p-type from its pO_2 dependence and thermopower measurements) with the iron concentration. As few as 3% Fe on the Ti site is sufficient to drastically enhance σ_{eon} while the activation energy drops from 0.95 eV to about 0.4 eV. This indicates a change in the conduction mechanism in accordance with ab initio calculations which predict the formation of an impurity band at about 10% of iron [1]. The partially occupied iron 3d-orbitals, overlapping with the oxygen valence band but extending also to higher energies, decrease the band gap and can therefore easily supply electrons for being transferred to adsorbed species in the course of the reaction pathway. Thus we will term the iron-rich materials ‘electron-rich’ in contrast to the ‘electron-poor’ (only slightly Fe-doped) $SrTiO_{3-\delta}$ samples.

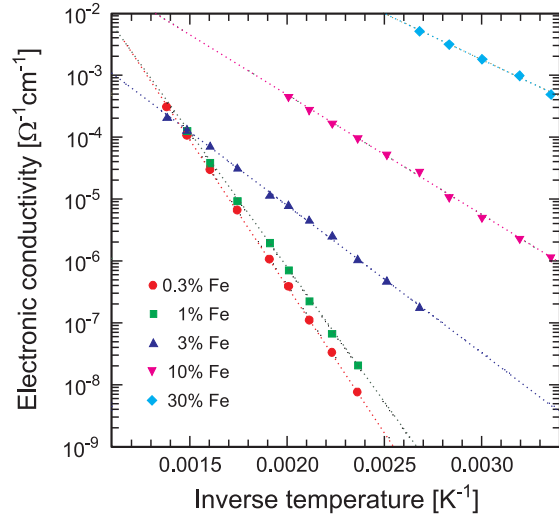


Figure 65: Bulk electronic conductivity of fully oxidized $Sr(Fe_xTi_{1-x})O_3$ samples.

For the mechanistic interpretation, we assume that one of the steps in the reaction sequence, the so-called rate determining step (*rds*), limits the overall reaction rate. A sudden change in the oxygen partial pressure pO_2 at constant temperature induces a sufficiently large change in the oxygen non-stoichiometry δ of the iron-rich samples so that the reaction rate can easily be followed by measuring the weight change. Samples with the relevant particle size ranging from μm (powders) up to mm (sintered pellets) allow one to cover a large temperature range of 250–800°C. Systematic variation of initial and final pO_2 values of such pO_2 changes yield the reaction order of oxygen in the *rds*. For samples with 10–50% of iron, this reaction order is found to be 1/2 in the whole temperature range studied. This means that the *rds* contains only atomic oxygen species such as adsorbed O^- . It is more difficult to draw conclusions about the point defects possibly involved in the *rds* because their concentrations cannot be varied independently (but do contribute to the overall pO_2 dependence of the reaction rate). For $(\text{Ln},\text{Sr})(\text{Mn},\text{Fe},\text{Co})O_{3-\delta}$ perovskites, a correlation of effective surface rate constants k^* and diffusion coefficients D^* for oxygen tracer exchange was found [2], which holds over several orders of magnitude when the materials composition is varied.

Table 3: Reaction mechanism for ‘electron-rich’ and ‘electron-poor’ oxides.

"electron-rich" (10-50% iron)	"electron-poor" (less than 3% iron)
$\text{O}_2 + 2 \text{Fe}^{3+} \rightleftharpoons 2 \text{O}_{\text{ads}}^- + 2 \text{Fe}^{4+}$ $\text{rds } \text{O}_{\text{ads}}^- + \text{V}_{\text{O}}^{\bullet\bullet} + \text{Fe}^{3+} \rightleftharpoons \text{O}_{\text{lattice}}^{2-} + \text{Fe}^{4+}$	$\text{O}_2 \rightleftharpoons \text{O}_{2\text{ads}}^- + \text{h}^+$ $\left. \begin{array}{l} \text{O}_{2\text{ads}}^- + \text{e}^- \rightleftharpoons \text{O}_{2\text{ads}}^{2-} \\ \text{O}_{2\text{ads}}^{2-} \rightleftharpoons 2 \text{O}_{\text{ads}}^- \end{array} \right\} \text{rds}$ $\text{O}_{\text{ads}}^- + \text{V}_{\text{O}}^{\bullet\bullet} \rightleftharpoons \text{O}_{\text{lattice}}^{2-} + \text{h}^+$

Since for these materials the oxygen vacancy concentration is the only variable quantity in the expression for D^* , this implies that oxygen vacancies are also involved in the *rds* of the surface reaction [2].

In contrast to the ‘electron-rich’ materials, the oxygen incorporation mechanism for the only slightly Fe doped ‘electron-poor’ materials contains molecular oxygen species in the *rds*. The acceleration by UV irradiation shows that the transfer of a conduction electron is involved in or before the *rds* [3] (UV light increases the conduction electron concentration, while the concentration of holes h^+ remains \approx constant since it is mainly determined by the iron dopant). Amounting to 2.7 eV, the activation energy is much higher than for the ‘electron-rich’ materials (about 1 eV), and the absolute reaction rates are lower by about three orders of magnitude. Table 3 displays our present knowledge of the reaction mechanism and highlights the mechanistic differences between the two materials classes addressed. For the ‘electron-rich’ materials the mechanistic details of the first steps cannot be resolved since they are summarized into a rapidly established pre-equilibrium, but owing to the high chemical similarity of the materials, it is highly plausible that the same intermediate species are involved as for the ‘electron-poor’ systems.

Since in the ‘electron-rich’ materials electrons are easily available for being transferred to ad-

sorbed oxygen species, all reactions up to and including the formation of the adsorbed O^- are fast. Therefore the last step which includes also the ionic motion of the O^- into an oxygen vacancy $\text{V}_{\text{O}}^{\bullet\bullet}$ can become the bottleneck.

The comparison of the ‘electron-rich’ and ‘electron-poor’ members of the $\text{Sr}(\text{Fe}_x\text{Ti}_{1-x})\text{O}_{3-\delta}$ solid solution series indicates that the different electronic structure is crucial for the observed change of the reaction mechanism. The acid-base properties – even though highly significant for the absolute rate – are expected to be less important with regard to the variations since they hardly change when Ti^{4+} is replaced by the slightly smaller Fe^{4+} . Although mechanistic details are not available in other oxides, the similar absolute reaction rates of oxygen exchange on ‘electron-poor’ $(\text{La,Sr})(\text{Ga,Mg})\text{O}_{3-\delta}$ perovskites and $(\text{Y,Zr})\text{O}_{2-\delta}$ fluorites suggest the crystallographic structure to be less decisive for the reaction mechanism as long as oxide ions are sufficiently mobile.

-
- [1] Evarestov, R.A., S. Piskunov, E.A. Kotomin and G. Borstel. Physical Review B **67**, 064101 (2003).
 - [2] De Souza, R.A. and J. Kilner. Solid State Ionics **126**, 153-161 (1999); Merkle, R., J. Maier and H.J.M. Bouwmeester. Angewandte Chemie International Edition **43**, 5069-5073 (2004).
 - [3] Merkle, R. and J. Maier. Physical Chemistry Chemical Physics **4**, 41404148 (2002).

Isotope effect on the heat capacity of the monatomic and diatomic semiconductors diamond and zinc oxide

R.K. Kremer, M. Cardona, G. Siegle and R. Lauck; S.K. Estreicher (Texas Tech University, USA); A.H. Romero (Unidad Querétaro, Mexico); M. Sanati (Texas Tech University, USA); J. Serrano (ESRF, France); T.R. Anthony (GE Corporate Research and Development, USA)

The availability of semiconductor crystals with different isotopic abundances has triggered profuse investigations of the effect of isotopic composition on thermodynamic, vibrational, and electronic properties [1]. Most of this work is concerned with monatomic semiconductors, i.e. diamond, Si, Ge, and α -Sn. The effect of the isotopic masses in multinary compounds on the thermodynamic properties should essentially depend on which mass is being considered. We have determined the effect of isotope variation on the heat capacity at constant pressure, C_p , for a monatomic example, namely diamond, and for the diatomic system zinc oxide and compare our results with first-principles calculations.

Historically, the low-temperature heat capacity of diamond has played a central role in the development of the quantum theory of the thermal properties of solids. Natural diamond is composed of two stable isotopes, ^{12}C ($\approx 99\%$) and ^{13}C ($\approx 1\%$). Meanwhile, artificial diamonds with different isotopic compositions which cover the range $^{12}\text{C}_{1-x}^{13}\text{C}_x$ ($0 \leq x \leq 1$) grown by a high-pressure high-temperature technique became available.

Zinc oxide is a wurtzite-like semiconductor with an electronic band gap of 3.4 eV that makes it suitable for fabrication of optoelectronic devices in the ultraviolet range. Therefore an appropriate characterization of the thermodynamic properties, such as the thermal conductivity and the heat capacity, is essential for the development of high-quality devices. Recently, small single crystals of ZnO with a wide range of isotopic abundances (highly enriched ^{64}Zn , ^{68}Zn , ^{18}O) have been grown by chemical vapor transport. The Zn mass affects mainly the acoustic phonons, thus leading to

isotopic effects on the heat capacity mostly at low temperatures, whereas the O mass affects mainly the optic phonons, which become thermally active at higher temperatures.

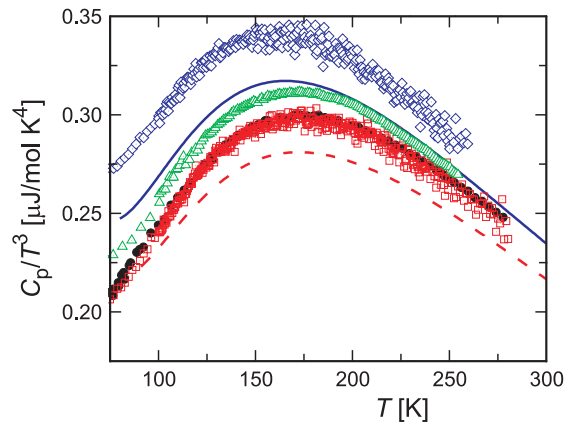


Figure 66: Temperature dependence of C_p/T^3 measured for three samples with different isotopic compositions (red \square ^{12}C ; green \triangle $^{12}\text{C}_{0.58}^{13}\text{C}_{0.42}$; blue \diamond ^{13}C). We have added to the figure the literature data reported for natural diamond (\bullet) and the theoretical results based on self-consistent, first-principles molecular-dynamics simulations based on local density-functional theory [3] for ^{12}C and ^{13}C (red dashed and blue solid curves, respectively).

Figure 66 displays the specific heat of a natural diamond, a crystal with isotopic composition $^{12}\text{C}_{0.58}^{13}\text{C}_{0.42}$ and a ^{13}C sample. We have added the data of Desnoyers and Morrison for natural diamond which agree with ours to within the scatter ($\pm 1\%$). The solid curves represent the calculations for ^{12}C and ^{13}C [3]. Whereas calculations fall, at the maxima of C_p/T^3 , about 7% short of the measurements, they reproduce rather well the general trend of C_p/T^3 vs. T . The 7% difference can be attributed to deficiencies of the fully *ab initio* model of the lattice dynamics, which uses a rather small 128 atom

periodic supercell. It is worth pointing out, however, that the relative change observed at the maximum of C_p/T^3 , between ^{12}C and ^{13}C (13%), is the same for the measured as for the calculated data.

Due to the lack of a sufficient experimental basis for the isotopic-mass dependence of the specific heat, a quantitative comparison of the calculated isotopic-mass dependence on the heat capacity with experimental data thus far was carried out by relating the derivative with respect to the isotopic mass with the derivative with respect to temperature. In the harmonic approximation (but otherwise exact) the following equation can be derived [3]:

$$\frac{d \ln(C/T^3)}{d \ln M} = \frac{1}{2} \left\{ 3 + \frac{d \ln(C/T^3)}{d \ln T} \right\}. \quad (13)$$

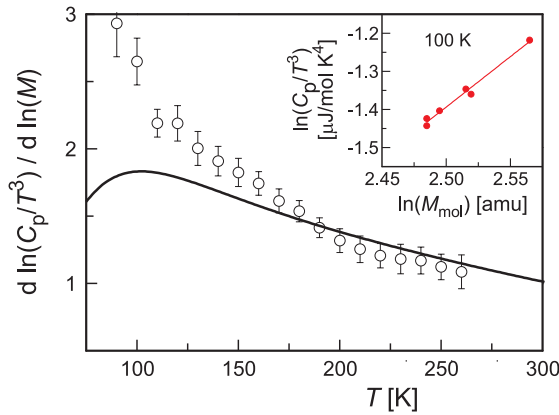


Figure 67: Logarithmic derivative of C_p/T^3 vs. isotopic mass gained from six diamond samples with isotopic compositions $^{12}\text{C}_{1-x}^{13}\text{C}_x$ ($0 \leq x \leq 1$) (\circ). The solid line represents the calculated temperature dependence [3]. Agreement is good above 170 K. Below this temperature, the experimental points deviate from the calculated curve, possible reflecting the presence of iron inclusions. The inset illustrates the procedure used to obtain the logarithmic derivative from the experimental data.

Our measurements on six different diamond samples with varying isotopic compositions (see Fig. 67) enabled us for the first time to obtain rather good experimental values for the

l.h.s. of Eq.(13). The agreement between measured and calculated results is excellent for $T > 170$ K. The upturn in the experimental results at lower temperatures is assigned to the presence of inclusions of metals used as catalyst for the crystal growth (for more details cf. Ref. [2](a)).

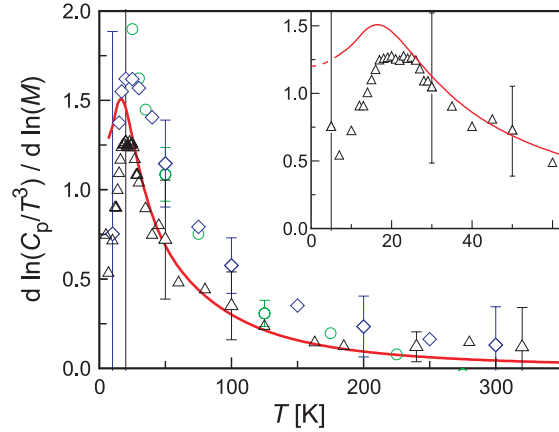


Figure 68: The logarithmic derivatives $d \ln(C_p/T^3) / d \ln M$ with respect to the mass of the Zn isotope. Solid (red) line: Result of the *ab initio* calculation. Experimental data: (black Δ) $^{p}\text{Zn}^{16}\text{O}$ ($p = 64, 65.4, 68$); (green \circ) $^{p}\text{Zn}^{16/18}\text{O}$ ($p = 64, 65.4, 68$); (blue \diamond) $^{p}\text{Zn}^{18}\text{O}$ ($p = 64, 66, 66, 68$). The inset shows the data for $^{p}\text{Zn}^{16/18}\text{O}$ in an enlarged scale, together with the calculation.

Figure 68 displays the logarithmic derivative of C_p/T^3 with respect to the mass of zinc isotope for all measured samples of ZnO grouped into blocks with different oxygen mass. A sharp peak is observed at ≈ 22 K that corresponds to acoustic vibrations, associated mainly to displacements of zinc atoms. The larger mass of zinc with respect to that of oxygen explains the presence of this peak at low temperatures. The *ab initio* calculations agree well with the experimental data at temperatures larger than 100 K. At low temperatures the peak position is described in a qualitative way by the calculations, although the latter yield the maximum at 4 K lower temperature than the experimental data (see inset Fig. 68).

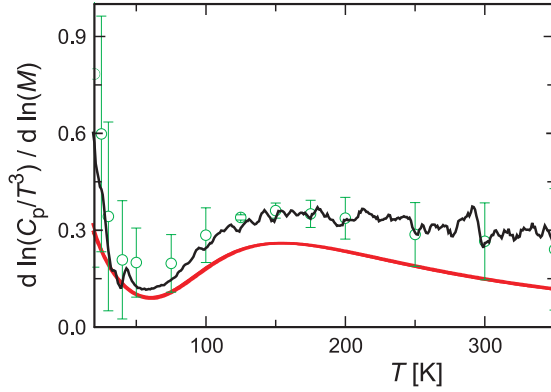


Figure 69: The logarithmic derivatives with respect to the mass of the oxygen isotope, $d\ln(C_p/T^3)/d\ln M_O$. Lower solid (red) line: Result of the theoretical calculation. Upper solid (black) line: Average of four derivatives with respect to the mass of the oxygen isotope. Open circles (green \circ): Derivative with respect to the mass of the oxygen isotope for the set $^{64}\text{Zn}^q\text{O}$ ($q = 16, 16/18, 18$).

The temperature dependence of the logarithmic derivative of C_p/T^3 with respect to the oxygen mass (Fig. 69) shows two distinct maxima at ≈ 20 K and 160 K. The first maximum corresponds to transverse acoustic vibrations of ω close to zero, which behave as sound waves and the atomic displacements depend on the total mass. Therefore they are also slightly affected by the oxygen mass. This maximum depends on the possible inhomogeneity of the isotopic distribution of the Zn atoms and overlaps with the maximum observed in Fig. 68. This is demonstrated in Fig. 69 by the difference between the solid line, corresponding to an average between four derivatives with respect to the oxygen isotope, and the open circles, corresponding to the set $^{64}\text{Zn}^q\text{O}$ ($q = 16, 16/18, 18$). Besides this low temperature peak, there is a broad asymmetric band with a maximum at 160 K. This band is related to the activation of lattice vibrations that predominantly involve displacements of oxygen atoms. The much lighter mass of oxygen as compared to that of zinc is responsible for the higher frequency of these modes, which in turn requires a higher activation temperature. The calculations, displayed by the lower solid curve

on Fig. 69, describe remarkably well the experimental behavior of $d\ln(C_p/T^3)/d\ln M$ as a function of temperature, taking into account the magnitude of $d\ln(C_p/T^3)/d\ln M$, the limited accuracy of the calculation of the logarithmic derivatives, and the error bars present at low and high temperatures.

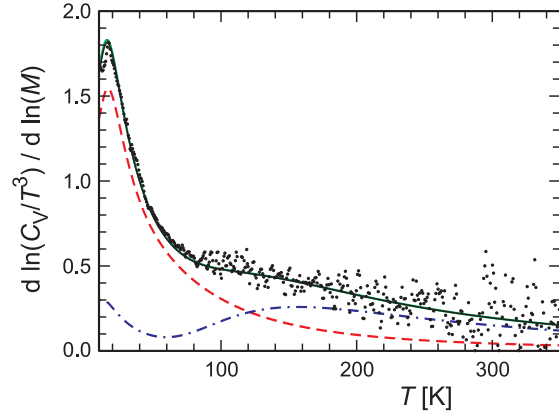


Figure 70: Calculated logarithmic derivatives $d\ln(C_p/T^3)/d\ln M$ with respect to M_{Zn} (red, dashed) and M_{O} (blue, dot-dashed), sum of both curves (green, solid), and r.h.s. of Eq.(13) (black, solid), the latter obtained from an average of the calculated heat capacity for 68/18 and 64/16 isotopic compositions. The filled circles (\bullet) correspond to the r.h.s. of Eq.(13) with the logarithmic derivative taken on the average of experimental data of two samples with isotopic composition 68/18 and 64/16. Note that the sum of the two dashed curves (green, solid) coincides with the solid black curve.

Equation (13) can be evaluated for monatomic crystals from the phonon DOS without any additional details about the lattice dynamics (e.g. the phonon eigenvectors). As illustrated in Fig. 70, this is not possible for binary or multinary materials. The r.h.s. of Eq.(13) calculated from an average of C_p of an 68/18 and 64/16 isotopic composition displays only one sharp peak at $T \approx 18$ K. In the actual partial derivatives this peak splits into two, one for the M_{Zn} derivative, at ≈ 20 K, and a broader one for the M_{O} derivative at ≈ 160 K. In order to obtain these partial derivatives with an expression similar to Eq.(13), some knowledge about the corresponding phonon eigenvectors would be needed. A general argument to explain these

differences between both partial derivatives is that the zinc components of the eigenvectors are larger for the phonons with lower frequencies, and viceversa, whereas the opposite situation happens for the oxygen components. The agreement found between measured and calculated curves of $d\ln(C_{p,V}/T^3)/d\ln M_{\text{Zn,O}}$ shown in Figs. 68 and 69 also reflects the quality of our *ab initio* calculations.

In summary, we have measured the heat capacity of diamond and zinc oxide on single crystals with a wide spread of isotopic compositions. Our data allow for the first time to obtain reliable values for the logarithmic derivatives of C_p/T^3 with respect to the atomic masses. For ZnO there is a distinct temperature dependence of the logarithmic derivatives with respect to Zn and O masses, which stems from the contribu-

tion of Zn and O atomic displacements to the lattice vibrations and the activation of the latter at different temperatures. This behavior, as well as the heat capacity, are reasonably well-reproduced by *ab initio* calculations that we have performed within the harmonic approximation.

-
- [1] Cardona, M. and M. Thewalt. Reviews of Modern Physics **77**, 1173-1224 (2005).
 - [2] (a) Cardona, M., R.K. Kremer, M. Sanati, S.K. Estreicher and T.R. Anthony. Solid State Communications **133**, 465-468 (2005);
(b) Kremer, R.K., M. Cardona, E. Schmitt, J. Blumm, S.K. Estreicher, M. Sanati, M. Bockowski, I. Grzegory, T. Suski and A. Jezowski. Physical Review B **72**, 075209 (2005); (c) Serrano, J. et al.. Physical Review B, submitted for publication.
 - [3] Sanati, M., S.K. Estreicher and M. Cardona. Solid State Communications **131**, 229-233 (2004).

Structure of complex solids

Knowledge of the structure is an essential prerequisite for an in-depth understanding of a solid. Two contributions at the beginning of this section deal with crystalline phases. Layered cobalt oxides are interesting in the context of novel superconductors. X-ray diffraction and Raman spectroscopy were carried out on NaCoO_2 and LiCoO_2 over a large pressure range and compared with density functional calculations. The structure analysis of a complex magnesium-containing mineral is the starting point for the understanding of the phase evolution in screed upon aging. In a following report, a number of experiments yielding information about short-range order were combined with computer simulations to develop models for the amorphous multicomponent ceramic $\text{Si}_3\text{B}_3\text{N}_7$. Simulations were also essential for the structure elucidation of $\text{La}_{\approx 0.7}\text{I}_{\approx 0.88}\text{Al}_{\approx 0.12}$ containing La_6Al clusters in a disordered but not random arrangement. The last two reports deal with the interpretation of observed crystal structures in terms of the underlying chemical bonding situation and its drastic variation with the material composition (A_2B intermetallic compounds with anti-PbFCl type structure) or an applied pressure (semiconductor-metal transition in tellurium involving lone pairs).

Layered cobalt oxides under pressure

X. Wang, I. Loa, K. Kunc, K. Syassen and C. Lin;
M. Amboage and M. Hanfland (ESRF, Grenoble)

The layered sodium cobaltites Na_xCoO_2 ($x \leq 1$) have attracted attention recently in the context of correlated-electron physics and superconductivity. The most remarkable property of the structurally related compounds Li_xCoO_2 is the possibility of reversible removal and reinsertion of Li ions as exploited in rechargeable Li batteries. We have studied the structural and lattice dynamical properties of the fully intercalated insulating compounds LiCoO_2 and NaCoO_2 at high pressures by synchrotron x-ray diffraction and Raman spectroscopy. The primary motivation was to explore the phase stability and obtain reference data for studies of deintercalated varieties.

The common modification of both compounds is the $\alpha\text{-NaFeO}_2$ -type phase (see Fig. 71). The structure can be derived from rocksalt-type

CoO by substituting alkali metals for Co in every second cation layer perpendicular to the cubic [111] direction (which results in a hexagonal supercell cell with $c/a = 2\sqrt{6}$) and then allowing for two types of relaxations, a small elongation along the hexagonal [001] axis and a pairing of close-packed oxygen layers. The resulting building blocks are tightly bound O-Co-O slabs separated by layers of alkali atoms. Being insulators (the optical gap of LiCoO_2 is ≈ 2 eV), the formal oxidation state of cobalt is 3+ in both compounds, corresponding to a d^6 configuration. The Co ions adopt a low-spin state. Within a molecular-orbital picture of the CoO_6 octahedral unit, three t_{2g} orbitals are fully occupied; they form the top of the valence band. The optical gap results from the splitting between weakly bonding t_{2g} and antibonding e_g^* states [1].

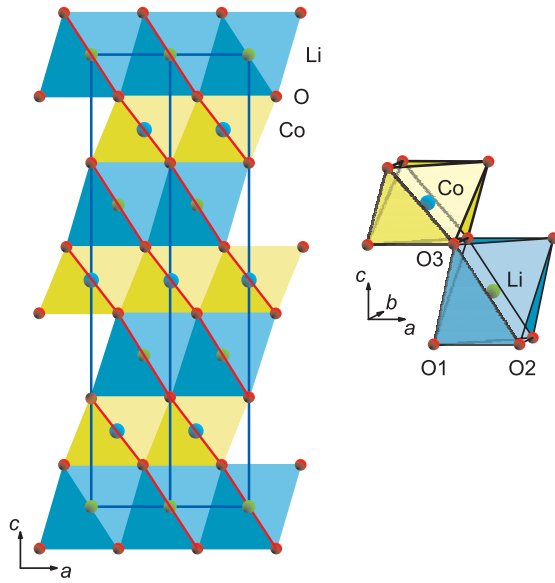


Figure 71: The crystal structure of the layered form of LiCoO_2 (space group $R\bar{3}m$, $Z=1$). The view is along the $[110]$ direction of the hexagonal unit cell. NaCoO_2 crystallizes in the same structure type.

Our powder diffraction data indicate that the layered phases do not undergo a phase transition in the pressure range up to 20 GPa. A phase change of LiCoO_2 to a cubic spinel-related structure, predicted to possibly occur near 3 GPa [2], was not observed, at least at room temperature. We find that the values of the bulk modulus B_0 are quite similar (≈ 150 GPa) for the two compounds (Fig. 72) and smaller compared to CoO (≈ 180 GPa). The compounds show anisotropic compressibility resulting in a reduction of the c/a ratio. The diffraction diagrams were analyzed by full-profile (Rietveld) refinements in order to determine the pressure dependence of the internal positional parameter of oxygen and thus the metal-oxygen distances. Compared to the Co-O bond, the Li-O (Na-O) bond length is about three times more compressible. Another way to illustrate the different bond compressibilities is to compare the ‘thicknesses’ of the octahedral layers, i.e., their heights projected onto the c -axis (Fig. 72). The projected thickness of the CoO_6 octahedra remains nearly constant; it is mainly the LiO_6 and NaO_6 octahedra which are compressed along $[001]$.

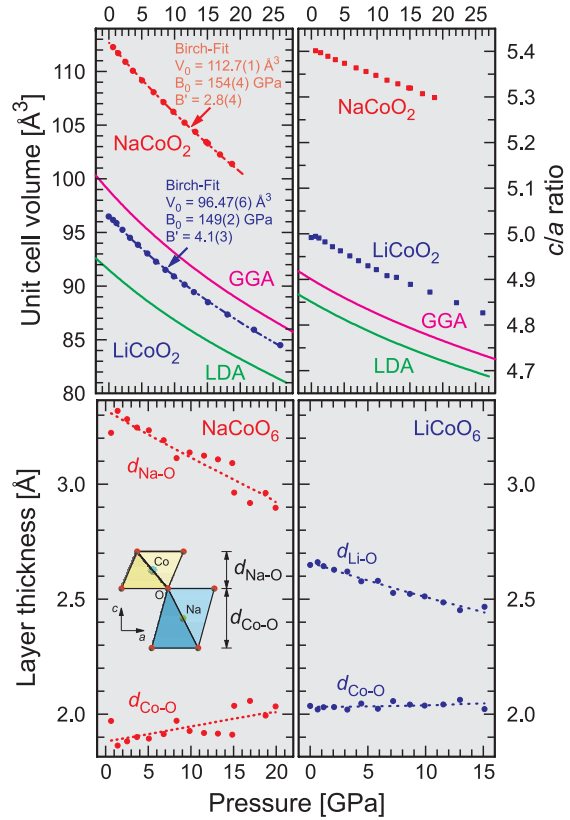


Figure 72: Top: Unit cell volume and c/a ratio of NaCoO_2 and LiCoO_2 versus pressure. Theoretical results for LiCoO_2 are shown for comparison. Bottom: The Co-O and Na-O (Li-O) layer thicknesses tend to equalize with increasing pressure.

We have compared the experimental high-pressure structural properties to results of *ab initio* total energy calculations performed within density functional theory. This approach is considered adequate, at least for LiCoO_2 [1]. The calculations yield pressure-induced changes of structural and elastic parameters of LiCoO_2 in quite good agreement with experimental data (see Fig. 72). Deviations on the absolute scale are within the margins usually encountered when comparing LDA and GGA calculations with experiment (e.g. of the order $\pm 1\%$ in lattice parameters).

Turning to Raman spectroscopy, for the layered structure we expect two Raman-active zone-center phonon modes. For propagation along the trigonal axis of the rhombohedral lattice, the two modes correspond to relative displacements

of neighboring oxygen layers with respect to each other, the displacement being along the c -axis for the A_{1g} mode and perpendicular to c for the E_g mode. The observed frequencies as a function of pressure are depicted in Fig. 73. The modes can be interpreted as predominantly Co–O stretching and O–Co–O bending motions. This interpretation is supported by comparing the ambient-pressure mode frequencies of LiCoO_2 and NaCoO_2 ; by substituting sodium for lithium, the E_g mode does not shift in frequency (within experimental resolution) and the shift of the A_{1g} mode is quite small, only about 2%. It is then not surprising that we also observe very similar pressure shifts and mode Grüneisen parameters for the Raman modes of LiCoO_2 and NaCoO_2 . In accordance with the diffraction experiments, the Raman spectra provide no indication for pressure-induced structural changes.

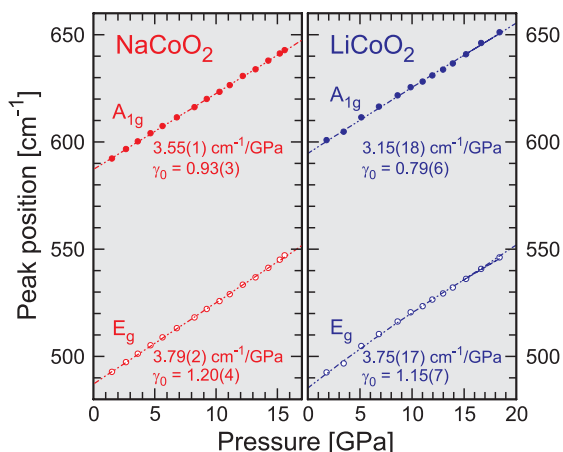


Figure 73: Raman peak positions of NaCoO_2 and LiCoO_2 as a function of pressure. Noted are the zero-pressure slopes and mode-Grüneisen parameters γ_0 , i.e. the relative change in frequency normalized to the relative change in density.

While no anomaly is evident in the phonon frequency shifts, Raman spectroscopy reveals pronounced changes in the line widths and intensity with pressure (see [3] for details). Identifying the physical effects leading to the line

width changes (whether caused by anharmonicity, band gap changes, or structural effects not detected in the diffraction measurements) is believed to require a more systematic study using suitable crystals. The fact that for the given experimental conditions, i.e. 1.96 eV excitation, the integrated intensity of the Raman peaks was observed to increase significantly under pressure (e.g. by a factor of seven for the A_{1g} mode of LiCoO_2) is taken as indication for changes in the electronic band gap. A brief check of Kohn-Sham eigenvalues in electronic band structure calculations corresponding to two different volumes indicates that the band gap of LiCoO_2 increases under applied pressure, as one would expect within a molecular-orbital picture.

We have also compared the experimental vibrational properties to results of frozen phonon calculations performed within density functional theory. The calculations of harmonic frequencies yield pressure-induced shifts in satisfactory agreement with experimental data. They also provide insight into anharmonic components in the restoring forces. For details see [3].

To conclude, the observation that the layered forms of LiCoO_2 and NaCoO_2 are found to be *not* susceptible to a pressure-driven structural instability or cation redistribution leads us to suggest that pressure could be an interesting parameter in the study of in-plane vacancy ordering in delithiated Li_xCoO_2 ($x < 1$) and other layered cobaltites.

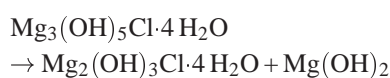
-
- [1] Van Elp, J., J.L. Wieland, H. Esdes, P. Kuiper, G.A. Sawatzky, F.M.F. de Groot and T.S. Turner. *Physical Review B* **44**, 6090-6103 (1991); Czyżyk, M.T., R. Potze and G.A. Sawatzky. *Physical Review B* **46**, 3729-3735 (1992).
 - [2] Wolverton, C. and A. Zunger. *Journal of the Electrochemical Society* **145**, 2424-2431 (1998).
 - [3] Wang, X., I. Loa, K. Kunc, K. Syassen and M. Amboage. *Physical Review B* **72**, 224102 (2005).

Chlorartinite, a volcanic exhalation product also found in industrial magnesia screed

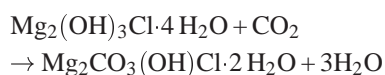
K. Sugimoto, R.E. Dinnebier and T. Schlecht

The pavement of high-quality industrial floors is mainly made from screed which is separated by a screening layer from the ferroconcrete of the base plate. Self leveling screed floors are easy to handle but require intensive and careful after-treatment. Generally, screed consists of aggregates, water, additives and binder. Depending on the required load, the largest differences between the different floor pavements are due to their binders. The most important binders are cement, anhydrite and calcium sulfate, mastic asphalt and magnesia. Typically, the binder makes up to about 15–25 wt% of the entire floor. Depending on the production and the setting process, the aging, and environmental influences, a variety of phases forms. With time, a typical floor not only consists of the original phases but also of degradation products. Manufacturers will be able to control the durability of the floor, if it is possible to clarify this process. Although wet chemical analysis provides some insight in the distribution of elements, the mineralogical composition is much more meaningful. In order to control the production or to evaluate structural damages in the construction business, a full quantitative phase analysis (QPA) using the Rietveld method is necessary, for which the knowledge of the crystal structures of the components is essential. The raw screed typically consists of quartz sand, technical magnesium oxide, technical magnesium chloride, inorganic pigments (usually iron oxides) and eventually kaolinite or other minerals to insure a proper workability of the mortar. After the binding and the consecutive drying process, a variety of magnesium hydroxide, magnesium chloride hydroxide and magnesium chloride hydroxide hydrate phases forms, of which at least 16 are reported in the ICDD database. For some of these compounds the crystal structure is missing, making a full QPA impossible.

The most important binder phases in industrial magnesia screed floors are $\text{Mg}(\text{OH})_2$ (magnesium hydroxide), $\text{Mg}_3(\text{OH})_5\text{Cl}\cdot 4\text{H}_2\text{O}$ ('F5'-Phase), $\text{Mg}_2(\text{OH})_3\text{Cl}\cdot 4\text{H}_2\text{O}$ ('F3'-Phase), and $\text{Mg}_2(\text{CO}_3)(\text{OH})\text{Cl}\cdot 3\text{H}_2\text{O}$ (Chlorartinite). The formation of the latter can be explained by the degradation of the F5 phase according to:



and consecutively



The amount of chlorartinite present in the binder varies from < 0.1 up to 30 wt%. Usually, very little chlorartinite is formed over long periods of time. On the other hand, chlorartinite was detected after a drying time in air of only two weeks in the laboratory, suggesting that its formation is a relatively fast process. Excess water is believed to be responsible for the formation of appreciable amounts of chlorartinite, possibly making it an indicator for bricolage.

In 1998, chlorartinite was also found as a naturally occurring mineral and was first described as an opaque white crystalline volcanic exhalation product on volcanic glass at the third cone of the Northern Breakthrough of the Main Tolbachik fracture eruption (1975-1976), Kamchatka, Russia. The name of chlorartinite as the chloride analog of artinite, named after the Italian mineralogist of E. Artini (1866-1928), was approved by IMA 1998.

Due to the lack of single crystals suitable for single crystal analysis, we determined its crystal structure from high-resolution synchrotron powder diffraction data using the technique of Monte Carlo simulated annealing and Rietveld refinement. Also, we performed a full quantitative phase analysis (QPA) using the Rietveld method for a real magnesia floor.

The sample of chlorartinite was synthesized by adding a 10 wt% solution of $(\text{NH}_4)\text{HCO}_3$ into a hot concentrated solution of magnesium chloride. Chlorartinite then precipitates after short time. The probe of the magnesia floor for quantitative analysis was drilled out of a one year old magnesia screed in an industrial manufacturing building. Pycnometric determination of the density of chlorartinite at $T = 295 \text{ K}$ using a He-Pycnometer lead to a density of $1.63(3) \text{ g/cm}^3$.

High resolution X-ray powder diffraction experiments were performed at the SUNY X3B1 and X16C beamlines of the National Synchrotron Light Source at Brookhaven National Laboratory. A structural starting model for Rietveld refinement was subsequently found with the Monte Carlo simulated annealing program FOX in space group $R3c$. The initial composition of chlorartinite $[\text{Mg}_2(\text{OH})\text{ClCO}_3] \cdot 3 \text{ H}_2\text{O}$ which was used as input for FOX was taken from the ICDD database (PDF 7-278). The CO_3 moiety was restrained assuming an ideal triangular geometry with a C–O bond length of 1.23 \AA and an O–C–O angle of 120.0° . Although the preferred coordination number of the magnesium atom is known to be six the actual distribution of the ligands between chlorine and oxygen atoms was not known *a priori*. Thus, no further geometrical constraints were introduced in the simulated annealing process. Hydrogen atoms were neglected. After about 20 million cycles (approximately 24 hours on a 2 GHz standard PC), a promising starting model in terms of crystal packing was found and subjected to Rietveld refinement using the GSAS program. Starting values for the lattice parameters, the background, and the peak profile were taken from the corresponding LeBail fit. In order to stabilize the Rietveld refinement, the CO_3 moiety was treated as an almost rigid triangular entity with an overall temperature factor and strong restraints on bond lengths and bond angles. All other non-hydrogen atoms of Mg, Cl and

O were freely refined using isotropic temperature factors. No hydrogen atoms were introduced in the Rietveld refinement. Although quick convergence was reached, the temperature factors of two oxygen atoms bonded to the magnesium atom turned slightly negative. A comparison with the crystal structure of artinite suggested the presence of hydrogen atoms in form of OH and OH_2 groups depending on the position of the oxygen atoms at the free vertex of a MgO_6 octahedron or at the corner of two edge sharing MgO_6 octahedra. Since the position of the hydrogen atoms could not be refined from powder diffraction data, the occupancy of the relevant oxygen atoms was increased to 1.125 for OH and 1.25 for H_2O , taking into account the additional electron density from the hydrogen atoms. This little trick immediately turned the temperature factors of these oxygen atoms into positive. Subsequent difference-Fourier cycling found disordered oxygen atoms in the honeycomb like channels, which can be attributed to water molecules. Thus, the formula of chlorartinite as determined from powder diffraction changed to $[\text{Mg}_2(\text{CO}_3)(\text{H}_2\text{O})(\text{OH})]\text{Cl} \cdot \text{H}_2\text{O}$. The final Rietveld refinement converged nicely with maximum residuals in the electron density map between -0.827 e\AA^{-3} and 0.666 e\AA^{-3} . No inversion center was found, confirming $R3c$ as the correct space group. The final Rietveld plot is given in Fig. 74.

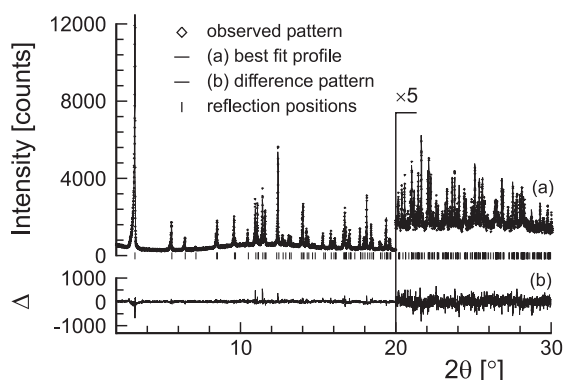


Figure 74: Rietveld plot of chlorartinite at $T = 295 \text{ K}$. The high angle part starting at 20° (2θ) is enlarged by a factor of 5. The wavelength was $\lambda = 0.64889(2) \text{ \AA}$.

Chlorartinite crystallizes in a complicated zeolite-like 3D-honeycomb framework structure with large 1D-channels running along *c*-direction. Chlorine atoms and disordered water molecules are located within the channels (Fig. 75). The two crystallographically distinct magnesium atoms are coordinated by distorted octahedra of the type $\text{Mg}(1)\text{O}_4(\text{OH}_2)(\text{OH})$ and $\text{Mg}(2)\text{O}_5(\text{OH})$. All Mg-polyhedra are connected to 5 neighboring Mg-polyhedra and to two triangular CO_3 groups sharing edges and corners. As building blocks of the channel walls, 15-membered puckered rings of Mg-polyhedra can be isolated where the triangular CO_3 moieties act as chelating ligands. The perspective crystal packing of chlorartinite is shown in Fig. 75. The chlorine atoms and the disordered water molecules in the channels are clearly visible. The most embossed atom within the channel structure is O1, which the distance of $\text{O1}\cdots\text{O1}$ is $6.454(15)\text{Å}$. The disordered water molecules are located within the triangle which is formed by these oxygen atoms. The shortest contact distances between channel structure and captured atoms are: $3.000(10)\text{Å}$ for $\text{Cl1}-\text{O6}[-x+y, y, z-0.5]$, $2.75(4)\text{Å}$ for $\text{O7}-\text{O1}[-y, x-y, z]$, and $2.68(3)\text{Å}$ for $\text{O8}-\text{O1}[-y, x-y, z]$, allowing the formation of hydrogen bonds. Likewise, hydrogen bonds are also formed by the non-coordinated chlorine atom and the free water in the channels, with a contact distance of $3.064(19)\text{Å}$ between Cl1 and O8. Although chlorartinite $[\text{Mg}_2(\text{CO}_3)(\text{H}_2\text{O})(\text{OH})]\text{Cl}\cdot\text{H}_2\text{O}$ was named as the chloride analog of artinite, $[\text{Mg}_2(\text{CO}_3)(\text{OH})_2]\cdot 3\text{H}_2\text{O}$, its crystal structure is completely different from that of artinite, where the magnesium atoms are octahedrally surrounded by three hydroxyl groups, two water molecules and one oxygen atom which is disordered between water molecule and carbonate group. Instead of forming rings, the Mg-octahedra of Artinite are arranged in 1D double zig-zag chains running along *b*-axis and are stabilized by a complicated framework of hydrogen bonds. In contrast, the crystal structure of chlorartinite consists of a 3D-framework with large channels in a honeycomb fashion

which captured free chlorine atoms and disordered water molecules. The chemical composition as found by the structure determination process differs slightly from previous reports in literature.

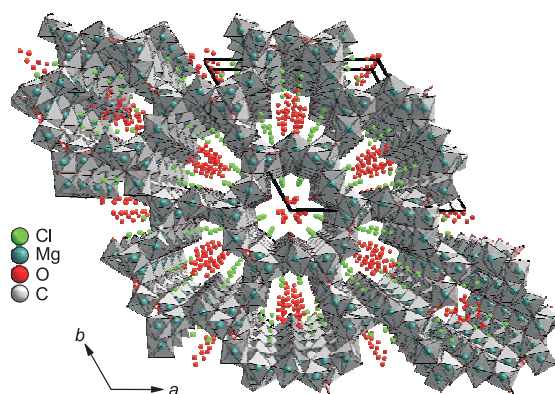


Figure 75: Perspective view of the crystal structure of chlorartinite in a central projection down to the crystallographic *c*-axis. Semi-transparent MgO_6 and CO_3 polyhedra are drawn.

A qualitative phase analysis of the synchrotron powder diffraction pattern of the industrial magnesia floor using the ICDD database revealed quartz (PDF 83-539), chlorartinite (PDF 7-278), calcite (PDF 83-577), microcline (PDF 76-1239) and clinotobermorite (PDF 88-1328). A QPA by the Rietveld method using the program GSAS revealed the following composition in weight%: 52.3(1)% for quartz, 28.9(2)% for chlorartinite, 9.9(1)% for microcline, 8.8(1)% for calcite and 0.13(3)% for clinotobermorite, respectively. The Rietveld plot of the QPA of the magnesia floor using a logarithmic intensity scale for better visibility of the minor phases is shown in Fig. 76. Quite unusually, the QPA of this particular sample revealed that literally all binder transformed into chlorartinite which might be caused by a bloomer during the blending or setting process of the screed.

Preliminary in situ synchrotron powder diffraction, DSC, TG and MAS on chlorartinite up to $T = 500^\circ\text{C}$ revealed a variety of phase transitions within a small temperature range starting at $T = 125^\circ\text{C}$ while decomposition into $\text{Mg}(\text{OH})_2$ slowly starts at about $T = 190^\circ\text{C}$.

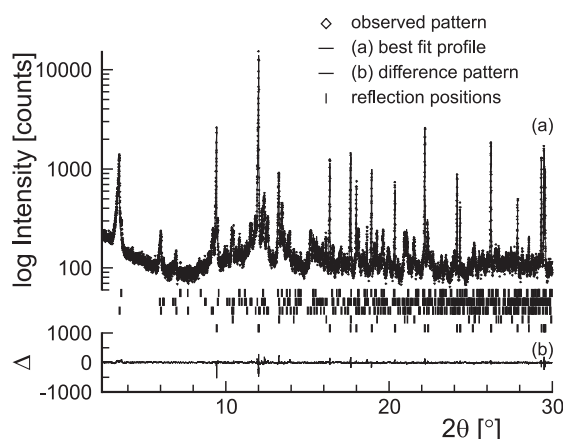


Figure 76: Rietveld plot (5 phases) of a magnesite screened at $T=295$ K. The intensity is plotted on logarithmic scale. The wavelength was $\lambda=0.70041(2)$ Å.

The different phases of chlorartinite are attributed to the step-wise loss of water molecules from the channel. It is interesting to note the water in the channels of chlorartinite is so loosely bound and that there is an immediate loss of crystal water if chlorartinite is ex-

posed to a dry inert-gas stream at room temperature. This also explains the difference between the density of $1.63(3)$ g/cm³ from a He-pycnometer and the X-ray density of 1.758 g/cm³. Removing the water molecules would decrease the X-ray density to 1.597 g/cm³ which is in excellent agreement to the pycnometrically determined value.

The ability of chlorartinite to quickly exchange crystal water along with a fast change in density of more than 15% makes it likely that industrial floors containing substantially amounts of chlorartinite are very sensitive to humidity conditions, leading to possible cracking damage. A quantitative analysis of chlorartinite can therefore be regarded as an indicator for the quality and the actual condition of these floors. We are currently in the process of collecting in situ powder diffraction data of chlorartinite in dependence on temperature- and humidity in order to fully understand the different phases of chlorartinite and their influence on the stability of magnesite floors.

Floating zone growth of lithium iron (II) phosphate single crystals

D.P. Chen, G. Götz and C.T. Lin

The need for compact, high-energy density, low cost, environmentally friendly and safe rechargeable batteries has led to the development of the lithium-polymer and lithium-ion battery concepts. During the past few years the search for cathode materials of rechargeable lithium batteries has focused mainly on lithium metal oxides. Among them, lithium iron phosphate, LiFePO_4 , is one of the most promising candidates, since it provides an attractive voltage of 3.5 V, high theoretical capacity (170 mAhg^{-1}), low cost, ease of synthesis, and stability when used with common organic electrolyte systems. However, large, high-quality crystals have not been available up to now but are required for the study of

the structural, physical and chemical properties, particularly for the electronic and magnetic anisotropies. Therefore, the growth of large and high-quality single crystals is of critical importance.

When sintering LiFePO_4 , difficulties appear due to the oxidation and the high volatilization of Li at temperatures above 500°C . Moreover, the compound melts incongruently and readily decomposes during the sintering process, leading to a multiphase mixture of Fe_2O_3 , Li_3PO_4 and $\text{Li}_3\text{Fe}_2(\text{PO}_4)_3$. Obviously, obtaining high-quality single crystals is rather difficult. In this contribution we present a floating zone method for preparing large and high-quality single crystals and demonstrate their structural behavior.

LiFePO_4 powders of stoichiometric composition were synthesized by solid-state reaction. The starting materials, Li_2CO_3 , $\text{FeC}_2\text{O}_4 \cdot 2\text{H}_2\text{O}$ and $\text{NH}_4\text{H}_2\text{PO}_4$, were mixed with acetone and milled for 4 hours using zirconia milling media. The mixtures were dried by argon flow for 24 hours and then stored in a glove box to avoid oxidation and water absorption in air. The polycrystalline material was obtained by calcining the dried mixtures at 350°C for 10 hours, followed by raising up to 600°C for a day in Ar atmosphere and finally slowly cooling down to room temperature at a rate of 120°C/h . The obtained polycrystalline powders were determined to be single phase LiFePO_4 by X-ray powder diffraction (XRD).

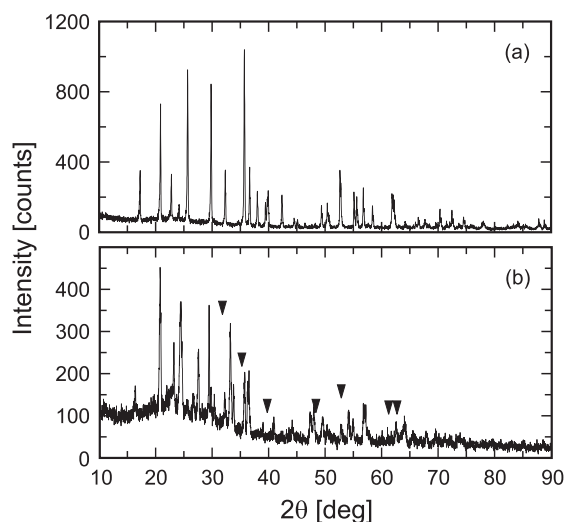


Figure 77: Powder XRD pattern of the sintered LiFePO_4 powders, (a) Greenish powder is a single phase of LiFePO_4 . (b) Orange powder consists of Fe_2O_3 (filled triangles) and $\text{Li}_3\text{Fe}_2(\text{PO}_4)_3$.

Sintered LiFePO_4 rods usually exhibit an orange skin covering the outer surface but are greenish inside. The orange powder is readily formed during the conventional solid-state reaction process. The amount is estimated to be less than 10% of the total weight. XRD diffraction patterns indicated that the orange powder consists mainly of Fe_2O_3 and $\text{Li}_3\text{Fe}_2(\text{PO}_4)_3$, which are the decomposition products. The greenish powder is determined to be LiFePO_4 with an orthorhombic cell: $a = 10.318(2)\text{Å}$,

$b = 6.001(2)\text{Å}$, $c = 4.688(1)\text{Å}$. XRD patterns for both greenish and orange powders are shown in Figs. 77(a) and 77(b), respectively.

The crystal growth was carried out in an optical floating zone furnace using $4 \times 300\text{ W}$ halogen lamps installed as infrared radiation sources. The feed rods used to grow crystals were formed using the greenish powders. Our growth experiments demonstrate that the surface of the feed rods was usually covered with the orange layer of Fe_2O_3 and $\text{Li}_3\text{Fe}_2(\text{PO}_4)_3$ after premelting of the greenish rods prior to the growth. These two phases could be again observed on the surface of the as-grown crystal ingot if the growth was carried out with the sintered or premelted rods, whereas the inner part of the ingot is always pure LiFePO_4 . This suggests that these two phases resulted from an overheating or multiple heating process, which led to the decomposition of the compound. Attempting to minimize the impurities, we used the as-pressed greenish rods directly to grow crystals without the conventional process of sintering and premelting, and the orange layer no longer appeared on the crystal surface.

The volatilization of Li may cause a non-stoichiometric or decomposed compound during growth. We found the volatilization products precipitated as fine powders on the inner wall of the silica tube. The volatilization increases with growth time and leads to a Li-poor compound of $\text{Li}_{1-x}\text{FePO}_4$ formed in the end part of the ingots. Therefore, growth time is an important parameter to take into account. We applied a variety of growth rates between 2 and 4 mm/h for optimizing the total growth time in order to minimize the volatilization. A rate of 2 mm/h was used for the first 8 mm and thereafter a faster rate of 4 mm/h was used to complete the growth. A 10 cm long ingot of pure LiFePO_4 was obtained within a day. Figure 78 shows a typical crystal ingot of LiFePO_4 . The crystal grains were found to grow preferably along the crystallographic b -axis, parallel to the ingot axis. The ingot with a diameter of

5 mm and length of 70 mm exhibits a crack-free, black surface with metallic luster. Crystal wafers were cut and polished to mirror face which appeared blackish green. Under a polarized light microscope only 3 or 4 large grains were found on the periphery. No inclusions, cracks or grain boundaries are observed in the inner area of about 4 mm diameter.

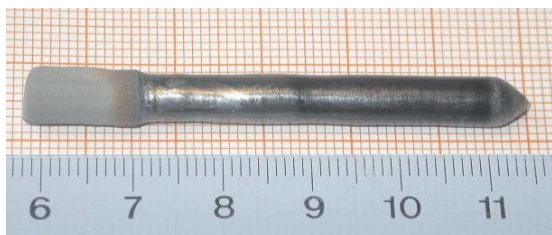


Figure 78: As-grown LiFePO_4 single crystal ingot. The grey part of the ingot was used as a seed from the polycrystalline rod.

XRD measurements were made on a number of as-grown crystals to identify their structure. A crystal plate was cleaved along the growth direction. The XRD pattern is shown in Fig. 79(a). All peaks are indexed to be $(0k0)$ reflections of LiFePO_4 . Using a fitting method with the Nelson-Riley (N-R) function, the b -axis lattice parameter is estimated to be $6.010(1) \text{ \AA}$. All the $(0k0)$ peaks are well-fitted by the N-R function that indicates good crystal quality. Figure 79(b) shows a typical XRD pattern of a powdered single crystal, indicating the single phase of LiFePO_4 . No traces of impurities or inclusions were observed for the entire ingot. The pattern can be indexed with the orthorhombic cell: $a = 10.278(3) \text{ \AA}$, $b = 5.998(1) \text{ \AA}$, $c = 4.6914(8) \text{ \AA}$. This cell volume is slightly larger than that of the powder sample in Fig. 77(b).

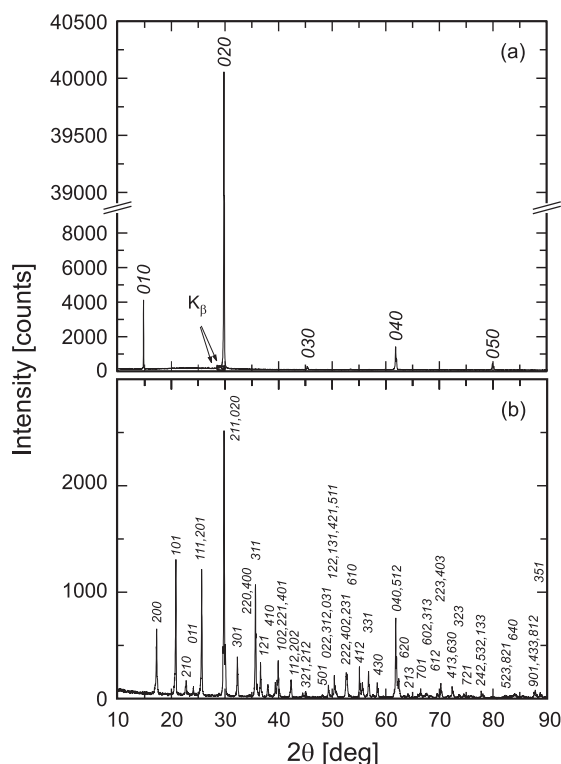


Figure 79: X-ray diffraction patterns of LiFePO_4 single crystals. (a) Showing the $(0k0)$ peaks of a sample surface cleaved along the growth direction (the appearance of the K_β is due to a high intensity of CuK_α applied). (b) Showing all (hkl) peaks corresponding to LiFePO_4 .

In conclusion, single crystals of LiFePO_4 can be grown using the floating zone technique. The XRD patterns indicate that the orange powder contains both Fe_2O_3 and $\text{Li}_3\text{Fe}_2(\text{PO}_4)_3$, while the greenish powder is pure LiFePO_4 . The availability of single crystals opens the door to structure (X-ray and neutron scattering) and transport studies for achieving a more accurate understanding of electronic and magnetic anisotropies and better insight into this interesting ionic compound.

Determining the structure(s) of the amorphous ceramic a-Si₃B₃N₇: a case study

J.C. Schön and A. Hannemann; L. van Wüllen (Universität Münster); M. Jansen

Among the states of condensed matter, those classified as ‘amorphous’ are probably the least understood, and dealing with them is still regarded a scientific and intellectual challenge. Most of the conceptual, experimental and theoretical intricacies related to this state of matter originate from its thermodynamically metastable nature – already determining the structure of amorphous compounds is highly difficult. While many experimental probes taken together can yield valuable information, a multitude of different atomic configurations can reproduce these data within the experimental limits, and it is hard to correlate the results and to generate a complete and consistent structural model. As a consequence, one might want to turn to theory for an answer. However, if we were to rely on theory alone, we would face the (currently) nearly impossible task of very precisely reproducing the synthesis process in the simulations. Therefore, our approach combines experiment with theoretical modeling, by sampling experimentally as many structural data of the material under consideration as possible, followed by theoretical model calculations to produce a full picture of the particular amorphous compound under investigation. Here, one would take in particular certain unambiguous experimental structural data into account, in order to focus on that part of the space of amorphous configurations, where the compound under investigation resides.

As an example system for this methodology, we have chosen the amorphous silicon boron nitride a-Si₃B₃N₇, a random network of silicon and boron, interconnected by nitrogen via chemical bonds of predominantly covalent character, which is a prototype for the technologically very interesting family of Si/B/N/C ceramics (concerning these systems, c.f. Jahrbuch 2000, Jahresberichte 1999, 2000). Si₃B₃N₇ is not produced via glass formation,

i.e. by quenching from a melt; instead, one employs the so-called sol-gel route starting from single component precursors such as TADB ((SiCl₃)(NH)(BCl₂)). These molecules are linked to oligomers via ammonolysis in NH₃ and subsequent condensation, followed by a pyrolysis in N₂ atmosphere.

The resulting ceramic a-Si₃B₃N₇ is a white powder of low density ($\rho = 1.9 \text{ g/cm}^3$) that is insensitive to air, and for which thermal decomposition, evolving N₂, starts at 1650°C and proceeds rapidly at 1750°C. Straightforward diffraction experiments have not produced Bragg reflections, neither with X-rays (synchrotron) nor with neutrons or electrons. Since it does not show any significant deviation from the ideal composition, a-Si₃B₃N₇ parallels in this respect the prototypical glassy system, quartz glass, and may be regarded as a ternary nitridic analogue of a-SiO₂. Of course, the more complicated composition of a-Si₃B₃N₇ implies that structure analyses are more difficult. On the other hand, the broader choice of ad-atoms for applying structural probes is expected to yield a greater variety of information.

Employing XANES, neutron, electron and X-ray diffraction techniques and MAS-NMR spectroscopy, the short range order is found to comprise tetrahedral SiN_{4/3} and trigonal planar BN_{3/3} and NB_{x/3}Si_{(3-x)/4} units. These local building blocks are the constituents of the amorphous network. Local deformations, which are due to inherent strains, seem to accumulate within the N–Si–N angles.

The connectivity of these building blocks has been probed employing dipolar NMR methods [1] and studying the pair correlation functions (PCF) obtained from neutron, X-ray and electron scattering experiments. The existence of Si–N–B linkages, as deduced from the neutron difference function employing isotopic contrast

techniques (c.f. Fig. 80), could be confirmed and quantified with the help of $^{11}\text{B}\{-^{29}\text{Si}\}$ -REDOR, $^{29}\text{Si}\{-^{11}\text{B}\}$ -REAPDOR and ^{29}Si spin echo NMR spectroscopy. The results suggest a partial segregation of metalloid nuclei of the same type on intermediate length scales (2–8 Å).

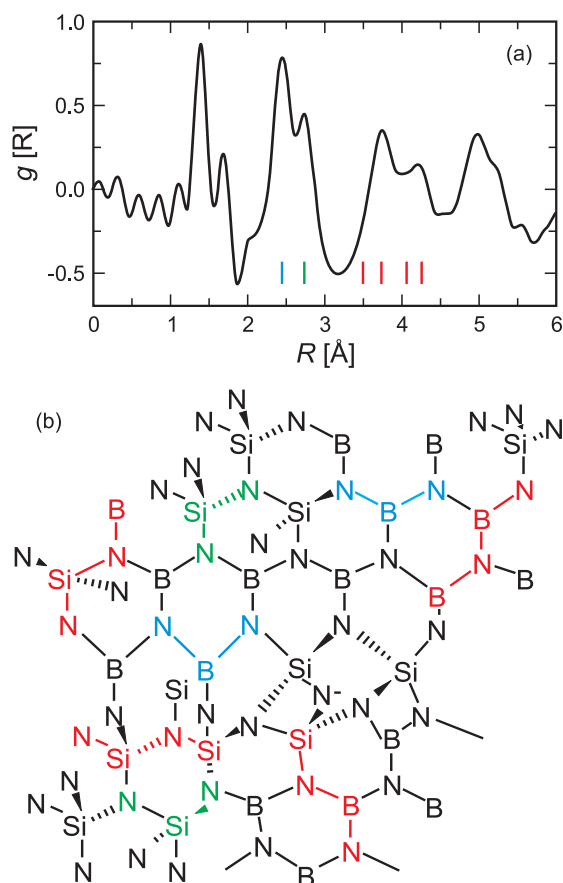


Figure 80: (a) Fourier transform $g(r)$ of the first-order neutron difference, $(\text{Si}_3^{11}\text{B}_3\text{N}_7 - \text{Si}_3^{11}\text{B}_3^{15}\text{N}_7)$. By taking this difference of the intensities, only terms including the correlation of the substituted element (nitrogen) are present in the difference function. (b) Excerpt from a hypothetical $\text{Si}_3\text{B}_3\text{N}_7$ network, with network fragments identified via scattering experiments being shown in color. Note that the connectivity of these fragments is not accessible from experiment.

According to the NMR results, a central boron atom is surrounded by 4–5 boron atoms and only 1–2 silicon atoms in the second coordination sphere. Correspondingly, a central silicon

atom is connected via the four nitrogen atoms in the first coordination sphere to an average number of six silicon atoms and two boron atoms in the second coordination sphere. However, high (lateral) resolution elemental maps of Si, B and N in $\text{Si}_3\text{B}_3\text{N}_7$ employing element specific imaging have been generated, which show that on length scales beyond ca. 1 nm the two cations are homogeneously distributed, with no indication of phase separation or clustering.

As was mentioned above, it is necessary to complement the results of the experimental probes by computer simulations. Structure models have been generated by computational techniques and validated by matching the results of the experimental probes [2]. Since it was not obvious at the outset, to what extent the actual synthesis route would determine the structural features of the amorphous ceramic, five different classes of models have been generated, each corresponding to a different hypothetical synthesis route (quench from melt, sintering of nanocrystals, growth and sintering of clusters, film deposition, and actual polymer-precursor route [3]).

When matching the properties of these models with experiment, one finds that the short range order is the same in all models, and in agreement with experiment. However, beyond the nearest-neighbor peaks, the PCFs of the different model classes exhibit statistically significant differences (as can be seen in Fig. 81 depicting models with heterogeneous and homogeneous cation distributions, respectively), and satisfactory agreement with the experimental data is only found for two models, the nano-crystallite and the precursor-route models. These two models also show the best agreement with experiment as far as the deviations of the next-nearest neighbor cation-cation distribution is concerned. One should note that the atom configurations belonging to these two classes of structural models possess systematically higher energies than the other three classes of structures.

In particular, this result implies that the partial separation of the cations on the sub-nanometer scale, which corresponds to a violation of Löwenstein's rule, cannot be understood on a purely thermodynamic basis using minimization of the energy as the only criterion.

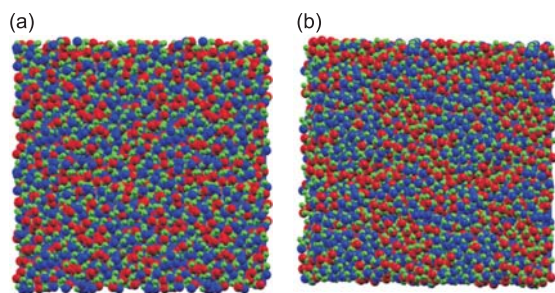


Figure 81: Structure models for $\text{a-Si}_3\text{B}_3\text{N}_7$ generated by quenching a $\text{Si}_3\text{B}_3\text{N}_7$ melt (a) and following the sol-gel route (b), respectively. The homogeneous cation distribution in the melt-route model contrasts with the heterogeneous distribution found in the sol-gel model. The structures are shown as ball models, with red, blue and green spheres corresponding to Si, B and N, respectively.

The best models even agree well with details found experimentally, e.g. most deviations from an ideal local environment are found for silicon visible in e.g. departures of the local coordination number from $\text{CN}=4$, and in a broad distribution in the N-Si-N angles. Even the edge-sharing of polyhedra found in the calculations can be assigned to measurement features previously not identified, such as shoulders in the experimental PCF. Such agreement in both global and local structural properties makes us confident that a structural model coming close to reality has been achieved.

The rather low bulk density seen in experiment (only 2/3 of the value expected from a binary mixture of BN and Si_3N_4) indicates that $\text{a-Si}_3\text{B}_3\text{N}_7$ possesses a rather open structure.

Such a low density is also found during the simulations of the precursor route (as the only one of the five model classes), and constant temperature simulations starting from configurations that already contain sub-nanometer size pores show quite a high stability up to relatively high temperatures. Further bulk properties such as the specific heat, the bulk modulus, or the thermal conductivity, can now be calculated; however, the corresponding experiments have not yet been performed.

To conclude, our investigations presented here strongly emphasize the fact that the structure of a given amorphous material can only be successfully modeled if as many features as possible of the synthesis route for the material are taken into account. While our investigations were motivated in part by the desire to better understand this new class of ceramic materials that have promising versatile and attractive high-temperature applications, the main driving force has been to utilize $\text{a-Si}_3\text{B}_3\text{N}_7$ in a case study aimed at testing and sharpening the tools available for analyzing the microstructures of amorphous materials. This system has served us as a 'Drosophila' for the development and validation of our experimental and theoretical methods. Only by their joint application has it been possible to generate and analyze reasonable structure models for this compound.

-
- [1] *van Wüllen, L. and M. Jansen. Journal of Materials Chemistry* **11**, 223-229 (2001).
 - [2] *Hannemann, A., J.C. Schön, H. Putz, T. Lengauer and M. Jansen. Physical Review B* **70**, 144201 (2004).
 - [3] *Schön, J.C., A. Hannemann and M. Jansen. Journal of Physical Chemistry B* **108**, 2210-2217 (2004); *Hannemann, A., J.C. Schön and M. Jansen. Journal of Materials Chemistry* **15**, 1167-1178 (2005).

Cluster disorder and ordering principles in Al-stabilized ‘LaI’

O. Oeckler (LMU München); T. Weber (ETH Zürich); L. Kienle, Hj. Mattausch and A. Simon

Diffuse X-ray scattering is frequently dismissed in conventional structure analyses. However, it contains valuable information in many respects, particularly concerning the chemical constitution of a crystal. The quantitative measurement of the continuous intensity distribution in reciprocal space became routinely feasible with the advent of area detectors, and quantitative structure refinement against diffuse data will become more and more accessible in the future. Here we present a case, where only the refinement against diffuse scattering data led to detailed insight into the chemical nature of a compound [1]. This study is part of our work on reduced lanthanide halides which in recent time developed into a new area in inorganic chemistry with a plethora of phases, most of them characterized by discrete or condensed metal clusters in their structures. The majority of the compounds contain in the cluster centers endohedral atoms, metallic as well as nonmetallic elements.

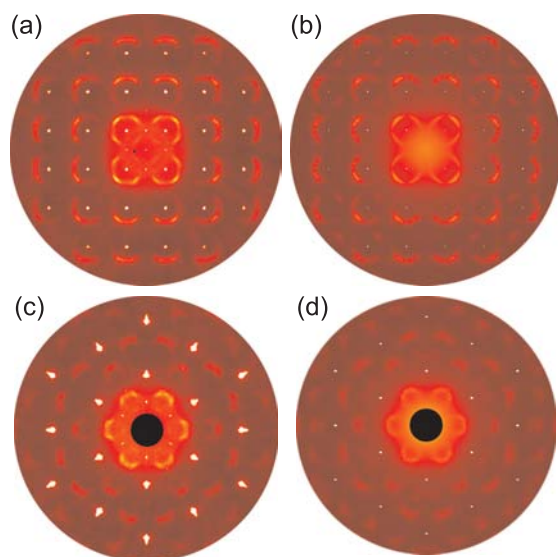


Figure 82: (a),(c) Experimental and (b),(d) calculated X-ray diffraction patterns for $\text{La}_{\approx 0.7}\text{I}_{\approx 0.88}\text{Al}_{\approx 0.12}$: first layer perpendicular [100] (a),(b) and zero layer perpendicular [111] (c),(d); the calculated images are based on the best refinement result.

A phase with the approximate composition $(\text{La}_{1-x}\text{Al}_x)\text{I}$ ($x < 0.15$) can be refined down to $R \approx 5\%$ in a NaCl-type structure on the basis of sharp Bragg reflections. In spite of the convincing value this structural characterization is incomplete or even misleading. A correct structural model can be derived only by taking into account the pronounced diffuse scattering that shows up as sections of hollow spheres (Fig. 82).

A hint to an interpretation of the diffraction data comes from the extended cluster chemistry of the rare earth metals: The $\text{M}_6\text{X}_{12}\text{Z}$ entity can be viewed as a section of the rocksalt structure, and if we assume the presence of $\text{La}_6\text{I}_{12}\text{Al}$ clusters in the title compound, the occurrence of structured and narrow diffuse scattering indicates their non-random distribution.

The presence of spheres and their location only around odd Bragg reflections is due to some spherical modulation characterized by a complementary behavior of cation and anion sites, and the higher intensity on the large-angle side indicates lattice distortions due to a size effect, with the stronger scatterer being the larger structural motif. A quantitative structure solution is gained via a new, very efficient evolutionary algorithm [2].

A (defect-)NaCl-type structure with the appropriate composition can be derived from a *fcc* lattice of I atoms by statistically substituting a variable number of I atoms (11% to 15%) by La_6Al units to create a set of 80 different structures (‘individuals’) each defined by a specific set of parameters. In Monte-Carlo calculations we used 13 parameters, including different interactions for edge and corner sharing octahedra and all possible relative cluster positions up to a distance of 13.4 Å. Furthermore, the cluster concentration and local relaxation around vacancies and interstitial atoms are parameters of the disorder model.

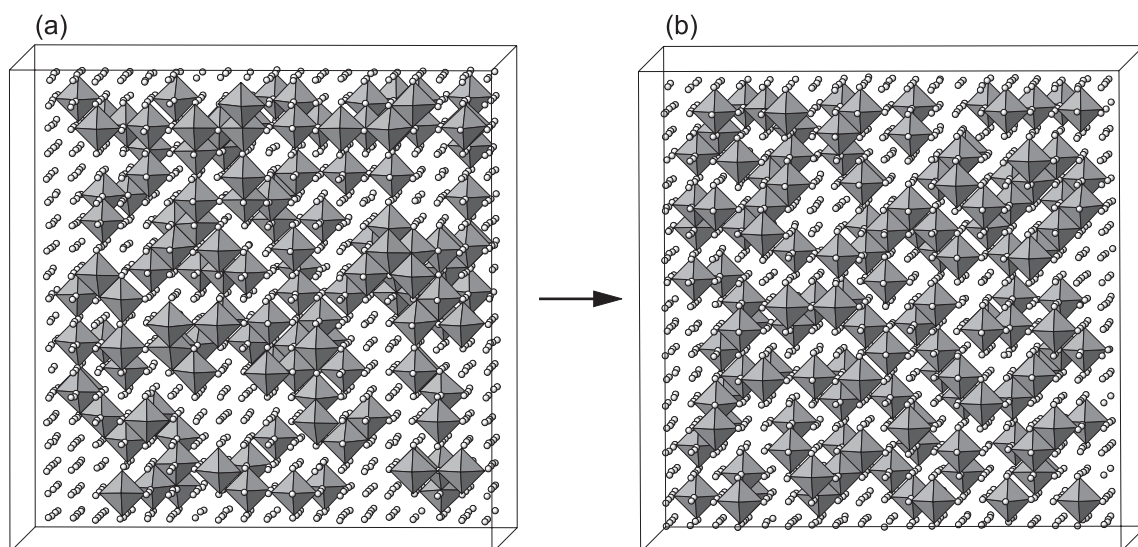


Figure 83: Representative parts of the model crystal ($x = 0.136$; La_6Al octahedra, I atoms) before MC calculation and the final model crystal (after MC simulation with the refined parameters).

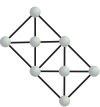
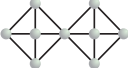
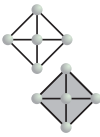
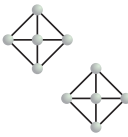
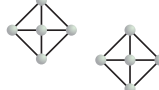
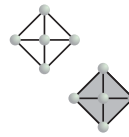
The pixelwise comparison of the scattering intensities calculated for these model structures with observed intensities is quantified by an R-factor for each individual. Then the next generation of structures strictly related to the specific parents and hence comprising the same number of individuals as the starting set, is created by admixing a certain percentage of another parent's parameter set, and those members of the new generation are dismissed whose structures lead to an inferior fit to the experimental data. In a late generation the calculation converges to a set of statistically identical structures which optimally represents the experimental scattering pattern. This final model is analyzed in terms of the structural features actually present.

Figure 83 illustrates that the final structure model exhibits a uniform cluster distribution in contrast to the random arrangement for the refined cluster concentration x . This refinement yields $x = 0.136$ and a formula $\text{La}_{0.69}\text{I}_{0.86}\text{Al}_{0.14}$ which is confirmed by chemical analyses. The deviation of La and I atoms from the ideal NaCl positions as refined from diffuse data is in good

agreement with the corresponding numbers derived from Bragg data, however, now the displacements can be interpreted directly in terms of a contraction of the clusters. The cluster geometry is in very good agreement with that of $\text{La}_6\text{I}_{12}\text{Al}$ or related clusters in other compounds. Based on this result, a reasonable interpretation of Bragg data can be obtained, too, in a constrained refinement assuming one anion site with x Al and $(1-x)$ I and implying Ln_6Al octahedra by placing $6x$ Ln on the cation site around Al. In accordance with the result from diffuse data, x amounts to 0.110(1). However, information on the interconnection of clusters can only be derived from the final structure model.

Table 4 shows that edge or corner sharing octahedra are very unfavorable in this compound as their frequency amounts to 49% and 31%, respectively, of the random arrangement. Configurations that do not allow complete relaxation are observed less frequently, and the tendency to avoid local strain is evident from the most favorable relative cluster position in which the centers are on opposite corners in $[111]$ direction of the NaCl cell.

Table 4: Comparison of relative cluster positions – characterized by lattice vectors corresponding to a NaCl unit cell – for (a) random cluster distribution with $x = 0.136$ before Monte Carlo calculation and (b) the final model crystal. The frequencies of intercluster arrangements are denoted n_i for (a) and n_f for (b).

Relative cluster positions						
	[0.5, 0.5, 0]	[1, 0, 0]	[0.5, 0.5, 1]	[1, 1, 0] ¹⁾	[1.5, 0.5, 0]	[1, 1, 1] ²⁾
n_i	55856	27875	111602	55976	111759	37203
n_f	27108	8687	95275	59479	148168	59708
n_i/n_f	0.49	0.31	0.85	1.06	1.33	1.60

¹⁾ fc in $2a2b2c$ supercell ²⁾ bc in $2a2b2c$ supercell

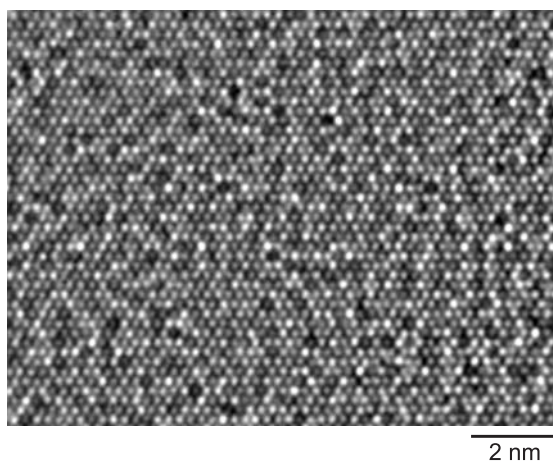


Figure 84: HRTEM image of a disordered crystal of $\text{La}_{\approx 0.7}\text{I}_{\approx 0.88}\text{Al}_{\approx 0.12}$ along zone axis [111].

Additional evidence for the preference of this relative cluster orientation has also been obtained from high-resolution electron microscopy (HRTEM) studies. Images taken along the zone axis [111] (Fig. 84) show the disordered structure as light spots for rows of La and I, and dark spots for rows of Al and voids. Prolonged exposure to the electron beam as well as long time annealing does not remove the disorder which indicates the impossibility of the title compound to order in small unit cells with high symmetry.

Summing up, the disorder in the cluster distribution is far from a statistical random function. The uniform (not *random*) cluster distribution leads to an approximately harmonic radial distribution function of intercluster vectors that is reflected in the diffuse spheres. The preferred relative cluster arrangement allows a unique possibility to avoid short distances in a dense packing by contraction of both Ln_6 units around endohedral Al atoms and of I_6 octahedra around voids.

Finally, we point out that our investigation, though addressing a special system, is relevant to the extended structural chemistry of NaCl-type transition metal oxides, nitrides, and carbides. They form ordered cluster structures in a few instances, e.g. NbO or TiO, and frequently show diffuse scattering effects due to local order and long-range disorder.

- [1] Oeckler, O., T. Weber, L. Kienle, HJ. Mattausch and A. Simon. *Angewandte Chemie* **117**, 3985-3989 (2005), *Angewandte Chemie International Edition* **44**, 3917-3921 (2005).
- [2] Weber, T. and H.-B. Bürgi. *Acta Crystallographica A* **58**, 526-540 (2002).

Geometric variations and electron localizations in intermetallics: PbFCl type compounds

J. Nuss, U. Wedig and M. Jansen

The geometric structures of intermetallic phases are determined by a complex interplay of various bonding types. Ionic and covalent interactions caused by charge transfer among the atoms and by local electronic structures compete with the forces that itinerant electrons exert on the atomic cores. Compounds with the general formula A_2B , crystallizing in the anti-PbFCl type of structure, were investigated exemplarily by experimental and theoretical means to demonstrate the complexity of chemical bonding in intermetallic phases.

The PbFCl structure is adopted by about 540 known compounds. All of them are isopointal, i.e. they crystallize in the same space group ($P4/nmm$) and the atoms occupy the same sites $c2a$ ($tP6$): F in $2a$, Cl in $2c$ and Pb in $2c$. In the A_2B intermetallic compounds regarded here

[1], a transition metal A takes up the positions of F (A1) and Cl (A2) and a pnictogen atom B (As or Sb) that of Pb.

The variations in the structural details are reflected by different c/a ratios and the spread of the two free atomic parameters z_{A2} and z_B . The ratio of the latter ones $q = z_{A2}/(1 - z_B)$ (Fig. 85) is a measure of the unevenness of the (A2)B layer and may be plotted against $p = c/a$ in order to generate a structure field diagram. Compounds with q larger than 1.5 are generally ionic or very polar [2]. The section of the PbFCl structure map with q smaller than 1.5 is shown in Fig. 85. The low q value together with a rather low c/a ratio is characteristic for the intermetallic representatives and corresponds to a moderate or in the case of Cu_2Sb even reversed buckling of the (A2)B layers.

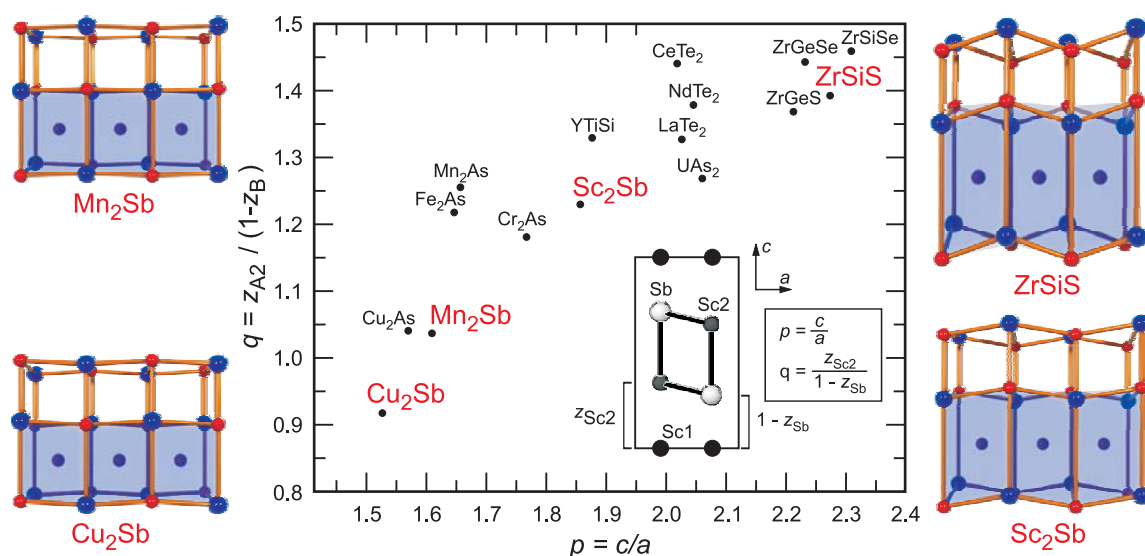


Figure 85: Structure map, showing selected A_2B compounds. Plotting q vs. p allows classifying the structural variation. The definition of q and p is shown at the example of Sc_2Sb as an insert. The structural fragments illustrate the corrugation of the NaCl-like structures of (A2)B, as forced by the interstitial A1 atoms.

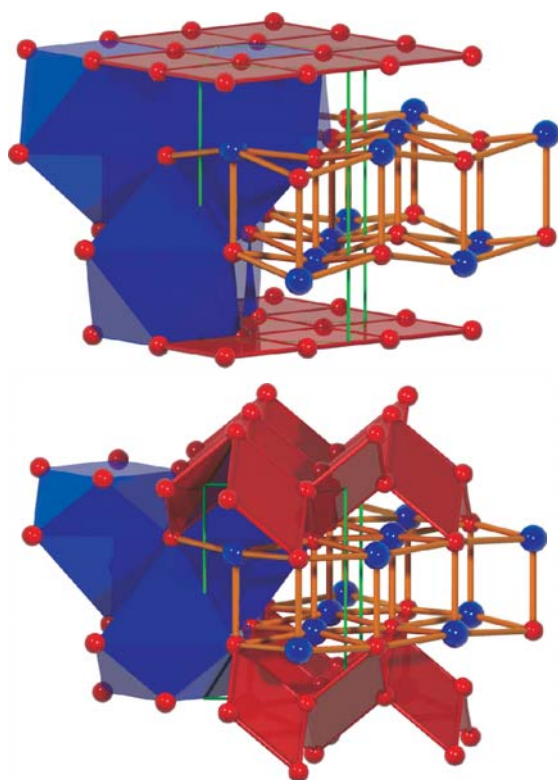


Figure 86: Top: Sc_2Sb structure, bottom: Cu_2Sb structure, with unit cells (green lines). The blue polyhedra emphasize the SbA_9 mono-capped, tetragonal antiprisms (left half). The red rods and planes emphasize the shortest metal-metal distances (Sc1-Sc1 left, Cu1-Cu2 right). The orange bonds between Sb (blue spheres) and Sc2, Cu2 (red spheres) illustrate the puckered double layer $[(\text{Sc}_2)\text{Sb}]$, $[(\text{Cu}_2)\text{Sb}]$ as a $[\text{NaCl}]$ analogous slab (right half).

Because of these geometrical features, the description of the structures in terms of coordination polyhedra (Fig. 86, left half), which is suitable for the more ionic compounds, is less clear. The intermetallic compounds may more appropriately be regarded as arrangements of stacked layers (Fig. 86, right half) or as variants of the NaCl structure, where half of the A_2B_4 heterocubane units are filled by A1 as shown in Fig. 85.

Cu_2Sb is unique among the compounds investigated here, being the only representative with $q < 1$. The Cu1-Cu2 distance (260 pm) is much

shorter than $d(\text{Cu1-Cu1}) = 283$ pm, suggesting at first sight Cu–Cu attractive interactions in the nonplanar 4^4 nets of Cu1 and Cu2, as highlighted by red planes in the right part of Fig. 86. However, $d(\text{Cu1-Cu1})$ is still larger than the atomic distance in elemental copper (256 pm). The relation of the geometrically different A–A distances is inverted when going from Cu_2Sb over Mn_2Sb to Fe_2Sb , and finally increases via Sc_2Sb continuously to ZrSiS . This trend is associated with an increase of p and q . The distance between two neighboring Sc1 atoms is 298 pm, 45 pm shorter than $d(\text{Sc1-Sc2})$ and even by 24 pm shorter than the atomic distance in metallic scandium. This indicates metal-metal interactions in the planar 4^4 nets formed by Sc1 only, which are highlighted by a red plane in the left part of Fig. 86. Even stronger interactions between the A1 components (Si) were expected in ZrSiS , according to its position in the structure map.

To understand the geometrical features of this class of compounds, in particular, the relation to their electronic structures, the results of DFT band structure calculations were analyzed. Considering the partial densities of states (Fig. 87) for the $3d$ -orbitals, a continuous lowering in energy, relative to the Fermi level, is observed when going from the left to the right in the first row of transition metals. For Cu_2Sb the $3d$ -bands are significantly below the Fermi level. As a consequence, the Sb $5p$ -levels get broadened, and their contribution to the DOS at E_F increases. The trends in the band structure can be related to the volumes of the atomic basins obtained from the topological analysis of the electron density and to the valence charges therein. The antimony basin in Sc_2Sb is considerably larger than the volume increment of Sb according to Biltz [3], whereas the Sc basins are smaller. This goes along with a charge transfer from the Sc sites to antimony. With increasing number of d -electrons, the volume relation and the charge transfer are reversed.

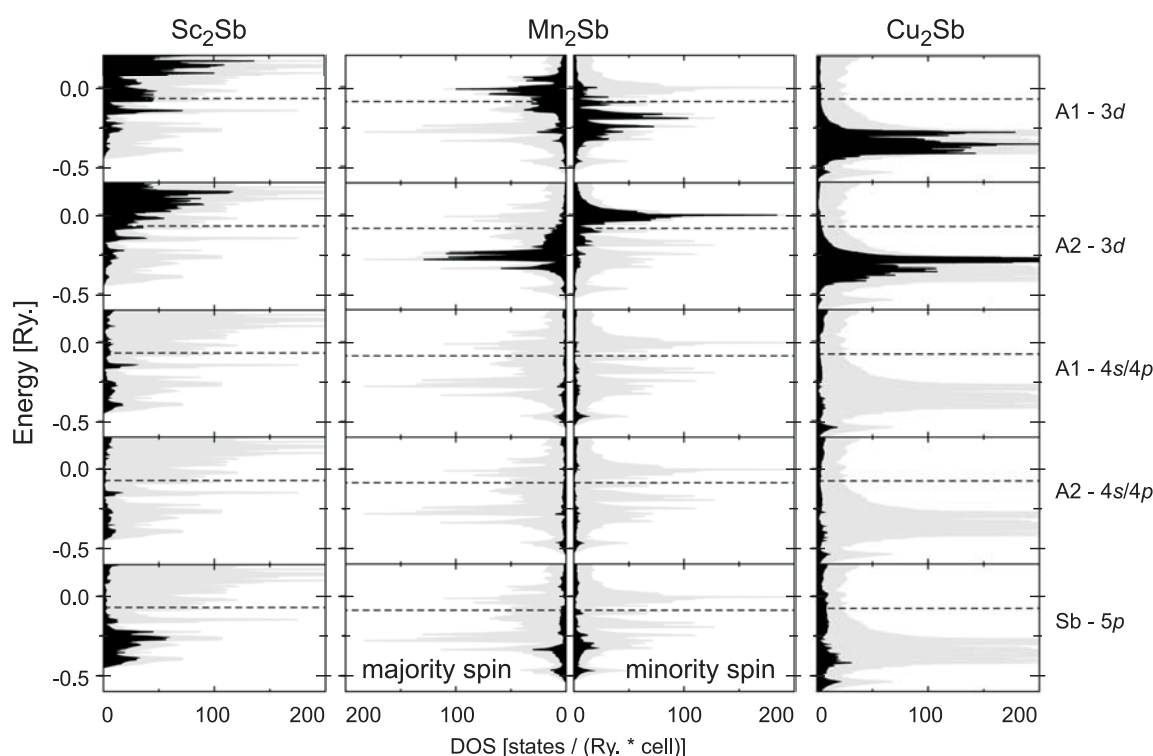


Figure 87: Total densities of states (grey) and selected partial densities of states (black) of Sc_2Sb , Mn_2Sb and Cu_2Sb , as obtained from DFT band structure calculations (TB-LMTO-ASA). The dashed line indicates the Fermi level.

To investigate how local bonding patterns influence the geometric structure, the corresponding scalar fields of the Electron Localization Function (ELF) were analyzed. Selected domains of the ELF are shown in Fig. 88. Two center Si–Si bonds with a bond order of 1/2 were deduced from the ELF of ZrSiS . In addition, the charge

distribution as obtained from the topological analysis of the ELF and of the electron density justifies the formal description of ZrSiS within the Zintl-Klemm concept as $[\text{Zr}^{4+}\text{S}^{2-}]^{2+}[\text{Si}]^{2-}$. Due to the strong interaction in the Si (A1) planes, ZrSiS holds one of the extreme positions within the structure map displayed in Fig. 85.

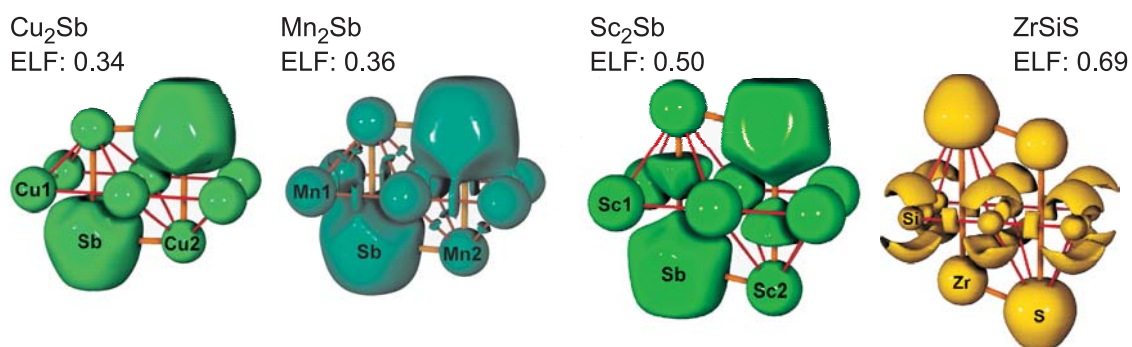


Figure 88: Structural fragments of Cu_2Sb , Mn_2Sb , Sc_2Sb and ZrSiS together with isosurfaces (domains) of the Electron Localization Function (ELF).

The other extreme position is occupied by Cu_2Sb , where no ELF attractors are found besides the domains that are attributed to the atoms. ELF domains in the valence region between the transition metal atoms appear in Mn_2Sb . The same ELF topology is observed in Cr_2As , Mn_2As and Fe_2As . Compounds like Sc_2Sb , containing early transition metal elements, exhibit large ELF basins in the pyramidal voids enclosed by the A1 and A2 atoms. The integrated valence electron density within this basin amounts to 1.3 electrons in the case of Sc_2Sb . This localization pattern, which also appears in YTiSi and YTiGe , is according to our detailed analysis an intrinsic property of the ELF topology of this family of compounds and is directly related to the bonding interaction within the planar 4^4 nets, formed by the A1 atoms.

When going from left to right in the first row of transition metals, the d -electrons become more localized. For the compounds A_2B under discussion, this leads, on one hand, to a continuous change of the charge transfer from the transition metal to the pnictogen atoms which in Cu_2Sb is even inverted. On the other hand, rather peculiar bonding conditions occur, which are reflected by the structural differences. We find multicenter bonding among the early transition metals and direct metal-metal interactions in the Cr, Mn and Fe representatives, whereas Cu_2Sb may be described as Cu atoms being embedded in metallic antimony.

-
- [1] Nuss, J., U. Wedig and M. Jansen. Zeitschrift für Kristallographie, submitted.
 - [2] Nuss, J. and M. Jansen. Zeitschrift für anorganische und allgemeine Chemie **628**, 1152-1157 (2002).
 - [3] Biltz, W. Raumchemie der festen Stoffe, Leopold Voss, Leipzig 1934.

Unusual lone pairs in tellurium

S. Deng, J. Köhler and A. Simon

Chalcogen elements exhibit a s^2p^4 valence electron configuration. The analysis of the chemical bonding within the VCDW (vector charge density wave) model in which the ns^2 pair is treated as a core state due to a large s - p separation results in a configuration np^4 with a threefold degeneracy, $(p_x^2p_y p_z)$, $(p_x p_y^2 p_z)$ and $(p_x p_y p_z^2)$. The existence and ordering of such p^2 -type lone pairs in the structures of the chalcogens have not been proven by well-defined quantities so far. Here we present results from *ab initio* calculations, which allow a quantitative description of this kind of lone pairs in a localized state, their breakdown and delocalization under pressure and their possible relevance for superconductivity.

The semiconducting ambient pressure phase Te-I is composed of helical chains with 283.5 pm intra- and 349.1 pm interchain distances. In the structure of metallic and

superconducting Te-II formed at approximately 4 GPa these discrete chains are condensed into puckered layers with shortest interlayer Te-Te distances of 333.3 pm and intralayer Te-Te distances ranging from 284.8 to 309.8 pm, see Fig. 89(a),(b).

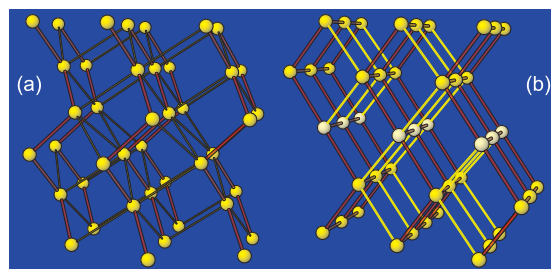


Figure 89: Perspective drawings of the crystal structures of (a) Te-I and (b) Te-II (Te1: light yellow spheres, Te2: yellow spheres). The red sticks correspond to the short Te-Te distances (284 pm in Te-I and 285 pm to 310 pm in Te-II) and the thinner yellow sticks to longer Te-Te distances (349 pm in Te-I and 333 to 340 pm in Te-II).

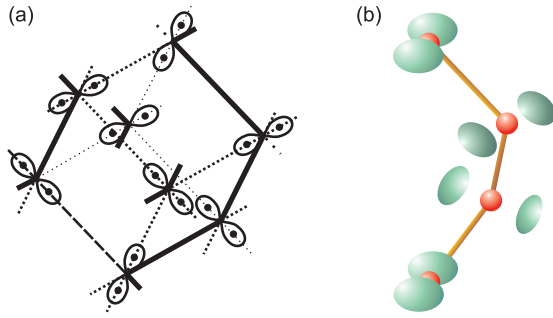


Figure 90: (a) Vector charge density wave (VCDW) on a cubic primitive lattice of tellurium. For clarity only lone pairs are shown with thick lines denoting the covalent bonds. (b) The calculated *ELF* isosurface corresponding to a value 0.8 is shown for a single helical chain of Te-I.

In Fig. 90(a) the lone pairs as described by the VCDW model for Te-I are shown and compared with the result of an *ab initio* TB-LMTO calculation visualized through *ELF* (electron localization function) in Fig. 90(b). For simplicity, the two single-electron components of the vector field on each lattice site have been omitted in Fig. 90(a). With respect to a primitive cubic arrangement of the atoms due to the repulsion from the lone pairs four nearest neighbor distances around each site are lengthened, while the two single electron components are involved in bonds as indicated by thick lines. The VCDW thus removes the lone pair degeneracy by lowering the symmetry to trigonal.

As first suggested by Fukutome, the unusual lone pair in a np^4 configuration results from Coulomb interaction U among the p electrons, as the four valence electrons should otherwise distribute evenly in the p_x , p_y and p_z orbitals with an occupancy of $4/3$. Here, we calculate U_p in the Te atom and, using the *ab initio* constrained occupation number approach [1] in Te-I. For the atom the bare parameter $U_p = 8.31$ eV is calculated to be compared with the experimental value 8.59 eV, referring to the fitted experimental atomic spectra. The repulsion is strongly reduced by Coulomb screening, which leads to a calculated value $U_p = 1.16$ eV for the atom and $U_p^{\text{solid}} = 1.09$ eV for Te-I, which is an estimation for the stability of its lone pairs. The small difference between both values clearly indicates that the screening is mainly due to interactions of the electrons in the single atom, and the repulsive Coulomb interaction is the origin of the lone pair. Energy changes of the order of 1 eV can break the lone pair, e.g. through a closer mutual approach of the Te atoms under high pressure. Band structure calculations for Te-I and Te-II show the relevant changes in chemical bonding. Within the energy window between -14 and 4 eV the band structure of Te-I is composed of four bunches of bands; see Fig. 91(a). Each bunch can be viewed as comprising three bands due to the helical modulation of a straight Te chain.

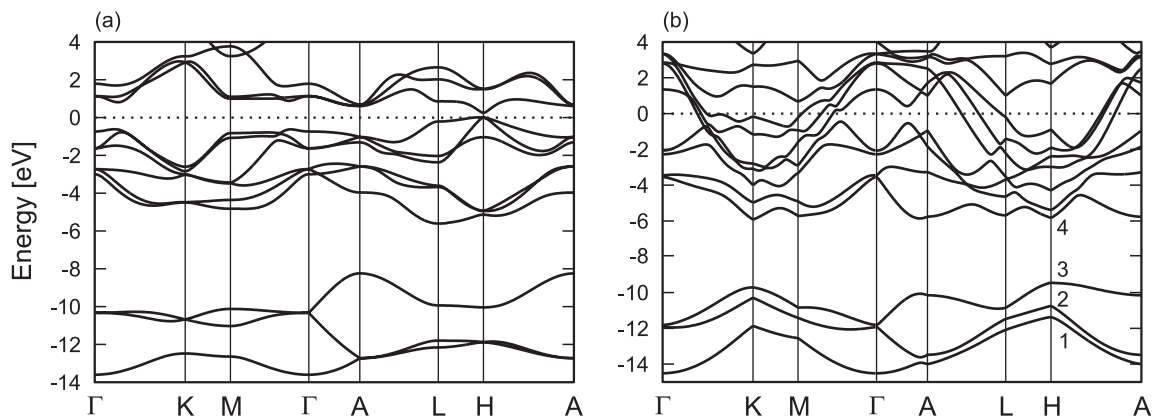


Figure 91: (a) Band structure from FP-LMTO calculations for Te-I, the band states at H point are numbered consecutively from bottom to top with only 1 to 4 indicated for clarity; (b) FP-LMTO band structure of Te-II calculated along specific symmetry lines.

The bunch centered at -12 eV is of mainly s -character, while those at -3 , -1 and 1 eV are of p -type bonding, non-bonding (lone pair) and antibonding character, respectively. The calculated band gap from TB-LMTO is 0.336 eV in very good agreement with the experimental value, 0.334 eV. As an important result, both our TB- and FP-LMTO calculations clearly show the importance of an s -component to the frontier orbitals as otherwise the band structure is dramatically changed, and Te-I becomes a metal without s - p hybridization. This result is in agreement with the features shown in Fig. 90(b), where the Te-Te-Te angle is 103.14° instead of 90° and the relative orientations of the lone pairs shown in the *ELF* plot deviate from 90° predicted by the VCDW model, though qualitatively this model agrees quite well with *ELF*. Clearly, the treatise of the $5s^2$ state as core-like is inappropriate as the s - p hybridization stabilizes the lone pair and changes the orientations of lone pairs.

The localized lone pairs are lost under pressure in Te-II, which is metallic. The change is clearly seen in the calculated band structure for Te-II presented in Fig. 91(b) with the same choice of a first Brillouin zone as for Te-I. The separation of s - and p -bands remains for Te-II, and the s -bands at the bottom do not change too much except for the removal of degeneracy at the zone boundaries due to the triclinic distortion. In particular, the band dispersions along Γ -A are rather unchanged reflecting similar interactions in the chain directions for both modifications. However, pronounced changes occur with the p -type bands due to the formation of interchain bonds in Te-II.

A comparison of the chemical bonding in Te-I and Te-II using COHP (crystal orbital Hamilton population) shows that in Te-I the intrachain interaction is much stronger than the interchain one. For Te-II the intra- and interchain interactions are comparable, however, with a more pronounced antibonding character around the Fermi level. The latter observation is easily rationalized in terms of an increased Coulomb repulsion between the lone pairs due to reduced

interchain distances. The rather small absolute values of COHP around the Fermi level as well as the band gap in Te-I and their changes from Te-I to Te-II together give another numeric evidence for the existence of lone-pairs in Te-I and their breakdown in Te-II. The calculated orbital composition reveals their p -character. The strong antibonding interaction transforms lone pair bands into highly dispersive ('steep') bands along several directions, e.g. H-A or A-L, see Fig. 91(b). In addition, parts of the p -type antibonding conduction band are pushed down in energy, e.g. at H, K, L, M points. This process results in a band with small dispersion along the Γ -K direction and the tiny flat feature along the M- Γ direction around the Fermi level. The lone pairs are broken into itinerant electrons. Indeed, *ELF* calculations for Te-II performed with the same value, 0.8 , as in Te-I reveal only insignificant lone pair characteristics for both kinds of Te atoms (see Fig. 89(b)).

Te-I is semiconducting, whereas Te-II is a metal and superconductor, and the band structure of the latter satisfies the condition for superconductivity in our flat/steep band scenario [2]. We have shown earlier that this condition is necessary but not sufficient. We suggest that the sufficient condition is intimately related with the lone pair configuration in Te-I and its 'virtual' presence via electron-phonon coupling in Te-II as has to be shown. The arguments can be mapped one-to-one onto other elements, e.g. bismuth and its change from a semimetal to a metal and superconductor under pressure and in the amorphous state.

-
- [1] Gunnarsson, O., O.K. Andersen, O. Jepsen and J. Zaanen. *Physical Review B* **39**, 1708-1722 (1989); Anisimov, V.I. and O. Gunnarsson. *Physical Review B* **43**, 7570-7574 (1991); McMahan, A.K., R.M. Martin and S. Satpathy. *Physical Review B* **38**, 6650-6660 (1988).
- [2] Simon, A. *Angewandte Chemie International Edition* **36**, 1788-1806 (1997); Deng, S., A. Simon and J. Köhler. *Angewandte Chemie International Edition* **37**, 640-643 (1998); Deng, S., A. Simon and J. Köhler. *Structure and Bonding* **114**, 103-141 (2005).

Scientometrics

An individual's research impact in a number: the Hirsch index

W. Marx

The number of articles published by a researcher provides only a measure of his productivity – it does not allow to judge the influence or quality of his work. The number of citations, however, can be seen as a measure for the resonance or the impact an article, a researcher or a research institute has generated so far. Although the number of citations cannot be equated with the final importance and quality of articles, citation data are frequently used for research evaluation. However, the reliable determination and competent interpretation of such data requires some experience and awareness of possibilities and limits.

Recently, an index has been introduced by Jorge Hirsch (a condensed matter theoretical physicist at the University of California, San Diego) as a measure of the cumulative impact of a researcher's scientific work within a given discipline. The Hirsch index* (h-index, h-number) can be easily obtained, provided one has access to the *Web of Science* (WoS), the search platform offered by *Thomson Scientific Inc.* (the former ISI, *Institute for Scientific Information*). The WoS includes the *Science Citation Index* (SCI) and has probably become the most versatile and user friendly citation analysis tool.

The *Web of Science* provides two basic search modes: The *General Search* mode and the *Cited Reference Search* mode. The *General Search* mode allows searching the articles in source journals (the so-called source items) published between 1900 to the present. The search results do not include books and conference proceedings not published in regular journals. Under *General Search* all search fields (topic, title,

author, address, source, publication year) can be searched and combined by logical operators (AND, OR, NOT). This is the standard search mode of literature databases. The *Cited Reference Search* mode enables access to the references appeared in source journal articles. All references, including the items published in non-source journals, the books or any other published material are searchable in this mode.

The h-index is simply defined as the number of articles in ISI source journals that have had h citations or more. For example, a researcher with an h-index of 40 will have published 40 articles that have received at least 40 citations each. The index can be determined by searching a given author name under the WoS General Search mode and sorting the selected articles by *times cited* using the WoS sort command. The result is unambiguous, provided that there are either no highly cited namesakes or they can be easily removed (e.g. by combining the author name with the relevant locations using the address search field). The *Cited Reference Search* mode is not practical to determine an h-index.

The h-index can be seen as a valuable contribution to the efforts of measuring the impact of a researcher by using citation data and as a useful alternative to other citation based indicators for research evaluation. It reflects a researcher's contribution based on a broad body of publications rather than based on a few high-impact papers. It avoids an overestimation of single or few highly-cited papers, sometimes being methodological contributions or reviews. The h-index favors researchers who consistently produce influential papers.

*Hirsch, J.E. Proceedings of the National Academy of Sciences **102**, 16569-16572 (2005).

According to the PNAS web site, the article by Hirsch has been the most often downloaded article from the PNAS server during November 2005.

There are, however, some important aspects to be taken into consideration when using the h-index to measure the impact of individual researchers:

- It should be emphasized that the measure of a researcher's impact by a single number can only be a rough approach to evaluate his work. For a comprehensive citation analysis, the topics of the highly-cited papers, whether mainstream research or not, their document types (articles, reviews or letters), the time-dependence of the overall impact, the fraction of first-author papers, the percentage of the non-cited papers, and other data should be taken into consideration. This obviously demands extra efforts, but it is essential for producing meaningful results.
- The h-index increases with the length of the scientific activity of a researcher, as predicted by Hirsch. This was verified by our own empirical studies, whereby the h-index increases approximately linearly with time and levels off when the researcher publishes less papers or stops publishing (either because of death, retirement or of having become an administrator). This time dependence of the h-index must be considered when comparing researchers with different periods of scientific activity.
- The impact of early papers and, thereby, the overall impact of early pioneers are highly underestimated. The proliferation of science implies a proliferation of citable papers, resulting in increasing ratios of references per paper (reference count) and citations per paper, respectively. These ratios have approximately doubled within the last half century. Hence, the Hirsch numbers of researchers who lived at different time periods are hardly comparable.
- Different disciplines have different citation patterns with different average citations per paper, varying by a factor of 10 between mathematics and molecular biology or genetics. Hence, also the average h-index depends strongly on the research discipline.

A comparison between different disciplines should be avoided unless a reliable relative calibration is available.

- The mean number of authors per paper differs considerably. In disciplines like high energy physics or genetics, papers sometimes are published by fifty or even more authors. A high number of concurrent authors is expected to increase the mean h-index in that sub-discipline. Thus, even the h-index of authors in different sub-disciplines may not be comparable.
- The distribution of citations to the articles of a researcher is always highly skewed: a large fraction of citations going to a small fraction of publications. The skewness of the citation distribution differs considerably between different authors. It strongly depends on the amount of cooperation with co-authors and personal publication practices (distributing research results on more or less papers). More data are needed to determine the influence of the skewness of the citation distribution on the h-index.

Nevertheless, the new index proposed by Hirsch has some advantages compared to other citation based indicators that are being used for research evaluation and are not clearly defined or not as easy to determine (e.g. the number of citations per paper or the impact time-curve). The index is a rough citation based measure for the impact of research activities. Naturally, research evaluation has to consider in addition other criteria than impact data. The latter should not be taken as an alternative for checking the scientific content by peers but as an additional and independent indicator ('informed peer review').

The h-index may be consulted to measure and compare the overall contribution of larger ensembles of scientific papers. The index can be extended to groups of researchers or research institutes, to scientific journals (instead of consulting their *Journal Impact Factors*, which are based on short time periods of about two years), to small countries, and to research topics. Further studies are needed to find out the usefulness for these purposes.